The Earliest Stage of Planet Formation: Numerical Simulations of Disk-planet Interaction and Observations of Protoplanetary Disks

Ruobing Dong

A Dissertation

Presented to the Faculty

of Princeton University

in Candidacy for the Degree

of Doctor of Philosophy

Recommended for Acceptance

by the Department of

Astrophysical Sciences

Advisers: Roman R. Rafikov

September 2013

Abstract

Planets form in protoplanetary disks. In disks, planets excite structures such as spiral density waves, and may clear material around their orbits to form gaps, through gravitational disk-planet interactions. By identifying these structures and comparing them with disk-planet interaction theory, we can study where, when, and how planets form in disks. In this work, we present studies of disk-planet interactions using numerical hydrodynamic simulations, and possible planet-induced signals in protoplanetary disks by direct imaging of disks.

With very high spatial resolution, accurate numerical solver, and precise planetary potential, we carry out 2D shearing sheet simulations to provide detailed quantitative comparisons of numerical results with both linear and nonlinear analytical theories on the density waves excited by planets. We achieve very good agreement with theories on primary physical variables. Also, we study issues which are ignored by the theories, such as the nonlinear effect in the linear stage. The effects of various numerical parameters are extensively investigated, and we provide a framework for future code test in this field.

Transitional disks are protoplanetary disks that have depleted inner regions. We obtain high spatial resolution Subaru images of a sample of transitional disks, as part of the SEEDS project, and carry out radiative transfer simulations to study their structure. We find that in some cases cavities are not present in the scattered light, which requires the decoupling between the sub-um-sized and mm-sized grains inside the cavity. For another group of transitional disks in which Subaru does reveal the cavities at NIR, we focus on whether grains at different sizes have the same spatial distribution or not (i.e. the cavity size and the depletion factor inside the cavity for different dust populations). With our modeling results, we examine various transitional disk formation theories, and in particular, their possible planets origin.

Acknowledgments

There are many people that I would like to thank when looking back to my years at Princeton. First and foremost, I am deeply indebted to my thesis advisor Roman Rafikov, who is always there whenever I need him (yes, I mean ALWAYS). Roman's continuous support of my research all these years, as well as his patience, motivation, enthusiasm, and immense knowledge, are essential for the completion of this work. I simply could not ask for a better advisor. It is also a great pleasure for me to thank the rest of my thesis committee, Jill Knapp, Jim Stone, and Ed Turner, for their encouragement, guidance, and insightful suggestions throughout my Ph.D. study. The road to my graduate degree has been long and winding, with major difficulties on the way. Without the firm support from my wonderful committee, I could not make it today. They are not only advisors, but also my dear friends.

Apart from having a wonderful committee, this thesis would not be possible without the help from many others. Firstly, I would like to sincerely thank Pascale Garaud and Doug Lin, for organizing the International Summer Institute for Modeling in Astrophysics (ISIMA) at Kavli Institute for Astronomy and Astrophysics, Beijing. It was at this wonderful summer school that I was connected with a key mentor in my career, Lee Hartmann, and two of my most important collaborators, Takayuki Muto and Zhaohuan Zhu, who essentially helped me jump-start the observational part of my thesis. I am particularly grateful to Lee, who has gone far beyond being a summer school advisor to me, and has helped me ever after in every way he can. The observational part of my thesis was only made possible by the Subaru-based SEEDS project, with great support from Motohide Tamura. In SEEDS, I enjoyed very fruitful collaboration and great relationships with many friends, in particular Tim Brandt, Markus Janson, Michael McElwain, and Jun Hashimoto. Specially, Jun's insights in observations and enthusiasm in science have made many great things possible. I would also like to express my heartfelt gratitude to another key figure in my thesis work – Barbara Whitney. I bothered her all the time with silly and tedious questions, and what I have got in return is persistent support and encouragement. Thank you very much Barb!

During my years in Princeton, I am blessed to have the opportunities to work with many others in our department. When I started my first semester project in Peyton Hall with Jim Stone, I just arrived in this new country, and could hardly make any sense out of the classroom, needless to say doing research. With great patience and kindness, Jim taught me hand by hand, and helped me go through this transition period. I am also extremely grateful to Bruce Draine, whose carefulness and preciseness in science have greatly shaped my view of how to do research; to Jenny Greene, who rescued me when I was in trouble in my research, and encouraged me a lot during my job application; to Michael Strauss, who always had time for me when I knocked on the door and for numerous times poked others to find answers to my questions; and with my deepest gratitude, to Jim Gunn, who together with Jill not only guided me through the world of

astronomy, but also took great care of me in life. Whenever I had any problem, Jill and Jim were always there for me.

My sincere thanks also go to Luis Ho, John Mulchaey, and Jesper Rasmussen, for offering me the summer research opportunities in the Carnegie Observatory (twice!) and leading me working on diverse exciting projects. Particularly, I am glad to thank Luis for his career advises all these years following my summer at OCIW. By sharing with me their insightful opinions and giving me very valuable suggestions, many people have greatly helped me in my thesis research, in particular Sean Andrews, Tilman Birnstiel, Brendan Bowler, John Carpenter, Eugene Chiang, Catherine Espaillat, Andrea Isella, James Owen, Cristobal Petrovich, and many, many others. I deeply thank them all. Also, I would like to thank Charlotte Zanidakis for easing the thesis submission process.

I must thank all my fellow colleges in the basement, who have made Princeton a very special place for me. In particular, special acknowledgment to Mike Belyaev, my kayaking/hiking/climbing/shopping partner, in particular for being generous enough to share Roman with me, and being brave enough to sit in my car on high ways when I was practicing driving; to Simone Ferraro, for having me over dinner at your places numerous times; to Pete Pattarakijwanich, for reminding me to go grocery every week; to Fabian Schmidt, for all the fun we had on the walls; to Elisa Chisari, Ena Choi, and Wenhua Ju, for your greatest friendship; to Jason Li, for sharing your views of the world with me; to Tim Brandt, for your excellent suggestions to my research projects and for being a wonderful roommate; to Xuening Bai, Feng Dong, Shirley Ho, KG Lee, Xin Liu, and Yue Shen for your help in my early days in Peyton hall; and to Konstantin Bochkarev, Jose Garmilla, Munan Gong, Brandon Hensley, Colin Hill, Alex Howe, Chelsea Huang, Yanfei Jiang, Andrea Kulier, Cristobal Petrovich, Sasha Philippov, Sudhir Raskutti, Emmanuel Schaan, Blake Sherwin, Kedron Silsbee, Ai-Lei Sun, Chris White, Daan Meerburg, Jose Prieto, as well as the folks upstairs, Matt Kunz, Kengo Tomida, and the folks all the way in IAS, Subo Dong, Hanno Rein, Dave Spiegel, the list can simply just go on and on and on...

And finally, needless to say, I am deeply indebted to my parents, for their persistent support, as always.

Preface

The thesis is organized into four chapters and is based on seven papers (five first author, one second author, and one third author paper) that have been accepted or submitted to *The Astrophysical Journal*. Chapter 1 is a introduction of the general topic. Chapter 2 is based on two published work (both are first author), with the necessary rearrangement to make the content clear and to avoid repetition. Chapters 3 is based on two published work with little modification (one first author, one third author). Chapter 4 is based on two published work (one first author, one second author) and one submitted work (first author), again with the necessary rearrangement to make the content clear and to avoid repetition. Chapter 2 was completed under the guidance of Roman Rafikov and Jim Stone, and Chapters 3-5 under the guidance of Roman Rafikov and are carried out in the SEEDS collaboration. Some of the research from this thesis has been presented on a serious of conferences, including

1. Apr 2013 2013 Transformational Science with ALMA Conference, The Big Island, Hawaii,
2. Jan 2013 221st AAS Meeting, Long Beach, CA,
3. Aug 2012 IAU Symposium 293, Beijing, China,
4. Jun 2012 Origins of stars and their planetary systems, McMaster University, Hamilton, Canada,
5. Oct 2011 The 2nd SEEDS General Workshop, Max Planck Institute for Astronomy, Heidelberg, Germany,
6. Jun 2011 The International Summer Institute for Modeling in Astrophysics, Kavli Institute for Astronomy and Astrophysics, Peking University, Beijing, China,
7. May 2010 KIAA-DoA-NAOC Joint Program on Dynamics of Astrophysical Disks, Kavli Institute for Astronomy and Astrophysics, Peking University, Beijing, China,

Chapter 2

In this chapter I present hydro numerical simulations of disk-planet interactions, and in particular discuss the properties of the density waves excited by the planets in disks in both the linear and nonlinear regimes. This chapter is entirely based on the publications Dong et al. (2011b) and Dong et al. (2011a) (taken verbatim most of the time), with some necessary modifications in order to confine the two papers into a coherent chapter. All of the content in this chapter was written by me, and I performed all simulations. The supercomputers used to perform the simulations are *Artemis*, which belongs to Princeton University and *Pleiades*, which belongs to NASA.

Chapter 3

In this chapter, I identify the "missing cavity" phenomenon found in Subaru direct imaging of a group of transitional disks, and present a general disk model to account for this finding. This chapter is almost entirely based on the publication of Dong et al. (2012b). Some of the arguments

presented in this chapter, particularly the possibility of enabling the dust filtration model to explain the apparent contrast between the scattered light image and the dust thermal continuum emission observation, are also discussed in Zhu et al. (2012), in which I am the third author and performed the radiative transfer modeling part in that paper. All of the content in this chapter was written by me, and I performed all simulations. The observational results used in these works are produced by Subaru telescope as part of the SEEDS research program, which is mainly carried out by the National Astronomical Observatory of Japan (NAOJ), Princeton University, and Max Planck Institute of Astrophysics.

Chapter 4

In this chapter, I present radiative transfer modeling of the observations of the transitional disk PDS 70. The physical structure of the disk are modeled based on both the spectral energy distribution, and the H-band Subaru scattered light image. Based on the disk model, various transitional disk formation theories are examined, in particular their possible planets origin. This chapter is almost entirely based on the publication Dong et al. (2012a). Some discussions of the chapter also appear in Hashimoto et al. (2012), in which I am the second author, and performed the modeling part and relevant discussion of transitional disk origin in that publication. All content and derivations contained in this chapter are my own work.

Chapter 5

In this chapter, I present radiative transfer modeling of the observations of the transitional disk Upper Scorpius J16042165-2130284. Spatially resolved observations at both NIR and sub-mm wavelengths are combined to study the distribution of the small (sub-micron-sized) and big (mm-sized) dust. This chapter contains sections taken verbatim from a manuscript that has been submitted, Dong et al. (2013). Some ideas and arguments in this chapter, as well as in chapters 3 and 4, have also been discussed in Tanii et al. (2012); Mayama et al. (2012); Grady et al. (2013); Follette et al. (2013), in all of which I am a co-author and contribute mostly in the modeling and discussion sections. All content and derivations contained in this chapter are my own work.

Bibliography

Dong, R., Hashimoto, J., Rafikov, R., Zhu, Z., Whitney, B., Kudo, T., Muto, T., Brandt, T., McClure, M. K., Wisniewski, J., Abe, L., Brandner, W., Carson, J., Egner, S., Feldt, M., Goto, M., Grady, C., Guyon, O., Hayano, Y., Hayashi, M., Hayashi, S., Henning, T., Hodapp, K. W., Ishii, M., Iye, M., Janson, M., Kandori, R., Knapp, G. R., Kusakabe, N., Kuzuhara, M., Kwon, J., Matsuo, T., McElwain, M., Miyama, S., Morino, J.-I., Moro-Martin, A., Nishimura, T., Pyo, T.-S., Serabyn, E., Suto, H., Suzuki, R., Takami, M., Takato, N., Terada, H., Thalmann, C., Tomono, D., Turner, E., Watanabe, M., Yamada, T., Takami, H., Usuda, T., & Tamura, M. 2012a, ApJ, 760, 111

Dong, R., Rafikov, R., & et al. 2013, (Submitted to ApJ)

Dong, R., Rafikov, R., Zhu, Z., Hartmann, L., Whitney, B., Brandt, T., Muto, T., Hashimoto, J., Grady, C., Follette, K., Kuzuhara, M., Tanii, R., Itoh, Y., Thalmann, C., Wisniewski, J., Mayama, S., Janson, M., Abe, L., Brandner, W., Carson, J., Egner, S., Feldt, M., Goto, M., Guyon, O., Hayano, Y., Hayashi, M., Hayashi, S., Henning, T., Hodapp, K. W., Honda, M., Inutsuka, S., Ishii, M., Iye, M., Kandori, R., Knapp, G. R., Kudo, T., Kusakabe, N., Matsuo, T., McElwain, M. W., Miyama, S., Morino, J.-I., Moro-Martin, A., Nishimura, T., Pyo, T.-S.,

Suto, H., Suzuki, R., Takami, M., Takato, N., Terada, H., Tomono, D., Turner, E. L., Watanabe, M., Yamada, T., Takami, H., Usuda, T., & Tamura, M. 2012b, ApJ, 750, 161

Dong, R., Rafikov, R. R., & Stone, J. M. 2011a, ApJ, 741, 57

Dong, R., Rafikov, R. R., Stone, J. M., & Petrovich, C. 2011b, ApJ, 741, 56

Follette, K. B., Tamura, M., Hashimoto, J., Whitney, B., Grady, C., Close, L., Andrews, S. M., Kwon, J., Wisniewski, J., Brandt, T. D., Mayama, S., Kandori, R., Dong, R., Abe, L., Brandner, W., Carson, J., Currie, T., Egner, S. E., Feldt, M., Goto, M., Guyon, O., Hayano, Y., Hayashi, M., Hayashi, S., Henning, T., Hodapp, K., Ishii, M., Iye, M., Janson, M., Knapp, G. R., Kudo, T., Kusakabe, N., Kuzuhara, M., McElwain, M. W., Matsuo, T., Miyama, S., Morino, J.-I., Moro-Martin, A., Nishimura, T., Pyo, T.-S., Serabyn, E., Suto, H., Suzuki, R., Takami, M., Takato, N., Terada, H., Thalmann, C., Tomono, D., Turner, E. L., Watanabe, M., Yamada, T., Takami, H., & Usuda, T. 2013, ApJ, 767, 10

Grady, C. A., Muto, T., Hashimoto, J., Fukagawa, M., Currie, T., Biller, B., Thalmann, C., Sitko, M. L., Russell, R., Wisniewski, J., Dong, R., Kwon, J., Sai, S., Hornbeck, J., Schneider, G., Hines, D., Moro Martín, A., Feldt, M., Henning, T., Pott, J.-U., Bonnefoy, M., Bouwman, J., Lacour, S., Mueller, A., Juhász, A., Crida, A., Chauvin, G., Andrews, S., Wilner, D., Kraus, A., Dahm, S., Robitaille, T., Jang-Condell, H., Abe, L., Akiyama, E., Brandner, W., Brandt, T., Carson, J., Egner, S., Follette, K. B., Goto, M., Guyon, O., Hayano, Y., Hayashi, M., Hayashi, S., Hodapp, K., Ishii, M., Iye, M., Janson, M., Kandori, R., Knapp, G., Kudo, T., Kusakabe, N., Kuzuhara, M., Mayama, S., McElwain, M., Matsuo, T., Miyama, S., Morino, J.-I., Nishimura, T., Pyo, T.-S., Serabyn, G., Suto, H., Suzuki, R., Takami, M., Takato, N., Terada, H., Tomono, D., Turner, E., Watanabe, M., Yamada, T., Takami, H., Usuda, T., & Tamura, M. 2013, ApJ, 762, 48

Hashimoto, J., Dong, R., Kudo, T., Honda, M., McClure, M. K., Zhu, Z., Muto, T., Wisniewski, J., Abe, L., Brandner, W., Brandt, T., Carson, J., Egner, S., Feldt, M., Fukagawa, M., Goto, M., Grady, C. A., Guyon, O., Hayano, Y., Hayashi, M., Hayashi, S., Henning, T., Hodapp, K., Ishii, M., Iye, M., Janson, M., Kandori, R., Knapp, G., Kusakabe, N., Kuzuhara, M., Kwon, J., Matsuo, T., Mayama, S., McElwain, M. W., Miyama, S., Morino, J.-I., Moro-Martin, A., Nishimura, T., Pyo, T.-S., Serabyn, G., Suenaga, T., Suto, H., Suzuki, R., Takahashi, Y., Takami, M., Takato, N., Terada, H., Thalmann, C., Tomono, D., Turner, E. L., Watanabe, M., Yamada, T., Takami, H., Usuda, T., & Tamura, M. 2012, ApJ, 758, L19

Mayama, S., Hashimoto, J., Muto, T., Tsukagoshi, T., Kusakabe, N., Kuzuhara, M., Takahashi, Y., Kudo, T., Dong, R., Fukagawa, M., Takami, M., Momose, M., Wisniewski, J. P., Follette, K., Abe, L., Akiyama, E., Brandner, W., Brandt, T., Carson, J., Egner, S., Feldt, M., Goto, M., Grady, C. A., Guyon, O., Hayano, Y., Hayashi, M., Hayashi, S., Henning, T., Hodapp, K. W., Ishii, M., Iye, M., Janson, M., Kandori, R., Kwon, J., Knapp, G. R., Matsuo, T., McElwain, M. W., Miyama, S., Morino, J.-I., Moro-Martin, A., Nishimura, T., Pyo, T.-S., Serabyn, E., Suto, H., Suzuki, R., Takato, N., Terada, H., Thalmann, C., Tomono, D., Turner, E. L., Watanabe, M., Yamada, T., Takami, H., Usuda, T., & Tamura, M. 2012, ApJ, 760, L26

Tanii, R., Itoh, Y., Kudo, T., Hioki, T., Oasa, Y., Gupta, R., Sen, A. K., Wisniewski, J. P., Muto, T., Grady, C. A., Hashimoto, J., Fukagawa, M., Mayama, S., Hornbeck, J., Sitko, M. L.,

Russell, R. W., Werren, C., Curé, M., Currie, T., Ohashi, N., Okamoto, Y., Momose, M., Honda, M., Inutsuka, S.-i., Takeuchi, T., Dong, R., Abe, L., Brandner, W., Brandt, T. D., Carson, J., Egner, S. E., Feldt, M., Fukue, T., Goto, M., Guyon, O., Hayano, Y., Hayashi, M., Hayashi, S. S., Henning, T., Hodapp, K. W., Ishii, M., Iye, M., Janson, M., Kandori, R., Knapp, G. R., Kusakabe, N., Kuzuhara, M., Matsuo, T., McElwain, M. W., Miyama, S., Morino, J.-i., Moro-Martín, A., Nishimura, T., Pyo, T.-S., Serabyn, E., Suto, H., Suzuki, R., Takami, M., Takato, N., Terada, H., Thalmann, C., Tomono, D., Turner, E. L., Watanabe, M., Yamada, T., Takami, H., Usuda, T., & Tamura, M. 2012, PASJ, 64, 124

Zhu, Z., Nelson, R. P., Dong, R., Espaillat, C., & Hartmann, L. 2012, ApJ, 755, 6

Contents

Chapter 1

Introduction

The quest for "other worlds" – planets around other stars, is among the most exciting and fastest growing fields in all of astrophysics. Planets form in protoplanetary disks, which are gaseous disks surrounding newly born stars. In disks, planets excite asymmetric structures such as spiral density waves (Goldreich & Tremaine, 1979, 1980), and may clear material around their orbits to form gaps (Lin & Papaloizou, 1986b,a; Ward, 1997), through gravitational disk-planet interactions. Due to the high level of variability of young stellar objects and the faintness of the planets relative to their host stars, it is very difficult to find protoplanets directly through methods such as radial velocity or transit observation. In contrast, planet-induced distortions in disks may be detectable in resolved observations with high spatial resolution. By identifying these structures and comparing them with theoretical models of disk-planet interactions, we can study where, when, and how planets form in disks, thus it opens up a novel path for constraining theoretical planet formation models. Further, since the properties of these structures depend on the properties of the disks, such as the distribution of material, temperature, and the nature of the turbulence, better understandings of disks themselves can be obtained from this study. This thesis presents both theoretical/numerical studies of disk-planet interactions in protoplanetary disks, and an endeavor of searching for possible signals from disk-planet interactions in resolved observations of disks.

Chapter 2 of this thesis (based on the publication of Dong et al. 2011b,a) presents a numerical study of the properties of the density waves excited by a low-mass planet in protoplanetary disks. With very high spatial resolution, accurate numerical solver, and precise planetary potential, we carry out 2D shearing sheet simulations to provide detailed quantitative comparisons of numerical results with both linear and nonlinear analytical theories on the density waves excited by planets in protoplanetary disks. We achieve very good agreement (at the level of *several percent*) with theories on *primary* physical variables. Also, we study issues which are ignored by the theories, such as the nonlinear effect in the linear stage. The effects of various numerical parameters are extensively investigated, and we provide a framework for future code test in the field of planet-disk interactions. Finally, we discover a commonly ignored but important numerical issue in simulations, which if not handled correctly will lead to incorrect simulation results and an artificial gap opening phenomenon.

Now, thanks to the advanced instruments that have recently come online, we have just entered a golden age in looking for signals of the forming planets in disks by studying the structure of disks using spatially resolved observations. A particular interesting group of objects which may bear the answers to a lot of unresolved issues in planet formation are transitional disks, which are protoplanetary disks that have depleted inner regions (i.e. cavities or gaps). Their existence was first suggested by their spectral energy distribution (SED, Strom et al. 1989, Skrutskie et al. 1990), and has subsequently been confirmed by resolved observations of the cavities at various

wavelengths (Andrews et al., 2011; Williams & Cieza, 2011). In the past few years, several ideas on the formation of transitional disks have been proposed, such as photoevaporation (Clarke et al., 2001; Alexander & Armitage, 2007; Owen et al., 2010), grain growth and evolution (Birnstiel et al., 2012), and maybe most excitingly, cavities or gaps opened by planet(s) (Zhu et al., 2011; Dodson-Robinson & Salyk, 2011).

Since 2010, Subaru has launched a major campaign – the SEEDS project (Strategic Explorations of Exoplanets and Disks with Subaru, Tamura 2009) – to directly image the polarized scattered light from a number of transitional disks at NIR wavelengths. The diffraction limited angular resolution (0.06", or about 8 AU at 140 pc, the typical distance to nearby star forming regions such as Taurus) and the small inner working angle (0.05"-0.1", or about 10 AU at 140 pc) in SEEDS enable us to well resolve the region where planets are likely to form.

Chapter 3 and 4 present some of the research done with the SEEDS project. Using radiative transfer simulations, we study the structure of transitional disks by simultaneously modeling the NIR Subaru images, the SED, and in some cases the sub-mm observations obtained from literature. We obtain physical disk+cavity structures, and constrain the spatial distribution of the dust grains, particularly inside the cavity and at the cavity edge. Chapter 3 (based on the publication Dong et al. 2012; Zhu et al. 2012) presents a finding that in some cases cavities are not present in the scattered light. In such cases we present a new model to simultaneously account for all observations. Decoupling between the sub-um-sized and mm-sized grains inside the cavity, which are responsible for resolved observations at different wavelengths, is required. This may necessitate a mechanism, such as dust filtration (Rice et al., 2006; Paardekooper & Mellema, 2006; Zhu et al., 2012), for differentiating the small and big dust in the cavity clearing process. Chapter 4 (based on the publications Dong et al. 2012; Hashimoto et al. 2012; Tanii et al. 2012; Mayama et al. 2012; Grady et al. 2013; Follette et al. 2013 presents the radiative transfer modeling results for another group of transitional disks, in which Subaru does reveal the cavities at NIR. In these cases, we focus on whether grains at different sizes have the same spatial distribution or not (i.e. the cavity size and the depletion factor inside the cavity for different dust populations). With our modeling results, we comment on various transitional disk formation theories, and in particular, their possible planets origin.

Bibliography

Alexander, R. D. & Armitage, P. J. 2007, MNRAS, 375, 500

Andrews, S. M., Wilner, D. J., Espaillat, C., Hughes, A. M., Dullemond, C. P., McClure, M. K., Qi, C., & Brown, J. M. 2011, ApJ, 732, 42

Birnstiel, T., Andrews, S. M., & Ercolano, B. 2012, A&A, 544, A79

Clarke, C. J., Gendrin, A., & Sotomayor, M. 2001, MNRAS, 328, 485

Dodson-Robinson, S. E. & Salyk, C. 2011, ApJ, 738, 131

Dong, R., Rafikov, R., Zhu, Z., Hartmann, L., Whitney, B., Brandt, T., Muto, T., Hashimoto, J., Grady, C., Follette, K., Kuzuhara, M., Tanii, R., Itoh, Y., Thalmann, C., Wisniewski, J., Mayama, S., Janson, M., Abe, L., Brandner, W., Carson, J., Egner, S., Feldt, M., Goto, M., Guyon, O., Hayano, Y., Hayashi, M., Hayashi, S., Henning, T., Hodapp, K. W., Honda, M., Inutsuka, S., Ishii, M., Iye, M., Kandori, R., Knapp, G. R., Kudo, T., Kusakabe, N., Matsuo,

T., McElwain, M. W., Miyama, S., Morino, J.-I., Moro-Martin, A., Nishimura, T., Pyo, T.-S., Suto, H., Suzuki, R., Takami, M., Takato, N., Terada, H., Tomono, D., Turner, E. L., Watanabe, M., Yamada, T., Takami, H., Usuda, T., & Tamura, M. 2012, ApJ, 750, 161

Dong, R., Rafikov, R. R., & Stone, J. M. 2011a, ApJ, 741, 57

Dong, R., Rafikov, R. R., Stone, J. M., & Petrovich, C. 2011b, ApJ, 741, 56

Follette, K. B., Tamura, M., Hashimoto, J., Whitney, B., Grady, C., Close, L., Andrews, S. M., Kwon, J., Wisniewski, J., Brandt, T. D., Mayama, S., Kandori, R., Dong, R., Abe, L., Brandner, W., Carson, J., Currie, T., Egner, S. E., Feldt, M., Goto, M., Guyon, O., Hayano, Y., Hayashi, M., Hayashi, S., Henning, T., Hodapp, K., Ishii, M., Iye, M., Janson, M., Knapp, G. R., Kudo, T., Kusakabe, N., Kuzuhara, M., McElwain, M. W., Matsuo, T., Miyama, S., Morino, J.-I., Moro-Martin, A., Nishimura, T., Pyo, T.-S., Serabyn, E., Suto, H., Suzuki, R., Takami, M., Takato, N., Terada, H., Thalmann, C., Tomono, D., Turner, E. L., Watanabe, M., Yamada, T., Takami, H., & Usuda, T. 2013, ApJ, 767, 10

Goldreich, P. & Tremaine, S. 1979, ApJ, 233, 857

Goldreich, P. & Tremaine, S. 1980, ApJ, 241, 425

Grady, C. A., Muto, T., Hashimoto, J., Fukagawa, M., Currie, T., Biller, B., Thalmann, C., Sitko, M. L., Russell, R., Wisniewski, J., Dong, R., Kwon, J., Sai, S., Hornbeck, J., Schneider, G., Hines, D., Moro Martín, A., Feldt, M., Henning, T., Pott, J.-U., Bonnefoy, M., Bouwman, J., Lacour, S., Mueller, A., Juhász, A., Crida, A., Chauvin, G., Andrews, S., Wilner, D., Kraus, A., Dahm, S., Robitaille, T., Jang-Condell, H., Abe, L., Akiyama, E., Brandner, W., Brandt, T., Carson, J., Egner, S., Follette, K. B., Goto, M., Guyon, O., Hayano, Y., Hayashi, M., Hayashi, S., Hodapp, K., Ishii, M., Iye, M., Janson, M., Kandori, R., Knapp, G., Kudo, T., Kusakabe, N., Kuzuhara, M., Mayama, S., McElwain, M., Matsuo, T., Miyama, S., Morino, J.-I., Nishimura, T., Pyo, T.-S., Serabyn, G., Suto, H., Suzuki, R., Takami, M., Takato, N., Terada, H., Tomono, D., Turner, E., Watanabe, M., Yamada, T., Takami, H., Usuda, T., & Tamura, M. 2013, ApJ, 762, 48

Hashimoto, J., Dong, R., Kudo, T., Honda, M., McClure, M. K., Zhu, Z., Muto, T., Wisniewski, J., Abe, L., Brandner, W., Brandt, T., Carson, J., Egner, S., Feldt, M., Fukagawa, M., Goto, M., Grady, C. A., Guyon, O., Hayano, Y., Hayashi, M., Hayashi, S., Henning, T., Hodapp, K., Ishii, M., Iye, M., Janson, M., Kandori, R., Knapp, G., Kusakabe, N., Kuzuhara, M., Kwon, J., Matsuo, T., Mayama, S., McElwain, M. W., Miyama, S., Morino, J.-I., Moro-Martin, A., Nishimura, T., Pyo, T.-S., Serabyn, G., Suenaga, T., Suto, H., Suzuki, R., Takahashi, Y., Takami, M., Takato, N., Terada, H., Thalmann, C., Tomono, D., Turner, E. L., Watanabe, M., Yamada, T., Takami, H., Usuda, T., & Tamura, M. 2012, ApJ, 758, L19

Lin, D. N. C. & Papaloizou, J. 1986a, ApJ, 307, 395

Lin, D. N. C. & Papaloizou, J. 1986b, ApJ, 309, 846

Mayama, S., Hashimoto, J., Muto, T., Tsukagoshi, T., Kusakabe, N., Kuzuhara, M., Takahashi, Y., Kudo, T., Dong, R., Fukagawa, M., Takami, M., Momose, M., Wisniewski, J. P., Follette, K., Abe, L., Akiyama, E., Brandner, W., Brandt, T., Carson, J., Egner, S., Feldt, M., Goto,

M., Grady, C. A., Guyon, O., Hayano, Y., Hayashi, M., Hayashi, S., Henning, T., Hodapp, K. W., Ishii, M., Iye, M., Janson, M., Kandori, R., Kwon, J., Knapp, G. R., Matsuo, T., McElwain, M. W., Miyama, S., Morino, J.-I., Moro-Martin, A., Nishimura, T., Pyo, T.-S., Serabyn, E., Suto, H., Suzuki, R., Takato, N., Terada, H., Thalmann, C., Tomono, D., Turner, E. L., Watanabe, M., Yamada, T., Takami, H., Usuda, T., & Tamura, M. 2012, ApJ, 760, L26

Owen, J. E., Ercolano, B., Clarke, C. J., & Alexander, R. D. 2010, MNRAS, 401, 1415

Paardekooper, S.-J. & Mellema, G. 2006, A&A, 453, 1129

Rice, W. K. M., Armitage, P. J., Wood, K., & Lodato, G. 2006, MNRAS, 373, 1619

Skrutskie, M. F., Dutkevitch, D., Strom, S. E., Edwards, S., Strom, K. M., & Shure, M. A. 1990, AJ, 99, 1187

Strom, K. M., Strom, S. E., Edwards, S., Cabrit, S., & Skrutskie, M. F. 1989, AJ, 97, 1451

Tamura, M. 2009, in American Institute of Physics Conference Series, Vol. 1158, American Institute of Physics Conference Series, ed. T. Usuda, M. Tamura, & M. Ishii, 11–16

Tanii, R., Itoh, Y., Kudo, T., Hioki, T., Oasa, Y., Gupta, R., Sen, A. K., Wisniewski, J. P., Muto, T., Grady, C. A., Hashimoto, J., Fukagawa, M., Mayama, S., Hornbeck, J., Sitko, M. L., Russell, R. W., Werren, C., Curé, M., Currie, T., Ohashi, N., Okamoto, Y., Momose, M., Honda, M., Inutsuka, S.-i., Takeuchi, T., Dong, R., Abe, L., Brandner, W., Brandt, T. D., Carson, J., Egner, S. E., Feldt, M., Fukue, T., Goto, M., Guyon, O., Hayano, Y., Hayashi, M., Hayashi, S. S., Henning, T., Hodapp, K. W., Ishii, M., Iye, M., Janson, M., Kandori, R., Knapp, G. R., Kusakabe, N., Kuzuhara, M., Matsuo, T., McElwain, M. W., Miyama, S., Morino, J.-i., Moro-Martín, A., Nishimura, T., Pyo, T.-S., Serabyn, E., Suto, H., Suzuki, R., Takami, M., Takato, N., Terada, H., Thalmann, C., Tomono, D., Turner, E. L., Watanabe, M., Yamada, T., Takami, H., Usuda, T., & Tamura, M. 2012, PASJ, 64, 124

Ward, W. R. 1997, Icarus, 126, 261

Williams, J. P. & Cieza, L. A. 2011, ARA&A, 49, 67

Zhu, Z., Nelson, R. P., Dong, R., Espaillat, C., & Hartmann, L. 2012, ApJ, 755, 6

Zhu, Z., Nelson, R. P., Hartmann, L., Espaillat, C., & Calvet, N. 2011, ApJ, 729, 47

Chapter 2

Density Waves Excited by Low-Mass Planets in Protoplanetary Disks

Abstract

Density waves excited by planets embedded in protoplanetary disks play a central role in planetary migration and gap opening processes. We carry out 2D shearing sheet simulations to study the linear and nonlinear regime of wave evolution with the grid-based code Athena, and provide detailed comparisons with the theoretical predictions. Low mass planets (down to $\sim 0.03 M_\oplus$ at 1 AU) and high spatial resolution (256 grid points per scale height) are chosen to seperate the linear and nonlinear regimes. To complement the existing numerical studies, we focus on the *primary* physical variables such as the spatial profile of the wave, torque density, and the angular momentum flux carried by the wave, instead of *secondary* quantities such as the planetary migration rate. In the linear regime, our results show *percent* level agreement with theory in both physical and Fourier space. New phenomena such as the change of the toque density sign far from the planet are discovered and discussed. Also, we explore the effect of the numerical algorithms, and find that a high order of accuracy, high resolution, and an accurate planetary potential are crucial to achieve good agreement with the theory. We find that the use of a too large time-step without properly resolving the dynamical time scale around the planet produces incorrect results, and may lead to spurious gap opening. Global simulations of planet migration and gap opening violating this requirement may be affected by spurious effects resulting in e.g. the incorrect planetary migration rate and gap opening mass. In the nonlinear regime, we found that the nonlinear evolution results in the wave steepening into a shock, causing damping and angular momentum transfer to the disk. On long timescales this leads to spatial redistribution of the disk density, causing migration feedback and potentially resulting in gap opening. Previous numerical studies concentrated on exploring these secondary phenomena as probes of the nonlinear wave evolution. Here we focus on exploring the evolution of the basic wave properties, such as its density profile evolution, shock formation, post-shock wave behavior, and provide comparison with analytical theory. The generation of potential vorticity at the shock is computed analytically and is subsequently verified by simulations and used to pinpoint the shock location. We confirm the theoretical relation between the shocking length and the planet mass (including the effect of the equation of state), and the post-shock decay of the angular momentum flux carried by the wave. The post-shock evolution of the wave profile is explored, and we quantitatively confirm its convergence to the theoretically expected N-wave shape. The accuracy of various numerical algorithms used to compute the nonlinear wave evolution is also investigated: we find that higher order spatial reconstruction and high resolution are crucial for capturing the shock formation correctly.

1 Introduction

The discovery of a number of "hot Jupiters" — extrasolar giant planets residing on very tight orbits — calls for understanding the dynamical pathways that brought these objects to their current orbits. Due to the difficulty of forming these planets *in situ*, it was suggested that potential hot Jupiter's form at larger separations from their stars and are subsequently transported inwards by some migration mechanism (Papaloizou & Terquem, 2006; Papaloizou et al., 2007). In protoplanetary disks, planets act as sources of nonaxisymmetric density waves (Goldreich & Tremaine, 1979, 1980, hereafter GT80), and coupling of planetary gravity to these waves acts to transfer angular momentum between the disk and the planet. This ultimately results in the orbital migration of embedded planets. At the same time, density waves generated by planets can affect the structure of the disk (potentially leading to gap opening) once the angular momentum that they carry is transferred to the disk material. Thus, better understanding of the density wave properties and processes of their excitation, propagation, and damping plays a crucial role in the global picture of planet formation.

Evolution of the density wave can be separated into the linear and nonlinear stages. The former applies to density waves excited by low-mass planets, which have not had enough time to propagate very far from their launching site (a more precise condition is formulated in §2). The linear theory of disk-planet interaction was pioneered by Goldreich & Tremaine (1979, GT80) who provided a description of the density wave excitation in two-dimensional (2D) gaseous disks. This theory has been subsequently refined in various ways, e.g. by calculating the asymmetry of planetary interaction with inner and outer portions of the disk (Ward 1986), and extending it to fully three-dimensional disks (Tanaka et al., 2002).

These studies concentrated on understanding the behavior of perturbed quantities Fourier decomposed in azimuthal angle (Artymowicz, 1993b,a; Korycansky & Pollack, 1993), often addressing only the *integral* wave properties such as the total angular momentum carried by the waves, or the differential Lindblad torque (Ward, 1986). Only recently has the linear evolution of the wave properties in *physical space*, namely the spatial dependence of the perturbed fluid velocity and surface density, been addressed by Goodman & Rafikov (2001, hereafter GR01) in the local shearing sheet approximation. Subsequently Ogilvie & Lubow (2002) and Rafikov (2002a) studied the shape of the density wake in the global setting. This paved way for subsequent exploration of the nonlinear wave evolution (GR01, Bate et al. 2002), understanding of which requires knowledge of the wave characteristics in physical space.

In parallel with these analytical and semi-analytical studies, numerous attempts to verify linear theory by direct hydrodynamical simulations were made. However, the majority of these studies compared with theoretical predictions only the *secondary* or derived properties of the planet-disk system related to the density wave excitation and evolution. For example, in their simulations Lin & Papaloizou (1993), Ward (1997), D'Angelo et al. (2003), and D'Angelo & Lubow (2008) measure the rate of planet migration due to its gravitational interaction with the disk — a quantity that is determined by the small difference between the summed (over all azimuthal harmonics) one-sided torques that the planet exerts on the inner and outer portions of the disk. Other studies (Lin & Papaloizou, 1993; Muto et al., 2010) tried to measure the planetary mass at which a gap opens in the disk — a process that depends not only on the magnitude of the angular momentum carried by the waves but also on the intricate details of their dissipation. In both situations the verification of the linear theory ends up being rather indirect.

It is certainly much more convincing and more robust to verify linear theory by comparing with its predictions the *primary* wave properties, such as the spatial distribution of the perturbed fluid properties derived from simulations. Recently some effort in this direction has been made. In particular, D'Angelo & Lubow (2008) investigated the distribution of the torque imparted by the planet on the disk as a function of radial distance. Muto et al. (2010) showed the spatial structure of the density perturbation associated with the wave obtained in their 2D simulations. Unfortunately, in both cases no quantitative comparison with linear theory predictions was provided.

On the other hand, the nonlinearity in the wave propagation can gradually change the state of the wave, and lead to evolution of the disk. In reality, density waves carry angular momentum as they travel away from the planet. Eventually, this angular momentum is deposited elsewhere in the disk, leading to the redistribution of the disk mass. For a migrating low-mass planet this density redistribution slightly enhances the disk surface density in front of the planet and reduces the density behind it, slowing down or even halting the migration (Hourigan & Ward, 1984; Ward & Hourigan, 1989; Ward, 1997; Rafikov, 2002b). This effect is called *migration feedback*. At higher planetary masses density redistribution by planetary torques is so severe that a gap may form near the planetary orbit. This shifts the planetary migration from type I to type II, and effectively slows the migration down, which may save planets from falling onto the central star (Lin & Papaloizou, 1986b,a; Ward, 1997).

It is important to emphasize that the change of the state of the disk by planetary density waves can only be accomplished by virtue of some damping processes (Goldreich & Nicholson, 1989), which can be either linear or nonlinear. Several possible linear wave damping mechanisms have been proposed, such as radiative damping (Cassen & Woolum, 1996) and viscous damping (Takeuchi et al., 1996). However, all of these mechanisms have drawbacks and may not be very efficient at dissipating angular momentum carried by the planet-generated density waves (GR01).

GR01 proposed another wave damping process, which results from the nonlinear wave evolution into a shock. This process could serve as a universal nonlinear wave damping mechanism working at regimes where alternatives fail (specifically, it does not require a background disk viscosity) (Larson 1989, 1990, GR01). GR01 analytically investigated the nonlinear propagation of the density wave in the local shearing-sheet approximation, and predicted the dependence of the shocking length $l_{\rm sh}$, the radial separation between the orbit of the planet and the point where the shock first appears, on the equation of state and the planet mass. Subsequently, Rafikov (2002a) extended the local treatment of GR01 into the global case to include the effects of surface density and temperature variations in the disk as well as the disk cylindrical geometry and nonuniform shear.

Previously, Lin & Papaloizou (1993) have suggested the following condition for the gap opening:

$$M_{\rm p} \gtrsim M_{\rm th} = \frac{c_{\rm s}^3}{\Omega G} \tag{2.1}$$

where $c_{\rm s}$ is the sound speed in the disk and Ω_p is the angular velocity of the planet. The thermal mass $M_{\rm th}$ is the mass of a planet at which the Hill radius and the Bondi radius $R_B \equiv GM_{\rm p}/c_s^2$ of the planet are comparable to the scale height of the gaseous disk h (Rafikov, 2006). For a MMSN model (Hayashi, 1981, Minimum Mass Solar Nebulae) and $M_\star = M_\odot$

$$M_{\rm th} \approx 12 \left(\frac{c}{1\ {\rm km\ s^{-1}}}\right)^3 \left(\frac{r_{\rm p}}{1\ {\rm AU}}\right)^{3/4}\ M_\oplus, \tag{2.2}$$

where $r_{\rm p}$ is the semi-major axis of the planetary orbit.

GR01 found that planets with $M_{\rm p} \gtrsim M_{\rm th}$ generate density waves which are nonlinear from the very start, and shock as soon as they are produced. Their angular momentum is deposited in the immediate vicinity of the planet, within $(1 \sim 2)h$, leading to the surface density evolution and gap opening close to the planet. On the other hand, Rafikov (2002b) demonstrated that density waves produced by lower mass planets are still able to dissipate efficiently further out through the nonlinear damping, even if they are only weakly nonlinear to begin with. In fact one should expect that given enough time, even a very low mass planet at a fixed semi-major axis should be able to open a gap in an inviscid disk. Based on this argument, Rafikov (2002b) explored gap opening mediated by the nonlinear dissipation of density waves and indeed found that the low mass planets which do not satisfy the condition (2.1) can be capable of stalling their migration via the migration feedback and opening a gap in a low viscosity disk.

However, most previous numerical studies have failed to capture gap opening by small planets ($M_{\rm p} \lesssim M_{\rm th}$). This is most likely because these simulations have studied flows with significant viscosity (artificial or numerical). In a viscous disk there is another condition (Lin & Papaloizou, 1993; Rafikov, 2002b)

$$M_p \gtrsim M_{\rm th} \left(\frac{\alpha}{0.043} \frac{a}{h} \right)^{1/2} \tag{2.3}$$

that has to be fulfilled simultaneously with (2.1) for the gap to open, where the effective Shakura-Sunyaev $\alpha = \nu/hc_{\rm s}$ (ν is the kinematic viscosity). It is quite likely that the levels of viscosity in these simulations were too high (in particular, the numerical viscosity due to the low spatial resolution) for the torques induced by the low mass planets to overcome viscous filling of the gap, *i.e.* the viscous criterion (2.3) was not fulfilled.

Only recently has the GR01 theory been confirmed in numerical work. Paardekooper (2006) first found evidence for the distance over which density waves damp to *increase* with decreasing $M_{\rm p}$, exactly as predicted by GR01. Subsequently, using two-dimensional hydrodynamic simulations of migration of low-mass planets in nearly inviscid disks, Li et al. (2009) found the migration rate to drop due to the migration feedback. They also showed that high disk viscosity ($\alpha \gtrsim 10^{-3}$) could wash out this effect, making fast type I migration persist. In addition, they confirmed the existence of a critical planet mass which eventually halts the migration, and found reasonable agreement with the theoretical prediction of Rafikov (2002b). Muto et al. (2010) also investigated nonlinear wave evolution by 2D hydrodynamical simulations and confirmed that low mass planets (a few tenths of $M_{\rm th}$) indeed are able to open gaps in an inviscid disk. They successfully detected shock formation and density redistribution in the disk, resulting from the nonlinear wave evolution. However, these simulations investigated only *secondary* consequences of the nonlinear wave evolution, such as the slowdown of the migration due to migration feedback and the limit on gap opening planet mass.

It is obvious from this discussion that elucidating the mechanisms of nonlinear wave dissipation in protoplanetary disks is not only interesting in and of itself, but is also crucial for understanding the migration feedback and the gap opening issue, both of which could significantly increase the planetary migration timescale. In this chapter we also investigate the evolution of density waves via numerical simulations, and provide detailed quantitative comparisons with analytical results of GR01.

In this work, we use 2D local inviscid hydrodynamical simulations in the shearing sheet geometry to verify the linear theory. For the first time we provide direct comparison of the primary physical variables — perturbed surface density profile, torque density in both *physical*

and *Fourier* space, and angular momentum flux — derived from simulations with the theoretical predictions. Our verification effort is the most thorough, sophisticated and quantitative to date, and we achieve agreement with theory at the level of *several per cent* for all physical variables explored. In addition, using our numerical results we address some remaining issues in the linear theory, such as the different expressions for the torque density in Fourier space (GR80,Artymowicz 1993b). We also formulate a set of requirements which should be satisfied by simulations to reach convergence and to reliably reproduce the linear theory results. The way in which we make the comparison an d the agreement we achieve can serve as a standard for checking the performance of different codes.

The chapter is structured as follows. We briefly summarize the main results of the linear density wave theory in §2, and the main results of the nonlinear theory in § 3, where we also analytically study the potential vorticity generation at the shock, which we use to pinpoint the shock location. A description of the code and our numerical setup are given in §4, including a discussion of potential problems associated with implementing orbital advection algorithm in studies of the disk-satellite interaction. We present our numerical results in the linear regime and compare them with theoretical predictions in §5, followed by the results in the nonlinear regime in § 6. The investigation of the sensitivity of simulation outcomes to the different numerical algorithms in §7. In §5 we discuss some numerical issues that emerge from our simulations, as well as the implications for realistic disks. Finally, a summary is provided in §6.

2 Summary of Linear Theory Results.

In linear theory of disk-planet interaction laid out in cylindrical geometry (Goldreich & Tremaine, 1979, GT80), the planetary potential is normally decomposed into a series of Fourier harmonics. Assuming all perturbed fluid variables to be proportional to $\exp[i(m(\varphi-\Omega_p t)+\int^r k_r(r')dr')]$ (m is a positive integer) and neglecting the self-gravity of the disk, one can obtain the dispersion relation for the m-th wave harmonic in the WKB limit in the form

$$m^2\left[\Omega(r)-\Omega_p\right]^2=\kappa^2+k_r^2c_s^2, \tag{2.4}$$

where κ is the epicyclic frequency ($\kappa=\Omega$ for a Newtonian potential), k_r is the wavenumber, Ω is the fluid angular frequency, and Ω_p is the pattern speed of the perturbation equal to the angular frequency of the point-mass perturber moving on a circular orbit with semi-major axis r_p, that is $\Omega_p=\Omega(r_p)$. As Eq. (2.4) demonstrates, there are two (inner and outer) Lindblad resonances (LR) where $k_r\to 0$ and m-th harmonic of planetary potential couples best to the wave-like perturbation. These resonances are located at radii $r_{L,m}$ given by $\Omega(r_{L,m})=\Omega_p m/(m\pm 1)$, which in the limit of $m\gg 1$ results in

$$x_{L,m}=\pm\frac{2h}{3\mu}, \tag{2.5}$$

where $x\equiv r-r_p$, $h=c_s/\Omega_p$ is the vertical disk scale length, and $\mu\equiv mh/r_p$.

The superposition of all the harmonics with different azimuthal wavenumbers m forms inner and outer spiral density waves. In physical space fluid perturbation associated with the wave is concentrated in narrow wake (with azimuthal extent of order h), the location of which is described in the local limit by (GR01)

$$y_w\approx -\mathrm{sgn}(x)\frac{3}{4}\frac{x^2}{h}, \tag{2.6}$$

where $y \equiv r_p(\varphi - \varphi_p)$ and azimuthal angle φ is counted in the prograde sense (with respect to planetary orbital motion). This location corresponds to the stationary phase of different Fourier harmonics composing the wave, as can be easily seen from Eq. (2.4). The wake shape in the global setting accounting for cylindrical geometry of the disk and Keplerian profile of $\Omega(r)$ was explored by Ogilvie & Lubow (2002) and Rafikov (2002a).

Each of the perturbation harmonics carries angular momentum flux, which for the m-th harmonic is given by (GT80).

$$F_H(m) = F_H^{\rm WKB}(m) \frac{F_H(m)}{F_H^{\rm WKB}(m)}, \tag{2.7}$$

$$F_H^{\rm WKB}(m) = \frac{4}{3}\frac{m^2\Sigma_0}{\Omega_p^2}\left(\frac{GM_{\rm p}}{r_p}\right)^2 \left[2K_0(2/3) + K_1(2/3)\right]^2. \tag{2.8}$$

Here Σ_0 is the unperturbed surface density of the disk, $F_H^{\rm WKB}(m)$ is the asymptotic Fourier contribution of the flux reached beyond the launching region on one side of the disk calculated in the WKB approximation (K_0 and K_1 are the modified Bessel functions of zeroth and first order), and the expression is only accurate for $m \gg 1$. The ratio $F_H(m)/F_H^{\rm WKB}(m)$ accounts for the difference between the precise value of $F_H(m)$ and $F_H^{\rm WKB}(m)$. This difference becomes important for $m \gtrsim r_p/h \gg 1$ since, as demonstrated by GT80, $F_H(m)$ decays exponentially with m at high azimuthal wavenumbers — the so-called "torque cutoff" phenomenon. As a result, the total angular momentum flux carried by the wave

$$F_H = \sum_{m=1}^{\infty} F_H(m) \approx 0.93\,(GM_{\rm p})^2\,\frac{\Sigma_0 r_p \Omega_p}{c_s^3}, \tag{2.9}$$

is dominated by harmonics with $m \sim r_p/h$ (or $\mu \sim 1$), which are excited within a radial separation of order h from the planet, see Eq. (2.5). This local nature of the wave excitation has important implications for the possibility of analytical treatment of the wave evolution.

In real protoplanetary disks, the torques acting on the inner and outer disks are slightly different (fractional difference $\sim h/r_p \ll 1$), giving rise to a net torque on the planet and leading to Type I planetary migration (Ward, 1986). However, in shearing sheet configuration the inner and outer parts of the disk are identical so there is no net torque acting on the planet and migration does not arise.

There is an important planetary mass scale characterizing excitation and propagation of the density waves, the so called *thermal mass* (GR01), which we define[1] here as

$$M_{\rm th} = \frac{c_s^3}{G\Omega_{\rm p}} \approx 12\ M_\oplus \left(\frac{c_s}{1\ {\rm km\ s^{-1}}}\right)^3 \left(\frac{M_\odot}{M_\star}\right)^{1/2} \left(\frac{r_p}{\rm AU}\right)^{3/2}. \tag{2.10}$$

There are several reasons for the significance of this mass scale. First, a Hill radius of the planet with $M_{\rm p} = M_{\rm th}$ is of order the scale height of the gaseous disk h. Second, the Bondi radius $R_B \equiv GM_{\rm p}/c_s^2$, which is the size of a region in which planetary gravity strongly perturbs local pressure distribution, also becomes comparable to h for $M_{\rm p} = M_{\rm th}$ (Rafikov 2006). Third, and most importantly for our present study, planets with $M_{\rm p} \gtrsim M_{\rm th}$ generate density waves which are nonlinear from the very start ($\delta\Sigma/\Sigma_0 \gtrsim 1$).

[1]This definition differs from that of GR01 who used $M_1 = 2c_{\rm s}^3/(3\Omega_p G) = (2/3)M_{\rm th}$ instead of $M_{\rm th}$.

In the small planet mass limit of

$$M_{\rm p} \lesssim M_{\rm th} \tag{2.11}$$

perturbations induced by the planetary gravity are weak ($\delta\Sigma/\Sigma \lesssim 1$) and *excitation* of the density wave by the planet can be studied purely in the linear approximation. It is in this limit that the linear theory of wave *driving* developed by GT80 and all of its results are valid. In the opposite limit of $M_{\rm p} \gtrsim M_{\rm th}$ the nonlinear effects must be accounted for even at the stage of wave excitation, which is not feasible analytically.

As mentioned above, the generation of the wave is largely completed at a distance of order h away from the planet, because this is where the most important Lindblad resonances lie. After that, in the absence of viscosity, the wave travels freely, no longer affected by the planetary gravity. At this stage of *propagation* nonlinear effects start to accumulate and finally result in wave breaking, formation of a shock, and transfer of wave energy and angular momentum to the disk fluid. Prior to the steepening into a shock the angular momentum flux F_H carried by the wave far from the planet (outside of the excitation region $|x| \sim h$) is exactly conserved in the absence of linear dissipation. This nonlinear stage has been explored analytically in GR01 in the limit (2.11).

We do not cover this stage in this work, but we mention the result of GR01 for the radial separation away from the planetary orbit at which the shock induced by the nonlinear effects first occurs:

$$l_{\rm sh} \approx 0.8 \left(\frac{\gamma+1}{12/5} \frac{M_{\rm p}}{M_{\rm th}} \right)^{-2/5} h, \tag{2.12}$$

where γ is the adiabatic index of gas. For $M_{\rm p} \ll M_{\rm th}$ one finds the shock to be well separated from the planet, $l_{\rm sh} \gtrsim h$, so that the wave excitation occurs in the linear regime, as asserted before. However, even for $M_{\rm p} \ll M_{\rm th}$ the linear theory of wave propagation fails for $x \gtrsim l_{\rm sh}$. In this work we are always exploring the low planetary mass limit (2.11) and consider only $|x| \lesssim l_{\rm sh}$ so that linear theory applies.

3 Nonlinear Theory of the Density Wave Propagation

Here we briefly summarize the results of GR01 for the nonlinear density wave evolution. For a planet of sufficiently low mass (*i.e.* $M_{\rm p} \ll M_{\rm th}$), the excitation and initial propagation of the wave are linear processes, which are not affected by the nonlinearity. Far from the planet, the wave excitation is no longer important, while the nonlinear effects start to accumulate. In the shearing sheet geometry (as usual, $x = r - r_{\rm p}$ and $y = r_{\rm p}(\theta - \theta_{\rm p})$ denote pseudo-Cartesian radial and azimuthal coordinates in a corotating system centered on the planet, and (u, v) represents the perturbed velocity in (x, y) plane) GR01 have shown that under the assumption of weak nonlinearity the fully nonlinear system of fluid equation can be reduced to a single first-order nonlinear equation:

$$\partial_t \chi - \chi \partial_\eta \chi = 0, \tag{2.13}$$

which is the inviscid Burger's equation. The dimensionless variables appearing here are related to radius, azimuth, and density contrast as follows:

$$t \equiv \frac{3^{7/2}}{2^{11/4}5}\left|\frac{x}{h}\right|^{5/2}\frac{M_{\rm p}}{M_{\rm th}}, \tag{2.14}$$

$$\eta \equiv \frac{3}{2}\left[\frac{y}{h}+\frac{3x^2}{4h^2}\mathrm{sign}(x)\right], \tag{2.15}$$

$$\chi \equiv \frac{2^{3/4}(\gamma+1)}{3^{3/2}}\left|\frac{h}{x}\right|^{1/2}\frac{\Sigma-\Sigma_0}{\Sigma_0}\frac{M_{\rm th}}{M_{\rm p}}\ . \tag{2.16}$$

where h is the scale height and $c_{\rm s}$ is the sound speed of the disk, and γ is the adiabatic index in the equation of state. Paardekooper (2006) has demonstrated that in the case of an isothermal disk in definition (2.16) $(\Sigma-\Sigma_0)/\Sigma_0$ should be replaced with $\ln(\Sigma/\Sigma_0)$. However, since we are interested only in the *weakly* nonlinear wave evolution the assumption of $(\Sigma-\Sigma_0)/\Sigma_0 \ll 1$ is always made and Eq. (2.16) holds even in the isothermal case.

In the absence of linear damping mechanisms such as viscosity, for almost any choice of smooth initial conditions in Burger's Eq. (2.13), the solution will eventually become double-valued, which means that a shock must appear. This phenomenon is analogous to the nonlinear evolution of sound waves, except that for planetary density waves (in the linear regime) the conservation of the wave angular momentum flux (AMF) and differential rotation lead to the wave amplitude *increasing*, and the radial wavelength *decreasing* with distance from the excitation point in the linear regime. Both effects conspire to accelerate wave steepening, and the formation of shocks close to the planet. GR01 provided an analytical formula for the nonlinear shocking length $l_{\rm sh}$:

$$l_{\rm sh} \approx 0.8\left(\frac{\gamma+1}{12/5}\frac{M_{\rm p}}{M_{\rm th}}\right)^{-2/5} h, \tag{2.17}$$

which indicates that if $M_{\rm p} \gtrsim M_{\rm th}$, the shock appears very close to planet ($l_{\rm sh} \sim h$), *i.e.* in the region where the wave excitation is taking place. GR01 also predicted that deep into the post shock regime ($x \gg l_{\rm sh}$) the density wave profile should attain the N-wave shape (Landau & Lifshitz, 1959). The amplitude of the N-wave scaled by $x^{1/2}$

$$\Delta = \frac{\delta\Sigma}{\Sigma_0}\left|\frac{h}{x}\right|^{1/2}\frac{M_{\rm th}}{M_{\rm p}} \tag{2.18}$$

and its azimuthal width w should scale with distance from the planet as:

$$\Delta \propto t^{-1/2}, \quad w \propto t^{1/2}, \tag{2.19}$$

where the time-like coordinate t is defined by Eq. (2.14). Note that $\Delta \propto t^0$ (stays roughly constant) in the linear regime of wave evolution due to the angular momentum conservation.

After the shock formation, the wave gradually damps out, transferring its angular momentum to the mean flow, and forcing the disk to evolve. The angular momentum flux $F_H(x)$ carried by the wave decays in the post-shock region as (GR01):

$$F_H(x) \propto |x|^{-5/4} \quad (|x| \gg l_{\rm sh}) \tag{2.20}$$

Where the shearing-sheet geometry is assumed. In the global setting the post-shock wave evolution was investigated in Rafikov (2002a).

3.1 Generation of Potential Vorticity

A very useful diagnostic of the density wave evolution is provided by the so-called *potential vorticity*, sometimes also called *vortensity*. This quantity is defined in the shearing box coordinates as

$$\zeta \equiv \frac{\mathbf{e}_z \cdot (\nabla \times \mathbf{v}) + 2\Omega}{\Sigma}, \tag{2.21}$$

where $\mathbf{v}$ is the fluid velocity in the frame of the shearing sheet, and $\mathbf{e}_z$ is the unit vector perpendicular to the disk plane. The background value of this quantity for $\mathbf{v} = 0$ is $\zeta_0 = \Omega/(2\Sigma_0)$. In an inviscid, barotropic fluid, potential vorticity is conserved everywhere, except across shocks. At the shock ζ experiences a jump $\Delta\zeta$ the magnitude of which depends on the strength of the shock and the orientation of the shock front with respect to the incoming flow. Thus, the potential vorticity perturbation $\Delta\zeta = \zeta - \zeta_0$ can be interpreted as the evidence for the appearance of shock waves and provides a useful diagnostic of the flow.

Here we theoretically calculate the behavior of $\Delta\zeta$ as a function of distance from the planet and planetary mass M_p based on the weakly-nonlinear theory of GR01. We start with the following expression for the jump in ζ at the isothermal shock (Kevlahan, 1997; Li et al., 2005; Lin & Papaloizou, 2010):

$$\Delta\zeta = \frac{c_s}{\Sigma}\frac{\left(M^2-1\right)^2}{M^4}\frac{\partial M}{\partial S} = \frac{c_s}{2\Sigma M^5}\left(\frac{\Delta\Sigma}{\Sigma}\right)^2\frac{\partial}{\partial S}\left(\frac{\Delta\Sigma}{\Sigma}\right), \tag{2.22}$$

where M is the Mach number of the flow perpendicular to the shock, $\Delta\Sigma$ is the surface density jump at the shock front and S is the distance along the shock. To arrive at the last expression we used the relation $M^2 - 1 = \Delta\Sigma/\Sigma$ valid in the isothermal case.

We can write $\partial/\partial S = \left[1 + (dy_{sh}/dx)^2\right]^{-1/2}\partial/\partial x$, where $y_{sh}(x) \approx -(3/4)h(x/h)^2$ is the theoretical shock position in the $x - y$ plane. For $x \gtrsim h$ we find then

$$\frac{\partial}{\partial S} \approx \frac{2}{3}\frac{h}{x}\frac{\partial}{\partial x}. \tag{2.23}$$

We now use Eq. (2.16) to relate $\Delta\Sigma/\Sigma$ to the jump across the shock $\Delta\chi_{sh}$ of the function χ, satisfying the Eq. (2.13):

$$\frac{\Delta\Sigma}{\Sigma} = \frac{3^{3/2}}{2^{3/4}(\gamma+1)}\left|\frac{x}{h}\right|^{1/2}\frac{M_{\rm p}}{M_{\rm th}}\Delta\chi_{sh}\left(t(x)\right), \tag{2.24}$$

where $t(x)$ is given by Eq. (2.14).

Combining Eqs. (2.14), (2.22)-(2.24), and setting $M \approx 1$ (shock is weak) in Eq. (2.22), we find

$$\Delta\zeta(x) = \frac{3^{7/2}}{2^{13/4}(\gamma+1)^3}\left[5\frac{\partial \ln \Delta\chi_{sh}}{\partial \ln t} + 1\right]\left[\Delta\chi_{sh}(t(x))\right]^3\frac{\Omega}{\Sigma_0}\left|\frac{h}{x}\right|^{1/2}\left(\frac{M_{\rm p}}{M_{\rm th}}\right)^3. \tag{2.25}$$

Note $\Delta\zeta \neq 0$ only for $x > l_{sh}$, where the shock exists. Eq. (2.25) shows that potential vorticity generation is a steep function of M_p: at a fixed distance x away from the planetary orbit $\Delta\zeta \propto M_{\rm p}^3$. Thus, low mass planets are very inefficient at generating potential vorticity and detecting its production in numerical experiments with small planets is a non-trivial task.

Using Eq. (2.17) and setting $\gamma = 1$ we can rewrite Eq. (2.25) as:

$$\Delta\zeta(x/l_{sh}) \approx 1.3\frac{\Omega}{\Sigma_0}\left|\frac{l_{sh}}{x}\right|^{1/2}\left(\frac{M_{\rm p}}{M_{\rm th}}\right)^{16/5}\left[\frac{\partial \ln \Delta\chi_{sh}}{\partial \ln(x/l_{sh})}+\frac{1}{2}\right]\left[\Delta\chi_{sh}(t(x/l_{sh}))\right]^3. \tag{2.26}$$

This particular form is natural since $\Delta\chi_{sh}$ is a function of $t \approx |x/l_{sh}|^{5/2}$ (for isothermal gas) only, as follows from Eq. (2.13), which does not contain any free parameters. Thus, a fixed x/l_{sh} corresponds to a unique value of t and $\Delta\chi_{sh}$.

For instance, if we choose x/l_{sh} (and t) to correspond to the point where $\Delta\chi_{sh}$ (and $\Delta\zeta$) attains its maximum value, the corresponding $\Delta\zeta_{max}$ would scale with M_p as $\propto (M_{\rm p}/M_{\rm th})^{16/5}$. More generally, one expects $\Delta\zeta\,(M_{\rm th}/M_{\rm p})^{16/5}$ to depend on x/l_{sh} *only*.

We compare these theoretical predictions with numerical results in §6.2.

4 Numerical Setup

Most analytical work on the linear evolution of density waves was carried out in application to two-dimensional (2D) disks. To provide a meaningful comparison with these studies, in our current work we employ 2D hydrodynamical simulations in local shearing box configuration. The computational tool for this investigation is Athena, a grid-based code for astrophysical gas dynamics using higher-order Godunov methods. Athena is written in conservative form, so it conserves mass, momentum, and energy down to machine precision. The mathematical foundations of the algorithms are described in Gardiner & Stone (2005, 2008), and a comprehensive description of the implementation and tests of the algorithms is given in Stone et al. (2008).

The implementation of the shearing box approximation in Athena is described in Stone & Gardiner (2010). This approximation adopts a frame of reference located at radius r_p corotating with the disk at orbital frequency $\Omega_p = \Omega(r_p)$. In this frame, the 2D hydrodynamics equations are written in a Cartesian coordinate system (x, y, z) that has unit vectors $\hat{\mathbf{i}}$, $\hat{\mathbf{j}}$, and $\hat{\mathbf{k}}$ as (Stone & Gardiner, 2010):

$$\frac{\partial\Sigma}{\partial t} + \nabla\cdot(\Sigma\mathbf{v}) = 0, \tag{2.27}$$

$$\frac{\partial\Sigma\mathbf{v}}{\partial t} + \nabla\cdot(\Sigma\mathbf{v}\mathbf{v} + p) = \Sigma\Omega_p^2(2qx\hat{\mathbf{i}}) - 2\Omega_p\hat{\mathbf{k}}\times\Sigma\mathbf{v} - \Sigma\nabla\Phi_p, \tag{2.28}$$

$$\frac{\partial E}{\partial t} + \nabla\cdot(E\mathbf{v} + p\cdot\mathbf{v}) = \Omega_p^2\Sigma\mathbf{v}\cdot(2qx\hat{\mathbf{i}}) - \Sigma\mathbf{v}\cdot\nabla\Phi_p, \tag{2.29}$$

where $\Phi_{\rm p}$ is the gravitational potential of the planet (whose form we will discuss in the next section), p is the gas pressure, E is the total energy density (sum of the internal and kinetic energy, but excluding the gravitational energy). The shear parameter q is defined as:

$$q = -\frac{d\ln\Omega}{d\ln r} \tag{2.30}$$

so that for Keplerian flow $q = 3/2$. The equation of state (EOS) we use in the simulations is the ideal gas law with

$$E_{\rm in} = \frac{p}{\gamma - 1} \tag{2.31}$$

where $E_{\rm in}$ is the internal energy and $\gamma = 5/3$. We also use an isothermal EOS, in which case $p = \Sigma c_{\rm s}^2$, where $c_{\rm s}$ is the isothermal sound speed. We do not include explicit viscosity (i.e. there is no explicit linear dissipation in the system) and we do not account for the self-gravity of the disk (thus we concentrate on studying the low mass disks).

To accurately resolve the flow in the vicinity of a gravitating mass without making the time step too short one usually resorts to softening the potential of the perturber. There are many ways of doing this but all of them come up with the form of the potential that converges to the Newtonian potential $\Phi_K = -GM_{\rm p}/\rho$ at large separations $\rho = \sqrt{x^2 + y^2}$, beyond the softening length $r_{\rm s}$. At small separations, $\rho \ll r_{\rm s}$ smoothed potentials become finite allowing the time step of simulations to stay finite. To test the sensitivity of our results to the specific method of potential softening we tried three different forms of the softened planetary potential. The second order potential

$$\Phi_{\rm p}^{(2)} = -GM_{\rm p}\frac{1}{(\rho^2 + r_{\rm s}^2)^{1/2}} \tag{2.32}$$

converges to Φ_K at $\rho \gg r_{\rm s}$ as $(r_{\rm s}/\rho)^2$ (which means the fractional error is $\mathrm{O}((r_s/\rho)^2)$ as $r_s/\rho \to 0$). This is a standard form of the potential used in a majority of numerical hydrodynamic studies. We also studied the fourth order potential

$$\Phi_{\rm p}^{(4)} = -GM_{\rm p}\frac{\rho^2 + 3r_{\rm s}^2/2}{(\rho^2 + r_{\rm s}^2)^{3/2}} \tag{2.33}$$

converging to the point mass potential as $(r_{\rm s}/\rho)^4$ for $\rho \gg r_{\rm s}$, and the sixth order potential

$$\Phi_{\rm p}^{(6)} = -GM_{\rm p}\frac{\rho^4 + 5\rho^2 r_{\rm s}^2/2 + 15r_{\rm s}^4/8}{(\rho^2 + r_{\rm s}^2)^{5/2}} \tag{2.34}$$

converging to Φ_K at $\rho \gg r_{\rm s}$ as $(r_{\rm s}/\rho)^6$. The difference in accuracy with which these potentials represent Φ_K at large ρ can be quantified by the distance from the planet at which a given potential deviates from Φ_K by 1%. This distance is $7r_{\rm s}$ for $\Phi_{\rm p}^{(2)}$, $2.3r_{\rm s}$ for $\Phi_{\rm p}^{(4)}$, and $1.5r_{\rm s}$ for $\Phi_{\rm p}^{(6)}$. Note that the first-order potential $\Phi_{\rm p}^{(1)} = -GM_{\rm p}/|\rho + r_{\rm s}|$, which we do not use here, gives only 10% accuracy relative to Φ_K even at $\rho = 10r_{\rm s}$, and we strongly discourage its use. The effects of different potential prescriptions will be discussed in detail in §7.3.

To guarantee accuracy and convergence of our results we carry out an exhaustive exploration of various numerical parameters characterizing our simulations, described in §7. Unless noted otherwise, our results shown in §5 are obtained with the following numerical parameters: an isothermal equation of state, the Roe solver with third order reconstruction in characteristic variables, and the corner transport upwind (CTU) unsplit integrator (Stone et al., 2008), a resolution of 256 grid points per scale length h (subsequently denoted $256/h$ for brevity), and fourth order accurate potential $\Phi_{\rm p}^{(4)}$ given by Eq. (2.33) with softening length $r_{\rm s} = h/32$.

High order of accuracy, high resolution and an accurate form of planetary potential used in our runs allow us to properly capture the details of wave evolution. High resolution ensures low levels of numerical viscosity and prevents the angular momentum accumulated by the wave from spurious dissipation (see Section 7 for more discussion). We run a series of test simulations with otherwise identical conditions but different explicit Navier-Stokes viscosity, and measure the wave properties. As the explicit viscosity decreases the simulation results gradually converge to the one

with zero explicit viscosity, which indicates the numerical viscosity dominates the explicit viscosity. For a typical simulation with low $M_{\rm p} = 2.09 \times 10^{-2} M_{\rm th}$ and an isothermal equation of state, the effective Shakura-Sunyaev α-parameter ($\alpha = \nu/hc_{\rm s}$) characterizing our numerical viscosity is found to be below 10^{-5}. Such small levels of viscosity are expected in dead zones of protoplanetary disks (Gammie, 1996), where magnetorotational instability (MRI) may not operate effectively (Fleming & Stone, 2003). Also note even when the MRI operates, MHD turbulence may not act like a Navier-Stokes viscosity.

For the standard simulations in this work to fit the parabolic wake (see Eq. 2.6) in the box we use box size $12h \times 64h$, thus the overall grid resolution in our runs is about 3072×16384 (for the standard resolution of $256/h$). In a few cases with very small $M_{\rm p}$, we extend the simulation box size to $20h \times 156h$ to trace linear wave evolution further out in x, since smaller $M_{\rm p}$ delays shock formation (see eq. (2.12)). Our simulations are run for at least 10 and in some cases up to 50 orbital periods. Figure 2.1 presents a typical snapshot of one of our simulations showing the density structure and the spiral waves.

We use the following boundary conditions (BCs). On x (radial) boundaries, we keep values of all physical variables in ghost zones fixed at their respective unperturbed Keplerian values (*i.e.* keep the ghost zones as their initial states), and the waves leave through the x boundaries when they reach the edge. In our shearing sheet simulations, experiments show that this x BC has less wave reflection and outflowing of the fluid than the conventional outflow x BC, in which case the ghost zones are copied from the last actively-updated column of cells of the simulations at every time-step (see also Muto et al. 2010). We do not expect our adopted radial BC to affect wave evolution since significant radial fluid motions are not expected to arise in our simulations anyway.

On the y (azimuthal) boundary, we experimented with two BCs: the conventional outflow BC, as described above, and an inflow/outflow BC. In the latter case, the variables in the ghost zones are fixed at their initial values if they are the physical "inflow" boundaries (the regimes $y < 0, x < 0$ and $y > 0, x > 0$), or copied from the last actively-updated row of cells if they are the physical "outflow" boundaries (the regimes $y > 0, x < 0$ and $y < 0, x > 0$). For the purposes of this work, the difference between these two BCs is not significant and resultant density profiles and torque calculation are almost identical (of the level of 10^{-3}). We found that with the pure outflow BC fluid entering the simulation box accumulates some non-zero velocity perturbation on top of the pure linear shear velocity profile. This affects calculation of variables derived from the simulated velocity field, such as potential vorticity, which will be discussed below. We use the inflow/outflow y BC for our simulations.

At the start of a simulation run we instantaneously turn on the potential of the planet in the center of the linearly sheared fluid flow with uniform surface density. This gravitational perturbation immediately excites an inner and an outer density wave propagating away from the planet, as well as strong transients: vortices that appear near the planet but travel on horseshoe orbits away from it. Before measuring the wave properties, we run simulations for ~ 15 orbital periods to let these time-dependent structures move away from the planet. We also tried gradually turning on planetary gravity by linearly increasing strength of the potential from zero to its full value within several orbital periods (Muto et al., 2010; Li et al., 2009), but did not find this trick as effective at removing transient structures as simply waiting for them to move away from the planet.

5 Result and Discussion in the Linear Regime

We now present our main results and compare them with the predictions of linear theory. To mitigate possible nonlinear effects we consider only very low planetary masses in our calculations, ranging between $3.2 \times 10^{-2} M_{\rm th}$ and $2.8 \times 10^{-3} M_{\rm th}$. According to Eq. (2.10) at 1 AU this mass range corresponds to $M_{\rm p}$ between 0.4 $M_\oplus$ and 3 Lunar masses (note that they are sound speed dependent). As the basis for comparison we primarily use the distribution of the perturbed density (§5.1) and the evolution of the angular momentum flux carried by the density wave (§5.2). We carry out linear theory verification both in physical (coordinate) space and in Fourier space.

5.1 The Density Wave Profile

The most basic and direct comparison between numerical simulations and theory can be performed using the spatial distribution of the perturbed fluid variables. In this work we choose the perturbed surface density $\delta\Sigma \equiv \Sigma - \Sigma_0$ as the primary variable for comparison. Since $\delta\Sigma$ is spatially concentrated along a narrow wake it makes sense to compare with theory both the *overall shape* of the wake in $x - y$ coordinates, and the density distribution *across* the wake.

We determine the wake shape in the following way. At each value of x we find the value of y, called $y_w(x)$, at which $\delta\Sigma$ reaches its maximum value $\delta\Sigma_{max}(x)$. We then compare the run of $y_w(x)$ with the theoretical prediction (2.6), which applies in the shearing sheet geometry (GR01). The results are shown in Figure 2.2. The two curves agree well far from the planet, at $|x| \gtrsim h$. The discrepancy at $|x| \lesssim h$ is not surprising because in this region (a) the density wave is not yet fully formed and (b) the dispersion relation (2.4) is significantly affected by the κ^2 term, which causes the wake profile to deviate from the theoretical prediction (2.6) valid far from the planet, see Ogilvie & Lubow (2002) for details.

Next we investigate the evolution of the wave amplitude as it travels away from the planet by looking at the behavior of maximum amplitude $\delta\Sigma_{max}(x) \equiv \delta\Sigma(x, y_w(x))$ as a function of x. We plot this quantity scaled by $\Sigma_0(M_{\rm p}/M_{\rm th})$ (this normalization removes the dependence of $\delta\Sigma_{max}$ on Σ_0 and $M_{\rm p}$) in Figure 2.3a.

At small $x \lesssim h$ the value of $\delta\Sigma_{max}$ is large and decreases with x. This behavior has nothing to do with the density wave since the region in the immediate vicinity of the planet represents a quasi-static atmosphere that forms inside the planetary potential well right after the planetary gravity is switched on. This structure is rarely mentioned in the analytical calculations of planet-disk interaction but it shows prominently in realistic simulations. In hydrostatic balance (in the absence of background velocity caused by differential rotation) density profile in the vicinity of the planet should be given by (assuming isothermal equation of state with constant sound speed c_s)

$$\Sigma_{\rm atm}(\rho) = \Sigma_0 e^{-\Phi_{\rm p}(\rho)/c_s^2} \tag{2.35}$$

In real disks, the background velocity field distorts the atmospheric profile from the circularly-symmetric (with respect to planet) shape predicted by this equation. This explains why $\Sigma_{\rm atm}(x)$ shown Figure 2.3b slightly overestimates $\delta\Sigma_{max}$ at small x.

The effect of the atmosphere on $\delta\Sigma_{max}$ rapidly decreases beyond several h from the planet, and $\delta\Sigma_{max}$ starts to rise with increasing x. This is because density wave excitation occurs at $|x| \sim h$ and from now on the behavior of $\delta\Sigma_{max}$ is determined by the wave-like density perturbation. Conservation of the angular momentum flux $F_{\rm H}$ carried by the wave forces the wave

amplitude to increase with distance $\propto x^{1/2}$ (GR01). As Figure 2.3a shows this scaling agrees reasonably well with the numerically computed $\delta\Sigma_{max}(x)$ far from the planet.

Note that initially, at separations of several h from the planet, $\delta\Sigma_{max}$ increases with x *faster* than the theoretical $x^{1/2}$ scaling, which is caused by the still ongoing accumulation of the angular momentum flux F_H at these separations. In other words, at this location F_H has not yet reached its asymptotic value given by Eq. (2.9), see §5.2 for more details.

Far from the planet, beyond $x = l_{\rm sh}$ ($l_{\rm sh} = 7.5h$ in the case shown in Figure 2.3a), the peak $\delta\Sigma$ rapidly goes down relative to the analytical $x^{1/2}$ scaling. This behavior is caused by the appearance of the shock at $l_{\rm sh}$ and subsequent dissipation of the angular momentum flux carried by the wave.

Finally, we examine evolution of the density profile across the wake as a function of radial separation x. We do this by making an azimuthal cut through the density field at fixed x and shifting the resultant one-dimensional density profile in y by y_w given in Eq. (2.6). To eliminate the increase of $\delta\Sigma$ resulting simply from the angular momentum flux conservation we normalize the density perturbation by $x^{1/2}$. We additionally scale $\delta\Sigma$ by $\Sigma_0(M_{\rm p}/M_{\rm th})$, as in Figure 2.3a. As mentioned before, in linear theory the normalized density profile should be independent of $M_{\rm p}$ at a fixed separation x. This is indeed seen in Figure 2.4a, where we plot scaled profiles of $\delta\Sigma$ computed for several values of $M_{\rm p}$ at $x = 1.33h$, and find no significant difference between them. The adopted value of x is small enough for the linear theory to apply even for the highest $M_{\rm p}$ ($\approx 0.03M_{\rm th}$) used in making this Figure, i.e. x is always considerably smaller than $l_{\rm sh}$ (cf. Figure 2.3b and the discussion in §5.4).

Previously, GR01 computed the evolution of the density profile as a function of x in the linear regime. In Figure 2.3b we provide an analogue of Figure 1 of GR01 by showing the scaled density cuts at the same values[2] of x — $1.33h$, $2.67h$, $4h$, $5.33h$ — as in GR01. This particular calculation uses a very small planet mass $M_{\rm p} = 3.7 \times 10^{-3} M_{\rm th}$ corresponding to $l_s \approx 8h$, see Eq. (2.12), which puts the values of x used in making this Figure well inside the shock position and reduces the impact of nonlinearity on the density profile, see §5.4.

The effective width of the density profile in this Figure does not significantly vary with x and stays at the level of several h at all times. We note, however, that this property holds only for the density cuts passing through the wake at fixed x, as shown in Figure 2.3b. On the contrary, the width of the density profile cutting through the wake at fixed y (not shown here) is *shrinking* as $|x|^{-1}$, which follows directly from the dispersion relation (2.4) since $k_r \propto |x|$ for $x \gtrsim h$.

Our numerical results agree with linear calculations of GR01 quite well, with quantitative differences at the level of 10% or less. In particular, we are able to reproduce several subtle features of the wake profile evolution found in GR01, which are highlighted by arrows in Figure 2.3b. These are (a) the increase of $\delta\Sigma$ with x in the density trough in front of the wake, (b) the decrease of $\delta\Sigma$ with x in the density trough behind the wake, and (c) the slight drift of density profile with respect to theoretical wake position $y = y_w(x)$ given by Eq. (2.6) as x increases. There are also some minor differences between the Figure 2.3b and the results presented in GR01, e.g. the lower (by about 10%) amplitude of $\delta\Sigma$ far from the planet, at $x \gtrsim 3h$, in our case (note that the vertical axis of 2.3b is different from the vertical axis in Figure 2 of GR01, since we use $M_{\rm th}$ and h instead of M_1 and $l = 2h/3$ as mass and length units). We speculate that this may be

[2]Note that GR01 normalized x by the "Mach 1"distance $l = (2/3)h$ rather than h as we do here. However, the physical values of x for the density cuts shown in Figure 2.3a are the same as in GR01.

explained by the gradually accumulating nonlinear effects in our simulations, which are absent in linear calculations of GR01.

Previously, Muto et al. (2010, Figure 6) have shown density profiles resulting from their 2D hydro simulations in cylindrical geometry, which are similar to those presented in Figure 2.3. However, their calculations were carried out for planetary masses (*minimum* $M_{\rm p} = 5 \times 10^{-2} M_{\rm th}$) larger than used in our work (*maximum* $M_{\rm p} = 3.2 \times 10^{-2} M_{\rm th}$), which does not allow them to isolate linear effects clearly. Also, Muto et al. (2010) did not attempt quantitative comparison of their numerical results with the linear theory predictions.

5.2 The Angular Momentum Flux and Torque Density

We now investigate the behavior of the angular momentum flux (AMF) carried by the wave $F_H(x)$ as a function of x. Linear calculations of this quantity in Fourier space have been first performed in GT80, and later refined in Artymowicz (1993b,a) and Korycansky & Pollack (1993). The torque density dT_H/dx, which is a spatial derivative of $F_H(x)$ has been inferred from simulations in Bate et al. (2003) and D'Angelo & Lubow (2008, 2010), although no direct comparison with the linear theory was provided in these studies.

The analytical expression (2.9) for the integrated angular momentum flux scales linearly with the planetary semi-major axis r_p. In the shearing sheet geometry employed in our simulations r_p is ill-defined, and it makes sense to redefine angular momentum flux as $\tilde{F}_H \equiv F_H/r_p$. Subsequently we will drop tilde for brevity and denote such normalized momentum flux as F_H. We compute $F_H(x)$ from our data according to the following definition:

$$F_H(x) = \Sigma_0 \int\limits_{-\infty}^{\infty} dy \delta v_y v_x, \tag{2.36}$$

where v_x is the radial velocity of the fluid, and δv_y is the velocity perturbation with respect to the background shear profile in the azimuthal direction.

We compute the torque density (normalized by r_p) exerted by the planet on the fluid at separation x as

$$\frac{dT_H}{dx} = -\int\limits_{-\infty}^{\infty} dy \delta\Sigma \frac{\partial \Phi_{\rm p}}{\partial y}, \tag{2.37}$$

and the integrated torque accumulated by the wave at x is just

$$T_H(x) = \int\limits_{0}^{x} \frac{dT_H}{dx} dx. \tag{2.38}$$

Conservation of angular momentum ensures that the derivative of Equation (2.45) (the slope of the AMF) coincides with the torque density (2.52) in the absence of dissipation.

Comparison with Theory in Fourier Space

We first compare our simulation results with linear theory in Fourier space by studying the behavior of the torque cutoff function $F_H(m)/F_H^{WKB}(m)$, see §2. Previously GT80 computed variation of this quantity as a function of m, and the result is shown in Figures 2 and 3 of their

paper, providing a basis for comparison. Artymowicz (1993b) subsequently refined this calculation by arguing that evaluating the planetary potential at separations slightly displaced from the classical Lindblad resonance position (2.5) should lead to more accurate results. Adopting this approach Artymowicz (1993a) provided a simple analytical prescription (Eq. (25) of Artymowicz 1993a) to reproduce the behavior of $F_H(m)/F_H^{WKB}(m)$, which can also be compared with our calculations.

Substituting v_x and δv_y in the form of their Fourier integrals in Eq. (2.45) and manipulating the resulting expression one can write $F_H(x)$ as the integral over the azimuthal wavenumber k_y:

$$F_H(x) = \int_0^\infty dk_y F_{H,k}(x), \tag{2.39}$$

$$F_{H,k}(x) = 4\pi\Sigma_0 \left[\mathrm{Re}\left(v_{x,k}\right)\mathrm{Re}\left(\delta v_{y,k}\right) + \mathrm{Im}\left(v_{x,k}\right)\mathrm{Im}\left(\delta v_{y,k}\right)\right], \tag{2.40}$$

where $v_{x,k}$ and $\delta v_{y,k}$ are the Fourier transforms of v_x and δv_y, which themselves are functions of x. Even though the available analytical calculations of the torque cutoff function were performed only in the limit $x \gg 1$, we chose to retain the dependence of $F_H(x)$ on x to explore the evolution of the harmonic content of the AMF with distance from the planet.

Instead of the discrete theoretical WKB Fourier harmonics of the flux $F_H^{WKB}(m)$ given by (2.8) we use the following continuous version[3]:

$$F_{H,k}^{WKB} = \frac{4}{3}\Sigma_0 \left(k_y h\right)^2 \left(\frac{GM_\mathrm{p}}{c_s}\right)^2 \left[2K_0(2/3) + K_1(2/3)\right]^2, \tag{2.41}$$

where we also normalized the final expression by r_p.

We can now compute real and imaginary components of $v_{x,k}$ and $\delta v_{y,k}$ using our numerical data and then obtain $F_{H,k}(x)$ from Eq. (2.40). Dividing the result by $F_{H,k}^{WKB}$ provides us with the ratio $F_{H,k}(x)/F_{H,k}^{WKB}$, which can then be compared with the existing theoretical calculations of the torque cutoff. This is done in Figure 2.18 where we plot the numerical $F_{H,k}(x)/F_{H,k}^{WKB}$ computed at different separations from the planet against the semi-analytical calculations of the same quantity (in the limit $|x| \gg h$) performed by GT80 and Artymowicz (1993a). These calculations were done for rather small $M_\mathrm{p} = 1.2 \times 10^{-2} M_\mathrm{th}$ (corresponding to $l_\mathrm{sh} \approx 5h$) allowing us to see linear wave evolution out to large separations.

One can see in Figure 2.18a that the agreement between theory and simulations is generally quite good. Our results seem to agree better with GT80 torque cutoff prescription than with Artymowicz (1993a). However, at the level of accuracy available to us we are not able to firmly discriminate between these two torque cutoff prescriptions. At intermediate values of $\mu = k_y h \approx 0.5 - 5$ our numerical results for $F_{H,k}(x)/F_{H,k}^{WKB}$ are essentially independent of x and pass between the two aforementioned analytical torque cutoff prescriptions. Only weak sensitivity of $F_{H,k}(x)/F_{H,k}^{WKB}$ on x is expected since beyond $|x| = 2h$ the power in azimuthal harmonics corresponding to this range of $k_y h$ should have already been fully accumulated by the density wave, and no evolution should arise. Good agreement with the GT80 results is also illustrated in Figure 2.18b, which shows the torque cutoff function (multiplied by μ^2) in linear space, as in Figure 3 of GT80.

[3]Transition between the discrete and integral representations of the AMF is performed by replacing m with $k_y r_p$ and summation over m with integration over $r_p dk_y$.

The situation is different for smaller values of $k_y h \lesssim 0.5$, where the numerical curves fall below the analytical asymptotic behavior $F_{H,k}/F_{H,k}^{WKB} \to 1$ as $k_y h \to 0$. Also, there is noticeable evolution of $F_{H,k}(x)/F_{H,k}^{WKB}$ with x, with nonzero power extending down to smaller and smaller values of k_y as the wave travels further from the planet. This is because the low-order harmonics corresponding to small $k_y h$ contribute to the wave flux predominantly at separations larger than $\sim h$ (Korycansky & Pollack, 1993), see Eq. (2.5). As a result, the further the wave travels, the more power gets collected by the wave from these lower-order azimuthal harmonics of the planetary potential, but the very small values of $k_y \lesssim 0.05$ never contribute to the wave flux even at $|x| = 5h$.

Our numerical results also exhibit noticeable disagreement with theory and clear evolution with x at large values of $k_y h \gtrsim 5$, and we comment on their origin in §5.4.

Comparison with Theory in Physical Space

We now study the behavior of the AMF and torque density in physical space. Understanding the spatial distribution of the latter quantity is important for properly computing the AMF in disks with non-uniform distribution of Σ in the vicinity of the planet, and is thus important for understanding the early stages of gap formation by massive planets.

Here we look at disks with uniform distribution of Σ. In Figure 2.6 we show the behavior of the AFM $F_H(x)$ computed according to the definition (2.45) and also of the accumulated torque $T_H(x)$ given by Eqs. (2.52). We display our results for four different values of M_p, normalizing $F_H(x)$ and $T_H(x)$ by $\Sigma_0 (G M_\mathrm{p})^2/(h c_\mathrm{s}^2)$ — according to linear theory the shape of the resultant curves should then be independent of M_p. Theoretical scaling of the torque $\propto M_\mathrm{p}^2$ is indeed largely confirmed by this Figure, but see §5.4 for more details.

To facilitate the comparison with the torque calculation, AMF curves have all been vertically shifted by a small offset to cancel the non-zero value of $F_H(0)$ at $x = 0$ resulting from the residual gas motion in the horseshoe region and a small intrinsic non-zero starting value of the AMF (Rafikov & Petrovich, 2012). This brings them in perfect accord with $T_H(x)$ curves close to the planet, which is expected to be the case in the absence of dissipation[4]. At large separations, beyond l_sh, the $F_H(x)$ curve starts falling below the $T_H(x)$ curve, which is caused by shock formation and dissipation of the wave AMF past this point. Quite naturally, this effect is more pronounced for higher M_p, e.g. $M_\mathrm{p} = 3.2 \times 10^{-3} M_\mathrm{th}$ and $M_\mathrm{p} = 1.2 \times 10^{-3} M_\mathrm{th}$, corresponding to smaller l_sh. For smaller masses shocks occur outside the simulation box and essentially no difference between $F_H(x)$ and $T_H(x)$ can be seen.

In Figure 2.7 we plot the torque density $dT_H(x)/dx$ (2.37) as a function of x. The overall shape of the curve is consistent with previous numerical calculations of the same quantity in cylindrical coordinates performed by Bate et al. (2003) and D'Angelo & Lubow (2008, 2010). As expected from linear theory, beyond $\approx 2h$ torque density drops dramatically, and the AMF rises only weakly, with $|x|$, which is evident from the flattening of AMF curves in Figure 2.6. This justifies the localization of the wave excitation to the immediate vicinity (within $\sim 2h$) of the planet, as described in §2.

To the best of our knowledge, no quantitative analytical description of how $F_H(x)$ should vary with distance from the planet exists in the literature, despite its potential importance for the gap opening problem. To fill this gap we first tried the following theoretical prescription $F_H^\mathrm{LR}(x)$

[4]This additionally confirms low levels of numerical viscosity in our runs.

motivated by the calculations of GT80: at each x we compute the lowest azimuthal wavenumber $\mu_{min}(x)$ for which the location of the Lindblad resonance $x_{L,m} < x$ using Eq. (2.5) and then calculate the AMF as the sum of all Fourier contributions $F_H(m)$ given by Eq. (2.7) that correspond to $m > (r_p/h)\mu_{min}(x)$. The result, which we denote by $F_H^{\rm LR}(x)$, is given by:

$$F_H^{\rm LR}(x) = \frac{4}{3}\frac{\Sigma_0 (G M_{\rm p})^2}{c_s^2 h}\left[2K_0(2/3) + K_1(2/3)\right]^2 \int\limits_{\mu_{min}(x)}^{\infty} d\mu \mu^2 \frac{F_H(\mu)}{F_H^{\rm WKB}(\mu)}, \tag{2.42}$$

$$\mu_{min}(x) = \frac{2}{3}\frac{h}{x}, \tag{2.43}$$

where we adopt the torque cutoff function $F_H(\mu)/F_H^{\rm WKB}(\mu)$ calculated in GT80. Note that $F_H^{\rm LR}(x)$ is in fact independent of the adopted value of r_p since its calculation can be rephrased fully in terms of μ rather than m.

This prescription essentially assumes that the AMF contribution $F_H(m)$ corresponding to a particular azimuthal wavenumber m gets picked up by the density wave in a step-like fashion, solely at a *single discrete* location corresponding to the position of the m-th Lindblad resonance. Previously, this recipe was used in GT80 to compute the asymptotic behavior of the torque density in the limit $|x| \gtrsim h$, considering azimuthal harmonics with $1 \lesssim m \lesssim r_{\rm p}/h$. Here we essentially extend this prescription to the case of arbitrary m and $|x|$. Linear calculations by Korycansky & Pollack (1993) show that this approximation is not very accurate, and AMF contribution due to each potential harmonic is in fact accumulated by the wave over an extended range of x. Thus we should not expect $F_H^{\rm LR}(x)$ given by Eq. (2.42) to accurately represent the real coordinate dependence of the AMF in the linear regime. Nevertheless, this prescription still provides a useful reference point and we plot it in Figure 2.6(a) (the dotted line, denoted by LR theory). We also plot in Figure 2.7 the theoretical prescription for the torque density $dT_H^{\rm LR}(x)/dx$ obtained by differentiating Eq. (2.42) with respect to x.

One can see from these Figures that the simple-minded theoretical prescription (2.42) overestimates the torque density at small x and underestimates it at larger x. While the areas under the numerical and theoretical curves in Figure 2.7, which represent the full accumulated AMF, are close to each other, the profiles of the two curves are quite different. As a result, $F_H^{\rm LR}(x)$ initially rises faster than the numerical $F_H(x)$ in Figure 2.6, but eventually the two asymptote to a similar final value. The small remaining difference is caused by both the intrinsic numerical inaccuracy and the fact that unlike the AMF theoretical curve the numerical AMF curve has been shifted to have a zero starting point.

As the next level of approximation to the behavior of the $F_H(x)$ and $T_H(x)$ we used the semi-analytical calculations of these quantities in the linear regime by Rafikov & Petrovich (2012). The run of corresponding $T_H(x)$ is displayed in Fig. 2.6 by the dash-dotted curve (the curve has also been shifted downward to cancel the non-zero starting value, and we use the label "Linear theory" to indicate Rafikov & Petrovich 2012 in all the figures) and clearly demonstrates good agreement between the simulation results and the semi-analytical linear theory. Theoretical torque density based on this $T_H(x)$ is shown in Fig. 2.7 and also agrees well with the numerical results, much better than the derivative of $F_H^{\rm LR}(x)$. This additionally emphasizes the point that assigning the planetary torque produced by a particular potential harmonic to a single location corresponding to the respective Lindblad resonance (as done in Eq. (2.42)) is not a very accurate procedure.

Finally, we also compare our numerical results with another quantity that can be computed in the linear approximation, namely the "pseudo-AMF" f_J introduced in GR01 as

$$f_J(x) = \frac{2}{3}\frac{c_s^3}{\Omega\Sigma_0|x|}\int_{-\infty}^{\infty}(\delta\Sigma)^2\,dy. \tag{2.44}$$

This quantity reduces to $F_H(x)$ at large separations from the planet $|x| \gtrsim h$, where $\delta\Sigma$ is determined solely by the density wave, propagating away from the planet. However, for $|x| \lesssim h$ the pseudo-AMF is strongly affected by the presence of the aforementioned atmosphere around the planet (see §5.1), which is not a propagating density perturbation and cannot be associated with the density wave (this explains the prefix "pseudo-").

We compute the theoretical value $f_J(x)$ in the linear approximation using unpublished data from GR01 and also derive $f_J(x)$ from our numerical data using the definition (2.44). The comparison between the two is shown in Figure 2.8 for very small $M_\mathrm{p} = 3.7\times10^{-3}M_\mathrm{th}$. One can indeed see that at small $|x|$ the pseudo-AMF *increases* with decreasing $|x|$, analogous to $\delta\Sigma$ in Figure 2.3a, which is explained by the presence of the atmosphere accumulated in the planetary potential well. Comparison with Figure 2.6 also shows that $f_J(x)$ indeed reduces to $F_H(x)$ at large $|x|$. Most importantly, the agreement between the theoretical $f_J(x)$ derived from linear theory and the numerical $f_J(x)$ is very good in the whole range of x explored, which provides additional verification of linear theory of the planetary density wave evolution.

5.3 Sensitivity to EOS

In linear theory the dynamics of the density wave is independent of the adopted equation of state (EOS), and depends only on adiabatic sound speed of the gas c_s. To check this property we have run several test simulations with two different EOS: isothermal EOS and EOS with $\gamma = 5/3$, while keeping c_s the same. The results do not show any significant difference between the runs with different EOS in linear stage thus confirming theoretical expectations.

5.4 Emergence of the Nonlinear Effects

We now discuss the nonlinear effects that arise in our simulations even prior to the appearance of the shock, i.e. at $|x| \lesssim l_\mathrm{sh}$. Nonlinear distortion of the wave profile is unavoidable even for the very low amplitude density waves and even during the mostly linear phase of their evolution. The rate of accumulation of the nonlinear effects (which eventually become strong and lead to shock formation) scales with planetary mass and is lower for low M_p.

This point is illustrated in Figure 2.4b, which is very similar to Figure 2.4a and presents azimuthal density cuts through the wake for different values of M_p, but now recorded further out from the planet, at $x = 4h$. While in Figure 2.4a, at $x = 1.33h$, the density profiles for all M_p are essentially overlapping and agree with the analytical profile from GR01, the situation at $x = 4h$ is quite different.

At this location the (normalized) wake profiles for the two smallest masses, $M_\mathrm{p} = 2.8\times10^{-3}M_\mathrm{th}$ (corresponding to $l_s \approx 8.9h$) and $M_\mathrm{p} = 5.7\times10^{-3}M_\mathrm{th}$ ($l_s \approx 6.7h$), still agree with each other and the semi-analytical linear calculation from GR01 quite well. However, already for $M_\mathrm{p} = 1.2\times10^{-2}M_\mathrm{th}$ ($l_s \approx 5h$) one can see a noticeable distortion of the profile compared to the linear solution, with the leading edge (at the left) becoming *steeper* and the profile peak *shifting* to the left, towards incoming fluid. The wave for even higher

$M_{\rm p} = 3.2 \times 10^{-2} M_{\rm th}$ ($l_s \approx 3.4h$) has already shocked at $x = 4h$, which is clearly reflected in its density profile: its leading edge is essentially vertical, exhibiting a discontinuity in the fluid variables across the shock. Thus, the role of the nonlinear effects, which is measured at a given x both by the slope of the leading edge of the profile and the shift of its peak relative to the linear solution, progressively increases with the planet mass.

Nonlinear effects also manifest themselves in a variety of other, more indirect ways. In particular, they explain the evolution of the torque cutoff function in Fourier space and its deviation from theoretical predictions at high $k_y h \gtrsim 5$ (see §5.2). Figure 2.18a clearly shows a growing amount of excess power at the high values of $k_y h$ as the wave propagates to larger x. This behavior is naturally accounted for by the nonlinear wave steepening, which causes the transfer of the AMF power in Fourier space from the low-k_y to high-k_y harmonics.

Nonlinearity also affects the AMF behavior in physical space. Close inspection of Figure 2.6 reveals that the numerical torque and AMF curves tend to asymptote to lower levels for higher $M_{\rm p}$, when nonlinearity is stronger. The difference in asymptotic values at large x between the largest and the smallest planet cases is about 5%. Variation of $M_{\rm p}$ also affects the height of $dT_H(x)/dx$ curve at smaller $x \approx h$, increasing the peak value of $dT_H(x)/dx$ for lower $M_{\rm p}$, as shown in Figure 2.7. This explains the dependence of normalized AMF and $T_H(x)$ curves on $M_{\rm p}$ in Figure 2.6: the area under the differential torque curve is slightly (by $\approx 3\%$) higher for $M_{\rm p} = 2.8 \times 10^{-3} M_{\rm th}$ (the think solid line) than for $M_{\rm p} = 1.2 \times 10^{-2} M_{\rm th}$ (the thin solid line), explaining the difference seen between the asymptotic values of integrated torque $T_H(x)$ in Figures 2.6b and 2.6d. Spurious dissipation related to numerical viscosity cannot be blamed for this effect since its effect on the AMF should be independent of $M_{\rm p}$.

We suggest that this behavior may be explained (at least partly) by the stronger nonlinear evolution of the wave profile for higher $M_{\rm p}$. According to Eq. (2.37) nonlinear distortion of $\delta\Sigma$ away from the theoretically expected-value should have an effect (growing with $M_{\rm p}$) on the calculation of the torque density $dT_H(x)/dx$. Since for $M_{\rm p}$ not too close to $M_{\rm th}$ this profile distortion becomes significant only far from the planet, where the planetary potential is weak, the impact of this nonlinear torque modification on the AMF curves is not very dramatic, but it is definitely non-zero. We also note that one expects simulations with smaller $M_{\rm p}$ to exhibit better agreement with the theory since they are less affected by the nonlinear effects. However in reality this is not always the case because the optimal set of numerical parameters for achieving the best possible numerical result for different $M_{\rm p}$ is different (see §7).

5.5 "Negative torque" Phenomenon

Close inspection of Figure 2.7 reveals an interesting feature in the behavior of the torque density at large x. The inset in this Figure clearly shows that $dT_H(x)/dx$ becomes *negative* beyond $x_- \approx 3.2h$, which is at odds with linear theory since according to GT80 $dT_H(x)/dx$ should not change sign at any non-zero x. The contribution of this negative torque density to the total integrated torque T_H is rather small (under one per cent level), but its existence presents a challenge to the results of GT80. Further investigation reveals that this "negative torque" phenomenon is present also in previous lower resolution numerical calculations of Bate et al. (2003, Figure 12) and D'Angelo & Lubow (2008, Figure 7).

To understand the nature of this effect we varied the numerical parameters of our simulations. For a given $M_{\rm p} = 1.2 \times 10^{-2} M_{\rm th}$ we tried varying softening length $r_{\rm s}$ from $h/16$ to $h/32$ at fixed resolution of $256/h$, and then varied resolution from $h/64$ to $h/256$ for a fixed $r_{\rm s} = h/16$. As

Figure 2.7 shows this does not make the negative torque go away and $dT_H(x)/dx$ still changes sign at the same value of x_-. Even more interestingly, changing the planetary mass M_p to lower $M_\mathrm{p} = 2.8 \times 10^{-3} M_\mathrm{th}$ while keeping everything else the same (resolution of $256/h$ and $r_\mathrm{s} = h/32$) also does not affect the position of x_-, as the same Figure clearly shows. Analogously, experiments with different sizes of the simulation box and different prescriptions of gravitational potential show that the existence of negative torque and the position of x_- are independent of these parameters as well. Moreover, simulations of D'Angelo & Lubow (2008, Figure 12) suggest that the negative torque phenomenon shows up only at *low* planetary masses ($M_\mathrm{p} \lesssim 0.03$ M$_J \approx 10$ M$_\oplus$ in their case), which makes possible explanations based on nonlinear effects unlikely.

This point is confirmed in Rafikov & Petrovich (2012) who demonstrate that the sign change of the torque density at large separation from the planet is in fact a purely linear effect. It can be understood by carefully accounting for the complex spatial structure of the torque density produced by each azimuthal harmonic of the planetary potential, which goes beyond the simple calculation presented in GT80.

6 Results and Discussion in the Nonlinear Regime

In this section, we present our numerical results on the density wave properties in the nonlinear regime, and make detailed quantitative comparison with the theory.

6.1 Density Profile in the Post Shock Region

The nonlinear evolution of the wave is depicted in Figure 2.13a, where we show the azimuthal density profile at two pre-shock locations, the theoretically predicted shocking distance l_sh, and four post-shock positions. In accord with linear theory, before the shock the numerical peak amplitude of the wave stays roughly constant (we see only a slight increase with x expected as a result of the continuing accumulation of the torque from low azimuthal wavenumber harmonics by the wave). At the same time the leading edge of the density profile gradually steepens as the wave propagates away from the planet. At $x \approx l_\mathrm{sh}$ the leading edge becomes vertical and the wave shocks. After that the leading edge stays vertical while the height of the profile Δ (see Fig. 2.13a for an illustration of its definition) decreases due to the dissipation of energy and angular momentum.

We note that the N-wave shape does not quite appear in our wave profile, because the second (trailing) shock does not emerge until very large distance ($x \sim 7(M_\mathrm{th}/M_\mathrm{p})^{2/5} h$), which our simulation boxes do not cover. Nevertheless, the leading segment of the N-wave does appear and we use its behavior to quantitatively explore the N-wave evolution. In Figure 2.13b, we plot the dependence of Δ and the azimuthal width of the wave w (the $y/h - 3(x/h)^2/4$ value at the mid point of the leading edge, as indicated in Fig. 2.13a) on the coordinate $t(x)$ defined by Eq. (2.14) in the post shock regime, as well as the theoretical scaling relations (Eq. 2.19) with arbitrary normalization. Far in the post shock regime ($t \gg 1$) our numerical results on the N-wave behavior agree well with theory.

Evolution of the wave profile in the nonlinear regime was first studied by Muto et al. (2010), who demonstrated the steepening of the wave profile and the decay of Σ after the shock formation (their Figure 6). However, they did not make quantitative comparison between the numerical results and theoretical scaling relations, as we do here.

6.2 Excitation of Potential Vorticity

In Figure 2.14 we show a typical spatial patten of potential vorticity deviation $\Delta\zeta = \zeta - (\Omega/2\Sigma_0)$ from its background value in our simulations (only one half of the simulation box is shown). Because of the velocity shear, the fluid enters the box from the two inflow y boundaries ($x > 0$ & $y > 0$ and $x < 0$ & $y < 0$) with initial background $\Delta\zeta = 0$, and maintains this value until it reaches the spiral wave. If the fluid element meets a spiral wave at $|x_{\rm cross}| \lesssim l_{\rm sh}$, the shock is not crossed and the original $\Delta\zeta$ value is conserved. The fluid element carries it until it leaves the simulation domain through the outflow y boundary ($x < 0$ & $y > 0$ and $x < 0$ & $y > 0$).

On the other hand, if $|x_{\rm cross}| \gtrsim l_{\rm sh}$, the fluid element crosses the shock, potential vorticity conservation is broken and ζ gets a kick. The amplitude of the ζ jump depends on $|x_{\rm cross}|$. A larger $|x_{\rm cross}|$ results in a weaker ζ jump because further from the planet the shock becomes weaker and the incidence angle of the fluid on the shock is more oblique. After the shock, the fluid element conserves the new value of ζ until it leaves the box. Note that ζ is ill defined right at the shock front, which produces the feature along the spiral (also visible in Lin & Papaloizou, 2010, Fig.1), and the noisy structure at small $|x|$ is due to the vortex generation in the co-orbital region (Koller et al., 2003; Lin & Papaloizou, 2010). Measured as a function of $|x|$ at large $|y| \ll h$, $\Delta\zeta$ maintains the background value as small $|x|$ until $|x| \approx l_{\rm sh}$, where it first grows with x, and then gradually decreases, as the wave decays and the shock becomes weaker and weaker.

In Figure 2.15a we plot the maximum value of the vorticity jump $\Delta\zeta_{max}$ (scaled by Ω/Σ_0 to make it dimensionless) as a function of the planetary mass $M_{\rm p}$. The value of $\Delta\zeta_{max}$ was derived by varying x at fixed $y \gg y_{\rm sh}(l_{\rm sh})$ behind the shock and finding the maximum of $\Delta\zeta(x)$ at the shock in a simulation with a given $M_{\rm p}$. Analytical calculation of $\Delta\zeta$ generation in §3.1 based on weakly nonlinear theory of GR01 predicts that $\Delta\zeta_{max} \propto M_{\rm p}^{16/5}$. However we find that our results are fit marginally better by the dependence $\Delta\zeta_{max} \propto M_{\rm p}^{2.95}$ over more than 2 orders of magnitude in planetary mass. This result confirms the low efficiency of the potential vorticity excitation by low-mass planets.

In Figure 2.15b we plot the full radial profiles of $\Delta\zeta$ produced after a single shock crossing for three different $M_{\rm p}$. For better graphic representation, we smooth the ζ curve by averaging value over $h/32$ in x to reduce the noise. We display the data scaled by $M_{\rm p}^{2.95}$ as a function of $x/l_{\rm sh}$. The exponent 2.95 of the mass scaling is the same as in Figure 2.15a so that the resultant curve has a universal shape, independent of $M_{\rm p}$.

One can see that, as expected, $\Delta\zeta$ stays close to zero for $x < l_{sh}$, i.e. prior to the appearance of the shock. At the shock $\Delta\zeta$ very rapidly (within radial distance $\lesssim 0.1 l_{sh}$) attains its maximum value, as the shock front develops. Subsequently $\Delta\zeta$ decreases because the shock rapidly weakens with increasing x: its amplitude is reduced by the dissipation and also the shock becomes more oblique to an incoming flow. As stated in §3 far from the planet shock evolves into an N-wave with χ decaying[5] as $\Delta\chi_{sh} \propto t^{-1/2} \propto (x/l_{\rm sh})^{-5/4}$, see Eqs. (2.14) and (2.19). As a result, according to Eq. (2.26), at $x \gg l_{\rm sh}$ the amplitude of $\Delta\zeta$ should generally decrease $\propto |x/l_{\rm sh}|^{-17/4}$.

At smaller $x \gtrsim l_{\rm sh}$ $\Delta\chi_{sh}$ does not obey the N-wave scaling and decays with x rather slowly, as can be directly seen from Figure 2.13b, where Δ acts as a proxy for $\Delta\chi_{sh}$. Also, at these separations the factor in square brackets in Eq. (2.25) varies in a non-trivial fashion. Initially $\partial \ln \Delta\chi_{sh}/\partial \ln t$ is small, see Figure 2.13b, and the factor in square brackets (as well as the $\Delta\zeta$) is positive. However, at large separations N-wave evolution results in $\partial \ln \Delta\chi_{sh}/\partial \ln t \to -1/2$ and

[5]In the N-wave regime one can identify $\Delta\chi_{sh}$ from Eq. (2.24) with Δ defined by Eq. (2.18).

the factor in square brackets approaches $-3/2$, making $\Delta\zeta$ negative. From our numerical calculations we find that $\Delta\zeta$ changes sign at $x \approx 1.5 l_{\rm sh}$. This result agrees well with numerical calculations of other authors (Li et al., 2005).

Previously, potential vorticity generation at the shock was studied by Koller et al. (2003), who focused on the co-orbital region of the protoplanet, and by Li et al. (2005), who numerically investigated the dependence of potential vorticity on spatial resolution in 2D inviscid disks. Both studies addressed the flow instability caused by the potential vorticity generation. Recently, Yu et al. (2010) explored the time evolution of the potential vorticity and its dependence on $r_{\rm s}$. Muto et al. (2010) also studied the possibility of using potential vorticity to identify the shock formation in an attempt to verify the theoretical $l_{\rm sh} - M_{\rm p}$ scaling relation in GR01. However, their potential vorticity profiles were rather noisy preventing meaningful quantitative comparison.

Lin & Papaloizou (2010) investigated the potential vorticity generation by a massive planet ($M_{\rm p} \gtrsim M_{\rm th}$, so the wave shocks immediately after being excited). They followed fluid elements on horseshoe orbits, and confirmed that the potential vorticity is generated as material passes through the two spiral shocks. In a global cylindrical geometry employed in their work, a fluid element gets a kick in the potential vorticity every time it passes a spiral shock, so the potential vorticity in the simulation box increases with time. This is also the case in our 2D local shearing sheet geometry when we switch the y boundary condition to periodic. However, while in Lin & Papaloizou (2010) the potential vorticity stops increasing and reaches a plateau after $30 - 50$ orbits, in our low mass planet ($M_{\rm p} \ll M_{\rm th}$) and high resolution cases we do not see this saturation. In one experiment with 100 orbits, our $\Delta\zeta$ linearly increases with time throughout the entire simulation time. It is not clear what causes this difference, but we suspect that the low resolution (which introduces larger numerical viscosity) might be responsible for it in the Lin & Papaloizou (2010) case.

6.3 Effect of Equation of State

In linear regime, the density wave evolution does not depends on the equation of state, as long as the sound speed of the gas is fixed. However, the EOS has a prominent effect in the nonlinear regime, which results in a dependence of the shock location on γ (Eq. 2.17). We show in Figure 2.16 the radial $\Delta\zeta$ profiles for two simulations with otherwise identical parameters (including the sound speed) but with different EOS ($\gamma = 1$ and $\gamma = 5/3$). There are two major differences between them. First of all, $l_{\rm sh}$ for the two cases are different, with larger γ resulting in earlier shock. The difference between $l_{\rm sh}$ in two cases is consistent with the theoretical prediction for these γ ($\sim 10\%$). Second, the peak $\Delta\zeta$ value in the $\gamma = 5/3$ case is about 25% higher than in the $\gamma = 1$ case. On the other hand, the decay of the $\Delta\zeta$ profiles is qualitatively similar for different EOS.

6.4 The $l_{\rm sh} - M_{\rm p}$ Relation

One of the most important results of the analytical theory by GR01 is the relation (2.17) between the shocking length $l_{\rm sh}$ and the mass of the planet $M_{\rm p}$. This relation plays a central role in the calculation of every process driven by the nonlinear evolution, such as the migration feedback and gap opening (Rafikov, 2002b). Here we provide the numerical confirmation of this relation, as shown in Figure 2.17.

We define the shock location as the value of x at which ζ reaches half of its maximum value at the jump. The numerical data points nicely agree with the theoretical expectation $l_{\rm sh} \propto M_{\rm p}^{-2/5}$

for about *2.5 orders of magnitude* in $M_{\rm p}$, with deviation $< 10\%$ for most of the $M_{\rm p}$ range. The smallest $M_{\rm p}$ presented here ($3.69 \times 10^{-3} M_{\rm th}$) corresponds to ~ 4 Lunar mass and the largest $M_{\rm p}$ ($0.667 M_{\rm th}$) corresponds to $\sim 8 M_\oplus$ at 1 AU for a MMSN model. The numerical result deviates from theory at the largest $M_{\rm p}$ as expected, because the wave excitation and the shock formation regions are no longer separated there. At the small $M_{\rm p}$ end we also see a trend of deviation from theory. This is because the nonlinearity for such low-mass planets is so small that the linear dissipation due to numerical viscosity becomes non-negligible and starts to damp the wave prior to the theoretically expected location (see discussion in § 8.2). We expect that modeling the disk at even higher resolution than we have ($256/h$) or more accurate algorithms will resolve this problem (§ 7).

Previous attempts to verify $l_{\rm sh} - M_{\rm p}$ relation (2.17) were pioneered by Paardekooper (2006), who inferred $l_{\rm sh}$ from the width of the gap opened by the planet. They found $l_{\rm sh}$ to *increase* with decreasing $M_{\rm p}$, in agreement with GR01 theory. However, the resolution of his simulations was insufficient for quantitative verification of Eq. (2.17). Subsequently, Yu et al. (2010) confirmed $l_{\rm sh} - M_{\rm p}$ relation using potential vorticity as means of shock detection. Their calculations spanned only about an order of magnitude in $M_{\rm p}$ and were not fully converged (*e.g.* in terms of softening length $r_{\rm s}$). Since their simulations were run in cylindrical geometry, Yu et al. (2010) found $l_{\rm sh}$ in the inner disk to be smaller than in the outer disk. This is to be expected, since global shear rate is higher in the inner disk, which causes faster nonlinear evolution there in agreement with Rafikov (2002a). Nevertheless, the results of Yu et al. (2010) for $l_{\rm sh} - M_{\rm p}$ relation are in reasonable quantitative agreement with Eq. (2.17).

6.5 The decay of Angular Momentum Flux

The spatial patten of the decay of the angular momentum flux carried by the density wave determines how the disk will respond to the presence of the protoplanets, which subsequently determines the efficiency of the density feedback and the gap opening. GR01 studied the post-shock AMF decay, and predicted the asymptotic behavior of AMF at large distance (Eq. (2.20), also see Figure 3 in GR01.). Numerically, we calculate the AMF as:

$$F_H(x) = \Sigma_0 \int_{-\infty}^{\infty} uv dy, \tag{2.45}$$

where u and v are the azimuthal and radial velocity perturbation of the fluid with respect to the background shear profile. In theoretical calculation, GR01 showed that $F_H(x)$ is given by

$$F_H(x) = \frac{27\, c_{\rm s}^3 \Sigma_0}{2^{3/2}(\gamma+1)^2 \Omega} \left(\frac{M_{\rm p}}{M_{\rm th}}\right)^2 \Phi(t) \tag{2.46}$$

where the dimensionless AMF $\Phi(t)$ is defined as

$$\Phi(t) \equiv \int \chi^2(\eta, t)\, d\eta. \tag{2.47}$$

and χ, η, and t are defined in Eqs. (2.14-2.16). Here we follow their notation and measure $\Phi(t)$ from our simulations by calculating $F_H(x)$ and using Eq. (2.46).

We plot the numerically measured $\Phi(t)$ in Figure 2.18 for three different values of $M_{\rm p}$. Our numerical results agree well with the theoretical prediction at large distance after the shock,

which is the working range of the theory, showing that the AMF decay is indeed close to $|x|^{-5/4}$. To the left of the theoretical shocking distance is the linear evolution regime, where AMF increases as the wave accumulates angular momentum. Note that in the linear region, a pattern of AMF increase with x should not depend on $M_{\rm p}$. The apparent dependence is because t in Figure 2.18 has been scaled by $M_{\rm p}^{-1}$. At $l_{\rm sh}$ the wave AMF stops increasing and starts to dissipate. To the right of $l_{\rm sh}$, in the nonlinear regime the patten of AMF decay with x does depend on $M_{\rm p}$. However, we remove this dependence and make the AMF decay pattern independent of $M_{\rm p}$ by using t instead of x in Figure 2.18.

7 Sensitivity of Results to Numerical Parameters

We now explore how the results presented in previous sections and their agreement with analytical theory are affected by the variation of purely numerical parameters in our simulations. Table 2.1 lists the numerical parameters that we varied and the values we explored. Values corresponding to our standard case are indicated in boldface. Figure 2.9, 2.19, and 2.10 show various physical quantities for different values of various numerical algorithms, and we discuss the effect of each of them in detail below.

7.1 Numerical Solver and Order of Accuracy

In our simulations we compare two different Riemann solvers — Roe's linearized solver (Roe 1981) and HLLC — with three different algorithms for the spatial reconstruction step (Stone et al., 2008): second order with limiting in the characteristic variables (denoted `2` in this work), which is the predominant choice in literature in this field, third order with limiting in either the characteristic variables (`3c`), or in the primitive variables (`3p`). We find that Roe and HLLC solvers yield nearly identical results both in terms of the density profile and in terms of $F_H(x)$ and $T_H(x)$ (differences are at the 0.1% level).

In the linear regime, the effect of using a different order of accuracy on the profile of the density wave is shown in Figure 2.9a, where we plot azimuthal density cuts obtained with different numerical settings at $x = 1.33h$ (together with semi-analytical profile computed by GR01 in the framework of linear theory) and $x = 4h$. One can see that density perturbation is rather insensitive to variation of the order of accuracy.

The sensitivity of the AMF calculation to varying order of accuracy is illustrated in Figure 2.10a, where the linear theory curve based on the semi-analytical calculation by Rafikov & Petrovich (2012) is overplotted for reference. One can see that the higher order of accuracy (`3c` and `3p`) results in a slightly lower asymptotic value of torque and AMF, and the difference in the asymptotic value for the two between the `2` case and the `3p` case is about 5%. Furthermore, `3c` and `3p` cases agree with each other on the position where the AMF curve starts to deviate from the torque, $\sim 4h$, which is still somewhat smaller than the theoretical prediction $l_{\rm sh} \approx 5h$ in this case due to the relatively low resolution. However, the second order of accuracy moves this point inward, which means that the angular momentum carried by the wave starts to dissipate earlier in this case. In particular, we find that using a second order accuracy solver compared with the third order accuracy solver has similar effect to decreasing the resolution by a factor of 2 (in term of advancing the displacement of the AMF-torque separation point, see §7.2 and Figure 2.10b).

In the nonlinear regime, the two kinds of solvers yield almost identical results on the $\Delta\zeta$ profile. On the other hand, different orders of accuracy do make significant differences. `3p`

accuracy (not shown in this figure) introduces large high frequency fluctuations on $\Delta\zeta$ profile compared to `2` and `3c` accuracy. For the two spatial reconstruction steps with limiting in the characteristic variables, as shown in Figure 2.19a `2` accuracy generates a much smoother rise of the $\Delta\zeta$ profile around $l_{\rm sh}$, compared with the sharp jump in the `3c` accuracy case. In addition, `2` case advances shock formation, causing the numerical $l_{\rm sh}$ to disagree with theoretical prediction (2.17). Analogous to the linear regime, we find that the effect of reducing the accuracy from third order to second order is very similar to reducing the resolution by a factor of 2.

A critical ingredient to any total variation diminishing (TVD) reconstruction scheme, as are used in Athena, are the slope limiters used to ensure monotonicity. We have not explored the use of different limiter in this work, but this may affect the accuracy of the `3p` and `3c` methods.

7.2 Resolution

In Figure 2.9b we show the effect of varying resolution of our simulations on the density profile. In general, increasing resolution from $64/h$ to $256/h$ improves the agreement with linear theory, but only slightly. Lower resolution simulations overestimate the amplitude of $\delta\Sigma$ by just several per cent compared to $256/h$ simulations. Thus, for the study of the density wave profile our simulations essentially reach convergence in terms of resolution already at $64/h$.

In Figure 2.10b we show that the AMF and torque calculations are more sensitive to resolution, especially when the nonlinear effects become important. Increasing resolution causes the asymptotic values of $F_H(x)$ and $T_H(x)$ to decrease, and the difference in the asymptotic value for the two between the $256/h$ case and the $64/h$ case is about 10%. The key factor that clearly shows the downside of low resolution is the location, at which the numerical AMF curve deviates from the numerical torque calculation. Calculations shown in Figure 2.10 use $M_{\rm p} = 1.2 \times 10^{-2} M_{\rm th}$, which according to Eq. (2.12) corresponds to shocking length $l_{\rm sh} \approx 5h$. In our highest resolution simulations ($256/h$), the AMF curve starts to deviate from the accumulated torque curve precisely at $l_{\rm sh} \approx 5h$, as expected from theory. But as we reduce resolution, the radial separation at which $F_H(x)$ starts departing from $T_H(x)$ moves closer to the planet violating the agreement with theory. In $64/h$ simulations such departure starts already at $3.2h$, considerably closer to the planet than the nominal shock location $l_{\rm sh}$. This behavior is caused by the higher level of numerical viscosity arising at low resolution, which leads to the dissipation of angular momentum carried by the wave prior to shock formation (we verified this point by conducting some runs with explicit viscosity, see below, which show behavior qualitatively similar to our low resolution runs here). Thus, high resolution is crucial to correctly capture the details of the nonlinear wave evolution.

Resolution has a strong influence on the shock formation, as shown in Figure 2.19b. Lower resolution considerably accelerates shock formation, causing $l_{\rm sh}$ to deviate from the theoretical prediction. Furthermore, the shape of the rising edge of the $\Delta\zeta$ profile depends on resolution. Increasing resolution steepens the edge of the $\Delta\zeta$ curve, and eventually makes it almost vertical in the case of $256/h$ (which is a sign that the convergence on resolution has been achieved). We also find that at low resolution ($64/h$ in our case), the $\Delta\zeta$ profile always demonstrates a double peaked structure, which is a purely numerical artifact.

7.3 Planetary Potential and Softening Length $r_{\rm s}$

The rate at which a given smoothed potential converges to Φ_K is important for the problem of density wave generation. Indeed, the amplitude and spatial distribution of fluid perturbation is in

the end determined solely by the potential behavior. As a result, if Φ is substantially different from Φ_K in the region where most of the torque is exerted by the planet, i.e. at $|x| \approx 0.2 - 2h$, see Figure 2.7, then one can expect significant spurious effects modifying the density wave properties.

A specific form of the potential can have a two-fold effect on the properties of the density wave excited by the planet. First, there is a deviation of the potential from Newtonian, which directly affects the wave excitation at a given separation from the planet. But in addition, different potentials result in different structures of the quasi-static atmospheres (see §5.1) that get collected in the planetary potential well. This has an effect on the pressure distribution in the vicinity of the planet and can also affect wave excitation by modifying the dispersion relation and displacing the effective positions of Lindblad resonances. In practice disentangling these two effects based on the results of simulations may be non-trivial.

In the linear regime, in Figure 2.9c we show that for a fixed $r_s = h/16$ varying the order of the potential does not have a significant effect on the density wave profile. However, the AMF and torque calculations are more sensitive to the form of the potential, as Figure 2.10c demonstrates. In particular, AMF in calculations with less accurate potential (e.g. $\Phi_p^{(2)}$) is lower than it is in more accurate potential (5% for $\Phi_p^{(4)}$). We note that the seemingly better agreement with theory in the $\Phi_p^{(2)}$ case is an accidental phenomenon at this set of other numerical parameters. For example, panel (d) shows that using softening length $h/8$ instead of $h/16$ could shift the curves downward by $\sim 8\%$, so if switching to $h/8$ in panel (c) then the $\Phi_p^{(6)}$ case would come to perfect agreement with the linear theory (see §7.4 for additional discussion). In Figure 2.9d we explore the effect of varying r_s for a fixed form of the potential $\Phi_p^{(4)}$. We discover that lowering r_s results in a higher amplitude of the density perturbation. On the other hand, Figure 2.10d shows that a lower r_s leads to a higher numerical AMF and torque, and the difference in the asymptotic value for the two between the $r_s = h/8$ case and the $r_s = h/32$ case is about 16%. Again, the better agreement between the theory and the $h/8$ case is accidental. Our calculations presented in §5 use $\Phi_p^{(4)}$ potential with $r_s = h/32$.

In the nonlinear regime, the effect of various Φ_p is shown in panel (c), and that of different r_s in panel (d). We find that switching to Φ_p one level higher in accuracy increases $\Delta\zeta_{peak}$ by $\sim 10 - 15\%$, steepens the edge of the $\Delta\zeta$ profile, and slightly advances the shock formation. Reducing r_s by a factor of 2 has quantitatively similar effects. But in general the variation of Φ_p and r_s has far less prominent effect on the $\Delta\zeta$ evolution than the accuracy of solver and resolution. Based on this discussion we can state that in order to accurately follow the nonlinear wave evolution and capture the shock formation, it is crucial to use high order of accuracy of the numerical solver, and high spatial resolution. Simulations which do not satisfy these criteria may be affected by numerical artifacts and may not be able to resolve properly either the nonlinear wave evolution or its consequences — the migration feedback and the gap opening.

7.4 Summary of Convergence Study

We conclude that the overall shape of the density wave profile is generally less sensitive to the variations of numerical parameters (unless these values are very different from the ranges explored in this work, see below) than the spatial dependence of the AMF or integrated torque. This emphasizes the importance of these integrated quantities as diagnostics of various subtle effects influencing the wave properties.

In the course of this numerical exploration we have also discovered that the "optimal" value of a particular numerical parameter (e.g. softening length r_s) showing closest agreement with the linear theory depends on the values of other numerical parameters (e.g. resolution, type of the potential, etc.) and on M_p. In other words, there is no universal best choice for each numerical parameter of simulations. In both Figure 2.9 and 2.10, only the relative position of the curves representing different parameters matters, not their exact locations and the discrepancies between them and the linear theory. On the other hand, high order of accuracy, high resolution, and highly accurate form of the potential with small softening length are critical to properly resolve the nonlinear stage of the wave evolution.

Hydrodynamic simulations of the disk-planet interaction must often be run for many orbital periods. This is the case *e.g.* in studies of planetary migration or gap opening, in which substantial effects appear on timescales of hundreds to thousands of orbital periods (depending on M_p). This severely restricts the choice of resolution and softening length at which such simulations can run. Typical resolutions in global disk simulations found in the literature (Kley, 1999; Bryden et al., 1999; Nelson et al., 2000; D'Angelo et al., 2002, 2003; Li et al., 2009; Yu et al., 2010; Muto et al., 2010) range from $32/h$ to $1/h$, and r_s is usually taken to be between $0.1h$ to h, in combination with a second order of accuracy solver and the second (see Eq. (2.32)) or even lower order representation of the planetary potential. On the other hand, accurate description of the migration rate and gap opening may only be possible if properties of the density wave excited by the planet are properly captured by the simulation.

To test how reliably the wave structure can be reproduced in global simulations we compare two sets of simulations in our local setting with $M_p = 1.2 \times 10^{-2} M_{th}$. We run one simulation with the typical numerical parameters for local shearing box simulations found in recent literature (typical global simulations in literature use even smaller resolution and r_s): second order of accuracy, resolution $32/h$ and $\Phi_p^{(2)}$ potential with $r_s = h/4$. Another simulation is run with our fiducial parameters — third order of accuracy, resolution $256/h$, and $\Phi_p^{(4)}$ potential with $r_s = h/16$ — and their results are compared in Figure 2.11.

There are noticeable differences between the two runs. The simulation with typical literature parameters produces smoother density profile, which deviates from analytical solution by about 20%, see Figure 2.11a. At the same time, our fiducial run shows deviations from analytical profile only at the level of 1%.

The difference is even more pronounced when we compare the AMF and torque behavior in Figure 2.11b. Our fiducial simulation yields asymptotic values of $F_H(x)$ and $T_H(x)$ which are within several per cent of the expected theoretical value (2.9). As expected, $F_H(x)$ agrees with $T_H(x)$ all the way until $x \approx 5h$, which is precisely the shock location for the M_p used, according to Eq. (2.12). On the contrary, in the typical literature simulation AMF $F_H(x)$ starts deviating from the integrated torque curve $T_H(x)$ already at $x \approx 2.5h$, significantly in advance of the expected shock position (a factor of 2). This indicates that dissipation and transfer of the angular momentum carried by the wave to the disk fluid start earlier in the typical literature case than they should in reality. The most likely explanation for this behavior is the high level of numerical viscosity in the typical literature run. Moreover, the absolute asymptotic values of $F_H(x)$ and $T_H(x)$ disagree with the theoretical prediction for asymptotic F_H by $\sim 23\%$ (comparing with $\sim 2\%$ in our fidicual simulation), which is quite significant. We note that the differences between our fiducial and the typical literature simulations persist also in experiments with larger planet masses, $M_p \lesssim M_{th}$, while the linear regime of wave excitation still holds.

Underestimate of the wave angular momentum flux in the low-resolution simulations may result in an underestimate of the planetary migration rate in global simulations. In our shearing sheet setup we cannot investigate the effect of resolution on the planetary migration rate: by design one-sided torques exerted by the inner and outer parts of the disk on the planet exactly cancel each other, while the migration speed relies on the small imbalance between them. But the very fact that the one-sided torques in low-resolution case deviate by tens of per cent from the high-resolution case is suggestive that the migration speed should be adversely affected by poor resolution at the same level. Furthermore, the relative imbalance between the one-sided torques can also be a function of resolution potentially exacerbating the problem.

The discrepancy in the AMF should also affect the fidelity of gap opening by the planet in typical literature global simulations. Lower AMF carried by waves means that the planet is less effective at repelling gas away from its semi-major axis, which would require higher $M_{\rm p}$ to open a gap. In addition, the gap opening process is sensitive to the *spatial distribution* of the AMF dissipation (Rafikov, 2002b). As a result, spurious dissipation of wave AMF prior to shock formation in low-resolution simulations and the accelerated AMF decay after the shock may introduce artificial effects in the gap opening picture. To summarize, any numerical studies of processes in which density wave production and dissipation plays important role need to use high order of accuracy, high resolution, and accurate representation of the planetary potential with small softening length.

8 Discussions

8.1 A Numerical Issue in Planet-disk Simulations

In this section we describe a commonly ignored numerical problem that we discover in disk-planet interaction simulations. Namely, we find that if the time-step dt of the simulation is too large, the code cannot resolve the motion of the fluid in regions where the fluid experiences large gravitational acceleration. This issue applies to simulations in general, but it is especially problematic when the orbital advection algorithms is implemented (the FARGO algorithm, citealtmas00).

Masset (2000) introduced a modification of the standard transport algorithm (Fast Advection in Rotating Gaseous Objects, FARGO) for simulations of differentially rotating systems, which significantly speeds up the calculations. By getting rid of the average azimuthal velocity when applying the Courant condition, this technique results in a much larger time step dt, which is limited by the small perturbed velocity, than the usual procedure, where dt is limited by the full fluid velocity dominated by the differential rotation. FARGO has been implemented in Athena by Stone & Gardiner (2010).

In a shearing box without planets, the dynamical time scale is Ω^{-1} and is uniform throughout the box. However, when the planet is introduced, the dynamical timescale is spatially varying, and could be characterized by the free-fall time, which is the time that it takes a fluid element to fall on the planet assuming a constant acceleration at the grid point. For gravitational potential in the form of Eq. (2.33), the free-fall time is:

$$t_{ff} = \sqrt{\frac{2(\rho^2 + r_{\rm s}^2)^{5/2}}{{\rm G}M_{\rm p}(\rho^2 + 2.5r_{\rm s}^2)}} \tag{2.48}$$

Note that t_{ff} depends on a specific form of the gravitational potential, and a more smoothed potential results in a larger t_{ff}. The smallest free-fall time in the entire domain, which is the limiting timescale for the simulation, occurs at the grid points that are adjacent to the planet, which have the smallest ρ ($1/\sqrt{2}$ of the cell size r_c in Athena; the separation where the smallest t_{ff} occurs also depends on the form of potential). In our simulations, we always keep $r_{\rm s}^2 \gg r_c^2$ (usually $r_{\rm s} = 8r_c$), so the smallest free-fall time is:

$$t_{ff,s} \approx \sqrt{\frac{0.8 r_{\rm s}^3}{{\rm G}M_{\rm p}}} \tag{2.49}$$

On the other hand, according to the Courant condition when varying the resolution the time step $dt \propto r_c$. So the ratio $t_{ff,s}/dt$ scales with numerical parameters and $M_{\rm p}$ as

$$\frac{t_{ff,s}}{dt} \propto \frac{r_{\rm s}^{1.5}}{\sqrt{M_{\rm p}} r_c} \tag{2.50}$$

To properly resolve fluid dynamics in the vicinity of the planet, the ratio $t_{ff,s}/dt$ should be kept above a certain threshold.

Our calculations without orbital advection and with dt determined by the Courant condition usually have $t_{ff,s}/dt \sim 150$. However when we turn on the orbital advection algorithm, dt typically increases by a factor of ~ 10, and the ratio $t_{ff,s}/dt$ decreases by the same factor. We find that when the time-step is *too large* to properly resolve the fluid motion around the planet, the numerical results will be *incorrect*, as described below.

Figure 2.12 shows the azimuthal density profiles $\delta\Sigma$ at $x = 1.33h$ for a set of simulations using identical numerical parameters and orbital advection algorithm but with different $t_{ff,s}/dt$ ratio, which we achieve by manually setting dt to be a fraction of the dt set by the Courant condition in FARGO. The two cases with highest $t_{ff,s}/dt$ yield the density profile in agreement with the theoretical prediction, also demonstrating the convergence of the result at high $t_{ff,s}/dt$. However, the density profiles in simulations with lower $t_{ff,s}/dt$ clearly deviate from theory, with smaller $t_{ff,s}/dt$ leading to larger discrepancy. In the run with the smallest used $t_{ff,s}/dt = 18$ which corresponds to dt set by the Courant condition in FARGO (representing maximum FARGO speed up), the density peak even becomes a density trough. By experimenting with Athena, we generally find that our simulations of the disk-planet interaction produce converged results agreeing with theory only when

$$t_{ff,s}/dt \gtrsim 100, \tag{2.51}$$

while this critical number may depend on the numerical method used in a particular code or some other numerical conditions. We note that in principle all disk-planet simulations have to satisfy condition (2.51) to ensure correct results, but in experiments we find simulations with the orbital advection algorithm tend to violate this condition much more easily than simulation without the orbital advection algorithm.

Apart from incorrectly reproducing density perturbation, disk-planet simulations violating the $t_{ff,s}/dt$ constraint exhibit other serious problems. In particular, simulations with small $t_{ff,s}/dt$ do not achieve a steady state. We illustrate this in Figure 2.12 by showing the density profile at half simulation time for two cases. While the $t_{ff,s}/dt = 144$ case reaches a steady state and develops time independent density profile at half time, the $t_{ff,s}/dt = 72$ case does not, and its density perturbation decreases with time.

In simulations with $t_{ff,s}/dt$ lower then the critical value, the fluid element approaching the planet at small $|x|$, instead of moving on a horseshoe orbit, gets trapped by the planetary potential, leading to the formation of a fluid loop around the planet. As simulation progresses the rotational velocity of the fluid loop becomes higher and higher, and eventually the centrifugal force evacuates the region around the planet. This effect, which is a purely numerical artifact of the too small $t_{ff,s}/dt$, is visually very similar to (and can easily be confused with) the gap opening phenomenon, which is a real physical effect. Simulations exploring the gap opening process with large planet mass and low resolution are likely to have small $t_{ff,s}/dt$ violating condition (2.51, see Eq. 2.50), which may have detrimental effects on the results. We note that using Athena with orbital advection algorithm, numerical simulations with $M_{\rm p} \sim M_{\rm th}$ and a large $r_{\rm s} = h/4$ must have an effective resolution at least $64/h$ in the vicinity of the planet to avoid this problem (a more smoothed potential may weaken this condition, through). However, again we emphasize that the critical value of $t_{ff,s}/dt$ in simulations with the same numerical parameters but using different code and solver may be different from ours.

The $t_{ff,s}/dt$ threshold severely limits the ability of FARGO to speed up calculations of disk-satellite interaction. For most of our simulations, $t_{ff,s}/dt$ is already rather close to the threshold value without orbital advection algorithm, so there is not much room left to increase dt, which is what the orbital advection algorithm aims to achieve (all our simulations presented outside this section are done without orbital advection technique). However, in many other studies of differentially rotating systems, such as the investigation of magnetorotational instability (MRI) in accretion disks, the point mass objects are absent and the characteristic dynamical time scale is always long enough for the orbital advection algorithm to be a extremely useful tool for speeding up the simulations. At last, we note that both dt and $t_{ff,s}$ may vary during the simulation, and the constraint (2.51) on their ratio should be satisfied in the entire domain throughout the simulation time.

8.2 Nonlinear Evolution in Presence of Explicit Viscosity

Nonlinear evolution of density waves launched by the low-mass planets can be significantly affected by linear damping even if the latter is due to numerical viscosity. This is because the time it takes for nonlinearity to have an effect is longer for smaller $M_{\rm p}$, which enhances the relative contribution of the linear wave damping.

To explore the effect of linear damping on nonlinear wave evolution, we carry out an experiment with explicit Navier-Stokes viscosity. We choose kinematic viscosity ν to correspond to Reynolds number $Re \equiv hc_{\rm s}/\nu = 10^4$. This is equivalent to having effective Shakura-Sunyaev $\alpha = \nu/(hc_{\rm s}) = 10^{-4}$. We compare the results with another simulation under otherwise identical conditions but without explicit viscosity (our numerical viscosity is at least 10 times smaller in this case, which corresponds to Shakura-Sunyaev $\alpha \lesssim 10^{-5}$). The results of the comparison are shown in Figure 2.20.

Before the shock the numerical AMF and accumulated torque calculations should agree with each other, because of the angular momentum conservation. After the shock formation, dissipation damps the wave and transfers the angular momentum from the wave to the local disk material causing the AMF to drop below the accumulated torque curve. Accumulated numerical

torque in our simulations is calculated as:

$$T_H(x) = \int_0^x \frac{dT_H}{dx} dx = \int_0^x dx \int_{-\infty}^{\infty} dy \delta\Sigma \frac{\partial \Phi_{\rm p}}{\partial y}, \tag{2.52}$$

and its asymptotic value in the linear case is (GT80):

$$T_{H,\rm final} \approx 0.93 \left(G M_{\rm p}\right)^2 \frac{\Sigma_0 \Omega_p}{c_s^3}. \tag{2.53}$$

As shown in the panel (a), while in the inviscid case this deviation happens right at the theoretically predicted shocking length ($l_{\rm sh} \approx 4h$), in the viscous case AMF starts to deviate from the $T_H(x)$ much earlier (at $\sim 2.5h$). This indicates that dissipation happens earlier in the viscous case due to the linear damping, which then must be reflected in the disk density redistribution, eventually affecting migration feedback and gap opening. In addition, panel (b) shows that in viscous case $\Delta\zeta$ starts to rise from zero much earlier than in the inviscid case, also indicating premature dissipation. Furthermore, the rise of $\Delta\zeta$ in the viscous case is very gradual, in contrast to the sharp jump in the inviscid case, and the peak $\Delta\zeta_{\rm peak}$ is also significantly reduced (by a factor of ~ 4). The combination of the two effects makes the shock detection very ambiguous in the viscous case.

We note that normally disks with $\alpha = 10^{-4}$ are considered to have very low viscosity, if not inviscid. However, as we show here, the physics of the nonlinear density wave evolution is very subtle so that even an $\alpha = 10^{-4}$ viscosity can dramatically affect wave damping. In simulations which aim at investigating the nonlinear wave evolution, the low spatial resolution ($\leq 32/h$, typically employed in the literature) will likely introduce high numerical viscosity. This is likely to give rise to inaccurate numerical results in a way similar to our viscous simulation shown here, and via the improperly captured back reaction on the disk density distribution, affect the description of the migration feedback and gap opening.

8.3 Implications for Realistic Protoplanetary Disks

The analytical and numerical calculations presented in this work directly apply only to the case of a 2D, laminar disk, containing a single low mass planet. We now discuss the applicability of our results to more realistic protoplanetary disks.

First, we note that for typical $h/r_{\rm p}$ values of protostellar disks (on the order of 0.1, Hartmann et al., 1998; Chiang & Goldreich, 1997), the size of the radial domain in this work (up to $10h$ on one side) would imply global disk dimensions, which might be seen as contradictive to the essence of the shearing box simulation. However, our numerical calculation is an idealization needed for checking the GR01 theory. Extensions of the GR01 theory to the global case are available in Rafikov (2002a), with which global simulations should be compared. Here we just point out that qualitatively things are the same in the global case.

Excitation of density waves by planets in fully three-dimensional (3D) disks has been previously investigated by a number of authors (Lubow & Pringle, 1993; Korycansky & Pringle, 1995; Takeuchi & Miyama, 1998). These studies have generally shown that disks with vertical thermal stratification do not support the modes similar to the modes existing in a purely 2D disk (Korycansky & Pringle, 1995; Lubow & Ogilvie, 1998; Ogilvie & Lubow, 1999). Thus, the results of our study cannot be directly applied to such thermally stratified disks.

However, protoplanetary disks at advanced stages of planet formation are expected to be passive (Chiang & Goldreich, 1997), heated predominantly by the radiation of their central stars with only negligible contribution from accretional energy release. Because of the external illumination such disks are expected to be vertically isothermal. It was previously found (Lubow & Pringle, 1993; Takeuchi & Miyama, 1998) that in vertically isothermal disks planetary gravity always very effectively excites the two-dimensional mode with no vertical motion, which is similar to the density wave in a 2D disk studied here. Even though other modes with non-zero vertical velocity perturbation are also excited by the planet in 3D isothermal disks, these modes are found to carry only a small fraction of the total angular momentum flux (Takeuchi & Miyama, 1998). Thus, density wave excitation and nonlinear dissipation in realistic passive protoplanetary disks should be very similar to the picture outlined in GR01 and this work.

The assumption of the laminar inviscid background flow in the disk used in this work may be violated in realistic protoplanetary disk if it is strongly turbulent, e.g. due to the operation of the magnetorotational instability (MRI). However, this instability and associated deviations from the purely laminar flow are expected to be greatly suppressed in the so-called "dead zones" of protoplanetary disks (Gammie, 1996), which are so weakly ionized that the operation of MRI is not supported there because of non-ideal MHD effects (Fleming & Stone, 2003). These zones are expected to extend over the several-AU wide region where planet formation is expected to occur (Turner & Sano, 2008) and in this part of the disk our results obtained under the assumption of laminar flow should be applicable. One should also mention that because of the suppressed viscous dissipation inside the dead zone the assumption of a vertically isothermal thermal structure of these regions is well justified.

Protoplanetary disks may easily host a number of protoplanets simultaneously and one may wonder whether the overlap of the density waves excited by different objects can have some effect on their evolution. This effect is not important in the limit of low mass planets $M_p \lesssim M_{\rm th}$ explored in this work since the density waves excited by such objects are only *weakly* nonlinear. As a result, the possible overlap of such density waves is, to a good approximation, just a linear combination of the independent density waves excited by individual planets. To summarize, the results of our work should directly apply at the very least to the density wave evolution in low viscosity regions ("dead zones") of passive protoplanetary disks heated predominantly by their central stars.

9 Summary

We have conducted a series of hydrodynamical simulations to study the details of the gravitational interaction between low mass planets and a protoplanetary disk, and to test predictions of the linear and nonlinear theory of density wave evolution. Our simulations assume local shearing sheet geometry and are carried out in 2D at very high resolution to reduce the effect of numerical viscosity. We focus on both the excitation of the density waves and their propagation away from the planet in the linear regime. To mitigate the effects of nonlinearity we consider very small planetary masses, starting at several $M_\oplus$ and going down to a few Lunar masses at 1 AU.

In the linear regime, we extract the spatial distribution of the density perturbation induced by the planet from our simulations and compare it with the predictions of linear theory. We find good agreement between the two, at the level of several per cent when high resolution (typically $256/h$) is employed. We also investigate the spatial dependence of the angular momentum flux carried by the wave and the distribution of torque induced by the planet on the disk, again

finding good agreement with theoretical predictions. In particular, we are able to reproduce the theoretical behavior of the torque cutoff in Fourier space.

We also find various manifestations of nonlinear effects in our simulations even while the waves are formally linear. These include (1) the noticeable steepening of the density profile at larger values of $M_{\rm p}$ far from the planet, (2) the slight variation of the asymptotic value of the AMF with planetary mass in addition to the expected $F_H \propto M_{\rm p}^2$ dependence, causing the discrepancy with linear theory prediction at the level of several per cent, and (3) the growth of power in high azimuthal wavenumber harmonics of the AMF in Fourier space.

By carefully studying the spatial distribution of the torque density $dT_H(x)/dx$ in our simulations we discover an interesting "negative torque" phenomenon: $dT_H(x)/dx$ changes sign at some radial separation from the planet (at $|x_-| \approx 3.2h$ in our simulations), which contradicts the analytical results of GT80. This effect can however be understood in the framework of the linear theory as shown in Rafikov & Petrovich (2012). This feature of the torque distribution has only weak effect on the total accumulated torque in our simulations.

We also carried out a detailed investigation of the effect of different numerical settings on our results in linear regime. We explored the influence on wave properties of (1) different Riemann solvers with different accuracy, (2) spatial resolution, (3) different forms of the softened planetary potential, and (4) softening length of the planetary potential. We find the spatial distribution of the AMF and torque to be a more sensitive probe of the effects of various numerical parameters on the wave evolution than the distortions of the density wave profile. Based on this study we conclude that a very high resolution (ensuring low numerical viscosity), high order of accuracy, and an accurate prescription of planetary potential with small softening length are critical for accurately reproducing the key features of the wave evolution in linear regime.

We demonstrate that low order of accuracy, low spatial resolution, and inaccurate potential with large softening length often employed in global disk-planet interaction studies can severely affect the fidelity of their results, especially in applications to planet migration and gap opening. Specifically, we conduct a test run with typical numerical parameters from recent literature. Comparing with the analytical theory, the test run produces a lower amplitude of the density wave (by $\sim 20\%$), a lower final accumulated torque (by $\sim 23\%$), and a largely advanced starting point of wave dissipation (a factor of ~ 2).

Most of our own calculations were carried out with third order of accuracy, resolution of $256/h$, softening length $r_{\rm s} = h/32$ and a potential that rapidly converges to Newtonian (as $(r_{\rm s}/\rho)^4$) at large separation ρ from the planet. This set of numerical parameters allows us to obtain excellent agreement with linear theory in Athena, but is not meant to be universal for other codes. However, the way in which we make the comparison with the theory and the agreement we achieve may serve as a standard framework for future code tests.

We also discover a numerical problem which is largely ignored in previous simulations of disk-planet interactions. To follow the fluid motion correctly, the time-step in a simulation has to be smaller than the local dynamical timescale by a certain factor (~ 100 in our case using Athena) in the entire domain, including the region where the fluid experiences the largest gravitational acceleration (*e.g.* the vicinity of the planet). In the context of numerical disk-planet studies, violation of this condition leads to inaccurate calculation of wave properties, lack of convergence on long time scales, and spurious repulsion of gas by planet similar to gap opening. This timescale issue applies to disk-planet simulations in general, but it particularly affects the ones which use the orbital advection algorithm (FARGO), in which cases a significant increase of the time step is usually allowed to speed up calculations.

In the nonlinear regime, we analytically study the potential vorticity generation at the shock location, and verify our calculation numerically. The scaling relation between $\Delta\zeta_{\rm peak}$ and $M_{\rm p}$ derived from the simulations is very close to the analytical result. We use the jump in potential vorticity as a way of pinpointing the shock location, based on which we numerically confirm with high accuracy (better than 10% in most of the $M_{\rm p}$ range) the theoretically predicted $l_{\rm sh} - M_{\rm p}$ relation for $M_{\rm p}$ varying by 2.5 orders of magnitude, from few lunar masses to several Earth masses at 1 AU. In addition, the theoretical dependence of the shocking length $l_{\rm sh} - M_{\rm p}$ relation on the equation of state of the gas is also verified.

We investigate the evolution of the density wave profile in the post-shock regime, and observe its evolution towards the N-wave shape. We verify the theoretical prediction for the evolution of the peak amplitude and the azimuthal width of the N-wave. The post-shock decay of the angular momentum flux carried by the wave also agrees with theory.

Furthermore, the effect of various numerical algorithms on the simulation results is explored, including numerical solver and its accuracy, resolution, planetary potential and the softening length. We find that in order to accurately follow the nonlinear wave evolution and capture the shock formation, high order of accuracy for the solver and high resolution are crucial. Simulations which do not satisfy these criteria will have trouble resolving shock formation and post-shock wave evolution driven by nonlinearity. The latter may further affect the consequences of the nonlinear wave evolution, such as the migration feedback and gap opening by low mass planets.

In addition, we find that the linear viscous damping strongly affects shock formation and the nonlinear wave evolution. Using an experiment with explicit viscosity, we find that the viscosity at the level of $\alpha \sim 10^{-4}$ can strongly modify the generation of potential vorticity at the shock, and accelerate the dissipation of the angular momentum carried by the wave. In low resolution simulations, the resulting high numerical viscosity may lead to similar effects on the nonlinear wave evolution and negatively impact the results on disk-planet interaction and planetary migration.

Table 2.1. Parameter Space of the Simulations

Parameters[a]	Range
Riemann solver (flux function) used	**Roe**, HLLC
Order of accuracy	`2`, **`3c`**, `3p`
Boundary conditions in y	Outflow, **Inflow/Outflow**
Resolution of the simulation (cells per h)	64, 128, **256**
Planetary potential[6]	$\Phi_{\rm p}^{(2)}$, $\mathbf{\Phi_{\rm p}^{(4)}}$, $\Phi_{\rm p}^{(6)}$
Softening length	1/8, 1/16, **1/32**
Equation of states of the fluid	$\gamma = \mathbf{1}$, $\gamma = 5/3$
Mass of the planet $M_{\rm p}$ ($0.01 M_{\rm th}$)	66.7, 24.2, 11.8, 4.28, 3.2, 2.09, 1.2, 0.757, 0.57, 0.37

[a]See Section 7 for details.

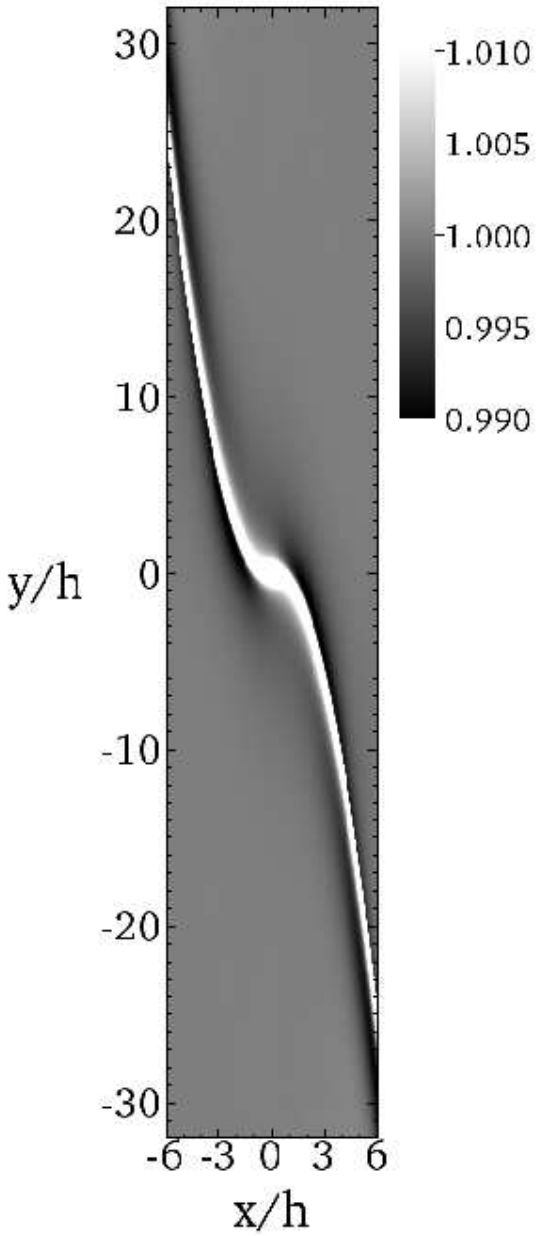

(a)

Figure 2.1 A typical image of our simulations, showing the density structure and the spiral waves. The quantity plotted here is Σ/Σ_0. $M_{\rm p} = 2.09 \times 10^{-2} M_{\rm th}$ in this case.

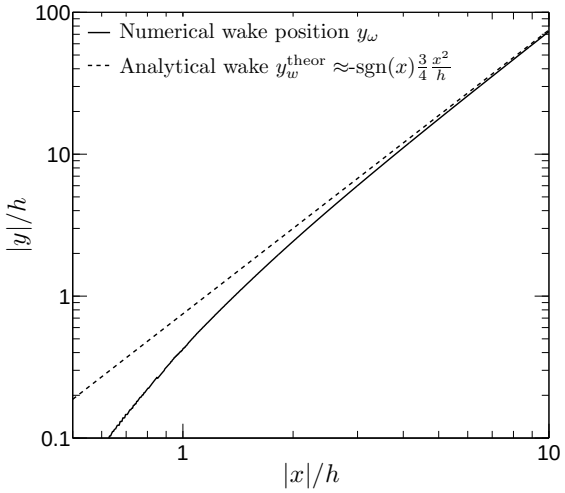

(a)

Figure 2.2 Location of the peak density in the wake in the $x-y$ plane measured from simulations (*solid curve*), compared to the analytical wake shape (*dashed curve*, Eq. (2.6)). As expected, they agree far from the planet. Numerical peak density position is nearly independent of the simulation parameters.

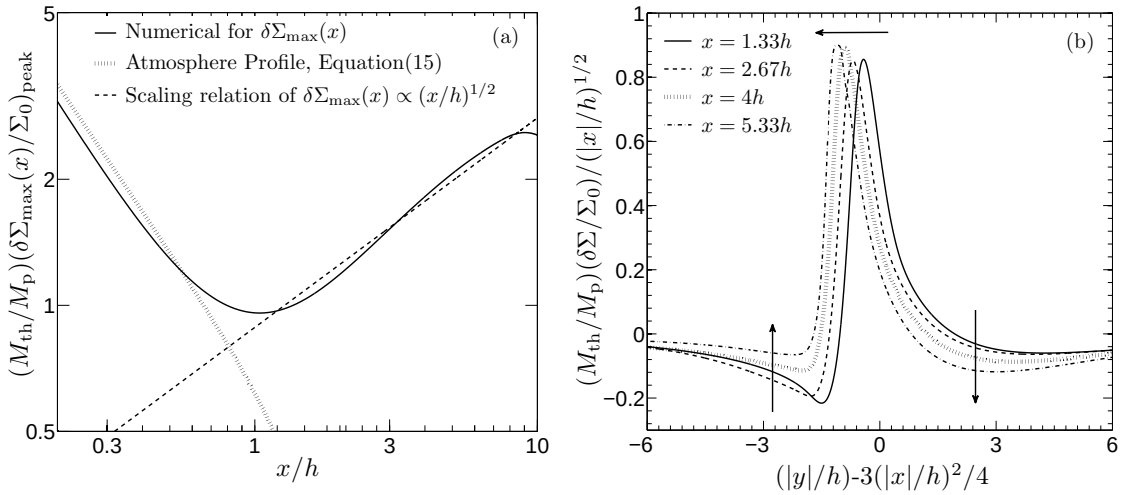

(a) (b)

Figure 2.3 Behavior of the density perturbation in a simulation with the following parameters: $M_{\rm p} = 3.7 \times 10^{-3} M_{\rm th}$ (corresponding to ≈ 3.6 Lunar masses at 1 AU), shocking distance $l_{\rm sh} \approx 8h$. (a) Variation of the peak value of the relative density perturbation $\delta\Sigma/\Sigma_0$ with x (*solid curve*). Analytical profile (2.35) of the quasi-static gaseous envelope collected inside the planetary potential well (without background shear) is shown by the dotted curve. Dashed line shows theoretical scaling $\delta\Sigma \propto x^{1/2}$ (normalization is arbitrary) resulting from conservation of the angular momentum flux carried by the wave. (b) Azimuthal density profiles $\delta\Sigma$ (scaled by the planetary mass and normalized by $(x/h)^{1/2}$) at several values of x. To be compared with theoretical density profiles computed in linear approximation at the same locations in GR01 (their Figure 1). See text for details.

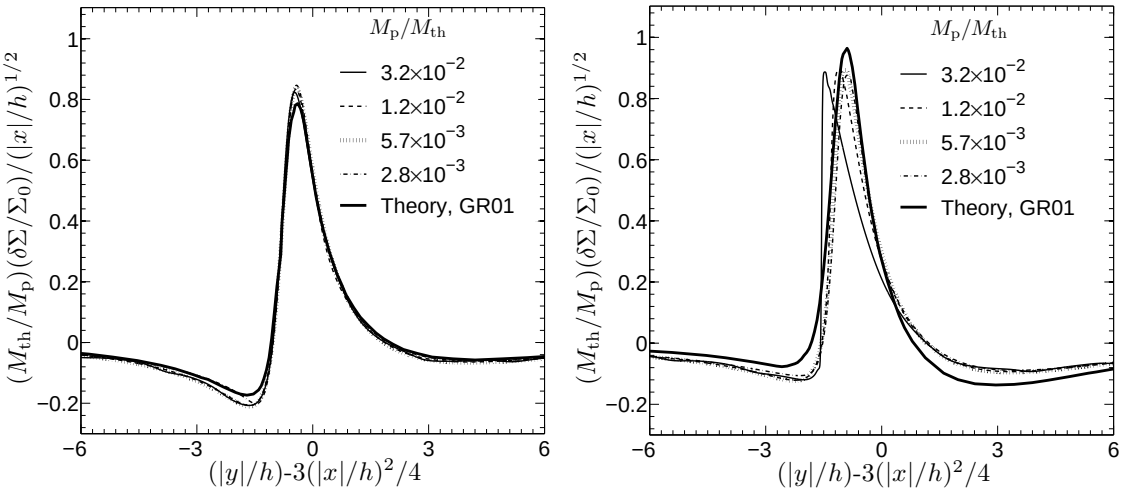

Figure 2.4 Azimuthal (normalized) profiles of the density perturbation for different M_p (labeled in panels) at two radial distances from the planet: (a) $x = 1.33h$ and (b) $x = 4h$. Analytical density profile from GR01 is shown by thick solid curve. See text for details.

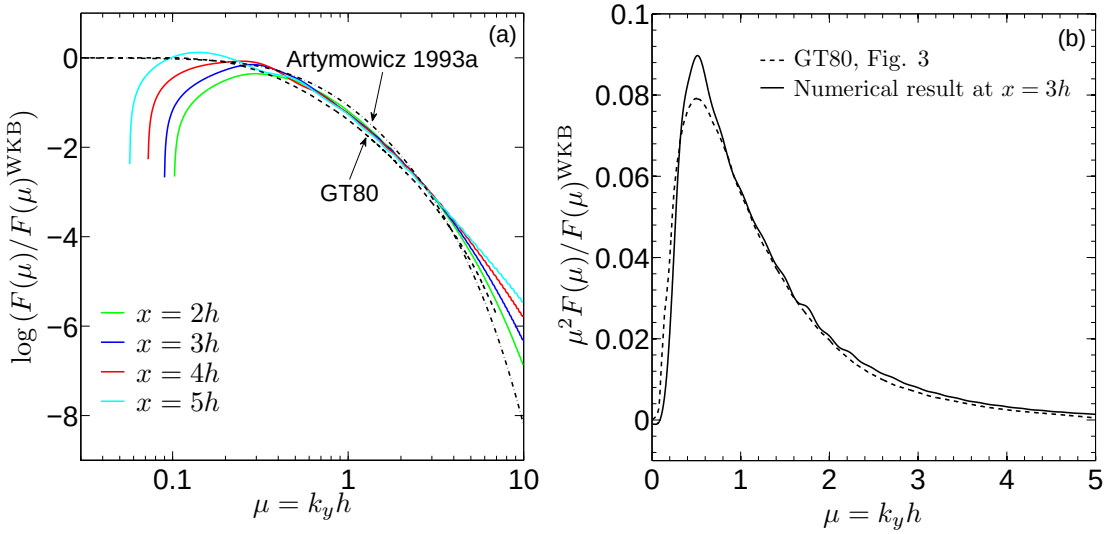

Figure 2.5 Spectral decomposition of the angular momentum flux $F_H(x)$ carried by the wave in azimuthal Fourier harmonics. Numerical results are based on isothermal simulation for $M_p = 1.2 \times 10^{-2} M_{th}$ (corresponding to 0.14 $M_\oplus$ at 1 AU and $l_{sh} \approx 5h$) with $128/h$ resolution, $r_s = h/16$. (a) Ratio $F_{H,k}(x)/F_{H,k}^{WKB}$ (the so-called *torque cutoff function*) of the numerical Fourier spectrum of the AMF to the analytical WKB calculation of GT80 as a function of $k_y h$, plotted at several values of x. For comparison we show analogous quantity (in the limit $|x| \to \infty$) computed by GT80 (see their Figure 2) and Artymowicz (1993b, their Eq. 25). The origin of excess power at high k_y is discussed in §5.4. (b) The same quantity multiplied by μ^2 (using the $x = 3h$ curve) and plotted on linear scale to facilitate comparison with Figure 3 of GT80.

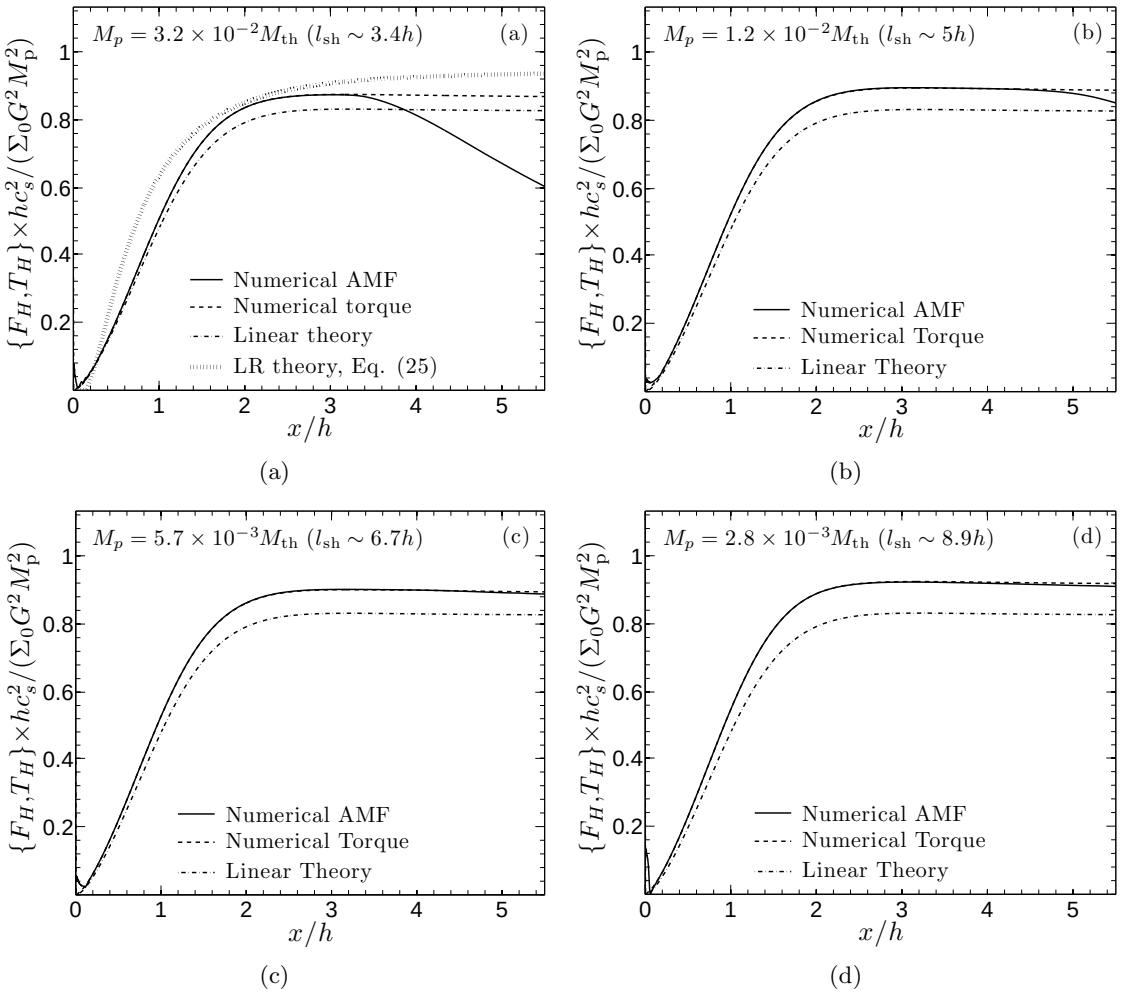

Figure 2.6 Integrated torque $T_H(x)$ and the angular momentum flux carried by the wave $F_H(x)$ (shifted vertically so that $F_H(0) = 0$ to simplify comparison with $T_H(x)$) as a function of x. Different panels correspond to different values of $M_{\rm p}$ (labeled on the plot, the same as in Figure 2.4). Analytical prescription (2.42) for $T_H(x)$ motivated by the results of GT80 is shown in panel (a) by the dotted curve. The theoretical prediction based on the linear semi-analytical calculation (Rafikov & Petrovich, 2012) is shown by the dash-dotted line in all panels. Both $F_H(x)$ and $T_H(x)$ are scaled by $\Sigma_0 (GM_{\rm p})^2/(hc_{\rm s}^2)$, which should make their shapes independent of $M_{\rm p}$ in the framework of linear theory.

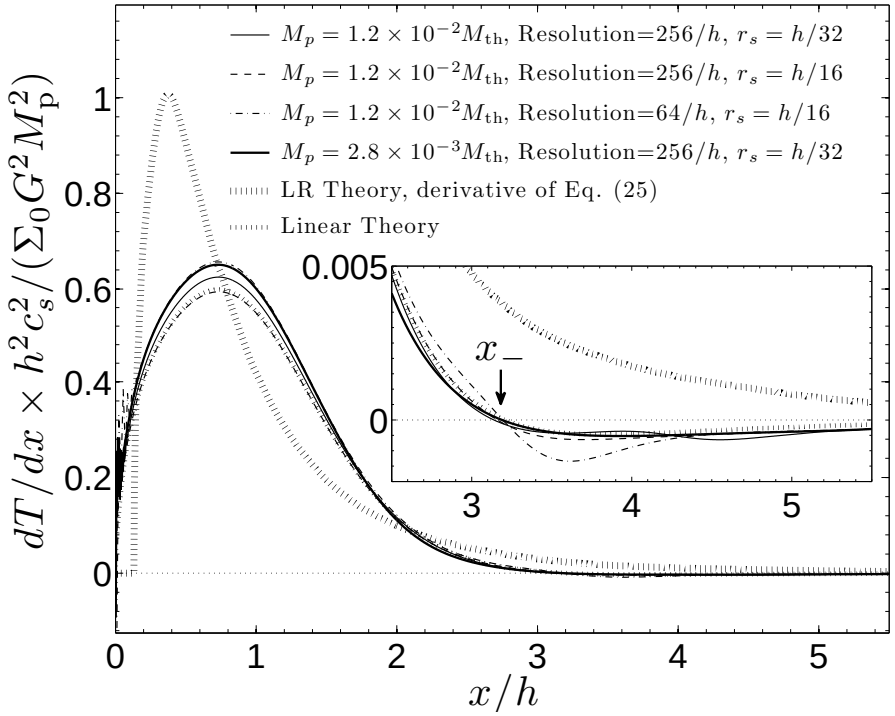

(a)

Figure 2.7 Torque density $dT_H(x)/dx$ (Eq. 2.37) as a function of x computed for two different values of $M_{\rm p}$ and different numerical parameters. The thick dotted curve shows the derivative of Eq. (2.42) motivated by the results of GT80, and the thin dotted curve shows the linear theory result based on the semi-analytical calculation by Rafikov & Petrovich (2012). Torque density is scaled by $\Sigma_0 (G M_{\rm p})^2/(h^2 c_{\rm s}^2)$ removing the dependence on $M_{\rm p}$ in linear approximation. For $M_{\rm p} = 1.2 \times 10^{-2} M_{\rm th}$ we show results from three simulations with different adopted resolution or $r_{\rm s}$. An inset zooms in on a region near $x = 3h$, where we find the torque density changing sign. The location ($x_- = 3.2h$, shown by arrow) at which this happens is found to be insensitive to variations of simulation parameters or $M_{\rm p}$ ($M_{\rm p} = 2.8 \times 10^{-3} M_{\rm th}$ was also explored).

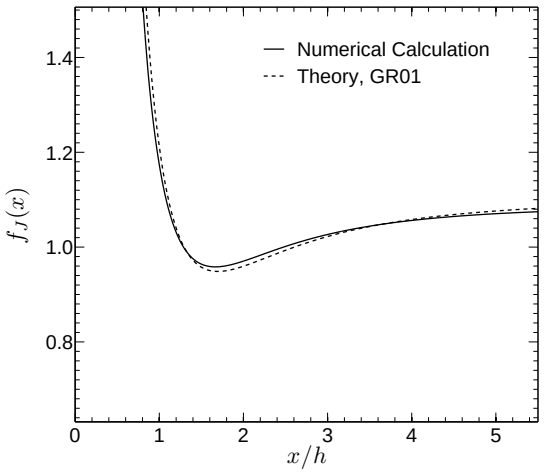

(a)

Figure 2.8 "Pseudo-AMF" defined by Eq. (2.44) from our numerical simulations (*solid curve*) and semi-analytical linear calculations of GR01 (*dashed curve*). The agreement between the two is very good in the linear regime (for $M_{\rm p} = 3.7 \times 10^{-3} M_{\rm th}$ used in simulation wave shocks at $l_{\rm sh} \approx 8h$).

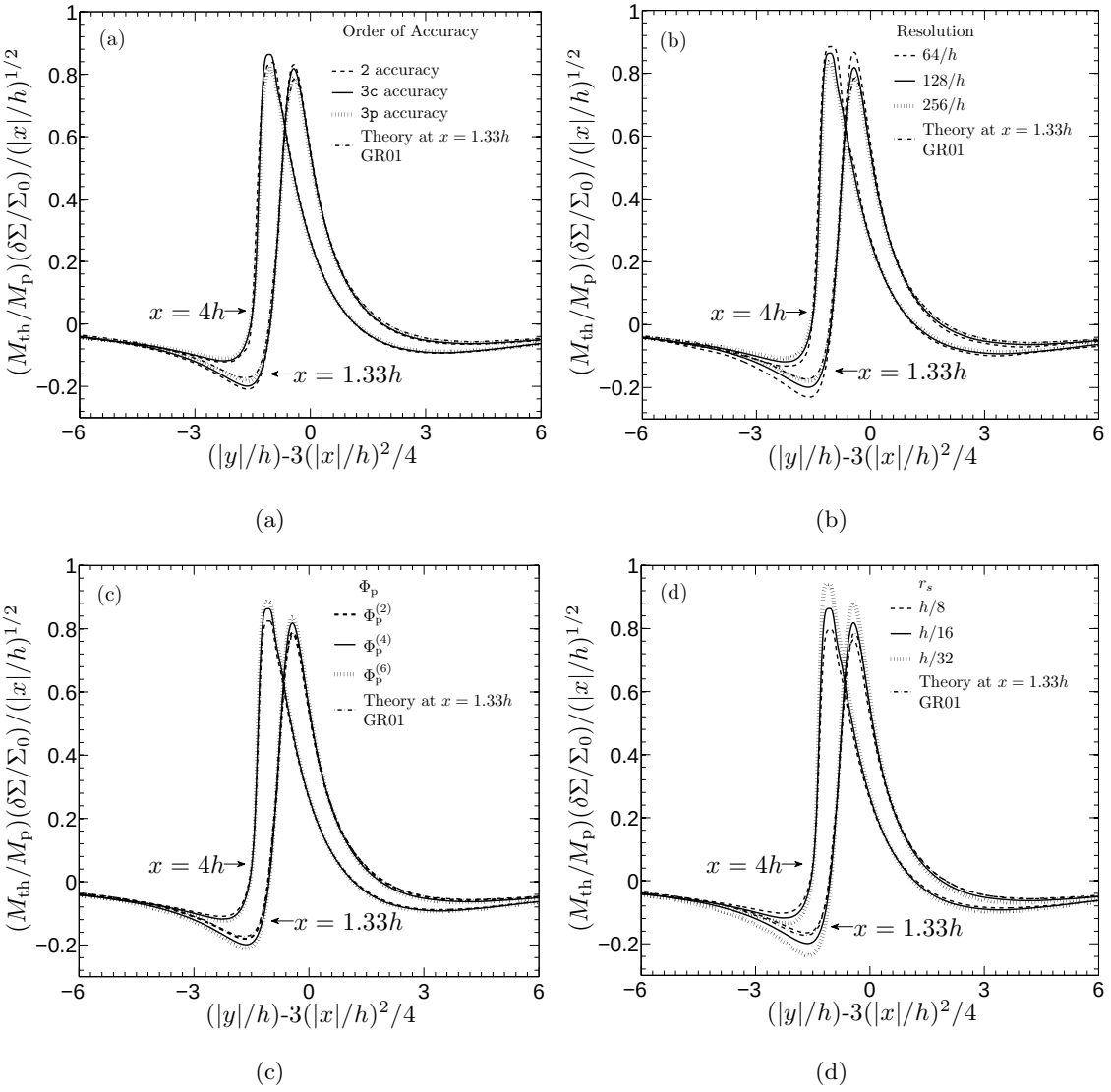

Figure 2.9 Results of the numerical convergence study. Different panels show results of simulations (normalized azimuthal density cuts, analogous to those shown in Figure 2.4, at $x = 1.33h$ and $x = 4h$) in which a single numerical parameter was varied: (a) order of accuracy for the solver, (b) resolution, (c) softened planetary potential, (d) softening length of the potential. The standard set of numerical parameters is $M_{\rm p} = 1.2 \times 10^{-2} M_{\rm th}$, $\Phi_{\rm p}^{(4)}$ potential, $r_{\rm s} = h/16$, $128/h$ resolution, and `3c` accuracy. Results of the simulation with this set are shown by solid line in all panels. The semi-analytical density profile from linear calculations of GR01 is shown only at $x = 1.33h$ to guide the eye.

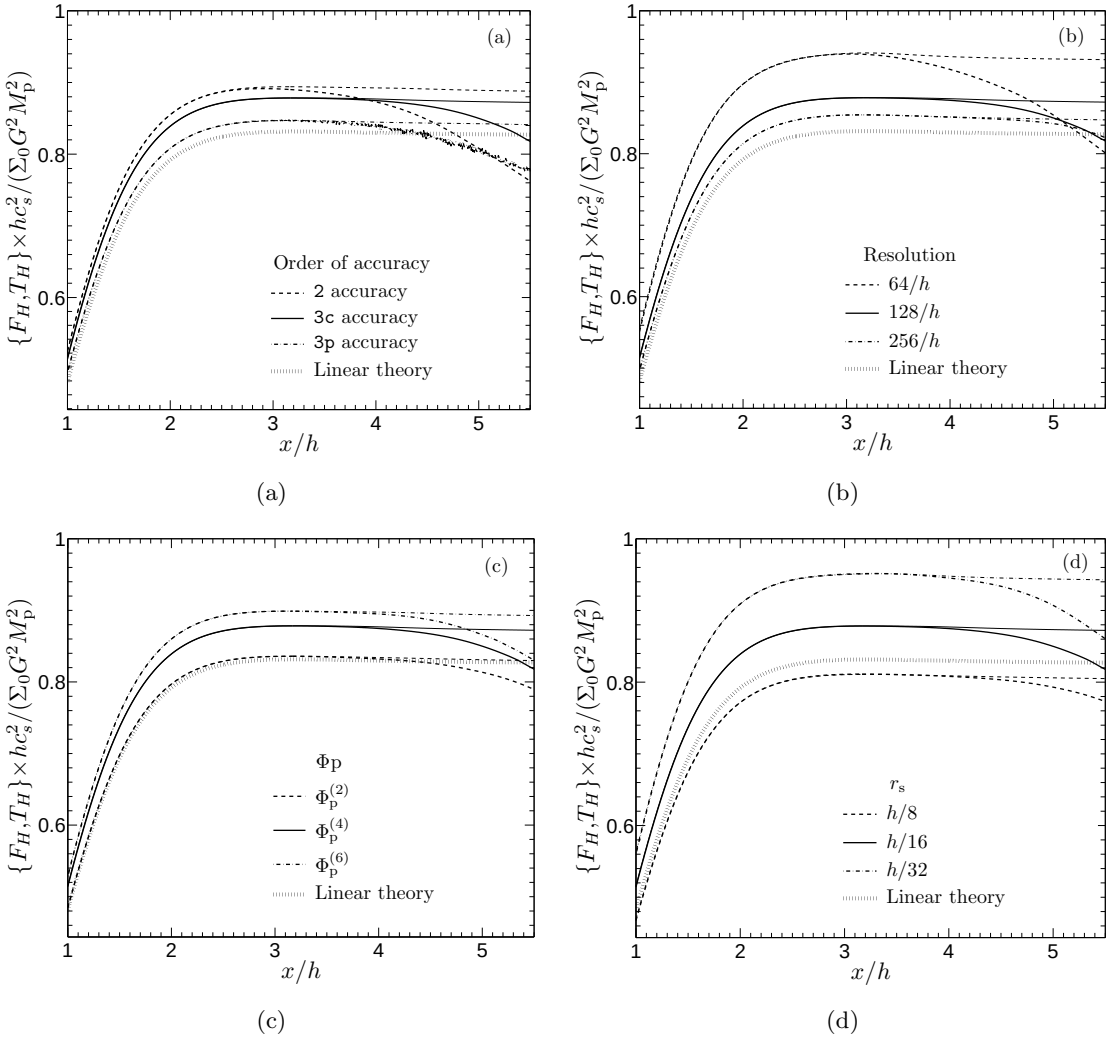

Figure 2.10 Same as Figure 2.9, but for the spatial behavior of the (properly scaled to remove the dependence on M_p) integrated torque $T_H(x)$ (the thin line of each line type) and AMF carried by the wave $F_H(x)$ (the thick line of each line type; shifted vertically so that $F_H(0) = 0$). The linear theory curve based on the semi-analytical calculation by Rafikov & Petrovich (2012) is shown for reference.

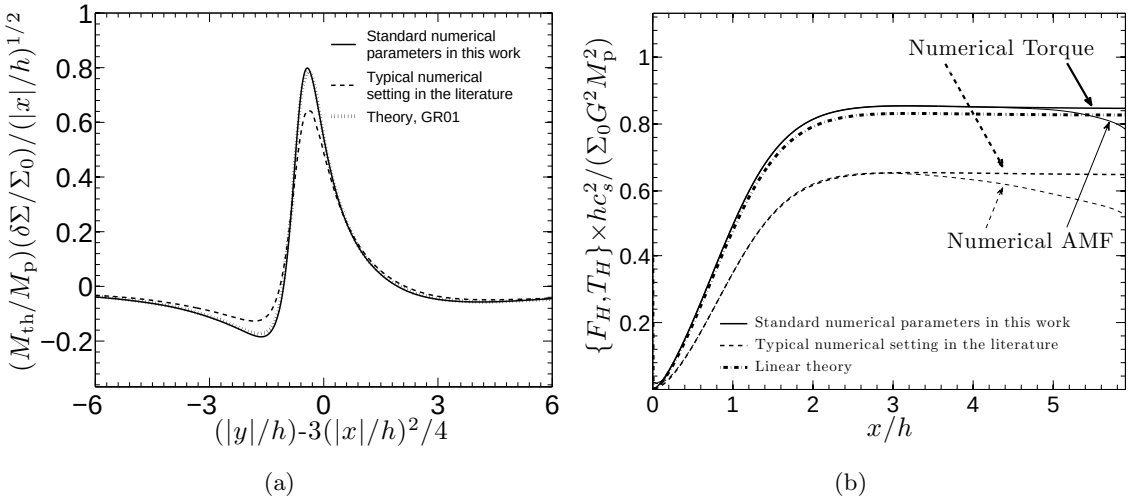

(a) (b)

Figure 2.11 Comparison between a simulation with our fiducial numerical parameters (solid line, third order of accuracy, resolution $256/h$, $\Phi_{\rm p}^{(4)}$ potential with $r_{\rm s} = h/16$), and a simulation with numerical parameters typically adopted in recent planet-disk simulations (dashed line, second order of accuracy, resolution $32/h$, $\Phi_{\rm p}^{(2)}$ potential with $r_{\rm s} = h/4$). We use $M_{\rm p} = 1.2 \times 10^{-2} M_{\rm th}$ ($l_{\rm sh} \sim 5h$) for both runs. (a) Azimuthal (scaled) density cut (similar to that in Figure 2.9) at $x = 1.33h$ showing lower amplitude of the density perturbation in the typical literature run. (b) AMF and integrated torque as a function of x (similar to Figure 2.10) for both runs. The amplitudes of the density perturbation, $F_H(x)$, and $T_H(x)$ are lower, and the AMF dissipation starts earlier in the typical literature case, compared to our fiducial simulation and the linear theory. The linear theory curve is based on the semi-analytical calculation by Rafikov & Petrovich (2012).

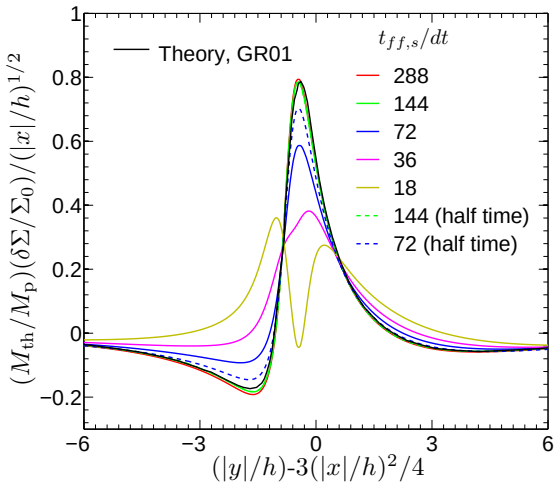

(a)

Figure 2.12 Azimuthal density profiles $\delta\Sigma$ (scaled by the planetary mass and normalized by $(x/h)^{1/2}$) at $x = 1.33h$, for simulations using orbital advection algorithm (FARGO) with different $t_{ff,s}/dt$ ratio (we manually set dt in different cases to be a fraction of the value of dt set by the Courant condition in FARGO). Dashed lines show the density profiles at half simulation time for two representative runs to illustrate whether temporal convergence has been achieved. Theoretical prediction (GR01) is also plotted to guide the eye. Simulations are done with resolution $64/h$, $\Phi_{\rm p}^{(4)}$ potential with $r_{\rm s} = h/8$, and $M_{\rm p} = 3.2 \times 10^{-2} M_{\rm th}$.

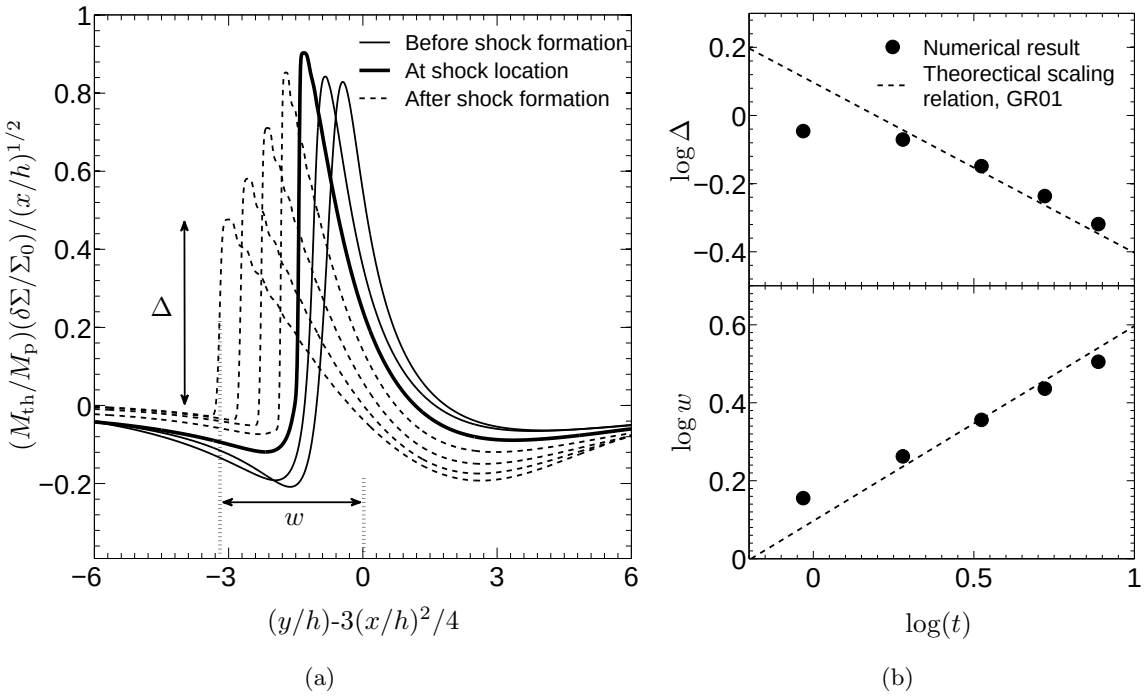

Figure 2.13 Left: Density profiles across the density wake for the $M_{\rm p} = 2.09 \times 10^{-2} M_{\rm th}$ (corresponding to $l_{\rm sh} \approx 4h$) case at two pre-shock locations ($1.33h$ and $2.67h$, thin solid curves), four post-shock locations ($5.33h$, $6.67h$, $8.0h$, and $9.33h$, dashed curves), and the theoretically predicted shocking length ($4h$, the thick solid curve). Right: Scaling of Δ and w with coordinate $t(x)$ defined by Eq. (2.14) in the post shock region. Theoretical scaling relations (Eq. 2.19) are over-plotted with arbitrary normalization.

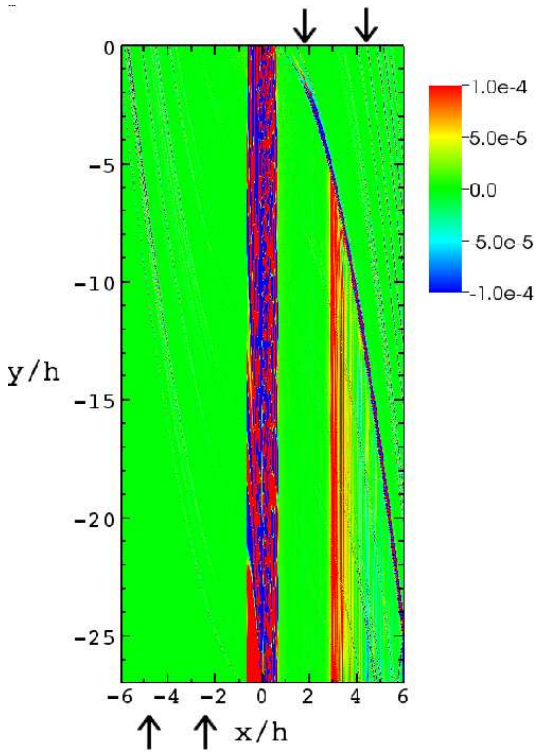

(a)

Figure 2.14 A typical snapshot of the potential vorticity perturbation $\Delta\zeta$ (normalized by Ω/Σ_0) in shearing sheet coordinates in our simulation (only half of the simulation domain is shown). A planet with $M_{\rm p} = 4.28 \times 10^{-2} M_{\rm th}$ (corresponding to $l_{\rm sh} \approx 3h$) is located at $x = y = 0$. Fluid enters from the upper right and the lower left boundaries. Note the vorticity generation at the shock position, with the amplitude of $\Delta\zeta$ decaying far from the planet (in x). Vorticity perturbation in the horseshoe region is not related to the shock. Narrow transient features in the preshock region are due to fluid activity in the horseshoe region.

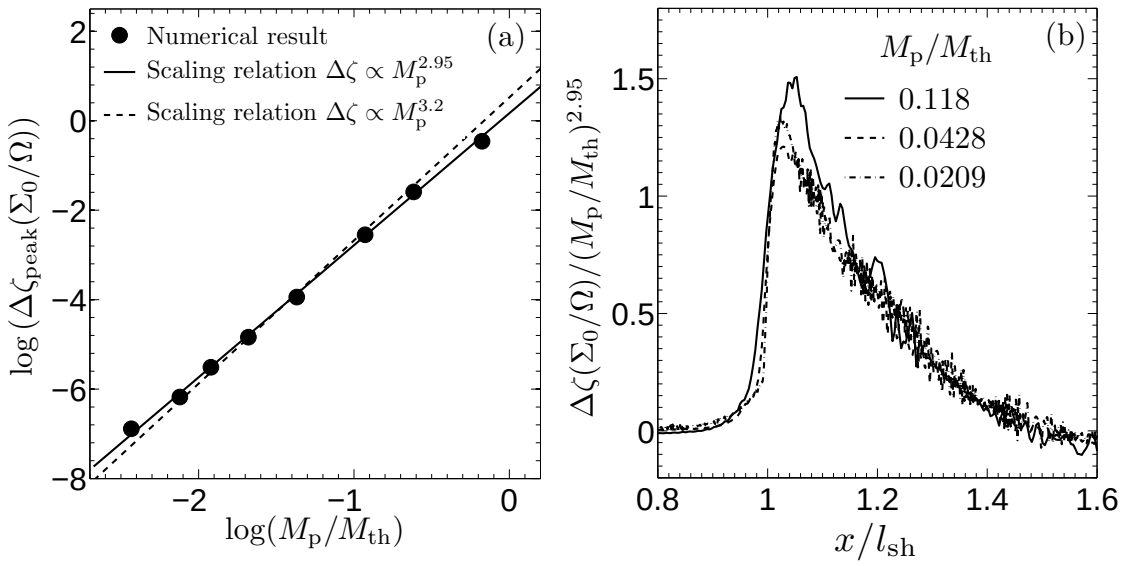

(a) (b)

Figure 2.15 Panel (a): Numerical peak $\Delta\zeta_{\rm peak}$ amplitude as a function of $M_{\rm p}$. Best fit relation $\zeta \propto M_{\rm p}^{2.95}$ and the theoretical scaling relation $\Delta\zeta_{\rm peak} \propto M_{\rm p}^{3.2}$ (Eq. 2.26) are shown. Panel (b): Radial profile of $\Delta\zeta$ (scaled by Ω/Σ_0) as a function of x (scaled by $l_{\rm sh}$). Different curves for different $M_{\rm p}$ have been scaled by $(M_{\rm p}/M_{\rm th})^{2.95}$ (the numerically best fit scaling factor) to remove the dependence on $M_{\rm p}$. See the discussion in §6.2.

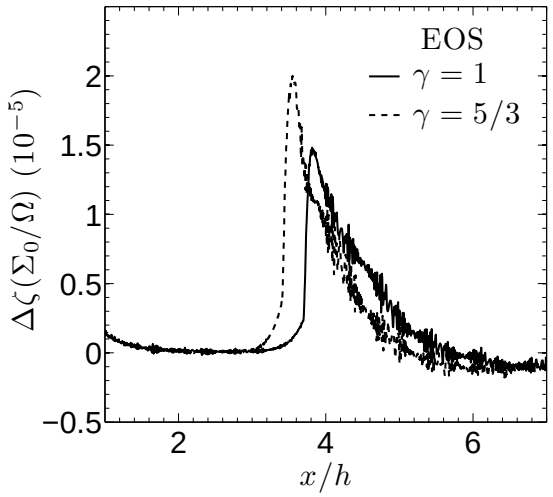

(a)

Figure 2.16 Radial $\Delta\zeta$ profile for two simulations with otherwise identical parameters (including the adiabatic sound speed) but different EOS ($\gamma = 1$ and $\gamma = 5/3$). $M_{\rm p} = 2.09 \times 10^{-2} M_{\rm th}$ in both cases, which corresponds to $l_{\rm sh} \approx 4h$ for $\gamma = 1$ and $l_{\rm sh} \approx 3.6h$ for $\gamma = 5/3$.

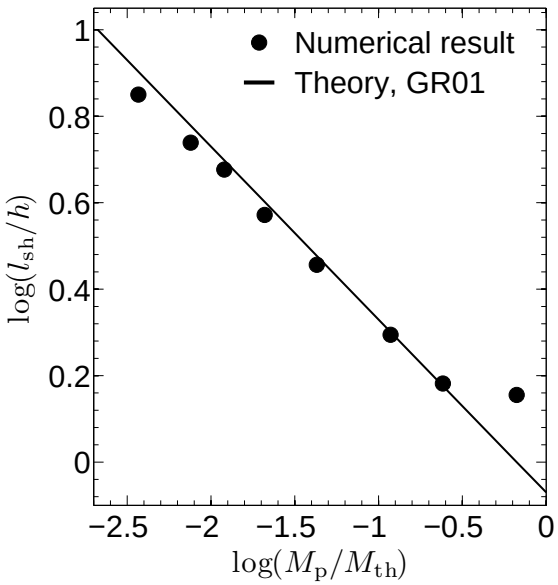

(a)

Figure 2.17 Numerical $l_{\rm sh}$ as a function of $M_{\rm p}$ (dots) as well as the theoretical prediction of GR01 (Eq. (2.17), solid line). $l_{\rm sh}$ is determined as the midpoint of the $\Delta\zeta$ jump at the shock, as we discussed in § 6.2. For the five low mass cases we use resolution=$256/h$ and $r_{\rm s} = h/32$, and for the three high mass cases we use resolution=$128/h$ and $r_{\rm s} = h/16$. The smallest and largest $M_{\rm p}$ here correspond to a few Lunar and Earth mass at 1 AU.

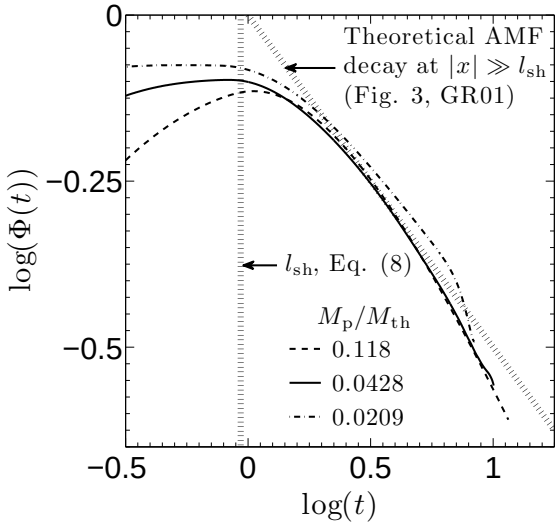

(a)

Figure 2.18 Numerical result for the AMF decay after the shock formation for three $M_{\rm p}$. The two axes are scaled to facilitate direct comparison with Fig. 3 in GR01 (see §6.5 for details). For the two low mass cases we use resolution $256/h$ and $r_{\rm s} = h/32$, and for the highest mass case we use resolution $128/h$ and $r_{\rm s} = h/16$. Theoretical asymptotic AMF decay scaling relation (Eq. (2.20)) at $x \gg l_{\rm sh}$ from GR01 and the position of $x = l_{\rm sh}$ are indicated by dotted lines.

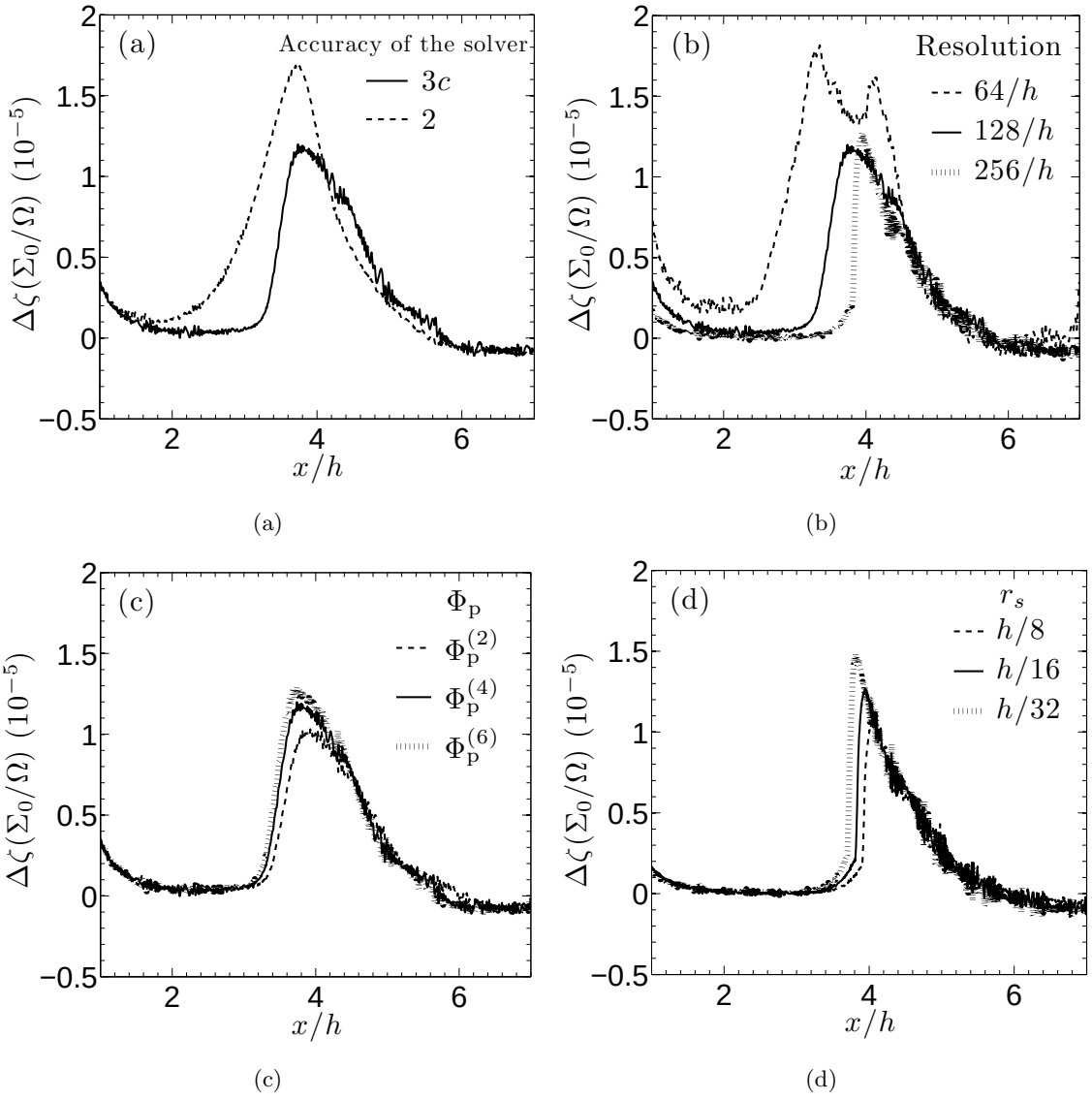

Figure 2.19 Radial profile of $\Delta\zeta$ for simulations with different order of accuracy (a, with resolution=$128/h$, $r_{\rm s} = h/16$), resolution (b, $r_{\rm s} = h/16$), $\Phi_{\rm p}$ (c, with resolution=$128/h$, and $r_{\rm s} = h/16$), and $r_{\rm s}$ (d). Other numerical algorithms which are not mentioned are drawn from our fiducial choices (§4). For all simulations we use $M_{\rm p} = 2.09 \times 10^{-2} M_{\rm th}$ (corresponding to $l_{\rm sh} \approx 4h$).

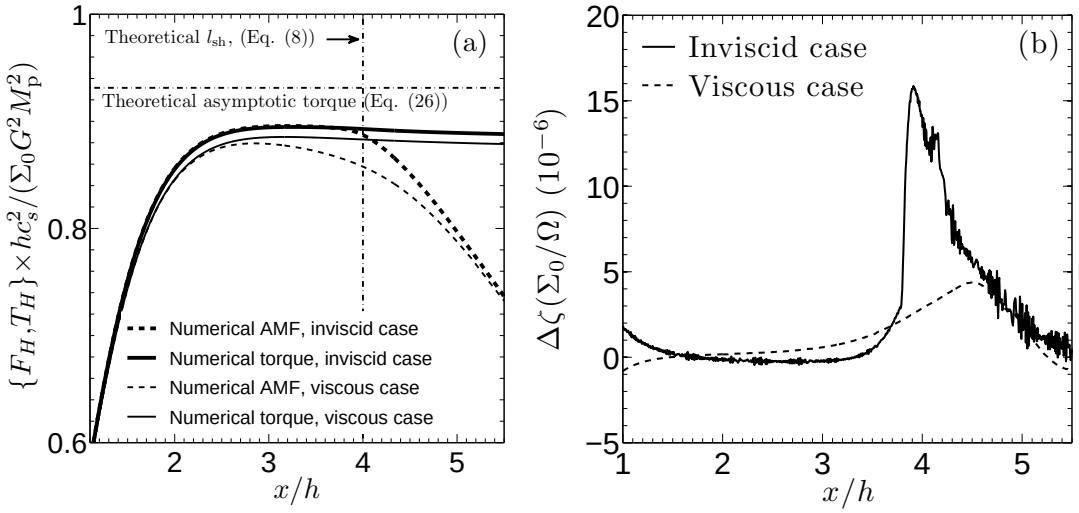

(a) (b)

Figure 2.20 The effect of explicit viscosity in our runs. The viscous simulation is done with an explicit Navier-Stokes viscosity (Shakura-Sunyaev $\alpha = \nu/(hc_{\rm s}) = 10^{-4}$), and the inviscid run is our standard simulation without explicit viscosity. Both simulations are done with $M_{\rm p} = 2.09{\times}10^{-2} M_{\rm th}$ (corresponding to $l_{\rm sh} \approx 4h$). Panel (a) shows the numerical AMF and torque calculation, and panel (b) shows the radial $\Delta\zeta$ profile.

Bibliography

Artymowicz, P. 1993a, ApJ, 419, 166

Artymowicz, P. 1993b, ApJ, 419, 155

Bate, M. R., Lubow, S. H., Ogilvie, G. I., & Miller, K. A. 2003, MNRAS, 341, 213

Bate, M. R., Ogilvie, G. I., Lubow, S. H., & Pringle, J. E. 2002, MNRAS, 332, 575

Bryden, G., Chen, X., Lin, D. N. C., Nelson, R. P., & Papaloizou, J. C. B. 1999, ApJ, 514, 344

Cassen, P. & Woolum, D. S. 1996, ApJ, 472, 789

Chiang, E. I. & Goldreich, P. 1997, ApJ, 490, 368

D'Angelo, G., Henning, T., & Kley, W. 2002, A&A, 385, 647

D'Angelo, G., Kley, W., & Henning, T. 2003, ApJ, 586, 540

D'Angelo, G. & Lubow, S. H. 2008, ApJ, 685, 560

D'Angelo, G. & Lubow, S. H. 2010, ApJ, 724, 730

Fleming, T. & Stone, J. M. 2003, ApJ, 585, 908

Gammie, C. F. 1996, ApJ, 457, 355

Gardiner, T. A. & Stone, J. M. 2005, Journal of Computational Physics, 205, 509

Gardiner, T. A. & Stone, J. M. 2008, Journal of Computational Physics, 227, 4123

Goldreich, P. & Nicholson, P. D. 1989, ApJ, 342, 1079

Goldreich, P. & Tremaine, S. 1979, ApJ, 233, 857

Goldreich, P. & Tremaine, S. 1980, ApJ, 241, 425

Goodman, J. & Rafikov, R. R. 2001, ApJ, 552, 793

Hartmann, L., Calvet, N., Gullbring, E., & D'Alessio, P. 1998, ApJ, 495, 385

Hayashi, C. 1981, Progress of Theoretical Physics Supplement, 70, 35

Hourigan, K. & Ward, W. R. 1984, Icarus, 60, 29

Kevlahan, N. K.-R. 1997, Journal of Fluid Mechanics, 341, 371

Kley, W. 1999, MNRAS, 303, 696

Koller, J., Li, H., & Lin, D. N. C. 2003, ApJ, 596, L91

Korycansky, D. G. & Pollack, J. B. 1993, Icarus, 102, 150

Korycansky, D. G. & Pringle, J. E. 1995, MNRAS, 272, 618

Landau, L. D. & Lifshitz, E. M. 1959, Fluid mechanics

Larson, R. B. 1989, in The Formation and Evolution of Planetary Systems, ed. H. A. Weaver & L. Danly, 31–48

Larson, R. B. 1990, MNRAS, 243, 588

Li, H., Li, S., Koller, J., Wendroff, B. B., Liska, R., Orban, C. M., Liang, E. P. T., & Lin, D. N. C. 2005, ApJ, 624, 1003

Li, H., Lubow, S. H., Li, S., & Lin, D. N. C. 2009, ApJ, 690, L52

Lin, D. N. C. & Papaloizou, J. 1986a, ApJ, 307, 395

Lin, D. N. C. & Papaloizou, J. 1986b, ApJ, 309, 846

Lin, D. N. C. & Papaloizou, J. C. B. 1993, in Protostars and Planets III, ed. E. H. Levy & J. I. Lunine, 749–835

Lin, M.-K. & Papaloizou, J. C. B. 2010, MNRAS, 405, 1473

Lubow, S. H. & Ogilvie, G. I. 1998, ApJ, 504, 983

Lubow, S. H. & Pringle, J. E. 1993, ApJ, 409, 360

Masset, F. 2000, A&AS, 141, 165

Muto, T., Suzuki, T. K., & Inutsuka, S.-i. 2010, ApJ, 724, 448

Nelson, R. P., Papaloizou, J. C. B., Masset, F., & Kley, W. 2000, MNRAS, 318, 18

Ogilvie, G. I. & Lubow, S. H. 1999, ApJ, 515, 767

Ogilvie, G. I. & Lubow, S. H. 2002, MNRAS, 330, 950

Paardekooper, S.-J. 2006, PhD thesis, Leiden Observatory, Leiden University, P.O. Box 9513, 2300 RA Leiden, The Netherlands

Papaloizou, J. C. B., Nelson, R. P., Kley, W., Masset, F. S., & Artymowicz, P. 2007, Protostars and Planets V, 655

Papaloizou, J. C. B. & Terquem, C. 2006, Reports on Progress in Physics, 69, 119

Rafikov, R. R. 2002a, ApJ, 569, 997

Rafikov, R. R. 2002b, ApJ, 572, 566

Rafikov, R. R. 2006, ApJ, 648, 666

Rafikov, R. R. & Petrovich, C. 2012, ApJ, 747, 24

Roe, P. L. 1981, Journal of Computational Physics, 43, 357

Stone, J. M. & Gardiner, T. A. 2010, ApJS, 189, 142

Stone, J. M., Gardiner, T. A., Teuben, P., Hawley, J. F., & Simon, J. B. 2008, ApJS, 178, 137

Takeuchi, T. & Miyama, S. M. 1998, PASJ, 50, 141

Takeuchi, T., Miyama, S. M., & Lin, D. N. C. 1996, ApJ, 460, 832

Tanaka, H., Takeuchi, T., & Ward, W. R. 2002, ApJ, 565, 1257

Turner, N. J. & Sano, T. 2008, ApJ, 679, L131

Ward, W. R. 1986, Icarus, 67, 164

Ward, W. R. 1997, Icarus, 126, 261

Ward, W. R. & Hourigan, K. 1989, ApJ, 347, 490

Yu, C., Li, H., Li, S., Lubow, S. H., & Lin, D. N. C. 2010, ApJ, 712, 198

Chapter 3

The Missing Cavities in Transitional Protoplanetary Disks

Abstract

Transitional circumstellar disks around young stellar objects have a distinctive infrared deficit around 10 microns in their Spectral Energy Distributions (SED), recently measured by the *Spitzer Infrared Spectrograph* (IRS), suggesting dust depletion in the inner regions. These disks have been confirmed to have giant central cavities by imaging of the submillimeter (sub-mm) continuum emission using the *Submillimeter Array* (SMA). However, the polarized near-infrared scattered light images for most objects in a systematic IRS/SMA cross sample, obtained by HiCIAO on the Subaru telescope, show no evidence for the cavity, in clear contrast with SMA and Spitzer observations. Radiative transfer modeling indicates that many of these scattered light images are consistent with a smooth spatial distribution for micron-sized grains, with little discontinuity in the surface density of the micron-sized grains at the cavity edge. Here we present a generic disk model that can simultaneously account for the general features in IRS, SMA, and Subaru observations. Particularly, the scattered light images for this model are computed, which agree with the general trend seen in Subaru data. Decoupling between the spatial distributions of the micron-sized dust and mm-sized dust inside the cavity is suggested by the model, which, if confirmed, necessitates a mechanism, such as dust filtration, for differentiating the small and big dust in the cavity clearing process. Our model also suggests an inwardly increasing gas-to-dust-ratio in the inner disk, and different spatial distributions for the small dust inside and outside the cavity, echoing the predictions in grain coagulation and growth models.

1 Introduction

Transitional disks have a small or no excess from $\sim 1\mu$m to $\sim 10\mu$m relative to their full disk cousins, but a significant excess at longer wavelength (Williams & Cieza, 2011), suggesting cleared out inner disk. This interpretation dates back to the era of the *Infrared Astronomical Satellite* (Strom et al. 1989, Skrutskie et al. 1990), and was later developed with the help of detailed near-infrared (NIR) to mid-infrared (MIR) spectra provided by the Infrared Spectrograph (IRS) on-board *Spitzer Space Telescope*. Detailed radiative transfer modeling suggests that this kind of SED is consistent with disk models which harbor a central (partially) depleted region (i.e. a cavity or a gap), while a "wall-like" structure at the outer edge of this region can be responsible for the abrupt rise of the SED at MIR (Calvet et al., 2005; Espaillat et al., 2007)[1].

[1]The objects with a small dust belt left at the center have been prototyped as pre-transitional objects, such as LkCa 15 (Espaillat et al., 2008), but for simplicity we use the term transitional disk for both types.

The disk+cavity model based on SED-only fitting usually contains large uncertainties, because the SED samples the emission from the whole disk; by tuning the ingredients in the fitting, one could fit the IRS SED with different models (see the example of UX Tau A, Espaillat et al. 2010, 2011 and Andrews et al. 2011, hereafter A11). Better constraints on the disk structure can be obtained from resolved images of the transitional disks. Using the *Submillimeter Array* (SMA) interferometer (Ho et al., 2004), resolved images of transitional disks at sub-mm wavelength have provided direct detections of these cavities (Andrews & Williams, 2007; Andrews et al., 2009), and measurements of their properties. Recently, A11 observed a sample of 12 nearby transitional disks (at a typical distance of ~ 140 pc). Combining both the SMA results and the SED, they fit detailed disk+cavity model for each object, and the cavity size ($\sim 15-70$ AU) is determined with $\sim 10\%$ uncertainty. They concluded that large grains (up to $\sim$mm-sized) inside the cavity are depleted by at least a factor of 10 to 100 (the "depletion" in this work is relative to a "background" value extrapolated from the outer disk). Under the assumption that the surface density of the disk is described by their model, the infrared spectral fitting demands that the small grains (micron-sized and smaller) inside the cavity to be heavily depleted by a factor of $\sim 10^5$.

Recently, most objects in this sample have been observed by the Subaru High-Contrast Coronographic Imager for Adaptive Optics (HiCIAO) at NIR bands, as part of the the Strategic Explorations of Exoplanets and Disks with Subaru project, SEEDS, (Tamura, 2009). SEEDS is capable of producing polarized intensity (PI) images of disks, which greatly enhances our ability to probe disk structure (especially at the inner part) by utilizing the fact that the central source is usually not polarized, so that the stellar residual in PI images is much smaller than in full intensity (FI) images (Perrin et al., 2004; Hinkley et al., 2009; Quanz et al., 2011).

The SEEDS results turned out to be a big surprise — in many cases the polarized NIR images do not show an inner cavity, despite the fact that the inner working angle of the images (the saturation radius or the coronagraph mask size, $\psi_{\rm in} \sim 0\farcs1 - 0\farcs15$, or $\sim 15-25$ AU at the distance to Taurus ~ 140 pc, see Section 2.3) is significantly smaller than the cavity sizes inferred from sub-mm observations. High contrast features such as surface brightness excesses or deficits exist in some systems, but they are localized and do not appear to be central cavities. Instead, the image is smooth on large scales, and the azimuthally averaged surface brightness radial profile (or the profile along the major axis) increases inward smoothly until $\psi_{\rm in}$, without any abrupt break or jump at the cavity edge (the slope may change with radius in some systems). Examples include ROX 44 (M. Kuzuhara et al. 2012, in prep.), SR 21 (Follette et al., 2013), GM Aur (J. Hashimoto et al. 2013, in prep.), and SAO 206462 (Muto et al., 2012). Some objects such as UX Tau A also do not show a cavity (Tanii et al., 2012), however the inner working angle of their SEEDS images is too close to the cavity size, so the status of the cavity is less certain. We note that LkCa 15 also does not exhibit a clear cavity in its PI imagery (J. Wisniewski et al. 2012, in prep.), but does exhibit evidence of the wall of a cavity in its FI imagery (Thalmann et al., 2010).

This apparent inconsistency between observations at different wavelengths reveals something fundamental in the transitional disk structure, as these datasets probe different components of protoplanetary disks. At short wavelengths (i.e. NIR) where the disk is optically thick, the flux is dominated by the small dust (micron-sized or so) at the surface of the disk (where the stellar photons get absorbed or scattered), and is sensitive to the shape of the surface; at long wavelength (i.e. sub-mm), disks are generally optically thin, so the flux essentially probes the disk surface density in big grains (mm-sized or so), due to their large opacity at these wavelengths (Williams & Cieza, 2011).

Combining all the three pieces of the puzzle together (SED, sub-mm observation, and NIR imaging), we propose a disk model that explains the signatures in all three observations simultaneously: the key point is that the spatial distributions of small and big dust are decoupled inside the cavity. In this model, a well defined cavity (several tens of AU in radius) with a sharp edge exists only in spatial distribution of the big dust and reproduces the central void in the sub-mm images, while no discontinuity is found for the spatial distribution of the small dust at the cavity edge. Inside the cavity, the surface density of the small dust does not increase inwardly as steeply as it does in the outer disk; instead it is roughly constant or declines closer to the star (while maintaining an overall smooth profile). In this way, the inner region (sub-AU to a few AU) is heavily depleted in small dust, so that the model reproduces the NIR flux deficit in the SED (but still enough small dust surface density to efficiently scatter near-IR radiation). Modeling results show that the scattered light images for this continuous spatial distribution of the small dust appear smooth as well, with surface brightness steadily increasing inwardly, as seen in many of the SEEDS observations.

The structure of this chapter is as follows. In Section 2 we introduce the method that we use for the radiative transfer modeling. In Section 3 we give the main results on the scattered light images: first a general interpretation of the big picture through a theoretical perspective, followed by the modeling results of various disk+cavity models. We investigate the sub-mm properties of these models in Section 4, and explore the degeneracy in the disk parameter space on their model SED in Section 5. We summarize the direct constraints put by the three observations on this transitional disk sample in Section 5, as well as the implications of our disk models. Our generic solution, which qualitatively explains the signatures in all the three observations, is summarized in Section 6.

2 Radiative Transfer Modeling

In this section, we introduce the model setup in our radiative transfer calculations, and the post processing of the raw NIR polarized scattered light images which we perform in order to mimic the observations. The purpose of this modeling exercise is to "translate" various physical disk models to their corresponding NIR polarized scattered light images, sub-mm emission images, and SED, for comparison with observations.

2.1 Model Setup

We use a modified version of the Monte Carlo radiative transfer code developed by Whitney et al. (2003b,a), Robitaille et al. (2006), and B. Whitney et al. 2013, in prep.; for the disk structure, we use A11 and Whitney et al. (2003a) for references. The NIR images (this section) and SED (Section 5) are produced from simulations with 4×10^7 photon packets, and for the sub-mm images (Section 4) we use 5×10^8 photon packets. By varying the random seeds in the Monte Carlo simulations, we find the noise levels in both the radial profile of the convolved images (Section 2.3) and the SED to be $\lesssim 0.5\%$ in the range of interest. In our models, we construct an axisymmetric disk (assumed to be at $\sim$140 pc) 200 AU in radius on a 600×200 grid in spherical coordinates (R, θ), where R is in the radial direction and θ is in the poloidal direction ($\theta = 0^\circ$ is the disk mid-plane). We include accretion energy in the disk using the Shakura & Sunyaev α disk prescription (Whitney et al., 2003b). Disk accretion under the accretion rate assumed in our models below (several $\times 10^{-9} M_\odot$ yr^{-1}) does not have a significant effect on the SED or the

images (for simplicity, accretion energy from the inner gas disk is assumed to be emitted with the stellar spectrum, but see also the treatment in Akeson et al. 2005). We model the entire disk with two components: a thick disk with small grains ($\sim \mu$m-sized and smaller, more of less pristine), and a thin disk with large (grown and settled) grains (up to $\sim$mm-sized). Figure 4.2 shows the schematic surface density profile for both dust population.

The parametrized vertical density profiles for both dust populations are taken to be Gaussian (i.e. $\rho(z) = \rho_0 e^{-z^2/2h^2}$, isothermal in the vertical direction z), with scale heights $h_{\rm b}$ and $h_{\rm s}$ being simple power laws $h \propto R^{\beta}$ (we use subscripts "s" and "b" to indicate the small and big dust throughout the chapter, while quantities without subscripts "s" and "b" are for both dust populations). Following A11, to qualitatively account for the possibility of settling of big grains, we fix $h_{\rm b} = 0.2 \times h_{\rm s}$ in most cases to simplify the models, unless indicated otherwise. Radially the disk is divided into two regions: an outer full disk from a cavity edge $R_{\rm cav}$ to 200 AU, and an inner cavity from the dust sublimation radius $R_{\rm sub}$ to $R_{\rm cav}$ ($R_{\rm sub}$ is determined self-consistently as where the temperature reaches the sublimation temperature $T_{\rm sub} \sim$1600 K, Dullemond et al. 2001, usually around 0.1$-$0.2 AU). At places in the disk where a large surface area of material is directly exposed to starlight, a thin layer of material is superheated, and the local disk "puffs" up vertically (Dullemond & Dominik, 2004a). To study this effect at the inner rim ($R_{\rm sub}$) or at the cavity wall, we adopt a treatment similar to A11. In some models below we manually raise the scale height h at $R_{\rm sub}$ or $R_{\rm cav}$ by a certain factor from its "original" value, and let the puffed up h fall back to the underlying power law profile of h within $\sim$0.1 AU as $e^{-(\delta R/0.1\ {\rm AU})^2}$. We note that these puffed up walls are vertical, which may not be realistic (Isella & Natta, 2005).

For the surface density profile in the outer disk, we assume

$$\Sigma_{\rm o}(R) = \Sigma_{\rm cav} \frac{R_{\rm cav}}{R} e^{(R_{\rm cav}-R)/R_c} \tag{3.1}$$

where $\Sigma_{\rm cav}$ is the surface density at the cavity edge (normalized by the total disk mass), R_c is a characteristic scaling length, and the gas-to-dust ratio is fixed at 100. Following A11, we take 85% of the dust mass to be in large grains at $R > R_{\rm cav}$. For the inner disk (i.e. $R < R_{\rm cav}$) three surface density profiles have been explored:

$$\Sigma_{\rm i}(R) = (\delta_{\rm cav}\Sigma_{\rm cav}) \frac{R_{\rm cav}}{R} e^{(R_{\rm cav}-R)/R_c} \quad \text{(rising } \Sigma_{\rm i}(R)\text{)}, \tag{3.2}$$

$$\Sigma_{\rm i}(R) = \delta_{\rm cav}\Sigma_{\rm cav} \quad \text{(flat } \Sigma_{\rm i}(R)\text{), and} \tag{3.3}$$

$$\Sigma_{\rm i}(R) = (\delta_{\rm cav}\Sigma_{\rm cav}) \frac{R}{R_{\rm cav}} \quad \text{(declining } \Sigma_{\rm i}(R)\text{)}, \tag{3.4}$$

and their names are based on their behavior when moving inward inside the cavity. We note that Equation (3.2) and (3.1) together form a single $\Sigma(R)$ scaling relation for the entire disk (with different normalization for the inner and outer parts), as in A11.

We define the depletion factor of the total dust inside the cavity as

$$\delta(R) = \frac{\Sigma_{\rm i}(R)}{\Sigma_{\rm i}^{\rm full}(R)}, \tag{3.5}$$

where $\Sigma_{\rm i}^{\rm full}(R)$ is found by extrapolating $\Sigma_{\rm o}(R)$ from the outer disk, i.e. evaluating Equation (3.1) at $R < R_{\rm cav}$ (or Equation (3.2) with $\delta_{\rm cav} = 1$). In addition, we define $\delta_{\rm s}(R)$ and $\delta_{\rm b}(R)$ as the cavity depletion factors for the small and big dust respectively as

$$\delta_{\rm s}(R) = \frac{\Sigma_{\rm i,s}(R)}{0.15 \times \Sigma_{\rm i}^{\rm full}(R)},\ \delta_{\rm b}(R) = \frac{\Sigma_{\rm i,b}(R)}{0.85 \times \Sigma_{\rm i}^{\rm full}(R)}, \tag{3.6}$$

where 0.15 and 0.85 are the mass fractions of the small and big dust in the outer disk. We note that unlike previous models such as A11, our cavity depletion factors are radius dependent (a constant $\delta_{\rm s}(R)$ or $\delta_{\rm b}(R)$ means a uniform depletion at all radii inside the cavity). Specifically, we define the depletion factor right inside the cavity edge as

$$\delta_{\rm cav} = \delta(R = R_{\rm cav} - \epsilon),\ \delta_{\rm cav,s} = \delta_{\rm s}(R = R_{\rm cav} - \epsilon),\ \delta_{\rm cav,b} = \delta_{\rm b}(R = R_{\rm cav} - \epsilon). \tag{3.7}$$

With the same $\delta_{\rm cav}$, different models with different $\Sigma_{\rm i}(R)$ profiles (Equations (3.2)-(3.4)) have similar $\Sigma_{\rm i}(R)$ (and $\delta(R)$) in the outer part of the cavity, but very different $\Sigma_{\rm i}(R)$ (and $\delta(R)$) at the innermost part. Lastly, the mass averaged cavity depletion factor $\langle\delta\rangle$ is defined as

$$\langle\delta\rangle = \frac{\int_0^{R_{\rm cav}} \Sigma_{\rm i}(R) 2\pi R dR}{\int_0^{R_{\rm cav}} \Sigma_{\rm i}^{\rm full}(R) 2\pi R dR}. \tag{3.8}$$

SMA observations have placed strong constraints on the spatial distribution of the big dust, while the constraints on the small grains from the SED are less certain, especially beyond $R \sim 10$ AU. Based on this, we adopt the spatial distribution of big grains in A11 (i.e. Equation (3.1), and no big grains inside the cavity), and focus on the effect of the distribution of small grains inside the cavity. Therefore, the sub-mm properties of our models are similar to those of the models in A11 (Section 4), since large grains dominate the sub-mm emission. We tested models with non-zero depletion for the big grains, and found that they make no significant difference as long as their surface density is below the SMA upper limit. From now on we drop the explicit radius dependence indicator (R) from various quantities in most cases for simplicity.

2.2 Dust Properties

For the small grains we try two models: the standard interstellar medium (ISM) grains (Kim et al. 1994, ∼micron-sized and smaller), and the model that Cotera et al. (2001) employed to reproduce the HH 30 NIR scattered light images, which are somewhat larger than the ISM grains (maxim size ∼20 μm). These grains contain silicate, graphite, and amorphous carbon, and their properties are plotted in Figure 3.2. The two grain models are similar to each other, and both are similar to the small grains model which A11 used in the outer disk and the cavity grains which A11 used inside the cavity and on the cavity wall. We note that for detailed modeling which aims at fitting specific objects, the model for the small grains needs to be turned for each individual object. For example, the strength and shape of the silicate features indicate different conditions for the small grains in the inner disk (Adame et al. 2011, and Furlan et al. 2011, who also pointed out that the silicate features in transitional disks typically show that the grains in the inner disk are dominated by small amorphous silicate grains similar to ISM grains). However, since we do not aim at fitting specific objects, we avoid tuning the small dust properties and assume ISM grains (Kim et al., 1994) for the models shown below, to keep our models generalized and simple.

For the large grains we try three different models, namely Models 1, 2, and 3 from Wood et al. (2002). The properties of these models are plotted in Figure 3.2. They adopt a power-law size distribution (i.e. as in Kim et al. 1994) with an exponential cutoff at large size, and the maxim size is ∼1 mm. These grains are made of amorphous carbon and astronomical silicates, with solar abundances of carbon and silicon. These models cover a large parameter space, however we find that they hardly make any difference in the scattered light image and the IRS SED, due to their small scale height and their absence inside the cavity. For this reason we fix our big grains as

described by Model 2 in Wood et al. (2002) (which is similar to the model of the big grains in A11). We note that small grains have much larger opacity than big grains at NIR, and it is the other way around at sub-mm (Figure 3.2).

2.3 Post Processing of the Scattered Light Images

To obtain realistic images which can be directly compared to SEEDS observations, the raw NIR images of the entire disk+star system from the radiative transfer simulations need to be convolved with the point spread function (PSF) of the instrument. SEEDS can obtain both the FI and the PI images for any object, either with or without a coronagraph mask. The observation could be conducted in several different observational modes, including angular differential imaging (ADI, Marois et al. 2006), polarization differential imaging (PDI, Hinkley et al. 2009), and spectral differential imaging (SDI, Marois et al. 2000). For a description of the instrument see Tamura (2009) and Suzuki et al. (2010).

In this work, we produce both the narrow band 880 μm images and H band NIR images. While at 880 μm we produce the full intensity images, for the NIR scattered light images we focus on the PI images (produced in the PDI mode, both with and without a coronagraph mask). This is because (1) PDI is the dominate mode for this sample in SEEDS, and (2) it is more difficult to interpret FI (ADI) images since its reduction process partially or completely subtracts azimuthally symmetric structure. Other authors had to synthesize and reduce model data in order to test for the existence of features like cavities (Thalmann et al., 2010) or spatially extended emission (Thalmann et al., 2011). For examples of PDI data reduction and analysis, see Hashimoto et al. (2011). When observing with a mask, $\psi_{\rm in}$ in the PI images is the mask size (typically $0\farcs15$ in radius), and when observing without a mask, $\psi_{\rm in}$ is determined by the saturation radius, which typically is $\sim 0\farcs1$.

To produce an image corresponding to observations made without a mask, we convolve the raw PI image of the entire system with an observed unsaturated HiCIAO H-band PSF. The resolution of the PSF is $\sim 0\farcs05$ ($\sim 1.2\lambda/D$ for an 8-m telescope) and the Strehl ratio is $\sim$40% (Suzuki et al., 2010). The integrated flux within a circle of radius $0\farcs25$ is $\sim$80% of the total flux ($\sim$90% for a circle of radius $0\farcs5$). We then carve out a circle at the center with $0\farcs1$ in radius to mimic the effect of saturation. We call this product the convolved unmasked PI image. To produce an image corresponding to observations with a mask, we first convolve the part of the raw PI image which is not blocked by the mask with the above PSF. We then convolve the central source by an observed PI coronagraph stellar residual map (the PSF under the coronagraph), and add this stellar residual to the disk images (the flux from the inner part of the disk which is blocked by the mask, $\sim$20 AU at $\sim$140 pc, is added to the star). Lastly, we carve out a circle $0\farcs15$ in radius from the center from the combined image to indicate the mask. We call this product the convolved masked PI image. We note that the stellar residual is needed to fully reproduce the observations, but in our sample the surface brightness of the stellar residual is generally well below the surface brightness of the disk at the radius of interest, so it doesn't affect the properties of the images much.

In this study, the disk is assumed to be face-on in order to minimize the effect of the phase function in the scattering, so that we can focus on the effect of the disk structure. This is a good approximation since most objects in this IRS/SMA/Subaru sample have inclinations around $\sim 25^\circ$ (i.e. minor to major axis ratio $\sim$0.9. An observational bias towards face-on objects may exist, since they are better at revealing the cavity). Additional information about the scattering

properties of the dust could be gained from analyzing the detailed azimuthal profile of the scattered light in each individual system, which we defer to the future studies. To calculate the azimuthally averaged surface brightness profiles, we bin the convolved images into a series of annuli $0\farcs05$ in width (the typical spatial resolution), and measure the mean flux within each annulus.

3 The NIR Polarized Scattered Light Images

With the tools described above, we investigate what kinds of disk structure could simultaneously reproduce the gross properties of all three kinds of observations described in Section 1. In this section, we first investigate the properties of the scattered light images from a semi-analytical theoretical point of view (Section 3.1), then we present the model results from the Monte Carlo simulations (Section 3.2).

3.1 Theoretical Considerations

In a single NIR band, when the (inner) disk is optically thick (i.e. not heavily depleted of the small grains), the scattering of the starlight can be approximated as happening on a scattering surface $z_{\rm s}$ where the optical depth between the star and surface is unity (the single scattering approximation). This surface is determined by both the disk scale height (particularly β in the simple vertically-isothermal models), and the radial profile of the surface density of the grains. The surface brightness of the scattered light $I_{\rm scat}(R)$ scales with radius as (Jang-Condell & Sasselov, 2003; Inoue et al., 2008)

$$I_{\rm scat}(R) \sim \zeta p \frac{L_\star}{4\pi R^2} \sin\gamma \tag{3.9}$$

where $L_\star$ is the stellar luminosity at this wavelength, ζ is a geometrical scattering factor, p is the polarization coefficient for PI ($p = 1$ for FI), and γ is the grazing angle (the angle between the impinging stellar radiation and the tangent of the scattering surface). We note that both ζ and p depend on azimuthal angle, inclination of the disk, and the scattering properties of the specific dust population responsible for scattering at the particular wavelength. However, if the disk is relatively face-on and not too flared, they are nearly position independent, because the scattering angle is nearly a constant throughout the disk and the dust properties of the specific dust population do not change much with radius.

The grazing angle is determined by the curvature of the scattering surface. In axisymmetric disks, assuming the surface density and scale height of the small dust to be smooth functions of radius, the grazing angle is also smooth with radius, and two extreme conditions can be constrained as follows:

1. For disks whose scattering surface is defined by a constant poloidal angle θ (such as a constant opening angle disk), $\gamma \sim R_\star/R$ (Chiang & Goldreich 1997, where $R_\star$ is the radius of the star), so the brightness of the scattered light scales with R as

$$I_{\rm scat}(R) \propto R^{-3}. \tag{3.10}$$

2. For flared disks (but not too flared, $h \lesssim R$), the grazing angle can be well approximated as

$$\sin\gamma \sim \gamma \sim \frac{dz_{\rm s}}{dR} - \frac{z_{\rm s}}{R}. \tag{3.11}$$

In this case, Muto (2011) explicitly calculated the position of the scattering surface z_s at various radii (see also Chiang & Goldreich 1997), and found $z_s = \eta h_s$ where the coefficient $\eta \sim$ a few and is nearly a constant. Combined with the fact that $h_s/R \propto R^{\beta-1}$ ($\beta \sim 1.25 - 1.3$ as typical values in irradiated disks, Chiang & Goldreich 1997; Hartmann et al. 1998), we have the intensity of the scattered light scales with radius as

$$I_{\rm scat}(R) \propto R^{\beta-3}. \tag{3.12}$$

Although the above calculations are under two extreme conditions (for complete flat or flared disks), and they are based on certain assumptions and the observed images have been smeared out by the instrument PSF, the radial profiles (azimuthally averaged, or along the major axis in inclined systems) of SEEDS scattered light images for many objects in this sample lie between Equations (3.10) and (3.12) in the radius range of interest. In order to guide the eye and ease the comparison between modeling results and observations, we use the scaling relation

$$I_{\rm scat}(R) \propto R^{-2.5} \tag{3.13}$$

to represent typical observational results, and plot it on top of the radiative transfer results, which will be presented in Section 3.2 (with arbitrary normalization).

On the other hand, an abrupt jump in the surface density or scale height profile of the small dust in the disk produces a jump in γ at the corresponding position. The effect of this jump will be explored in Section 3.2.

3.2 Modeling Results

First, we present the simulated H band PI images for a face-on transitional disk with a uniformly heavily depleted cavity with Σ_i as Equation (3.2) (Figure 3.3), and the associated surface brightness radial profiles (the thick solid curves in Figure 3.4). In each figure, the three panels show the raw image, the convolved unmasked image, and the convolved masked image, respectively. This model is motivated by the disk+cavity models in A11; we therefore use parameters typical of those models. Experiments show that the peculiarities in each individual A11 disk model hardly affect the qualitative properties of the images and their radial profiles, as long as the cavity is large enough ($\gtrsim 0\farcs2$) and the disk is relatively face-on.

This disk harbors a giant cavity at its center with $R_{\rm cav} = 42$ AU ($\sim 0\farcs3$ at 140 pc). The disk has the same inwardly rising Σ scaling both inside and outside the cavity as Equations (3.1) and (3.2). Outside the cavity both dust populations exist, with the big/small ratio as 0.85/0.15. Inside the cavity there is no big dust ($\delta_b = 0$), and the small dust is uniformly heavily depleted to $\delta_s = \delta_{\rm cav,s} \approx 10^{-5}$ ($\delta \approx 10^{-6}$). The surface density profiles for both dust populations can be found in Figure 4.2. The disk has total mass of $0.01 M_\odot$ (gas-to-dust mass ratio 100), $h/R = 0.075$ at 100 AU with $\beta = 1.15$, $R_c = 40$ AU, and accretion rate $\dot{M} = 5 \times 10^{-9} M_\odot$ yr^{-1}. The central source is a 3 $R_\odot$, $2M_\odot$, 5750 K G3 pre-main sequence star. We puff up the inner rim and the cavity wall by 100% and 200%, respectively.

The most prominent features of this model in both the unmasked and masked PI images are the bright ring at $R_{\rm cav}$, and the surface brightness deficit inside the ring (i.e. the cavity). Correspondingly, the surface brightness profile increases inwardly in the outer disk, peaks around $R_{\rm cav}$, and then decreases sharply. This is very different from many SEEDS results (such as the examples mentioned in Section 1), in which both the bright ring and the inner deficit are absent,

and the surface brightness radial profile keeps increasing smoothly all the way from the outer disk to the inner working angle, as illustrated by the scaling relation (3.13) in Figure 3.4.

This striking difference between models and observations suggests that the small dust cannot have such a large depletion at the cavity edge. Figure 3.4 shows the effect of uniformly filling the cavity with small dust on the radial profile for unmasked images (left) and masked images (right), leaving the other model parameters fixed. As $\delta_{\rm s}$ gradually increases from $\sim 10^{-5}$ to 1, the deviation in the general shape between models and observations decreases. The $\delta_{\rm s} = 1$ model corresponds to no depletion for small grains inside the cavity (i.e. a full small dust disk); this model agrees much better with the scattered light observations, despite a bump around the cavity edge produced by its puffed up wall (Section 3.2), although this model fails to reproduce the transitional-disk-like SED (Section 5).

We note that this inconsistency between uniformly heavily depleted cavity models and observations is intrinsic and probably cannot be solved simply by assigning a high polarization to the dust inside the cavity. The polarization fraction (PI/FI) in the convolved disk images of our models ranges from ∼0.3 to ∼0.5, comparable to observations (for example Muto et al. 2012). Even if we artificially increase the polarization fraction inside the cavity by a factor of 10, by scaling up the cavity surface brightness in the raw PI images (which results in a ratio PI/FI greater than unity) while maintaining the outer disk unchanged, the convolved PI images produced by these uniformly heavily depleted cavity models still have a prominent cavity at their centers. We also note that the contrast of the cavity (the flux deficit inside $R_{\rm cav}$) and the strength of its edge (the brightness of the ring at $R_{\rm cav}$) are partially reduced in the convolved images compared with the raw images. This is due both to the convolution of the disk image with the telescope PSF, which naturally smooths out any sharp features in the raw images, and to the superimposed seeing halo from the bright innermost disk (especially for the unmasked images).

In the rest of Section 3 we focus on the small grains inside the cavity while keeping the big grains absent, and study the effect of the parameters $\Sigma_{\rm i}$, $\delta_{\rm cav,s}$, and the puffing up of the inner rim and cavity wall on the scattered light images. The convolved images for three representative models are shown in Figure 3.5, and the radial profiles for all models are shown in Figure 3.6. Each model below is varied from one standard model, which is shown as the top panel in Figure 3.5 and represented by the thick solid curve in all panels in Figure 3.6. This fiducial model has a flat $\Sigma_{\rm i}$ with no discontinuity at the cavity edge for the small dust (i.e. $\delta_{\rm cav,s} = 1$), and no puffed up rim or wall, but otherwise identical parameters to the models above.

The Effect of $\Sigma_{\rm i}$

First we study the effect of three surface density profiles inside the cavity, namely rising (Equation (3.2)), flat (Equation (3.3)), and declining $\Sigma_{\rm i}$ (Equation (3.4)). The surface densities for these models are illustrated in Figure 4.2. Panel (a) in Figure 3.6 shows the effect of varying the surface density on the image radial profiles. Except for shifting the entire curve up and down, different $\Sigma_{\rm i}$ produce qualitatively very similar images and radial profiles, and all contain the gross features in many SEEDS observations (illustrated by the scaling relation (3.13)). This is due to both the fact that smooth surface density and scale height profiles yield a smooth scattering surface, and the effect of the PSF. We note that there is some coronagraph edge effect at the inner working angle in the masked images, which is caused by that the part of the disk just outside (but not inside) the mask is convolved with the PSF. This results in a narrow ring of flux deficit just outside the mask. In general, the flux is trustable beyond about one FWHM of the

PSF from $\psi_{\rm in}$ ($\sim 0\farcs05 + 0\farcs15 = 0\farcs2$) (Muto et al., 2012, some instrumental effects in observations may also affect the image quality within one FWHM from the mask edge as well).

The Effect of $\delta_{\rm cav,s}$

We investigate the effect of different $\delta_{\rm cav,s}$ with flat $\Sigma_{\rm i}$ (3.3). Panel (b) in Figures 3.6 shows the effect on the radial profile of the convolved images. When deviating from the fiducial model with $\delta_{\rm cav,s} = 1$ (i.e. a continuous small dust disk at $R_{\rm cav}$), a bump around the cavity edge and a surface brightness deficit inside the cavity gradually emerge. We quantify this effect by measuring the relative flux deficit at $0\farcs2$ ($\frac{2}{3}R_{\rm cav}$) as a function of $\delta_{\rm cav,s}$, the small-dust discontinuity at the cavity edge (subpanel in each plot). For each model we calculate the ratio of the flux at $0\farcs2$, $f_{0.2}$, to $f_{0.6}$, the flux at $0\farcs6$ ($= 2R_{\rm cav}$), normalized by $f_{0.2}/f_{0.6}$ in the fiducial, undepleted model. For the model with a 50% discontinuity in $\Sigma_{\rm s}$ at $R_{\rm cav}$ ($\delta_{\rm cav,s} = 0.5$), $f_{0.2}/f_{0.6}$ is $\sim$15% lower than in the fiducial model in the convolved unmasked images, and $\sim$20% lower in the convolved masked images. The latter is larger because the mask suppresses the halo of the innermost disk, thus the relative flux deficit in the masked image is closer to its intrinsic value, i.e. the deficit in the raw images. In this sense the masked images are better at constraining the discontinuity of the small dust than the unmasked images. The middle row in Figure 3.5 shows the model images for $\delta_{\rm cav,s} = 0.3$ (illustrated by the thin solid curve in Figure 4.2). The edge of the cavity is quite prominent in the raw image, while it is somewhat smeared out but still visible in the convolved images. For many objects in this IRS/SMA/Subaru cross sample, the SEEDS images are grossly consistent with a continuous small dust disk at the $R_{\rm cav}$, while in some cases a small discontinuity may be tolerated.

For the purpose of comparison with the observations, we now discuss the detectability of a finite surface density discontinuity at the cavity edge, given the sensitivity and noise level of the SEEDS data (the numerical noise level in our simulations is well below the noise level in the observations, see Section 2.1). In typical SEEDS observations with an integration time of several hundred seconds, the intrinsic Poisson noise of the surface brightness radial profile due to finite photon counts is usually a few tenth of one percent at radius of interests, smaller than the error introduced by the instrument and the data reduction process. Muto et al. (2012) estimated the local noise level of the surface brightness to be $\sim$10% at $R = 0\farcs5$ for the SEEDS SAO 206462 PI images, which should be an upper limit for the noise level in the azimuthally averaged surface brightness (more pixels) and in the inner region of the images (brighter). If this is the typical value for the instrument, then our modeling results indicate that SEEDS surface brightness measurements should be able to put relatively tight constraints on the surface density discontinuity for the small dust at $R_{\rm cav}$. For example, SEEDS should be able to distinguish a disk of small dust continuous at $R_{\rm cav}$ from a disk of small dust with a 50% density drop at $R_{\rm cav}$.

Thus, a lower limit on the small dust depletion factor at the cavity edge can be deduced from detailed modeling for each individual object. This lower limit is likely to be higher than the upper limit from SMA on the depletion factor of the big dust ($\lesssim 0.1 - 0.01$), for objects with relatively smooth radial profiles. If this is confirmed for some objects in which the two limits are both well determined, it means that the density distribution of the small dust needs to somehow *decouple* from the big dust at the cavity edge. We will come back to this point in Section 5.

The Effect of the Puffed Up Inner Rim and Cavity Wall

Lastly, we explore the effects of the puffed up inner rim and the cavity wall on the images, by comparing the fiducial model (no puffing up anywhere) to a model with the inner rim puffed up

by 100%, and another model with the cavity wall puffed up by 200%. Panel (c) in Figure 3.6 shows the effects. Puffing up the inner rim has little effect on the image, while the puffed up wall produces a bump at the cavity edge, similar to the effect of a gap edge. Images for the model with the puffed up wall are shown in Figure 3.5 (bottom row), where the wall is prominent in the raw image while been somewhat smeared out but still visible in the convolved images. Scattered light images should be able to constrain the wall for individual objects. Without digging deeply into this issue, we simply note here that the SEEDS images for many objects in this sample are consistent with no or only a small puffed up wall.

4 The Sub-mm Properties and Images

4.1 The Sub-mm Intensity Profile

For all models shown in Section 3, the disk is optically thin in the vertical direction at 880 μm ($\tau \sim \Sigma\kappa_\nu \lesssim 1$, where κ_ν is the opacity per gram at ν). In this case, the intensity $I_\nu(R)$ at the surface of the disk at a given radius may be expressed as:

$$I_\nu(R) \approx \int_{-\infty}^{\infty} \left(B_{\nu,T_{\rm b}(z)}\kappa_{\nu,{\rm b}}\rho_{\rm b}(z) + B_{\nu,T_{\rm s}(z)}\kappa_{\nu,{\rm s}}\rho_{\rm s}(z)\right) dz \tag{3.14}$$

where $\nu = 341$ GHz at 880 μm, $B_{\nu,T(z)}$ is the Planck function at $T(z)$ (the temperature at z), and $\rho(z)$ is the vertical density distribution (T and ρ depend on R as well). Outside the cavity, the big dust dominates the 880 μm emission, since the big dust is much more efficient at emitting at $\sim$880 μm than the small dust ($\kappa_{\nu,{\rm b}}/\kappa_{\nu,{\rm s}} \gtrsim 30$ at these wavelengths). Inside the cavity there is *no* big dust by our assumption, so the sub-mm emission comes only from the small dust. The thick curves in Figure 3.7 show the 880 μm intensity as a function of radius for the models in Section 3.2 (i.e. continuous small dust disks with rising, flat, or declining $\Sigma_{\rm i}$). In other words, this is an 880 μm version of the surface brightness radial profile for the "raw" image, without being processed by a synthesized beam dimension (the SMA version of the "PSF"). The bottom thin dashed curve is for the uniformly heavily depleted cavity model as in Figure 3.3 ($\delta_{\rm s} = \delta_{\rm cav,s} \approx 10^{-5}$, rising $\Sigma_{\rm i}$) and no big dust inside the cavity, which represents the sub-mm behavior of the models for most systems in A11.

Since the disk is roughly isothermal in the vertical direction near the mid-plane where most dust lies (Chiang & Goldreich, 1997), $T(z)$ may be approximated by the mid-plane temperature $T_{\rm mid}$. The Planck function can be approximated as $B_{\nu,T} \sim 2\nu^2 kT/c^2$ at this wavelength due to $h\nu \ll kT$ (880 μm $\sim$16 K, marginally true in the very outer part of the disk). In addition, since the two dust populations have roughly the same mid-plane temperature, but very different opacities ($\kappa_{\nu,{\rm b}} \gg \kappa_{\nu,{\rm s}}$), Equation (3.14) can be simplified to $I_\nu(R) \propto T_{\rm mid}\kappa_{\nu,{\rm b}}\Sigma_{\rm b}$ for $R > R_{\rm cav}$ and $I_\nu(R) \propto T_{\rm mid}\kappa_{\nu,{\rm s}}\Sigma_{\rm s}$ for $R < R_{\rm cav}$. For our continuous small disk models with a complete cavity for the big dust, the intensity at 880 μm drops by $\sim$2.5 orders of magnitude when moving from outside ($I_\nu(R_{\rm cav} + \epsilon)$) to inside ($I_\nu(R_{\rm cav} - \epsilon)$) the cavity edge, due to both the higher opacity of the big dust and the fact that big dust dominates the mass at $R > R_{\rm cav}$. Inside the cavity, the intensity (now exclusively from the small dust) is determined by the factor $T_{\rm mid}\Sigma$. For an irradiated disk $T_{\rm mid}$ increases inwardly, typically as $T_{\rm mid} \propto R^{-1/2}$ (Chiang & Goldreich, 1997), while $\Sigma_{\rm i}$ in our models could have various radial dependencies (Equations (3.2)-(3.4)). In the flat $\Sigma_{\rm i}$ models (Equation (3.3)), the intensity inside the cavity roughly scales with R as $I_\nu(R) \propto R^{-1/2}$ — the same as $\{T_{\rm mid}(R)\}$ — and is 1.5 orders of magnitude lower than

$I_\nu(R_{\rm cav}+\epsilon)$ in the innermost disk (around the sublimation radius). On the other hand, if there is no depletion of the small dust anywhere inside the cavity (i.e. the rising $\Sigma_{\rm i}$ with $\delta_{\rm s}=1$ case), the intensity at the center (thick dashed curve) can exceed $I_\nu(R_{\rm cav}+\epsilon)$ by two orders of magnitude.

In A11, for 880 μm images of models with no big dust inside the cavity, the residual emission near the disk center roughly traces the quantity $T\Sigma_{\rm i}\kappa$. In most cases, A11 found those residuals to be below the noise floor. Due to the sensitivity limit, the constraint on $T\Sigma_{\rm i}\kappa$ inside the cavity is relatively weak; nevertheless, A11 were able to put an upper limit equivalent to $\delta_{\rm b}\lesssim 0.01-0.1$ for the mm-sized dust (with exceptions such as LkCa 15). Here we use a mock disk model to mimic this constraint. The top thin dashed curve in Figure 3.7 is from a model with uniform depletion factors $\delta_{\rm s}=\delta_{\rm b}=0.01$ for *both* dust populations inside the cavity (so the entire disk has the same dust composition everywhere). The result shows that, qualitatively, various models with a continuous small dust disk and a complete cavity for the big dust are all formally below this mock SMA limit, though a quantitative fitting of the visibility curve is needed to constrain $\delta_{\rm s}$ and $\delta_{\rm cav,s}$, in terms of upper limits, on an object by object basis. This may line up with another SED-based constraint on the amount of small dust in the innermost disk, as we will discuss in the Section 5.

4.2 The 880 μm Images

While the intensity discussion qualitatively demonstrates the sub-mm properties of the disks, Figure 3.8 shows the narrow band images at 880 μm for two disk models. The top row is from the model which produces Figure 3.3 (also the bottom thin dashed curve in Figure 3.7 and the left panel in Figure 4.2), which is an A11 style model with a uniformly heavily depleted cavity with rising $\Sigma_{\rm i}$, $\delta_{\rm s}=\delta_{\rm cav,s}\approx 10^{-5}$, and no big dust inside the cavity. The bottom row is from the fiducial model in Section 3.2 (which produces the top row in Figure 3.5, and the thick solid curve in Figure 3.7 and in the left panel in Figure 4.2), which has a continuous distribution for the small dust with flat $\Sigma_{\rm i}$ and $\delta_{\rm cav,s}=1$, and no big dust at $R<R_{\rm cav}$ as well. The panels are the raw images from the radiative transfer simulations (left), images convolved by a Gaussian profile with resolution $\sim 0\farcs3$ (middle, to mimic the SMA observations, A11) and $\sim 0\farcs1$ (right, to mimic future ALMA observations (Section 6.3).

Both models reproduce the characteristic features in the SMA images of this transitional disk sample: a bright ring at the cavity edge and a flux deficit inside, agree with the semi-analytical analysis in Section 4.1, but *very different* NIR scattered light images. The intrinsic reason for this apparent inconsistency is, as we discussed above, that big and small dust dominate the sub-mm and NIR signals in our models, respectively. Thus two disks can have similar images at one of the two wavelengths but very different images at the other, if they share similar spatial distributions for one of the dust populations but not the other.

Lastly, we comment on the effect of big to small dust ratio, which is fixed in this work as 0.85/0.15 to simplify the model (see the discussion of depletion of the small dust in the surface layer of protoplanetary disks, D'Alessio et al. 2006). The scattering comes from the disk surface and is determined by the grazing angle, which only weakly depends on the small dust surface density, if it is continuous and smooth (Section 3.2). Changing the mass fraction of the big dust in the outer disk from 0.85 to 0.95 in our $\delta_{\rm cav,s}=1$ models (effectively a factor of 3 drop in surface density of the small dust everywhere) introduces a $\sim$20% drop in the surface brightness of the scattered light images, but a factor of 3 drop in the cavity 880 μm intensity ($I_\nu(R)\propto\Sigma_{\rm s}$ at $R<R_{\rm cav}$). Lastly, we note that since the big-to-small dust sub-mm emission ratio is

$\propto \kappa_{\nu,\rm b}\Sigma_{\rm b}/\kappa_{\nu,\rm s}\Sigma_{\rm s}$, the small grains must contain more than 90% of the total dust mass to dominate the sub-mm emission.

5 The Transitional-disk-like SED

In this section, we explore the parameter degeneracy in reproducing the transitional-disk-like SED with their distinctive NIR-MIR dips. SED fitting (particularly of the IRS spectrum) can only provide constraints on the spatial distribution of the small dust within a few or a few tens AU from the center, and it contains strong degeneracy in the parameter space (A11). Below, we show that disk models with different cavity structures can produce roughly the same SED, containing the transitional disk signature, as long as their innermost parts are modestly depleted (by a factor of ∼1000 or so). Except for the specifically mentioned parameters, the other parameters of these models are the same as for the fiducial model in Section 3.2; in particular there is no big dust inside the cavity.

5.1 The Degeneracy in SED Fitting

Figure 3.9 shows the SED for four disk models varied based on the fiducial model in Section 3.2. The model for the thick dashed curve has a uniformly heavily depleted cavity with rising $\Sigma_{\rm i}$, $\delta_{\rm s} \approx 10^{-5}$, and no big dust inside the cavity (illustrated by the thin dashed curve in the left panel of Figure 4.2). The scale height profile has $\beta = 1.15$ and $h/R = 0.085$ at 100 AU. The inner rim is puffed up by 100% and the outer wall is puffed up by 200%. The inclination is assumed to be 20°, $R_c = 15$ AU, and $R_{\rm cav} = 36$ AU. This model is motivated by the A11 disk+cavity structure. The full small dust disk model (the thin dashed curve) has otherwise identical properties but $\delta_{\rm s} = 1$ (i.e. completely filled cavity for the small dust). The other two smooth small-dust disk models have much more massive inner disks with $\delta_{\rm cav,s} = 1$ (i.e. a continuous small dust disk) and no puffed up inner rim or cavity wall. The solid curve model has flat $\Sigma_{\rm i}$ (Equation (3.3), illustrated by the thick solid curve in the left panel of Figure 4.2), $\beta = 1.33$ and $h/R = 0.08$ at 100 AU. The dash-dotted curve model has declining $\Sigma_{\rm i}$ (Equation (3.4), illustrated by the dash-dotted curve in the left panel of Figure 4.2), $\beta = 1.25$, and $h/R = 0.078$ at 100 AU.

The two smooth small dust disk models with flat or declining $\Sigma_{\rm i}$ produce qualitatively similar SED as the uniformly heavily depleted model (in particular, roughly diving to the same depth at NIR, and coming back to the same level at MIR, as the signature of transitional disks), despite the fact that they have very different structures inside the cavity. The minor differences in the strength of the silicate feature and the NIR flux could be reduced by tuning the small dust model and using a specifically designed scale height profile at the innermost part (around the sublimation radius or so). The main reasons for the similarity are:

1. The depletion factor (or the surface density) at the innermost part (from $R_{\rm sub}$ to ∼1 AU or so). While the two smooth small dust disk models differ by ∼5 orders of magnitude on the depletion factor (or the surface density) at the cavity edge from the uniformly heavily depleted model, the difference is much smaller at the innermost disk, where most of the NIR-MIR flux is produced. At the innermost disk, the small dust is depleted by ∼3 orders of magnitude in the flat $\Sigma_{\rm i}$ model, ∼5 orders of magnitude for the declining $\Sigma_{\rm i}$ model, and ∼5 orders of magnitude in the uniformly heavily depleted model (with rising $\Sigma_{\rm i}$). On the other hand, the integrated depletion factor $\langle\delta_{\rm s}\rangle$ for the small dust is ∼0.3 for the flat $\Sigma_{\rm i}$ model, ∼0.2 for the declining $\Sigma_{\rm i}$, and $\sim 10^{-5}$ for the uniformly heavily depleted model, more

in line with $\delta_{\rm cav,s}$, because most of the mass is at the outer part of the cavity. We note that the total amount of small dust is not as important as its spatial distribution inside the cavity, and the amount of dust in the innermost part, in determining the NIR-MIR SED.

2. The scale height of small grains $h_{\rm s}$ at the innermost part. The two smooth small dust disk models are more flared than the uniformly heavily depleted model. While the three have roughly the same scale height outside the cavity, the difference increases inward. At 1 AU, $h_{\rm s}$ for the uniformly heavily depleted model is 1.7× that of the flat $\Sigma_{\rm i}$ model and 2.4× that of the declining $\Sigma_{\rm i}$ model.

3. The puffed up inner rim. The inner rim scale height is doubled in the heavily depleted model, which increases the NIR flux and reduces the MIR flux since the puffed up rim receives more stellar radiation and shadows the disk behind it. The puffed up inner rim is removed in the flat or declining $\Sigma_{\rm i}$ models.

The surface density (or the depletion factor) and the scale height at the innermost part are considerably degenerate in producing the NIR to MIR flux in the SED (A11). In general, a disk which has a higher surface density and scale height at the innermost part and a puffed up inner rim intercepts more stellar radiation at small radii, and has more dust exposed at a high temperature, so it produces more NIR flux. On the other hand, the shadowing effect cast by the innermost disk on the outer disk causes less MIR emission (Dullemond & Dominik, 2004a,b). In this way, changes in some of these parameters could be largely compensated by the others so that the resulting SED are qualitatively similar.

However, in order to reproduce the characteristic transitional disk SED, the value of the depletion factor inside the cavity cannot be too high. The increasing surface density at small radii would eventually wipe out the distinctive SED deficit, and the resulting SED evolves to a full-disk-like SED, as illustrated by the full small dust disk model in Figure 3.9. In our experiments with not too flared β (comparing with the canonical $\beta \sim 1.25 - 1.3$ in irradiated disk, Chiang & Goldreich 1997; Hartmann et al. 1998), we find an upper limit on the order of 10^{-3} for the depletion factor in the innermost part in our smooth disk models. We note that this limit depends on the detailed choices of the disk and cavity geometry, such as R_c and $R_{\rm cav}$, and the big-to-small-dust ratio in the outer disk.

5.2 Discussion of the Disk Model in Producing the SED

The inner rim is puffed up in A11 to intercept the starlight and to shadow material at larger radii. At a given radius, the scale height h of the gas disk scales as

$$h \approx c_{\rm s}/\Omega, \tag{3.15}$$

where Ω is the orbital frequency and $c_{\rm s}$ is the isothermal sound speed in the disk

$$c_{\rm s} \approx \sqrt{kT/\mu}, \tag{3.16}$$

where T is the (mid-plane) temperature and μ is the average weight of the particles. If the scale heights of the dust and the gas are well coupled (e.g. for well-mixed-gas-dust models or a constant level of dust settling), tripling the rim scale height (not unusual in A11) means an order of magnitude increase in its temperature. Due to the sudden change of the radial optical depth from

$\sim$0 to unity in a narrow transition region directly illuminated by the star, some puffing up may be present, but probably not that significant. In addition, Isella & Natta (2005) pointed out that a realistic puffed up rim has a curved edge (away from the star) instead of a straight vertical edge due to the dependence of $T_{\rm sub}$ on pressure, which further limits the ability of the rim to shadow the outer disk. Based on these reasons, we choose not to have the rim puffed up in our models, though we note that a relatively weak puffing up, as in the uniformly heavily depleted model here, does not make a major difference in the results. Similar idea applies to the puffed up wall as well.

The typical β value assumed in A11 in this sample ($\beta \sim 1.15$) is small compared with the canonical values for irradiated disk models ($\beta \sim 1.25 - 1.3$, Chiang & Goldreich 1997; Hartmann et al. 1998). This leads to that the temperature determined by the input scale height ($T_{\rm input}$, Equation (3.15) and (3.16)) may increase inwardly too steeply compared with the output mid-plane temperature calculated in the code ($T_{\rm output}$). $T_{\rm input}$ at 100 AU in the three models are close to each other due to their similar scale height there, and all agree with $T_{\rm output}$ ($\sim$30 K) within 20%. However, at 1 AU, while $T_{\rm input}$ in our smooth small dust disk models is close to $T_{\rm output}$ ($\sim$220 K, within 30%), the input temperature in the uniformly heavily depleted model appears to be too high by a factor of $\sim$3.

6 Discussion

6.1 Direct Constraints from Observations and Our Generic Model

First, we review the *direct*, model-independent constraints on the disk structure which the three observations — the infrared SED, SMA sub-mm observations, and SEEDS NIR polarized scattered light imaging — put on many transitional disks in this cross sample:

1. IRS reveals a distinctive dip in the spectra around 10 μm, which indicates that the small dust ($\sim \mu$m-sized or so) in the inner part of the disk (from $R_{\rm sub}$ to several AU) must be moderately depleted. However, due to degeneracy in parameter space, the detailed inner disk structure is model dependent. Models with different cavity depletion factors, $\Sigma_{\rm i}$, and scale heights at the innermost disk could all reproduce the transitional disk signature. The IRS spectra are not very sensitive to the distribution of big dust.

2. The SMA images show a sub-mm central cavity, which indicates that the big dust (mm-sized or so, responsible for the sub-mm emission) is heavily depleted inside the cavity. However, while the observations can effectively constrain the spatial distribution of the big dust outside the cavity, they can place only upper limits on its total amount inside the cavity. SMA observations do not place strong constraints on the distribution of the small dust, though a weak upper limit for the amount of small dust inside the cavity may be determined based on the SMA noise level.

3. SEEDS NIR polarized scattered light images are smooth on large scales, and have no clear signs of a central cavity. The radial profiles of many images increase inwardly all the way from the outer disk to the inner working angle without sudden jumps or changes of slope, indicating that the scattering surfaces and their shapes are smooth and continuous (outside $\psi_{\rm in}$). On the other hand, scattered light images are not very sensitive to the detailed surface density profiles and the total amount of small dust inside the cavity. The NIR images normally do not provide significant constraints on the distribution of the big dust.

In this work, we propose a generic disk model which grossly explains all three observations simultaneously. Previous models in the literature which assume a full outer disk and a uniformly heavily depleted inner cavity can reproduce (1) and (2), but fail at (3), because they also produce a cavity in the scattered light images, which contradicts the new SEEDS results. Through radiative transfer modeling, we find that qualitatively (3) is consistent with a smooth disk of small dust with little discontinuity in both surface density and scale height profile. Table 3.1 summarizes the key points in various models and compares their performances in these three observations.

Since we focus on generic disk models only which reproduce the gross features in observations, and we do not try to match the details of specific objects, we more or less freeze many nonessential parameters in Sections 3-5 which do not qualitatively change the big picture for simplicity. The important ingredients include the dust properties (mostly for the small dust, both the size distribution and the composition), $\Sigma_{\rm s}$, the big-to-small-dust ratio, and $h_{\rm i}$ (both the absolute scale and β). NIR scattered light images are able to provide constraints on some of these parameters (particularly $h_{\rm i}$ and β), due to the dependence of the position and the shape of the disk surface on them. These parameters were not well constrained previously using sub-mm observations and SED due to strong degeneracies (A11).

We note that alternative models for explaining the scattered light images exist, but generally they require additional complications. As one example, if the small dust is not depleted in the outer part of the sub-mm cavity, but is heavily depleted inside a radius smaller than $\psi_{\rm in}$ ($\lesssim 15-20$ AU), then it is possible to fit all the three observations, in which case the *small dust cavity* does not reveal itself in the scattered light images due to its small size. However, in this case one needs to explain why different dust populations have different cavity sizes. Future scattered light imaging with even smaller $\psi_{\rm in}$ may test this hypothesis.

As another example, while we achieve a smooth scattering surface by having continuous surface density and scale height profiles for the small dust, it is possible to have the same result with discontinuities in both, but with just the right amount such that the combination of the two yields a scattering surface inside the cavity smoothly joining the outer disk. This may work if the cavity is optically thick (i.e. not heavily depleted), so that a well-defined scattering surface inside the cavity exists. Experiments show that for the models in Section 3.2, uniformly depleting the small dust by a factor of $\sim$1000 and tripling the scale height inside the cavity would roughly make a smooth scattering surface. However, fine tuning is needed to eliminate the visible edge from a small mismatch in the two profiles. Also, the thicker cavity shadows the outer disk, and makes it much dimmer in scattered light (by about one order of magnitude). Lastly, without tuning on the scale height and/or surface density in the innermost part, this model produces too much NIR-MIR flux and too small flux at longer wavelengths in its SED, due to its big scale height at small R and the subsequent shadowing effect.

6.2 The Structure of the Cavity in Transitional Disks

There are several important conclusions that can be drawn based on our modeling of the transitional disks at different wavelengths.

First, as we discussed in Section 3.2, for some objects the *lower* limit for the depletion of the *small* dust at the cavity edge (as constrained by the scattered light images) is likely to be above the *upper* limit for the *big* dust constrained by the SMA, based on the modeling results and the noise level in the two instruments. This essentially means that the small dust has to spatially

decouple from the big dust at the cavity edge. This is the first time that this phenomenon has been associated with a uniform sample in a systematic manner. Detailed modeling of both images for individual objects is needed, particularly in order to determine how sharp the big dust cavity edge is from the sub-mm observations, to pin down the two limits and check if they are really not overlapping. While we defer this to future work, we note that having the big dust the same surface density as the small dust inside the cavity probably cannot reproduce the sub-mm images. Experiments show that even with our declining $\Sigma_{\rm i}$ (3.4), a fixed big/small dust ratio and a continuous surface density for both throughout the disk (i.e. $\delta_{\rm cav,s} = \delta_{\rm cav,b} = 1$) produce a sub-mm cavity with a substantially extended edge, and the central flux deficit disappears in the smeared out image. If this is confirmed, it further leads to two possibilities: (a) whatever mechanism responsible for clearing the cavity have different efficiency for the small and big dust, or (b) there are other additional mechanisms which differentiate the small and big dust after the cavity clearing process. At the moment it is not clear which one of the two possibilities is more likely, and both need more thorough investigations.

Second, as we argued in Section 5, in order to reproduce the distinctive NIR deficit in the transitional disk SED, an effective "upper limit" of $\delta_{\rm s}$ at the innermost region is required, which in experiments with our disk parameters is on the order of 10^{-3}. This is far from the *lower limit* of $\delta_{\rm s}$ at the cavity edge (close to 1), constrained by the scattered light images. Together, the two limits indicate that the spatial distribution of the small grains is very different inside and outside the cavity — specifically, $\Sigma_{\rm s}$ tends to be flat or even decrease inwardly inside the cavity.

In addition, this implies that the gas-to-dust ratio needs to increase inwardly, given that most of these objects have non-trivial accretion rates ($\dot{M} \sim 10^{-8} - 10^{-9} M_\odot$/yr, A11). For a steady Shakura & Sunyaev disk, the accretion rate $\dot{M}$ is related to the gas surface density $\Sigma_{\rm gas}$ as:

$$\frac{\alpha c_{\rm s}^2 \Sigma_{\rm gas}}{\Omega} \approx \frac{\dot{M}}{3\pi}, \tag{3.17}$$

where α is the Shakura-Sunyaev viscosity parameter, Ω is the angular velocity of the disk rotation, and $c_{\rm s}$ is given by Equation (3.16). At $\sim$0.1 AU, equation (5.5) predicts $\Sigma_{\rm gas} \sim 10^3$ g cm^{-2}, assuming a temperature $T \sim 10^3$ K, $\dot{M} \sim 10^{-8} M_\odot$/yr, $\alpha \sim 0.01$, and $M \sim M_\odot$ as typical T Tauri values. This is very different from our upper limit of $\Sigma_{\rm gas} \sim$1 g cm^{-2} in the innermost disk, obtained assuming a fixed gas-to-dust ratio of 100 (the flat $\Sigma_{\rm i}$ models in Figure 4.2). To simultaneously have large $\Sigma_{\rm gas}$ but small $\Sigma_{\rm dust}$ in the innermost disk, the gas-to-dust ratio needs to increase substantially from the nominal value of 100 (by a factor of $\sim 10^3$ in our models, echos with Zhu et al. 2011). This could put constraints on the cavity depletion mechanism or dust growth and settling theory.

At the moment, the mechanism(s) which are responsible for clearing these giant cavities inside transitional disks are not clear (see summary of the current situation in A11). Regarding the applications of our model on this subject, we note two points here. The flat/declining surface density of the small grains inside the cavity in our models is consistent with the grain growth and settling argument, that the small grains in the inner disk are consumed at a faster rate due to higher growth rate there (Dullemond & Dominik, 2005; Garaud, 2007; Brauer et al., 2008; Birnstiel et al., 2010). Also, the so-called dust filtration mechanism seems promising for explaining why small dust but not big dust is present inside the cavity (Paardekooper & Mellema, 2006; Rice et al., 2006), since it could effectively trap the big dust at a pressure maximum in the disk but filter through the small dust. Particularly, combining the two (dust growth and dust filtration), Zhu et al. (2012) proposed a transitional disk formation model from a theoretical point

of view to explain the observations, and their predicted spatial distribution of both dust populations in the entire disk is well consistent with the ones here.

6.3 Future Observations

Imaging is a very powerful tool for constraining the structure of protoplanetary disks and the spatial distribution of both the small and big dust, and there are many ongoing efforts aiming at improving our ability to resolve the disks. In the direction of optical-NIR imaging, updating existing coronagraph and Adaptive Optics (AO) systems, such as the new Coronagraphic Extreme Adaptive Optics (SCExAO) system on Subaru (Murakami et al. 2010; Guyon et al. 2011, which could raise the Strehl ratio to ∼0.9), are expected to achieve better performance and smaller $\psi_{\rm in}$ in the near future.

To demonstrates the power of the optimal performances of these next generation instruments in the NIR imaging, Figure 3.10 shows the surface brightness radial profile of several masked H-band disk images convolved from the *same* raw image by *different* PSF. Except the dotted curve, all the other curves are from the model corresponding to the middle row in Figure 3.5, which has a $0\farcs3$ radius cavity, flat $\Sigma_{\rm i}$, and $\delta_{\rm cav,s} = 0.3$ (a 70% drop in $\Sigma_{\rm s}$ at $R_{\rm cav}$). We use three PSFs: the current HiCIAO PSF in H band, which could be roughly approximated by a diffraction limited core of an 8-m telescope (resolution $\sim 0\farcs05$) with a Strehl ratio of ∼0.4 plus an extended halo; mock PSF I (to mimic SCExAO), which is composed of a diffraction limited core of an 8-m telescope with a Strehl ratio of 0.9, and an extended halo similar in shape (but fainter) as the current HiCIAO PSF; model PSF II (to mimic the next generation thirty-to-forty meter class telescopes), which is composed of a diffraction limited core of a 30-m telescope (resolution $\sim 0\farcs013$) with a Strehl ratio of 0.7, and a similar halo as the previous two. Compared with the full small dust disk case, all the convolved images of the $\delta_{\rm cav,s} = 0.3$ model shows a bump at $R_{\rm cav}$ and a relative flux deficit at $R < R_{\rm cav}$. However, from the current HiCIAO PSF to model PSF I and II, the contrast level of the cavity becomes higher and higher, and closer and closer to the raw image (which essentially has an infinite spatial resolution). With these next generation instruments, the transition of the spatial distribution of the small dust at the cavity edge will be better revealed.

On the other hand, in radio astronomy, the Atacama Large Millimeter Array (ALMA[2]) is expected to revolutionize the field, with its much better sensitivity level and exceptional spatial resolution ($\sim 0\farcs1$ or better). As examples, the right panels in Figure 3.8 show images convolved by a Gaussian profile with resolution $\sim 0\farcs1$, which mimic the ability of ALMA and show two prominent improvements over the images under the current SMA resolution ($\sim 0\farcs3$, middle panels). First, the edge of the cavity is much sharper in the mock ALMA images. This will make the constraint on the transition of the big dust distribution at the cavity edge much better. Second, while the weak emission signal in the bottom model is overwhelmed by the halo of the outer disk in the mock SMA image, resulting in that the bottom model is nearly indistinguishable from the top model (which essentially produces zero cavity sub-mm emission), the mock ALMA image successfully resolves the signal as an independent component from the outer disk, and separates the two models. This weak emission signal traces the spatial distribution of the dust (both populations) inside the cavity, which is the key in understanding the transitional disk structure.

[2]http://www.almaobservatory.org/

At this stage, the total number of objects which have been observed by all three survey-scale projects (using IRS/SMA/Subaru) is still small. Increasing the number in this multi-instrument cross sample will help clear the picture. In addition, future observations which produce high spatial resolution images at other wavelengths, such as UV, optical, or other NIR bands (for example using HST, Grady et al. 2009, or the future JWST), or using interferometer (such as the Astrometric and Phase-Referencing Astronomy project on Keck, Adelman et al. 2007; Pott et al. 2009, and AMBER system on Very Large Telescope Interferometer, Petrov et al. 2007; Tatulli et al. 2007) should also be able to provide useful constraints on the disk properties.

7 Summary

We summarize this chapter by coming back to the question which we raised at the beginning: what kind of disk structure is consistent with and is able to reproduce the characteristic signatures in all three observations of transitional protoplanetary disks: a high contrast cavity in sub-mm images by SMA, a NIR deficit in SED by Spitzer IRS, and a smooth radial profile in NIR polarized scattered light images by Subaru HiCIAO. We propose one generic solution for this problem, which is feasible but by no means unique. The key points are:

1. A cavity with a sharp edge in the density distribution of big grains (up to ∼mm-sized) and with a depletion factor of at least 0.1-0.01 inside is needed to reproduce the SMA sub-mm images, as pointed out by A11.

2. Right inside the cavity edge (∼15-70 AU), the surface density for the small dust (∼micron-sized and smaller) does not have a big sudden (downward) jump (A small discontinuity may exist). The SEEDS NIR scattered light images, which typically detect the disk at $R \gtrsim 15$ AU (the inner working angle in SEEDS), generally require continuous/smooth profiles for the surface density and scale height of the small dust.

3. The small dust in the innermost region (i.e. within a few AU, on a scale smaller than measured by SEEDS) has to be moderately depleted in order to produce the transitional-disk-like SED, assuming the disk is not too flared, but the exact depletion factor is uncertain and model dependent.

As we discussed in Section 6.2, combining all the above points, our model suggests that the spatial distributions of the big and small dust are *decoupled* inside the cavity (particularly at the cavity edge). Also, our model argues that the surface density of the small dust inside the cavity is flat or decreases with radius, consistent with the predictions in dust growth models. Combined with the accretion rate measurement of these objects, it further implies that the gas-to-dust ratio increases inwardly inside the cavity of transitional disks.

Table 3.1 Model Comparison

	Our model	Uniformly heavily depleted cavity	Full small dust
$\Sigma_{\rm i,s}$	Equation (3.3)-(3.4)	Equation (3.2)	Equation (3.2)
$\delta_{\rm s}$ at $R_{\rm cav}$ ($\delta_{\rm cav,s}$)	1	$\sim 10^{-5}$	1
$\delta_{\rm s}$ at $R_{\rm sub}$	$\sim 10^{-5} - 10^{-3}$	$\sim 10^{-5}$	1
$\Sigma_{\rm i,b}$ (or $\delta_{\rm b}$)	0	0	0
$h_{\rm s}$ at $R_{\rm sub}$	thinner	thicker	—
puffed up inner rim	no or little	little to heavy	—
observation[a]: SED	Y	Y	N
observation: sub-mm	Y	Y	Y
observation: NIR	Y	N	Y

[a] Whether or not these models can reproduce the signatures in various observations: the infrared deficit around 10 microns in SED, the central cavity in sub-mm images, and the smooth radial profile of NIR images.

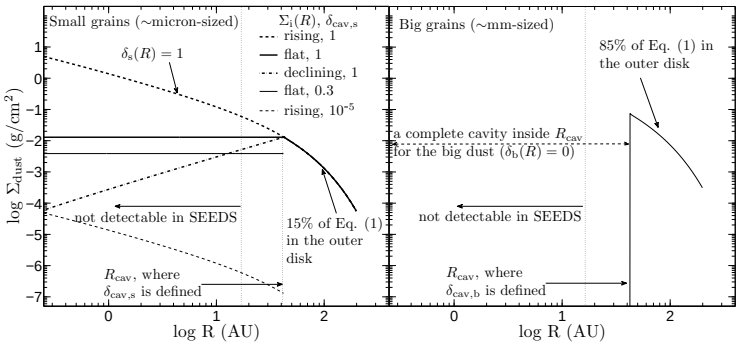

(a)

Figure 3.1 Various surface density profiles of the small dust (up to $\sim \mu$m-sized, left) and big dust (up to ∼mm-sized, right) in our model (gas-to-dust ratio is assumed to be 100:1 in this work). The big grains contain 85% of the dust mass outside the cavity, and are completely absent inside. The thick curves at $R < R_{\rm cav}$ in the left panel indicate three different $\Sigma_{\rm i}$ (rising, flat, and declining, as Equation (3.2)-(3.4), with names indicating their behavior when moving inward inside the cavity) for the small dust, all continous at the cavity edge ($\delta_{\rm cav,s} = 1$). The bottom thin dashed curve illustrates the surface density profile in typical A11 models, which have a uniformly heavily depleted cavity with $\delta_{\rm s} \approx 10^{-5}$, and the thin solid curve represents a slight small-grain depletion at the cavity edge ($\delta_{\rm cav,s} = 0.3$) with a flat $\Sigma_{\rm i}$. The vertical dotted curves indicate the cavity edge and typical SEEDS inner working angle ($\sim 0.1 - 0.15''$ or $\sim 15 - 20$ AU at Taurus). The labels on the axes are for Section 3 and 4.

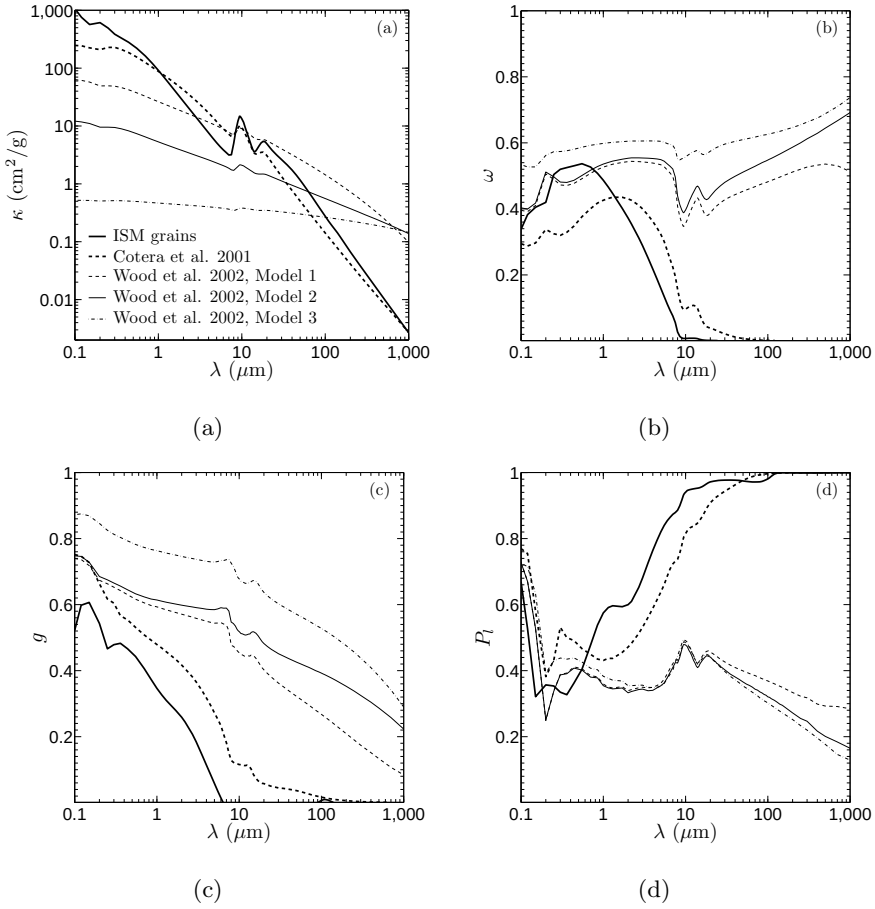

Figure 3.2 Dust properties of the grain models we use, showing opacity κ (a), albedo ω (b), average cosine scattering angle g (c), and maximum polarization P_l (d) (which typically occurs at a 90° scattering angle). The opacity is the dust+gas opacity assuming a gas-to-dust ratio of 100. Thick curves are for the small dust models, which dominate the scattered light due to their large scale height and NIR opacity. Thin curves are for the big dust models, which dominate the sub-mm emission due to their high opacity at these wavelengths. The solid curves are the fiducial choices in this work.

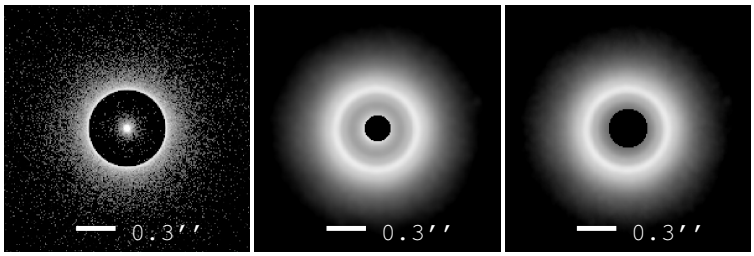

(a)

Figure 3.3 Simulated H band scattered light PI images for a face-on disk with a uniformly heavily depleted ($\delta_s \approx 10^{-5}$) cavity (see Section 3.2 for details), displayed with logarithmic stretches. The left panel shows the raw disk image from Whitney's radiative transfer simulation, the middle panel shows the unmasked image convolved with the HiCIAO PSF, and the right panel shows the convolved masked image (see Section 2.3 for details on the HiCIAO PSF). The cavity is 42 AU in radius ($\sim 0\farcs3$ at 140 pc), and the inner working angles are $\sim 0\farcs1$ without a coronagraph, and $\sim 0\farcs15$ with a coronagraph (the hole in the middle and right panels, respectively). The central surface brightness deficit and the bright ring at the cavity edge are prominent under both observation modes, which is qualitatively inconsistent with many SEEDS transitional disks observations. This indicates that the cavity is not heavily depleted in small dust.

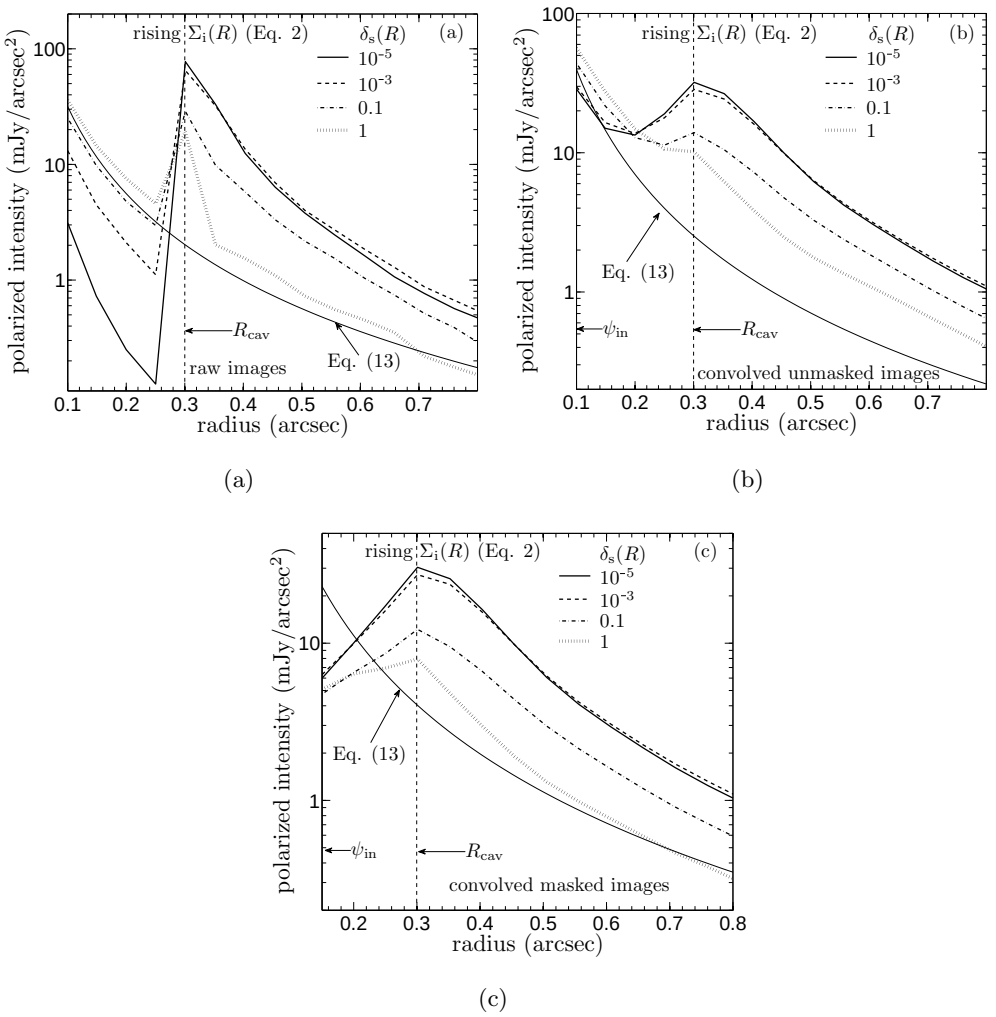

Figure 3.4 Surface brightness radial profiles of the raw images (a), convolved unmasked PI images (b), and convolved masked PI images (c), assuming a cavity completely devoid of large dust and uniformly depleted in small dust. The model with $\delta_s = 10^{-5}$ (thick solid curves) corresponds to Figure 3.3 and typical models in A11, while the $\delta_s = 1$ model (dotted curves) has no depletion in small grains at the cavity edge. The thin solid curves labeled as Equation (3.13) represent the scaling relation typical in SEEDS (with arbitrary normalization). The basic features of the uniformly heavily depleted models — an increase in intensity at the cavity edge and a drop inside — are inconsistent with typical SEEDS results, which smoothly increase in intensity up to the inner working angle.

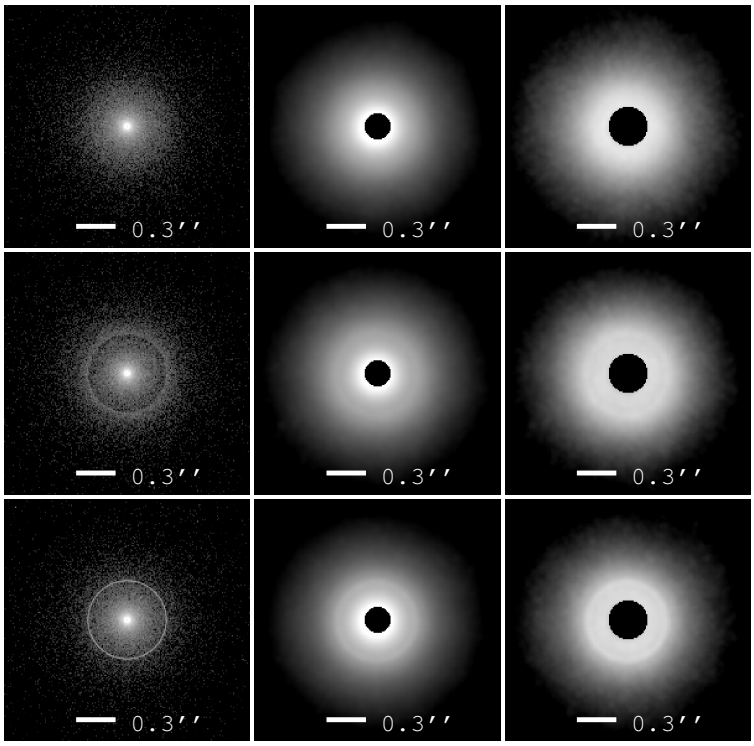

(a)

Figure 3.5 Simulated H band scattered light PI images for three face-on disks with a 42 AU cavity ($\sim 0\farcs3$ at 140 pc), which is devoid of big dust and filled with a uniform surface density of small dust (flat $\Sigma_{\rm i}$, Equation (3.3)), displayed with logarithmic stretches. Panels (from left to right) are raw images, convolved unmasked images, and convolved masked images (the same as in Figure 3.3). The top and middle rows show cavities undepleted and 70% depleted in small dust at the edge ($\delta_{\rm cav,s} = 1$ and $\delta_{\rm cav,s} = 0.3$, respectively), corresponding to the solid curves in Figure 3.3. The bottom row shows a cavity undepleted in small dust at the edge but with the cavity wall puffed up by 200%. For detailed model parameters see Section 3.2. Images in the top row are qualitatively similar to many SEEDS transitional disk observations in this sample, which are smooth on large scales and lack abrupt breaks or bumps at the cavity edge. Also, results show that both a modest surface density discontinuity (a 70% drop, middle row) and a puffed up cavity wall (bottom row) could well be visible.

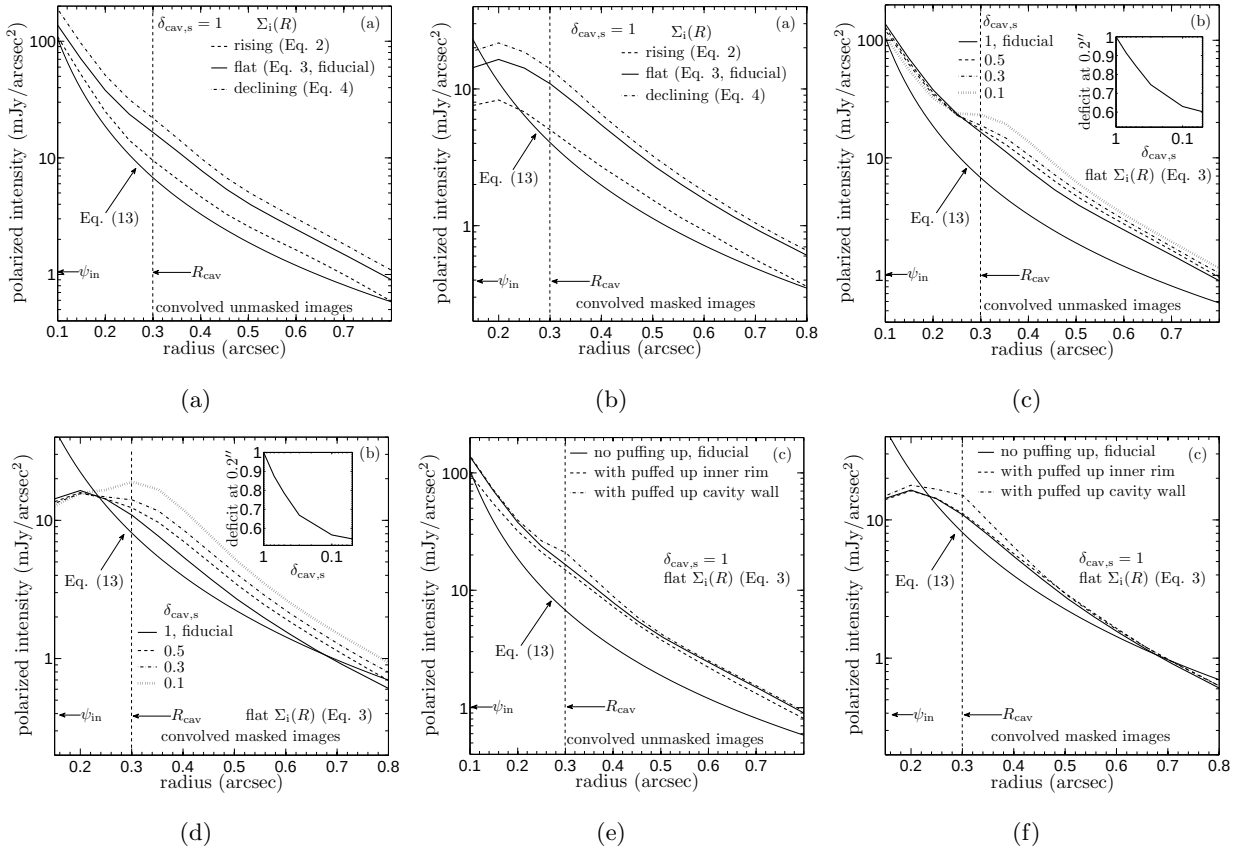

Figure 3.6 Surface brightness radial profiles of the convolved unmasked (left) and masked (right) PI images for the models in Section 3.2, showing the effect of $\Sigma_{\rm i}$ (a), $\delta_{\rm cav,s}$ (b), and the puffed up inner rim and cavity wall (c). The subpanel in panel (b) shows the relative flux deficit at $0\farcs2$ ($\frac{2}{3}R_{\rm cav}$) as a function of $\delta_{\rm cav,s}$ (Section 3.2). All models have no big dust inside the cavity. The curves labled "fiducial" are the same in all panels, which is from a model with flat $\Sigma_{\rm i}$, a continuous small dust surface density profile ($\delta_{\rm cav,s} = 1$), and no puffed up cavity wall (the top row in Figure 3.5). Results show that both a modest depletion in the small grains at $R_{\rm cav}$ and a puffed up cavity wall can add a bump to the originally smooth radial profile, while various forms of $\Sigma_{\rm i}$ with no discontinuity at $R_{\rm cav}$ produce similar surface brightness radial profile. Typical SEEDS results, as summarized in Section 1 and illustrated by the scaling relation (3.13) (with arbitrary normalization), is consistent with smooth small dust disks continuous in both surface density and scale height. The apparent inward surface brightness decrease near $\psi_{\rm in}$ in the masked images is a coronagraph edge effect (Section 3.2).

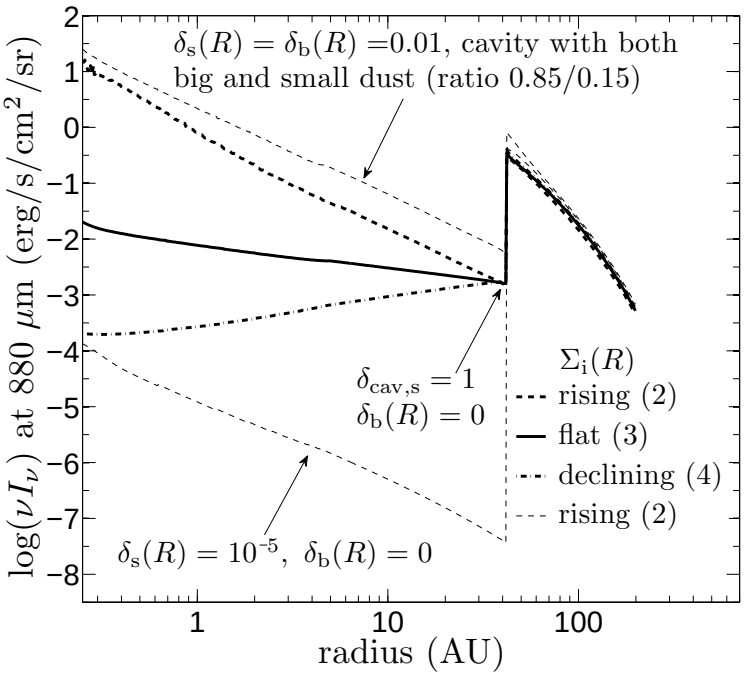

(a)

Figure 3.7 The 880 μm intensity $I_\nu(R)$ profile (Equation (3.14)) for disk models with various inner disk structures. The model for the top thin dashed curve has a uniformly depleted cavity with $\delta_s = \delta_b = 0.01$ (i.e. the same dust composition as the outer disk), in order to mimic a "mock" SMA upper limit on dust inside the cavity (A11), while all the other models have no big dust ($\sim$mm-sized) inside the cavity. The three thick curves are from models with different Σ_i and no discontinuity at the cavity edge, corresponding to the same curves in Figure 4.2 and panel (a) in Figure 3.6. The bottom thin dashed curve is from a model with a uniformly heavily depleted cavity ($\delta_s \approx 10^{-5}$). See Section 4.1 for details of the models. Qualitatively, the disk models with no big dust inside the cavity all produce a deficit in the intensity inside the cavity, since the small dust is very inefficient at sub-mm emission, and all are consistent with the mock upper limit set by the SMA results (A11).

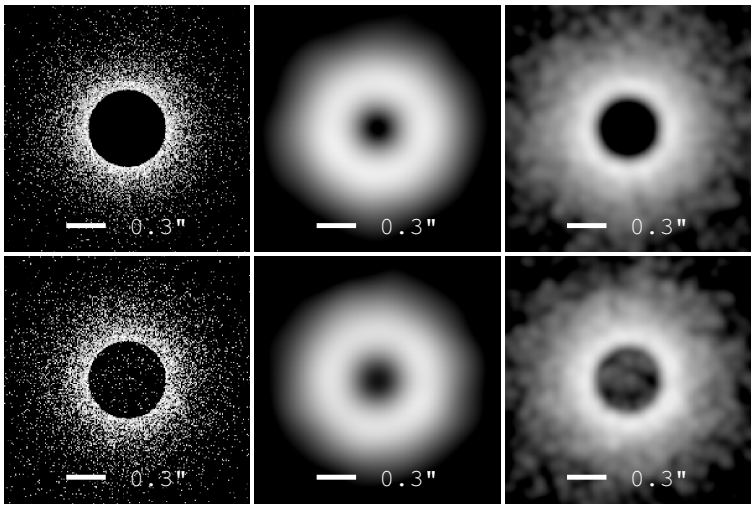

(a)

Figure 3.8 Narrow band 880μm images for two disk models with no big dust inside the cavity, displayed with logarithmic stretches. Panels are the raw images from the radiative transfer simulations (left), the processed imaged convolved with a Gaussian profile with resolution 0.″3 (middle), to mimic SMA observations (A11), and with resolution 0.″1 (right), to mimic ALMA observations. The top images are from the uniformly heavily depleted model in Figure 3.3 (rising $\Sigma_{\rm i}$ with $\delta_{\rm s} \approx 10^{-5}$, also the thin dashed curve in 3.7 and left panel in Figure 4.2). The bottom ones are from the same model as the top row in Figure 3.5 (also the thick solid curve in Figure 3.7 and left panel in Figure 4.2), which has a continuous distribution for the small dust ($\delta_{\rm cav,s} = 1$) with flat $\Sigma_{\rm i}$ (Equation (3.3)). See Section 4.2 for details of the models. The two models produce similar sub-mm images but very different NIR scattered light images (Figure 3.3 and 3.5). The bottom right panel shows that with its exceptional spatial resolution ($\sim$ 0.″1 or better), ALMA may reveal a sharper edge of the cavity and resolve the small sub-mm emission inside the cavity, which are the keys in a better understanding of the spatial distribution of the grains.

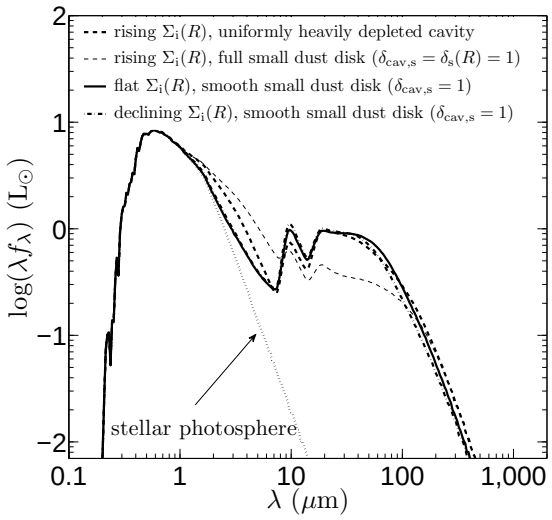

(a)

Figure 3.9 The SED for four disk+cavity models. The uniformly heavily depleted model is motivated by A11, which has an inner cavity with $\delta_s \approx 10^{-5}$, rising Σ_i, and puffed up inner rim and cavity wall. The full small dust disk model (the thin dashed curve) has otherwise identical properties but with the small dust cavity being uniformly filled up ($\delta_s = 1$). The other two smooth small dust disk models have $\delta_{cav,s} = 1$ (no discontinuity at the cavity edge) and no puffed up inner rim or wall. See Section 5.1 for detailed parameters in these models. The three thick curves show the parameter degeneracy in producing the SED — diving to roughly the same depth at NIR and coming back to the same level at MIR, as the signature of transitional disks. The full small dust disk model shows that increasing surface density at small radii would eventually wipe out the distinctive deficit in the NIR, and the resulting SED gradually evolves to a full-disk-like SED.

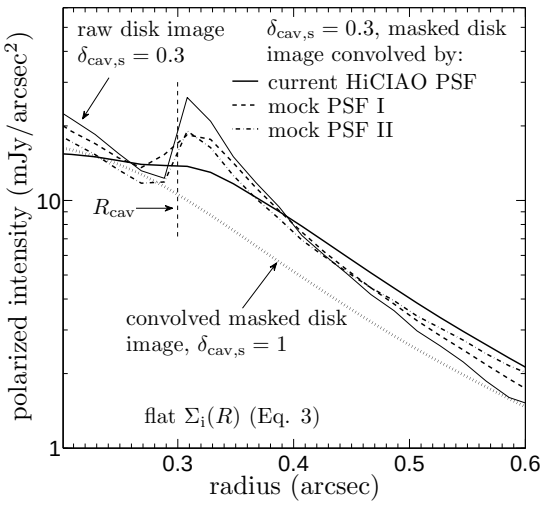

(a)

Figure 3.10 Examples of the power of the optimal performances of the next generation instruments in NIR imaging (such as the SCExAO on Subaru and thirty meter class telescopes). The thick solid, dashed, and dot-dashed curves show the surface brightness radial profile of several H band masked disk images convolved from the *same* raw image by several *different* PSF (indicated by the legend, see Section 6.3 for details). The base model corresponds to the middle row in Figure 3.5, which has a $0\farcs3$ radius cavity, flat $\Sigma_{\rm i}$, and $\delta_{\rm cav,s} = 0.3$ (a 70% drop in $\Sigma_{\rm s}$ at $R_{\rm cav}$). No coronagraph stellar residual (see Section 2.3) is added in order to isolate the effect of the PSF, and we bin the images into annulus $0\farcs02$ in width for better illustration. For comparision, the thin solid line is for the raw (unconvolved) image, and the dotted line is from the corresponding full small dust disk model (i.e. the top row in Figure 3.5). These examples show that with the ability of next generation instruments expected in the next decade or so, the transition of the spatial distribution of the small dust at the cavity edge could be constrained much better.

Bibliography

Adame, L., Calvet, N., Luhman, K. L., D'Alessio, P., Furlan, E., McClure, M. K., Hartmann, L., Forrest, W. J., & Watson, D. M. 2011, ApJ, 726, L3

Adelman, S. J., Gulliver, A. F., Smalley, B., Pazder, J. S., Younger, P. F., Boyd, L. J., Epand, D., & Younger, T. 2007, in Astronomical Society of the Pacific Conference Series, Vol. 364, The Future of Photometric, Spectrophotometric and Polarimetric Standardization, ed. C. Sterken, 255

Akeson, R. L., Walker, C. H., Wood, K., Eisner, J. A., Scire, E., Penprase, B., Ciardi, D. R., van Belle, G. T., Whitney, B., & Bjorkman, J. E. 2005, ApJ, 622, 440

Andrews, S. M. & Williams, J. P. 2007, ApJ, 659, 705

Andrews, S. M., Wilner, D. J., Espaillat, C., Hughes, A. M., Dullemond, C. P., McClure, M. K., Qi, C., & Brown, J. M. 2011, ApJ, 732, 42

Andrews, S. M., Wilner, D. J., Hughes, A. M., Qi, C., & Dullemond, C. P. 2009, ApJ, 700, 1502

Birnstiel, T., Ricci, L., Trotta, F., Dullemond, C. P., Natta, A., Testi, L., Dominik, C., Henning, T., Ormel, C. W., & Zsom, A. 2010, A&A, 516, L14

Brauer, F., Dullemond, C. P., & Henning, T. 2008, A&A, 480, 859

Calvet, N., D'Alessio, P., Watson, D. M., Franco-Hernández, R., Furlan, E., Green, J., Sutter, P. M., Forrest, W. J., Hartmann, L., Uchida, K. I., Keller, L. D., Sargent, B., Najita, J., Herter, T. L., Barry, D. J., & Hall, P. 2005, ApJ, 630, L185

Chiang, E. I. & Goldreich, P. 1997, ApJ, 490, 368

Cotera, A. S., Whitney, B. A., Young, E., Wolff, M. J., Wood, K., Povich, M., Schneider, G., Rieke, M., & Thompson, R. 2001, ApJ, 556, 958

D'Alessio, P., Calvet, N., Hartmann, L., Franco-Hernández, R., & Servín, H. 2006, ApJ, 638, 314

Dullemond, C. P. & Dominik, C. 2004a, A&A, 417, 159

Dullemond, C. P. & Dominik, C. 2004b, A&A, 421, 1075

Dullemond, C. P. & Dominik, C. 2005, A&A, 434, 971

Dullemond, C. P., Dominik, C., & Natta, A. 2001, ApJ, 560, 957

Espaillat, C., Calvet, N., D'Alessio, P., Hernández, J., Qi, C., Hartmann, L., Furlan, E., & Watson, D. M. 2007, ApJ, 670, L135

Espaillat, C., Calvet, N., Luhman, K. L., Muzerolle, J., & D'Alessio, P. 2008, ApJ, 682, L125

Espaillat, C., D'Alessio, P., Hernández, J., Nagel, E., Luhman, K. L., Watson, D. M., Calvet, N., Muzerolle, J., & McClure, M. 2010, ApJ, 717, 441

Espaillat, C., Furlan, E., D'Alessio, P., Sargent, B., Nagel, E., Calvet, N., Watson, D. M., & Muzerolle, J. 2011, ApJ, 728, 49

Follette, K. B., Tamura, M., Hashimoto, J., Whitney, B., Grady, C., Close, L., Andrews, S. M., Kwon, J., Wisniewski, J., Brandt, T. D., Mayama, S., Kandori, R., Dong, R., Abe, L., Brandner, W., Carson, J., Currie, T., Egner, S. E., Feldt, M., Goto, M., Guyon, O., Hayano, Y., Hayashi, M., Hayashi, S., Henning, T., Hodapp, K., Ishii, M., Iye, M., Janson, M., Knapp, G. R., Kudo, T., Kusakabe, N., Kuzuhara, M., McElwain, M. W., Matsuo, T., Miyama, S., Morino, J.-I., Moro-Martin, A., Nishimura, T., Pyo, T.-S., Serabyn, E., Suto, H., Suzuki, R., Takami, M., Takato, N., Terada, H., Thalmann, C., Tomono, D., Turner, E. L., Watanabe, M., Yamada, T., Takami, H., & Usuda, T. 2013, ApJ, 767, 10

Furlan, E., Luhman, K. L., Espaillat, C., D'Alessio, P., Adame, L., Manoj, P., Kim, K. H., Watson, D. M., Forrest, W. J., McClure, M. K., Calvet, N., Sargent, B. A., Green, J. D., & Fischer, W. J. 2011, ApJS, 195, 3

Garaud, P. 2007, ApJ, 671, 2091

Grady, C. A., Schneider, G., Sitko, M. L., Williger, G. M., Hamaguchi, K., Brittain, S. D., Ablordeppey, K., Apai, D., Beerman, L., Carpenter, W. J., Collins, K. A., Fukagawa, M., Hammel, H. B., Henning, T., Hines, D., Kimes, R., Lynch, D. K., Ménard, F., Pearson, R., Russell, R. W., Silverstone, M., Smith, P. S., Troutman, M., Wilner, D., Woodgate, B., & Clampin, M. 2009, ApJ, 699, 1822

Guyon, O., Martinache, F., Clergeon, C., Russell, R., Groff, T., & Garrel, V. 2011, in Society of Photo-Optical Instrumentation Engineers (SPIE) Conference Series, Vol. 8149, Society of Photo-Optical Instrumentation Engineers (SPIE) Conference Series

Hartmann, L., Calvet, N., Gullbring, E., & D'Alessio, P. 1998, ApJ, 495, 385

Hashimoto, J., Tamura, M., Muto, T., Kudo, T., Fukagawa, M., Fukue, T., Goto, M., Grady, C. A., Henning, T., Hodapp, K., Honda, M., Inutsuka, S., Kokubo, E., Knapp, G., McElwain, M. W., Momose, M., Ohashi, N., Okamoto, Y. K., Takami, M., Turner, E. L., Wisniewski, J., Janson, M., Abe, L., Brandner, W., Carson, J., Egner, S., Feldt, M., Golota, T., Guyon, O., Hayano, Y., Hayashi, M., Hayashi, S., Ishii, M., Kandori, R., Kusakabe, N., Matsuo, T., Mayama, S., Miyama, S., Morino, J.-I., Moro-Martin, A., Nishimura, T., Pyo, T.-S., Suto, H., Suzuki, R., Takato, N., Terada, H., Thalmann, C., Tomono, D., Watanabe, M., Yamada, T., Takami, H., & Usuda, T. 2011, ApJ, 729, L17

Hinkley, S., Oppenheimer, B. R., Soummer, R., Brenner, D., Graham, J. R., Perrin, M. D., Sivaramakrishnan, A., Lloyd, J. P., Roberts, Jr., L. C., & Kuhn, J. 2009, ApJ, 701, 804

Ho, P. T. P., Moran, J. M., & Lo, K. Y. 2004, ApJ, 616, L1

Inoue, A. K., Honda, M., Nakamoto, T., & Oka, A. 2008, PASJ, 60, 557

Isella, A. & Natta, A. 2005, A&A, 438, 899

Jang-Condell, H. & Sasselov, D. D. 2003, ApJ, 593, 1116

Kim, S.-H., Martin, P. G., & Hendry, P. D. 1994, ApJ, 422, 164

Marois, C., Doyon, R., Racine, R., & Nadeau, D. 2000, PASP, 112, 91

Marois, C., Lafrenière, D., Doyon, R., Macintosh, B., & Nadeau, D. 2006, ApJ, 641, 556

Murakami, N., Guyon, O., Martinache, F., Matsuo, T., Yokochi, K., Nishikawa, J., Tamura, M., Kurokawa, T., Baba, N., Vogt, F., Garrel, V., & Yoshikawa, T. 2010, in Society of Photo-Optical Instrumentation Engineers (SPIE) Conference Series, Vol. 7735, Society of Photo-Optical Instrumentation Engineers (SPIE) Conference Series

Muto, T. 2011, ApJ, 739, 10

Muto, T., Grady, C. A., Hashimoto, J., Fukagawa, M., Hornbeck, J. B., Sitko, M., Russell, R., Werren, C., Curé, M., Currie, T., Ohashi, N., Okamoto, Y., Momose, M., Honda, M., Inutsuka, S., Takeuchi, T., Dong, R., Abe, L., Brandner, W., Brandt, T., Carson, J., Egner, S., Feldt, M., Fukue, T., Goto, M., Guyon, O., Hayano, Y., Hayashi, M., Hayashi, S., Henning, T., Hodapp, K. W., Ishii, M., Iye, M., Janson, M., Kandori, R., Knapp, G. R., Kudo, T., Kusakabe, N., Kuzuhara, M., Matsuo, T., Mayama, S., McElwain, M. W., Miyama, S., Morino, J.-I., Moro-Martin, A., Nishimura, T., Pyo, T.-S., Serabyn, E., Suto, H., Suzuki, R., Takami, M., Takato, N., Terada, H., Thalmann, C., Tomono, D., Turner, E. L., Watanabe, M., Wisniewski, J. P., Yamada, T., Takami, H., Usuda, T., & Tamura, M. 2012, ApJ, 748, L22

Paardekooper, S.-J. & Mellema, G. 2006, A&A, 453, 1129

Perrin, M. D., Graham, J. R., Kalas, P., Lloyd, J. P., Max, C. E., Gavel, D. T., Pennington, D. M., & Gates, E. L. 2004, Science, 303, 1345

Petrov, R. G., Malbet, F., Weigelt, G., Antonelli, P., Beckmann, U., Bresson, Y., Chelli, A., Dugué, M., Duvert, G., Gennari, S., Glück, L., Kern, P., Lagarde, S., Le Coarer, E., Lisi, F., Millour, F., Perraut, K., Puget, P., Rantakyrö, F., Robbe-Dubois, S., Roussel, A., Salinari, P., Tatulli, E., Zins, G., Accardo, M., Acke, B., Agabi, K., Altariba, E., Arezki, B., Aristidi, E., Baffa, C., Behrend, J., Blöcker, T., Bonhomme, S., Busoni, S., Cassaing, F., Clausse, J.-M., Colin, J., Connot, C., Delboulbé, A., Domiciano de Souza, A., Driebe, T., Feautrier, P., Ferruzzi, D., Forveille, T., Fossat, E., Foy, R., Fraix-Burnet, D., Gallardo, A., Giani, E., Gil, C., Glentzlin, A., Heiden, M., Heininger, M., Hernandez Utrera, O., Hofmann, K.-H., Kamm, D., Kiekebusch, M., Kraus, S., Le Contel, D., Le Contel, J.-M., Lesourd, T., Lopez, B., Lopez, M., Magnard, Y., Marconi, A., Mars, G., Martinot-Lagarde, G., Mathias, P., Mège, P., Monin, J.-L., Mouillet, D., Mourard, D., Nussbaum, E., Ohnaka, K., Pacheco, J., Perrier, C., Rabbia, Y., Rebattu, S., Reynaud, F., Richichi, A., Robini, A., Sacchettini, M., Schertl, D., Schöller, M., Solscheid, W., Spang, A., Stee, P., Stefanini, P., Tallon, M., Tallon-Bosc, I., Tasso, D., Testi, L., Vakili, F., von der Lühe, O., Valtier, J.-C., Vannier, M., & Ventura, N. 2007, A&A, 464, 1

Pott, J.-U., Woillez, J., Akeson, R. L., Berkey, B., Colavita, M. M., Cooper, A., Eisner, J. A., Ghez, A. M., Graham, J. R., Hillenbrand, L., Hrynewych, M., Medeiros, D., Millan-Gabet, R., Monnier, J., Morrison, D., Panteleeva, T., Quataert, E., Randolph, B., Smith, B., Summers, K., Tsubota, K., Tyau, C., Weinberg, N., Wetherell, E., & Wizinowich, P. L. 2009, New A Rev., 53, 363

Quanz, S. P., Schmid, H. M., Geissler, K., Meyer, M. R., Henning, T., Brandner, W., & Wolf, S. 2011, ApJ, 738, 23

Rice, W. K. M., Armitage, P. J., Wood, K., & Lodato, G. 2006, MNRAS, 373, 1619

Robitaille, T. P., Whitney, B. A., Indebetouw, R., Wood, K., & Denzmore, P. 2006, ApJS, 167, 256

Skrutskie, M. F., Dutkevitch, D., Strom, S. E., Edwards, S., Strom, K. M., & Shure, M. A. 1990, AJ, 99, 1187

Strom, K. M., Strom, S. E., Edwards, S., Cabrit, S., & Skrutskie, M. F. 1989, AJ, 97, 1451

Suzuki, R., Kudo, T., Hashimoto, J., Carson, J., Egner, S., Goto, M., Hattori, M., Hayano, Y., Hodapp, K., Ito, M., Iye, M., Jacobson, S., Kandori, R., Kusakabe, N., Kuzuhara, M., Matsuo, T., McElwain, M., Morino, J.-I., Oya, S., Saito, Y., Shelton, R., Stahlberger, V., Suto, H., Takami, H., Thalmann, C., Watanabe, M., Yamada, H., & Tamura, M. 2010, in Society of Photo-Optical Instrumentation Engineers (SPIE) Conference Series, Vol. 7735, Society of Photo-Optical Instrumentation Engineers (SPIE) Conference Series

Tamura, M. 2009, in American Institute of Physics Conference Series, Vol. 1158, American Institute of Physics Conference Series, ed. T. Usuda, M. Tamura, & M. Ishii, 11–16

Tanii, R., Itoh, Y., Kudo, T., Hioki, T., Oasa, Y., Gupta, R., Sen, A. K., Wisniewski, J. P., Muto, T., Grady, C. A., Hashimoto, J., Fukagawa, M., Mayama, S., Hornbeck, J., Sitko, M. L., Russell, R. W., Werren, C., Curé, M., Currie, T., Ohashi, N., Okamoto, Y., Momose, M., Honda, M., Inutsuka, S.-i., Takeuchi, T., Dong, R., Abe, L., Brandner, W., Brandt, T. D., Carson, J., Egner, S. E., Feldt, M., Fukue, T., Goto, M., Guyon, O., Hayano, Y., Hayashi, M., Hayashi, S. S., Henning, T., Hodapp, K. W., Ishii, M., Iye, M., Janson, M., Kandori, R., Knapp, G. R., Kusakabe, N., Kuzuhara, M., Matsuo, T., McElwain, M. W., Miyama, S., Morino, J.-i., Moro-Martín, A., Nishimura, T., Pyo, T.-S., Serabyn, E., Suto, H., Suzuki, R., Takami, M., Takato, N., Terada, H., Thalmann, C., Tomono, D., Turner, E. L., Watanabe, M., Yamada, T., Takami, H., Usuda, T., & Tamura, M. 2012, PASJ, 64, 124

Tatulli, E., Millour, F., Chelli, A., Duvert, G., Acke, B., Hernandez Utrera, O., Hofmann, K.-H., Kraus, S., Malbet, F., Mège, P., Petrov, R. G., Vannier, M., Zins, G., Antonelli, P., Beckmann, U., Bresson, Y., Dugué, M., Gennari, S., Glück, L., Kern, P., Lagarde, S., Le Coarer, E., Lisi, F., Perraut, K., Puget, P., Rantakyrö, F., Robbe-Dubois, S., Roussel, A., Weigelt, G., Accardo, M., Agabi, K., Altariba, E., Arezki, B., Aristidi, E., Baffa, C., Behrend, J., Blöcker, T., Bonhomme, S., Busoni, S., Cassaing, F., Clausse, J.-M., Colin, J., Connot, C., Delboulbé, A., Domiciano de Souza, A., Driebe, T., Feautrier, P., Ferruzzi, D., Forveille, T., Fossat, E., Foy, R., Fraix-Burnet, D., Gallardo, A., Giani, E., Gil, C., Glentzlin, A., Heiden, M., Heininger, M., Kamm, D., Kiekebusch, M., Le Contel, D., Le Contel, J.-M., Lesourd, T., Lopez, B., Lopez, M., Magnard, Y., Marconi, A., Mars, G., Martinot-Lagarde, G., Mathias, P., Monin, J.-L., Mouillet, D., Mourard, D., Nussbaum, E., Ohnaka, K., Pacheco, J., Perrier, C., Rabbia, Y., Rebattu, S., Reynaud, F., Richichi, A., Robini, A., Sacchettini, M., Schertl, D., Schöller, M., Solscheid, W., Spang, A., Stee, P., Stefanini, P., Tallon, M., Tallon-Bosc, I., Tasso, D., Testi, L., Vakili, F., von der Lühe, O., Valtier, J.-C., & Ventura, N. 2007, A&A, 464, 29

Thalmann, C., Grady, C. A., Goto, M., Wisniewski, J. P., Janson, M., Henning, T., Fukagawa, M., Honda, M., Mulders, G. D., Min, M., Moro-Martín, A., McElwain, M. W., Hodapp, K. W., Carson, J., Abe, L., Brandner, W., Egner, S., Feldt, M., Fukue, T., Golota, T., Guyon, O.,

Hashimoto, J., Hayano, Y., Hayashi, M., Hayashi, S., Ishii, M., Kandori, R., Knapp, G. R., Kudo, T., Kusakabe, N., Kuzuhara, M., Matsuo, T., Miyama, S., Morino, J.-I., Nishimura, T., Pyo, T.-S., Serabyn, E., Shibai, H., Suto, H., Suzuki, R., Takami, M., Takato, N., Terada, H., Tomono, D., Turner, E. L., Watanabe, M., Yamada, T., Takami, H., Usuda, T., & Tamura, M. 2010, ApJ, 718, L87

Thalmann, C., Janson, M., Buenzli, E., Brandt, T. D., Wisniewski, J. P., Moro-Martín, A., Usuda, T., Schneider, G., Carson, J., McElwain, M. W., Grady, C. A., Goto, M., Abe, L., Brandner, W., Dominik, C., Egner, S., Feldt, M., Fukue, T., Golota, T., Guyon, O., Hashimoto, J., Hayano, Y., Hayashi, M., Hayashi, S., Henning, T., Hodapp, K. W., Ishii, M., Iye, M., Kandori, R., Knapp, G. R., Kudo, T., Kusakabe, N., Kuzuhara, M., Matsuo, T., Miyama, S., Morino, J.-I., Nishimura, T., Pyo, T.-S., Serabyn, E., Suto, H., Suzuki, R., Takahashi, Y. H., Takami, M., Takato, N., Terada, H., Tomono, D., Turner, E. L., Watanabe, M., Yamada, T., Takami, H., & Tamura, M. 2011, ApJ, 743, L6

Whitney, B. A., Wood, K., Bjorkman, J. E., & Cohen, M. 2003a, ApJ, 598, 1079

Whitney, B. A., Wood, K., Bjorkman, J. E., & Wolff, M. J. 2003b, ApJ, 591, 1049

Williams, J. P. & Cieza, L. A. 2011, ARA&A, 49, 67

Wood, K., Wolff, M. J., Bjorkman, J. E., & Whitney, B. 2002, ApJ, 564, 887

Zhu, Z., Nelson, R. P., Dong, R., Espaillat, C., & Hartmann, L. 2012, ApJ, 755, 6

Zhu, Z., Nelson, R. P., Hartmann, L., Espaillat, C., & Calvet, N. 2011, ApJ, 729, 47

Chapter 4

The Structure of Transitional Disks PDS 70

Abstract

Through detailed radiative transfer modeling, we present a disk+cavity model to simultaneously explain both the SED and Subaru H-band polarized light imaging for the pre-transitional protoplanetary disk PDS 70. Particularly, we are able to match not only the radial dependence, but also the absolute scale, of the surface brightness of the scattered light. Our disk model has a cavity 65 AU in radius, which is heavily depleted of sub-micron-sized dust grains, and a small residual inner disk which produces a weak but still optically thick NIR excess in the SED. To explain the contrast of the cavity edge in the Subaru image, a factor of $\sim$1000 depletion for the sub-micron-sized dust inside the cavity is required. The total dust mass of the disk may be on the order of $10^{-4} M_{\odot}$, only weakly constrained due to the lack of long wavelength observations and the uncertainties in the dust model. The scale height of the sub-micron-sized dust is ~ 6 AU at the cavity edge, and the cavity wall is optically thick in the vertical direction at H-band. If future observations at longer wavelengths reveal the cavity in the $\sim$millimeter-sized grains, then PDS 70 would not be a member of the class of (pre-)transitional disks identified by Dong et al. (2012), whose members only show evidence of the cavity in the millimeter-sized dust but not the sub-micron-sized dust in resolved images. The two classes of (pre-)transitional disks may form through different mechanisms, or they may just be at different evolution stages in the disk clearing process.

1 Introduction

Recent years have witnessed a rising interest in a special kind of protoplanetary disks, in which a giant central cavity is present and reveals itself in the spectral energy distribution (SED, i.e. Strom et al. 1989; Skrutskie et al. 1990; Calvet et al. 2005; Furlan et al. 2006; Espaillat et al. 2007a,b, 2008), or in sub-mm interferometry observations (i.e. Piétu et al. 2006; Hughes et al. 2007; Brown et al. 2009; Hughes et al. 2009; Isella et al. 2010; Andrews et al. 2011; Mathews et al. 2012; Cieza et al. 2012b; Isella et al. 2012; Andrews et al. 2012. Depending on whether a small residual optically thick inner disk is left at the center, these objects could be classified into two categories — pre-transitional disks (with an optically thick residual inner disk, Espaillat et al. 2010), and transitional disks (without an optically thick residual inner disk, Espaillat et al. 2007b). Studying these objects at multiple wavelengths is of great interests, because the inner disk clearing process may be signposts of planet formation and disk evolution in general (Zhu et al., 2011; Williams & Cieza, 2011; Dodson-Robinson & Salyk, 2011; Birnstiel et al., 2012; Cieza et al., 2012a).

So far, the study of (pre-)transitional disks was done primarily via measurements of the SED and resolved images at sub-mm wavelengths. More recently, direct imaging at optical to near

infrared (NIR) started playing a crucial role. Protoplanetary disks usually have dust grains with sizes ranging from sub-micron (called small dust in this study), similar to the pristine interstellar medium (ISM) dust, to mm or larger (big dust), forming as a result of grain growth and coagulation (Dullemond & Dominik, 2005; Birnstiel et al., 2012). The SED of a disk is degenerate with many disk parameters, since it is spatially integrated over the entire disk. Resolved images at sub-mm, on the other hand, provide more detailed information, but they are only sensitive to the distribution of big dust due to its dominance in opacity at these wavelengths. Using 8-m class ground based telescopes equipped with Adaptive Optics and/or coronagraph system, direct imaging at optical to NIR wavelengths provides resolved disk maps with high spatial resolution ($\sim 0.06''$) and small inner working angle ($\lesssim 0.2''$). These maps are directly related to the distribution of small dust.

An ongoing survey scale project, the Strategic Explorations of Exoplanets and Disks with Subaru (SEEDS, Tamura 2009), is directly imaging a large sample of protoplanetary disks at NIR (J, H, and K) bands in a systematic way, using the High-Contrast Coronographic Imager for Adaptive Optics (HiCIAO, Suzuki et al. 2010). SEEDS disk observations specialize in taking polarized intensity (PI=$\sqrt{Q^2+U^2}$, which Q and U are components in the Stokes vector) images of disks, which greatly enhances our ability to probe disk structure (especially at the inner part), by utilizing the fact that the central source is usually not polarized, so that the stellar residual in PI images is much smaller than in full intensity (FI) images (Perrin et al., 2004; Hinkley et al., 2009; Quanz et al., 2011). The signal in NIR imaging usually comes from scattering of starlight off the surface of the disk, since dust at separations of ~ 10 AU in the disk is not hot enough to contribute significantly at NIR wavelengths. A number of protoplanetary disks have been studied in SEEDS (LkCa 15, Thalmann et al. 2010, AB Aur, Hashimoto et al. 2011, SAO 206462, Muto et al. 2012, MWC 480, Kusakabe et al. 2012, and UX Tau A, Tanii et al. 2012), and more are on the way.

Recently, Dong et al. (2012, chapter 3) pointed out that in a large sample of (pre-)transitional disks whose central cavity have been confirmed in resolved images at sub-mm, SEEDS did not find the cavities in their NIR images. This discrepancy has been interpreted as evidence for the cavity existence *only in big dust*, with the small dust having a *continuous* distribution in surface density from the outer disk all the way to the inner working angle of SEEDS ($\sim 0\farcs1 - 0\farcs15$, or about $\sim 15 - 20$ AU in Taurus). This may be explained by the dust filtration model proposed by Paardekooper & Mellema (2006); Rice et al. (2006); Zhu et al. (2012). In their model, the pressure bump in the disk acts like a filter, which filters through the small dust but traps the big dust, resulting in the depletion of big dust inside the cavity.

In this chapter, we study the structure of the pre-transitional disk PDS 70 using detailed radiative transfer modeling, following the observational paper by Hashimoto et al. (2012). PDS 70 is a K5 type weak-lined T Tauri star located at the Centaurus star-forming region (coordinate 14 08 10.15 -41 23 52.5), with an age $<$ 10Myr and a distance estimated to be $\sim$ 140pc (Gregorio-Hetem & Hetem, 2002; Riaud et al., 2006; Metchev et al., 2004; Hashimoto et al., 2012). The photometry of this star has been measured at multiple wavelengths (i.e. Metchev et al. 2004; Kessler-Silacci et al. 2005), and its disk has been detected in scattered light by VLT K-band imaging (Riaud et al., 2006). SEEDS directly imaged PDS 70 in H-band using the polarization differential imaging (PDI) mode on Feb. 27, 2012. The Subaru observation and the data reduction were described in detail in Hashimoto et al. (2012, which also presented the Gemini L'-band imaging). Unlike most previous objects of this type, the cavity in PDS 70 is *first* detected

by SEEDS NIR imaging. And unlike the objects in chapter 3, it indeed has a cavity in the small dust, which also contradicts the predictions in various dust filtration models mentioned above.

Radiative transfer modeling of (pre-)transitional disks has been mostly used to fit the SED and sub-mm observations in the past (i.e. Hughes et al. 2009; Andrews et al. 2011; Mathews et al. 2012; Andrews et al. 2012). Here we demonstrate the power of modeling in NIR, by producing synthetic disk images in scattered light and comparing them with observations. Sensitive to dust at different sizes and locations, SED, sub-mm observations, and NIR imaging can be used to probe the disk structure in different and complementary ways. Particularly, NIR imaging can provide effective constraints on the scale height of the disk, and the depletion factor for the small dust inside the cavity, neither of which is well constrained using the other two types of observations (Andrews et al., 2011, chapter 3).

The chapter is arranged in the following way. In Section 2 we introduce the method for our radiative transfer modeling. The fiducial model of PDS 70 is presented in Section 3, where we simultaneously fit both its SED and scattered light image. The constraints on various disk+cavity parameters from current observations are discussed in Section 4, where we focus on the ones which are directly probed by NIR imaging and are important in revealing the disk evolution. We discuss the possible formation mechanisms of (pre-)transitional disks in Section 5, followed by a short summary in Section 6.

2 Radiative transfer modeling

We use the Monte Carlo radiative transfer (MCRT) code developed by B. Whitney (2012, in prep. see also Whitney et al. 2003b,a; Robitaille et al. 2006) to model the SED and SEEDS H-band PI imaging of PDS 70. The SED data collected from literature, the SEEDS observation, and its data reduction are described in detail in Hashimoto et al. (2012). MCRT simulations are run with 4×10^7 photons for high S/N images. Disk setup is largely adopted from the model in chapter 3, which is briefly summarized here. We construct an axisymmetric disk 200 AU in radius on a 600×200 grid in spherical coordinates (R, θ), where R is the radial component and θ is the poloidal component ($\theta = 0^\circ$ is the disk mid-plane). We uniformly deplete the central region of the disk to form a cavity with radius $R_{\rm cav}$, i.e. reduce dust surface density by a constant factor within this radius. The disk is assumed to be at $\sim$140 pc. The inner radius of the disk (within the cavity) is self-consistently determined by dust sublimation ($T_{\rm sub} \sim 1600$ K). The accretion rate of PDS 70 is considered to be very low, since the object has been identified as a weak line T Tauri object with an Hα equivalent width of 2Å (Gregorio-Hetem & Hetem, 2002). For the central source, we assume a pre-main sequence star of spectral type K5, radius 1.35 $R_\odot$, mass 1.0 $M_\odot$, and temperature 4500 K, as suggested by Gregorio-Hetem & Hetem (2002). The surface density $\Sigma(R)$ in the outer disk is taken as

$$\Sigma(R) = \Sigma_0 \frac{R_c}{R} e^{-R/R_c}, \text{ at } R \geq R_{\rm cav}, \tag{4.1}$$

where R_c is a characteristic scaling length assumed to be 50 AU, and the normalization Σ_0 is determined by the total dust mass of the disk $M_{\rm dust}$. The choices of the surface density radial profile and R_c are common in protoplanetary disk modeling (Williams & Cieza, 2011; Andrews et al., 2011), and represent a snapshot of a solution for a fully viscous disk with a constant α parameter (as in Shakura & Sunyaev 1973 α disk model) and $T \propto R^{-1/2}$ (Hartmann et al., 1998).

Inside the cavity, the disk is uniformly depleted, with surface density going as

$$\Sigma(R) = \delta_{\rm cav}\Sigma_0 \frac{R_c}{R} e^{-R/R_c}, \text{ at } R < R_{\rm cav}, \tag{4.2}$$

where $\delta_{\rm cav}$ is the constant depletion factor (which may be different for different dust populations).

Various grain evolution models predict that the pristine dust grains in the disk coagulate, grow to bigger size, and subsequently settle to the disk mid-plane (Dullemond & Dominik, 2004a,b, 2005). To take this effect into account, we assume a two component model of dust distribution: a thick disk with small grains (sub-micron-sized), and a thin disk with large grains (up to ∼mm-sized). Below we will use subscripts "b" and "s" for various quantities relating to big and small dust, respectively, and superscripts "o" and "c" to indicate the outer disk and the cavity, respectively (for example, Σ_s^c represents the surface density of the small dust inside the cavity). Both big and small grains are assumed to have a Gaussian density profile in the vertical direction,

$$\rho(R,z) = \frac{\Sigma(R)}{\sqrt{2\pi}h} e^{-z^2/2h^2}, \tag{4.3}$$

where h is the scale height, with $h_{\rm b}$ (scale height of the big dust) assumed to be much smaller than $h_{\rm s}$ (scale height of the small dust). We note that the scale heights are provided to the code as input parameters, instead of being self-consistently determined from the disk temperature calculated in the simulations. In our fiducial model shown below, we check this assumption and find that the input is consistent with the output (Section 3). Radially, both scale heights vary with radius as

$$h \propto R^{\beta}, \tag{4.4}$$

where β is the constant power law index. Our experiments show that as long as the big dust is settled to the disk mid-plane (i.e. $h_{\rm b} \ll h_{\rm s}$), the details of its vertical distribution hardly affect the details of NIR images and SED, while both crucially depend on the spatial distribution of the small dust, as we will show below in Section 4.3.

The total mass of the big dust in the disk is $f \times M_{\rm dust}$, where f is a variable parameter. For the small dust, we assume a size distribution as in the standard ISM dust model from Kim et al. (1994) up to a maximum size of 0.2 μm (roughly a power-law size distribution $n(s) \propto s^p$ with power index $p \sim 3.5$). The dust composition is assumed to be 70% mass in silicate and 30% mass in graphite, with the properties for both adopted from Laor & Draine (1993). Preferentially forward scattering (i.e. Mie scattering) is assumed. For the big dust we primarily use Model 2 from Wood et al. (2002) (from now on called steep-big-dust), which assumes a power-law size distribution $n(s) \propto s^p$ with $p = 3.5$ up to a maximum size of 1 mm, and a composition of amorphous carbon and astronomical silicates. In Section 4.2 Model 3 from Wood et al. (2002) is also tried (from now on called flat-big-dust), whose only difference from the steep-big-dust model is that it assumes $p = 3.0$ ("flatter" size distribution, so more mass at the large size end). As a consequence, the flat-big-dust model has lower opacity than the steep-big-dust model at wavelengths $\lambda \lesssim 1$mm. The opacity of these dust models are shown in Figure 5.1.

PDS 70 shows a cavity with radius $\sim 60 - 70$AU, and the disk is inclined by about $45° - 50°$ (Hashimoto et al., 2012). In our fiducial model shown below we choose 65 AU ($\sim 0\farcs46$) and 45° for the two, as they produce model SED and image which match observations reasonably well (Section 3). We note that a mild deviation from these "fiducial" values can be tolerated without much difficulty (i.e. ±5 AU in cavity size and ±5° in geometry). These parameters are fixed below to keep the models simple.

We produce H-band polarized images from MCRT simulations. To obtain realistic images which can be directly compared with SEEDS observations, the raw simulated images are post-processed, as described in detail in chapter 3. The SEEDS observations of PDS 70 were conducted in PDI mode without a coronagraph (Hashimoto et al., 2012), so that we produce mock images in the same mode in this work. The raw model images of the entire disk+star is convolved by a real H-band SEEDS point spread function (PSF). The inner working angle of the images, $\psi_{\rm in}$, is assumed to be $0\farcs15$ in radius ($\sim$21 AU at the estimated distance of PDS 70). We measure the surface brightness radial profile (SBRP) of the disk along major and minor axes, by calculating the average SB of the pixels within $\pm22.5^\circ$ on each side of the axes at various radial bins $0\farcs05$ in width, the same as we measured for the SBRP of the SEEDS PDS 70 image (Hashimoto et al., 2012).

3 The fiducial disk model for PDS 70

Here we present a fiducial disk model for PDS 70 to fit all the observations. The disk parameters in this model are listed in Table 5.3, and the surface density of the small dust is plotted in Figure 4.2. In summary, the disk has a heavily depleted cavity whose radius is 65 AU $R_{\rm cav}$, with a depletion factor of 1000 for both the big and small dust ($\delta_{\rm cav,b}$ and $\delta_{\rm cav,s}$, we note that only $\delta_{\rm cav,s}$ is constrained by the current observations, not $\delta_{\rm cav,b}$, see below). The inner-most disk (on AU scales) and the cavity wall are both optically thick in the vertical direction at 1 μm, representing the peak of the stellar spectra. The vertical optical depth due to the small dust is ~ 14 at the inner edge of the disk (~ 0.06 AU), and ~ 4 at the cavity wall. On the other hand, the gap in between the inner rim and the outer disk (i.e. from $\sim$1 AU to $R_{\rm cav}$) is optically thin to stellar radiation, which justifies the classification of PDS 70 as a pre-transitional disk (Espaillat et al., 2010). The total dust mass $M_{\rm dust}$ is $3\times10^{-5}M_\odot$, and most of it is in the big dust, with a big-to-small-dust ratio at about 30:1 (i.e. $f=0.97$). However, as we will discuss in Section 4.2, the constraints on the big dust are rather weak (including the total amount, its structure, and the big-to-small-dust ratio), given the current data. We assume scale height power law index 1.2 for both dust populations ($\beta_{\rm b}$ and $\beta_{\rm s}$), both inside and outside the cavity (indicated by subscripts "c" and "o"), reasonably close to the canonical value $\sim 1.25-1.3$ for irradiated disks (Chiang & Goldreich, 1997; Hartmann et al., 1998). The gas in the disk is in hydro-static equilibrium in the vertical direction, so that $h_{\rm gas}$ is set by the vertical temperature profile, through $h_{\rm gas}\approx c_{\rm s}/\Omega$ and $c_{\rm s}\approx\sqrt{k_BT/\mu}$, where $c_{\rm s}$ is the sound speed, Ω is the rotational angular velocity, T is the mid-plane temperature, and μ is the average molecular weight. Various grain settling models predict that the small grains tend to be well coupled with the gas (Dullemond & Dominik, 2004b), as a result the two would share similar vertical distribution, $h_{\rm s}\sim h_{\rm gas}$. The small dust scale height is 6.0 AU at $R_{\rm cav}$, both inside the cavity ($h_{\rm s}^{\rm c}$) and outside the cavity ($h_{\rm s}^{\rm o}$), which corresponds to a mid-plane temperature of 28.2K. This value is close to the output from the radiative transfer calculation, 31.8K. The big dust scale height inside and outside the cavity ($h_{\rm b}^{\rm c}$ and $h_{\rm b}^{\rm o}$) is 1/5 of the value for the small dust.

The model H band PI images are shown in Figure 4.3, along with the observed SEEDS image. The SED and SBRP (defined in Section 2) of the image are shown in Figure 4.4. Our model SED matches the observations very well. For the scattered light image, our fiducial model looks very similar to SEEDS image, both revealing a clear cavity with size $\sim 0\farcs5$ on the major axes. If fit by an ellipse, the disk center has an offset ~ 9 AU from the star, roughly along the minor axis, and towards the far side of the disk, which is due to the back illumination of the wall. This offset is

consistent with observation (the measured offset in SEEDS image is $\sim$ 6AU in the same direction, see Hashimoto et al. 2012). The small (bright) structures that appear close to the inner working angle in the SEEDS image is probably artificial, mostly likely caused by observational noise or the stellar residual in polarized light. The right side of the Subaru image is slightly brighter (in scattered light) than its left counterpart, which is not reproduced by our axisymmetric fiducial model. This asymmetry may be intrinsic, caused by differences in grain properties, or disk structure (i.e. scale height or the amount of dust), on the two sides. We note that since we focus on studying the global scale structure, particularly the general properties of the cavity (i.e. its size and depletion factor), using axisymmetric models, we do not address the local details and non-axisymmetric structures in this work.

Quantitatively, we reach good agreement with the measurement of the SBRP along the major axis. The only obvious deviation happens at large distance ($\gtrsim''1$, well beyond the cavity edge), where unlike the model, the observed image flattens out to a (roughly constant) background noise. Due to the axisymmetry of our model, the SBRPs along both directions at its semi-major axis are the same, while observationally these profiles are slightly different, due to reasons discussed above. Here we emphasize that we achieve good agreement not only for the radial dependence (i.e. the slope), but also for the *absolute scale* of the surface brightness (the vertical axis in all the SBRP plots in this study is in actual physical units, and the curves were not rescaled).

The agreement between our model and SEEDS observation on the minor axes is not perfect, but nevertheless the two agree on major qualitative features: the surface brightness on the far side of the disk peaks at a larger radius, and it decreases outward slower than on the near side. The flux in polarized scattered light is determined by the product of polarization fraction, and the intensity of the full intensity (i.e. PI=(PI/FI)$\times$FI). Along the major axis, the scattering angle is nearly 90°, which results in a maximum polarization fraction (PI/FI) due to the phase function of small dust. On the other hand, along the minor axis the scattering happens closer to the center, and at angles off 90°, resulting in small PI/FI. On the far side, both the upper and lower edge of the cavity are visible, so that the ring is wider; on the near side the lower edge is blocked by the outer disk, however forward scattering leads to a bigger FI there. We note that generally speaking, the comparison along the major axis is more valuable in constraining the disk+cavity structure, because disk is spatially more extended in this direction so that it is better resolved by observations with a fixed spatial resolution in all directions. Also, along the minor axis the features of interests (i.e. cavity edge) are present at closer separation from the center (also $\psi_{\rm in}$), where the photon noise is generally larger.

We note that the parameters and geometry of our fiducial model come from an overall consideration of fitting the SED, NIR image, and radial profile of the scattered light simultaneously, instead of simply measuring from the image as in Hashimoto et al. (2012). Also, the fiducial model presented here is by no means unique, i.e. the only one which can provide a good fit to all the observations, as the constraints on some of the disk+gap parameters are rather weak (Section 4).

At last, we comment on the previous VLT K-band imaging of PDS 70 reported by Riaud et al. (2006), and their derived disk model. Observationally, the inclination and position angle found by Riaud et al. (2006) is similar to our results (Hashimoto et al., 2012). However, our Subaru H-band PI images provide far more details and are at a higher quality than the VLT K-band full intensity images presented by Riaud et al. (2006), which detected the disk in scattered light, but did not reveal a clear giant cavity structure, and showed a jet structure that is not present in our observations. Riaud et al. (2006) employed a smooth disk model with radius larger than 500 AU,

and a total dust mass between 0.001 to 0.002 $M_\odot$ to reproduce the observations, which is one order of magnitude lager than in our fiducial model. The difference is mostly caused by the fact that the inner region is heavily depleted in our models but not in Riaud et al. (2006).

4 Constraints on various disk and cavity parameters

The fiducial model presented above provides a reasonably good fit to observations, and gives us a basic idea about the disk+cavity structure. In this section, we intend to determine the constraints on some of the parameters from modeling and fitting, so that we can understand what these observations are really telling us. In general, disk properties at short wavelengths (i.e. scattered light images and NIR excess in the SED) are sensitive to the spatial distribution of the small dust, while this dependence shifts to the big dust at long wavelengths (i.e. FIR excess and sub-mm observations), due to the difference in opacity of the two populations (Figure 5.1). Since there are too many free parameters in our model, it is not realistic to vary every one of them and study their effects. Rather, we narrow our scope to few *key* parameters:

1. The ones which are crucial in revealing the evolution of protoplanetary disk, and the formation mechanisms of (pre-)transitional disks. These are the depletion factor of both dust populations, and the total mass of the disk.

2. The ones which can *only* be effectively constrained by scattered light images, such as the scale height and depletion factor of the small dust, which has a large degeneracy in SED and sub-mm observations. Since SEEDS virtually opens a new window to systematically study a large uniform sample of disks using scattered light images, we intend to provide an example to demonstrate the power of NIR imaging for probing disk structure.

Below we study the role played by these factors both in disk SED and scattered light imaging, by exploring the corresponding parameter space around the fiducial model. We examine the cavity depletion factors for both dust populations (*dcb* and *dcs*) in Section 4.1, the total dust mass ($M_{\rm dust}$) in Section 4.2, and the scale height of the small dust in the cavity and the outer disk ($h_{\rm s}^{\rm c}$, $\beta_{\rm s}^{\rm c}$, $h_{\rm s}^{\rm o}$, and $\beta_{\rm s}^{\rm o}$) in Section 4.3. Models and their parameters in each section are listed and described in the corresponding block in Table 5.3. For the SED we focus on comparing with the photometry data, and for the scattered light we only look at the SBRP along the major axis.

4.1 The depletion factor inside the cavity

The cavity depletion factor of the small dust $\delta_{\rm cav,s}$ could be constrained by both the SED and the scattered light image. Qualitatively, depleting the cavity more in small dust reduces the short wavelength excess on the SED, and enhances the contrast of the cavity in the image. Technically, the SED is more sensitive to the depletion in the inner part of the cavity (at AU scales) since most of the short wavelength excess is produced there, while the scattered light images are more sensitive to the depletion in the outer part of the cavity, where the contrast of the cavity edge is produced (the inner part of the disk within $\psi_{\rm in}$ cannot be directly accessed in imaging observations). As a result, the two could in principle be constrained "independently". However, to simplify our discussion, we use a uniform instead of radius-dependent $\delta_{\rm cav,s}$ (and $\delta_{\rm cav,b}$), and note that this treatment does not affect our conclusion (see chapter 3) for a discussion on radius-dependent $\delta_{\rm cav}$).

Figure 4.5a shows the effect of $\delta_{\rm cav,s}$ on the SED ($\delta_{\rm cav,b}$ is locked to $\delta_{\rm cav,s}$, but this hardly affects our result, as shown below). The surface density profile of the small dust ($\Sigma_{\rm s}$) for these models is plotted in Figure 4.2. Whether $2-20\mu$m excess strongly correlates with $\delta_{\rm cav,s}$ sensitively depends on whether the innermost disk (at AU scale) is optically thick or not (characterized at the peak of the stellar spectra, $\sim 1\mu$m). When the innermost disk is optically thick (pre-transitional disks), the IR excess is almost independent of the amount of small dust inside the cavity (the fiducial model and model SCM1). However, once $\Sigma_{\rm s}$ at the inner disk decreases below the optically thick limit, and enters the transitional disk phase, the $2-20\mu$m excess drops significantly as a result of the decreasing $\delta_{\rm cav,s}$ (model SCM2 to SCM4). If the inner disk is completely depleted (SCM4), excess below $\sim$10 μm disappears, and a nearly blackbody thermal component peaking at $\sim 40\mu$m clearly reveals itself, which arises from the cavity wall. Though not as isolated as in SCM4, this wall emission signal is prominent in all models. Comparing with observation, we conclude that the NIR excess in PDS 70 is consistent with an optically thick innermost disk, which requires $\delta_{\rm cav,s} > 10^{-4}$.

Figure 4.5b shows the SBRP of the convolved image for the above models. As expected, decreasing $\delta_{\rm cav,s}$ makes the inner disk fainter. Moreover, the blocking effect due to the inner disk is reduced, so that a bigger area of the cavity wall is illuminated, and more starlight (rays closer to the disk mid-plane) reaches the wall and outer disk, increasing their brightness in scattered light. Similarly, increasing $\delta_{\rm cav,s}$ tends to wipe out the signal of the cavity in scattered light (i.e. the bump at $\sim 0\farcs05$), and makes the SBRP smoother. The observed SEEDS SBRP is broadly consistent with $\delta_{\rm cav,s} \sim 10^{-3}$, while a modest deviation (i.e. a factor of ~ 3) around this value could be tolerated without too much difficulty.

On the other hand, the cavity depletion factor of the big dust could only be directly constrained by sub-mm properties of the disk (Andrews et al., 2011; Cieza et al., 2012b; Isella et al., 2012; Mathews et al., 2012). Figures 4.5c,d show that changing $\delta_{\rm cav,b}$ hardly affects either the disk SED or NIR image (we fix the small dust to isolate the effect, i.e. the depletion factor for the small dust component inside of the cavity is fixed to $\delta_{\rm cav,s} \sim 10^{-3}$ in all the models plotted here). We leave the constraint on $\delta_{\rm cav,b}$ to future sub-mm observations.

To conclude, $\delta_{\rm cav,s} \sim 10^{-3}$ is needed for the models to be consistent with both the SED and SEEDS image. The constraint is modest, roughly half a dec around the fiducial value.

4.2 The total dust mass of the disk

The total dust mass of the disk $M_{\rm dust}$ is a quantity crucial for a thorough understanding of disk evolution. In general, $M_{\rm dust}$ is determined by the big dust since it dominates in mass over the small dust, and for (pre-)transitional disks like PDS 70, most of the mass resides in the outer disk since the inner disk is heavily depleted. $M_{\rm dust}$ is best constrained by sub-mm or mm observations, because the disk is usually optically thin at these wavelengths, so $M_{\rm dust}$ can be calculated from the measured sub-mm or mm flux, assuming a dust temperature and opacity model (i.e. Equation 2 and 3 in Williams & Cieza 2011). However, the total disk mass derived in this way normally contains large uncertainties, introduced by poorly unconstrained dust opacity and gas-to-dust-ratio, if converting dust mass to total gas mass (Panić et al., 2008).

For PDS 70, we constrain the disk mass using the longest wavelength photometric data point available, which is at 160μm. Our models are all vertically optically thin (sometimes only marginally) at 160μm given our dust models. Models BOM1 and BOM2 (both have the steep-big-dust model) in Figure 4.6a show the SED dependence on $M_{\rm dust}$. While the fiducial

choice of $M_{\rm dust} = 3 \times 10^{-5} M_\odot$ agrees well with the observed photometry at 160μm, a factor of ~ 3 deviation in $M_{\rm dust}$ from this value leads to a factor ~ 2 difference in 160μm flux, while the SED at wavelengths shorter than $\sim 100\mu$m is largely unchanged.

One issue which deserves special attention in this exercise of $M_{\rm dust}$ determination is the effect of the big dust model. Since the long wavelength flux in the optically thin regime is proportional to the opacity of the dust at that wavelength, changing the dust model for the big dust has a direct impact on $M_{\rm dust}$. Figure 4.6 shows two examples in which the flat-big-dust model is assumed instead of the steep-big-dust model. As mentioned in Section 2 and shown in Figure 5.1, the flat-big-dust has a flatter size distribution, resulting in smaller opacity at wavelengths shorter than ∼1mm. Model BOM3-flat has an identical set of disk parameters as the fiducial model. While the difference in SED between the two models is negligible at $\lambda \lesssim 100\mu$m, the IR excess in BOM3-flat sharply drops below the fiducial model at longer wavelengths. To pull the 160μm flux back to the observed value, the disk mass needs to rise to $1.5 \times 10^{-4} M_\odot$, as in model BOM4-flat. On the other hand, since all the BOM models have identical spatial distribution for the small dust, their scattered light images are almost the same, as shown in Figure 4.6b.

We conclude that the total dust mass of PDS 70 $M_{\rm dust}$ is probably on the order of $10^{-4} M_\odot$, depending on the dust model for the big dust: a flatter grain size distribution for the big dust corresponds to a larger $M_{\rm dust}$. Observations at longer wavelengths are needed to distinguish different big dust models and to pin down the disk mass.

4.3 The scale height of the small dust

The scale height of the small dust $h_{\rm s}$, which dominates the absorption of starlight, is a central quantity involved in determining almost all the observable properties of the disk[1]. Scale height and total mass of the small dust determine the shape of the disk surface, on which the stellar radiation is absorbed and re-emitted at longer wavelengths. Part of that emission escapes and gets observed, and part of it goes deeper into the disk interior to heat the disk, subsequently being reprocessed into disk emission at even longer wavelengths. Despite its importance, unfortunately very few types of observations can determine $h_{\rm s}$ in a straightforward manner (see the example in Muto et al. 2012, where the shape of the spiral waves in SAO 206462 is used to estimate $h_{\rm s}$). However, scattered light is an excellent tool for probing $h_{\rm s}$, since its signal comes right from the disk scattering surface, which is directly determined by $h_{\rm s}$.

In this section, we use several models to investigate the effects of $h_{\rm s}$ on disk SED and NIR image. Figure 4.7a,b show the result of models SOS1-4, in which the scale height at the outer disk $h_{\rm s}^{\rm o}$ is varied. We find that the radial dependence of $h_{\rm s}^{\rm o}$ has a minimal effect on both the SED and scattered light image (models SOS1 and SOS2), while the overall scale of $h_{\rm s}^{\rm o}$ plays a prominent role in both the SED and NIR image. A much larger area of the cavity wall in model SOS4, whose $h_{\rm s}^{\rm o}$ is 1.5 times the fiducial value, is directly exposed to the stellar radiation, due to its larger height. As a result, its SED is a factor of ~ 2 higher at the peak of the wall emission ($\sim 40\mu$m) compared with the fiducial model and the observed SED, and the cavity edge is $\sim 50\%$ brighter.

Figures 4.7c,d show the effect of $h_{\rm s}$ inside the cavity ($h_{\rm s}^{\rm c}$, model SCS1-4). Similar to $h_{\rm s}^{\rm o}$, the absolute scale of the scale height plays a bigger role than its radial dependence. Model SCS1 and

[1]The big dust is generally considered to have settled to the disk mid-plane, and its opacity at the peak of the stellar spectrum is much lower than that of the small dust. As a result, the detailed vertical distribution of the big dust does not have a prominent effect on the SED and the scattered light image.

SCS3, both having a thinner innermost disk, produce less NIR excess and slightly less scattered light from the inner disk. Also, since less starlight is blocked by the innermost disk and more of it reaches the cavity edge, the two have more MIR excess around 40μm and a slightly brighter cavity edge at H-band. On the contrary, model SCS4 has a thicker disk inside the cavity, resulting in more short wavelength excess and less long wavelength excess, due to less starlight reaching the outer disk. Its inner disk is also brighter and outer disk is fainter in the scattered light image. In general, the effect of $h_{\rm s}^{\rm c}$ on the SED is modest, echoing the finding in Section 4.1, that once the inner disk becomes optically thick, the NIR excess is insensitive to the distribution of small dust.

In sum, the scale height of the small dust at $R_{\rm cav}$, $h/R \sim 0.09$, is relatively well determined by both the SED and the scattered light image (note that this value is consistent with the output temperature from radiative transfer calculation, Section 3). On the other hand, the constraint on the radial dependence of $h_{\rm s}$ is weaker, as a broad range of β from 1.15 to 1.25 (both inside and outside the cavity) in the parameter space we explored here does not contradict the observations.

5 Indication on the formation of (pre-)transitional disks

PDS 70 is a special pre-transitional disk, in the sense that unlike most of its previous cousins, whose cavities were usually first inferred from the shape of the SED and then confirmed by resolved sub-mm images, the cavity in PDS 70 was *first* found in SEEDS scattered light image (see also Honda et al. 2010 for AB Aur). Follow up interferometer observations at long wavelengths, for example using the Submillimeter Array (SMA) or the Atacama Large Millimeter Array (ALMA), are needed to check the existence of the cavity in the big dust. If it is indeed confirmed, then this object will represent a class of (pre-)transitional disks which are in clear contrast to the ones discussed in chapter 3. In addition, observations at long wavelengths will help to determine the total dust mass of the disk, which is currently poorly contained to be $\sim 10^{-4} M_\odot$ due to the lack of long wavelength observations and the uncertainties in dust model.

There are only a handful of objects whose cavities have been revealed in resolved images at multiple wavelengths covering a broad range. A special group of them are circumbinary disks (with the secondary being a stellar or sub-stellar object), such as GG Tau. The cavity in GG Tau has been found in the optical (Krist et al., 2005), NIR (Itoh et al., 2002), mm (Piétu et al., 2011), and CO line emission (Guilloteau et al., 1999), all at roughly the same position. The formation mechanism of cavities in circumbinary systems has been studied by Artymowicz & Lubow (1994). It is thought that the gravitational interaction between the massive (sub-)stellar secondary and the disk naturally truncates the disk, and the cavity formed in this way exists in all disk components, including gas and dust at different sizes. The imaging at L' band shown in Hashimoto et al. (2012) has put an upper limit $\sim 30 - 50 M_J$ for any possible companion at the radii of interest (assuming their age of the system and the (sub-)stellar object evolution model), which rules out the possibility of a stellar mass companion. Future observations with better sensitivity and contrast performance are needed to answer whether a sub-stellar companion exists (i.e. a brown dwarf). On the other hand, the possibility of gap opening due to multiple Jovian planets has been explored by Zhu et al. (2011); Dodson-Robinson & Salyk (2011). The general picture in that scenario, that a wide deep gap is opened while a small optically thick inner-most disk is left at the center, qualitatively agrees with the observations of PDS 70, though it is generally harder to directly image Jovian planet(s) in a bright protoplanetary disk.

The dust filtration model has been proposed by Paardekooper & Mellema (2006) and Rice et al. (2006), in which the pressure maximum at the planet-induced gap outer edge acts like a

filter, so that big grains are trapped but small grains penetrate into the inner disk. As a result, it is predicted that the cavity must be depleted of big dust grains, but with a significant amount of small dust particles left inside. PDS 70, with its heavily depleted cavity in small dust grains, is inconsistent with the dust filtration model alone. On the other hand, Zhu et al. (2012) proposed a dust filtration + dust growth model as a possible explanation for the transitional disk GM Aur. The grain growth and coagulation at the innermost disk may turn the small grains into big grains, resulting in a (pre-)transitional-disk-like NIR excess (see also Birnstiel et al. 2012). The dust and gas components of the disk are decoupled in their model and provide an explanation for both the moderate accretion rate of GM Aur and its strong near-IR deficit. Furthermore, this dust size dependent filtration model may explain the different gap properties between near-IR and sub-mm reported in chapter 3. However, unlike GM Aur, PDS 70 is a WTTS, suggesting a very low gas accretion rate. Together with the clear cavity revealed in the NIR imaging, a consistent picture emerges for PDS 70, that both the small dust and the gas are heavily depleted at the inner disk, and there is no clear evidence for decoupling between the two. On the other hand, without sub-mm/mm observations, we do not know if small and big dust are decoupled or not.

Nevertheless, following the dust filtration + dust growth model, we can still provide an explanation for the PDS 70 class of objects. They may start as systems modeled in chapter 3, which do have a significant amount of small dust inside the cavity and the NIR cavity is not present. Later on, grain growth and coagulation, which happen at a faster rate in the inner disk due to high density and short dynamical timescale, gradually spread over the entire inner disk, eventually leading to the formation of a small dust cavity. If this scenario is true, then these two kinds of (pre-)transitional disks are just at different evolutionary stages in their cavity clearing process — the ones in chapter 3 are at an early stage, while PDS 70 is at a later stage. Consequently, we should expect to see a statistical "time delay" between the two types of objects. This time delay is partly supported by the facts that PDS 70 is a WTTS, and that it is a relatively old system. This argument can be further tested if a large sample of objects in both categories with accurate age determination could be provided by future observations. Also, another possible strong evidence in favor of this scenario would be the detection of objects in the intermediate phase of this process, such as (1) objects with a "partially cleared" small dust cavity whose edge is between the center and the edge of the big dust cavity, or (2) objects with a radius-dependent cavity depletion factor for the small dust (probably smaller at inner disk), showing that the clearing process is moving outward. Furthermore, the byproduct of grain growth and coagulation — a slight enhancement of the big dust signal inside the cavity at later stage — may be observable using a sub-mm interferometer with very high sensitivity, such as ALMA chapter 3.

6 Summary

We carry out a study of the disk+cavity structure for PDS 70, using radiative transfer modeling to fit both the observed SED and the SEEDS polarized scattered light image at H-band of this object. Good agreement with observations is achieved in our models. The disk has a giant cavity at its center with radius 65 AU. The small dust (sub-micron-sized) inside the cavity is depleted by a factor of ~ 1000, resulting in a low density but still vertically optically thick innermost disk, producing a pre-transitional-disk-like NIR excess. This heavy depletion is also needed to explain the surface density depression inferred from the scattered light image. The scale height of the small dust at the cavity edge is $\sim$6 AU, constrained by both the SED and the image, which is consistent with the output mid-plane temperature of the disk. On the other hand, the total mass

of the disk can be estimated only crudely to be on the order of $10^{-4} M_{\odot}$, due to the lack of sub-mm and mm data, and the degeneracy of the dust models for the big dust in the SED. This quantity, along with the cavity depletion factor for the big (mm-sized) dust, would be determined by future observations at longer wavelengths.

Unlike most previously classified (pre-)transitional disk, the cavity in PDS 70 is identified in NIR scattered light, which only informs us of the depletion in the small dust but tells us little about the spatial distribution of the big dust. Pending the confirmation of the cavity in the big dust by radio interferometer observations, PDS 70 may be a prototype of its group, in which the cavity is seen in both dust populations. If this is true, it is in clear contrast with the (pre-)transitional disks discussed in chapter 3, where the small dust cavities were not seen outside the inner working angle of the scattered light images. The (pre-)transitional disks with or without a NIR cavity may be formed through different mechanisms (i.e. binary vs planets or grain growth), or they may just be caught at different evolutionary stage in their disk clearing process. Observational predictions for both mechanisms are made in Section 5, and more objects with multi-wavelengths observations in both categories are needed to reveal the nature of (pre-)transitional disks.

Table 4.1. Disk Models

Name (1)	$M_{\rm dust}$ (2)	f (3)	$h_{\rm b}^{\rm o}$(100AU) (4)	$\beta_{\rm b}^{\rm o}$ (5)	$h_{\rm b}^{\rm c}$(100AU) (6)	$\beta_{\rm b}^{\rm c}$ (7)	$\delta_{\rm cav,b}$ (8)	$h_{\rm s}^{\rm o}$(100AU) (9)	$\beta_{\rm s}^{\rm o}$ (10)	$h_{\rm s}^{\rm c}$(100AU) (11)	$\beta_{\rm s}^{\rm c}$ (12)	$\delta_{\rm cav,s}$ (13)
Fiducial	3×10^{-5}	0.967	2	1.2	2	1.2	10^{-3}	10	1.2	10	1.2	10^{-3}
The Depletion Factor Inside the Cavity												
SCM1	3×10^{-5}	0.967	2	1.2	2	1.2	10^{-2}	10	1.2	10	1.2	10^{-2}
SCM2	3×10^{-5}	0.967	2	1.2	2	1.2	10^{-4}	10	1.2	10	1.2	10^{-4}
SCM3	3×10^{-5}	0.967	2	1.2	2	1.2	10^{-5}	10	1.2	10	1.2	10^{-5}
SCM4	3×10^{-5}	0.967	2	1.2	2	1.2	0	10	1.2	10	1.2	0
BCM1	3×10^{-5}	0.967	2	1.2	2	1.2	10^{-2}	10	1.2	10	1.2	10^{-3}
BCM2	3×10^{-5}	0.967	2	1.2	2	1.2	0	10	1.2	10	1.2	10^{-3}
The Total Dust Mass of the Disk												
BOM1	10^{-4}	0.99	2	1.2	2	1.2	2.9×10^{-4}	10	1.2	10	1.2	10^{-3}
BOM2	10^{-5}	0.9	2	1.2	2	1.2	3.3×10^{-2}	10	1.2	10	1.2	10^{-3}
BOM3-flat	3×10^{-5}	0.967	2	1.2	2	1.2	10^{-3}	10	1.2	10	1.2	10^{-3}
BOM4-flat	1.5×10^{-4}	0.993	2	1.2	2	1.2	2.0×10^{-4}	10	1.2	10	1.2	10^{-3}
The Scale Height of the Small dust												
SOS1	3×10^{-5}	0.967	2	1.2	2	1.2	10^{-3}	10	1.25	10	1.2	10^{-3}
SOS2	3×10^{-5}	0.967	2	1.2	2	1.2	10^{-3}	10	1.15	10	1.2	10^{-3}
SOS3	3×10^{-5}	0.967	2	1.2	2	1.2	10^{-3}	7.5	1.2	10	1.2	10^{-3}
SOS4	3×10^{-5}	0.967	2	1.2	2	1.2	10^{-3}	15	1.2	10	1.2	10^{-3}
SCS1	3×10^{-5}	0.967	2	1.2	2	1.2	10^{-3}	10	1.2	10	1.25	10^{-3}
SCS2	3×10^{-5}	0.967	2	1.2	2	1.2	10^{-3}	10	1.2	10	1.15	10^{-3}
SCS3	3×10^{-5}	0.967	2	1.2	2	1.2	10^{-3}	10	1.2	7.5	1.2	10^{-3}
SCS4	3×10^{-5}	0.967	2	1.2	2	1.2	10^{-3}	10	1.2	15	1.2	10^{-3}

Note. — Column (1): Name of the models. The first, second, and third letter indicates whether the model is about (1) big dust (B) or small dust (S); (2) outer disk (O) or cavity (C); and (3) mass (M) or scale height (S). In block "The Total Mass of the Disk", parameters are chosen in such a way that all the disk properties are the same except the mass of big dust in the outer disk (which essentially determines the total disk mass), and "flat" indicates that the flat-big-dust model is used instead of the steep-big-dust model (BOM3-flat has an identical set of parameters as the fiducial model). Column (2): Total dust mass of the disk, in unit of $M_\odot$. Column (3): Mass fraction of big dust in total dust. Columns (4), (6), (9), and (11): Scale height h at 100 AU, in unit of AU. Subscripts "b" and "s" indicate big and small dust, respectively. Superscripts "o" and "c" indicate outer disk and cavity, respectively. Columns (5), (7), (10), and (12): Power index β in Equation 5.3 in various disk components. Column (8) and (13): Depletion factor of the big and small dust disk.

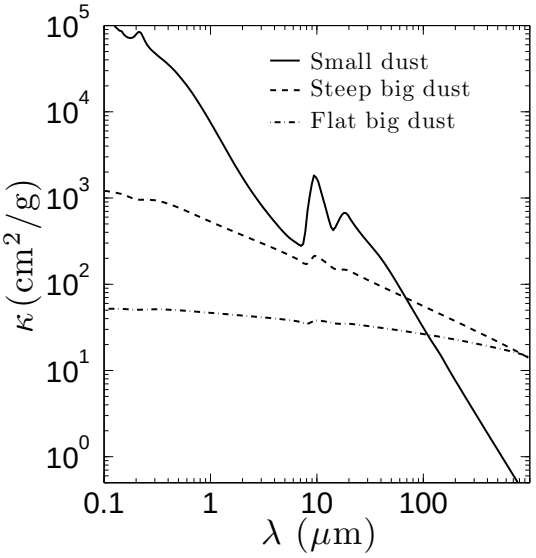

(a)

Figure 4.1 Opacity κ for the dust models used in this study (showing the dust opacity only).

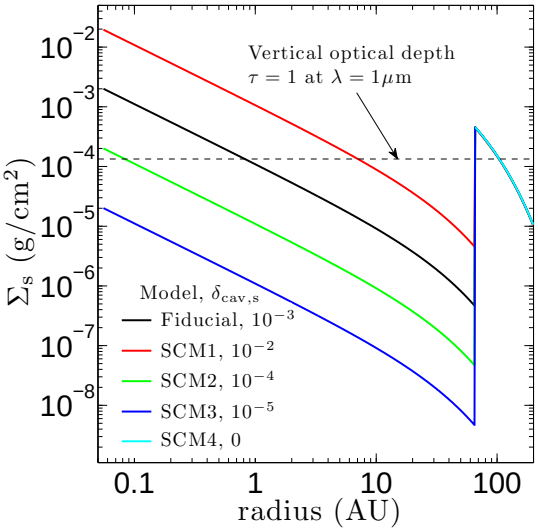

(a)

Figure 4.2 Surface density radial profile of the small dust $\Sigma_{\rm s}$, for models shown in Figure 4.5a,b. The horizontal dashed line indicates where the vertical optical depth is 1 at 1μm (characteristic wavelength of the stellar radiation). The fiducial model and model SCM1 have vertically optically thick innermost disks, and models SCM3 and SCM4 have optically thin innermost disks, while model SCM2 is on the margin.

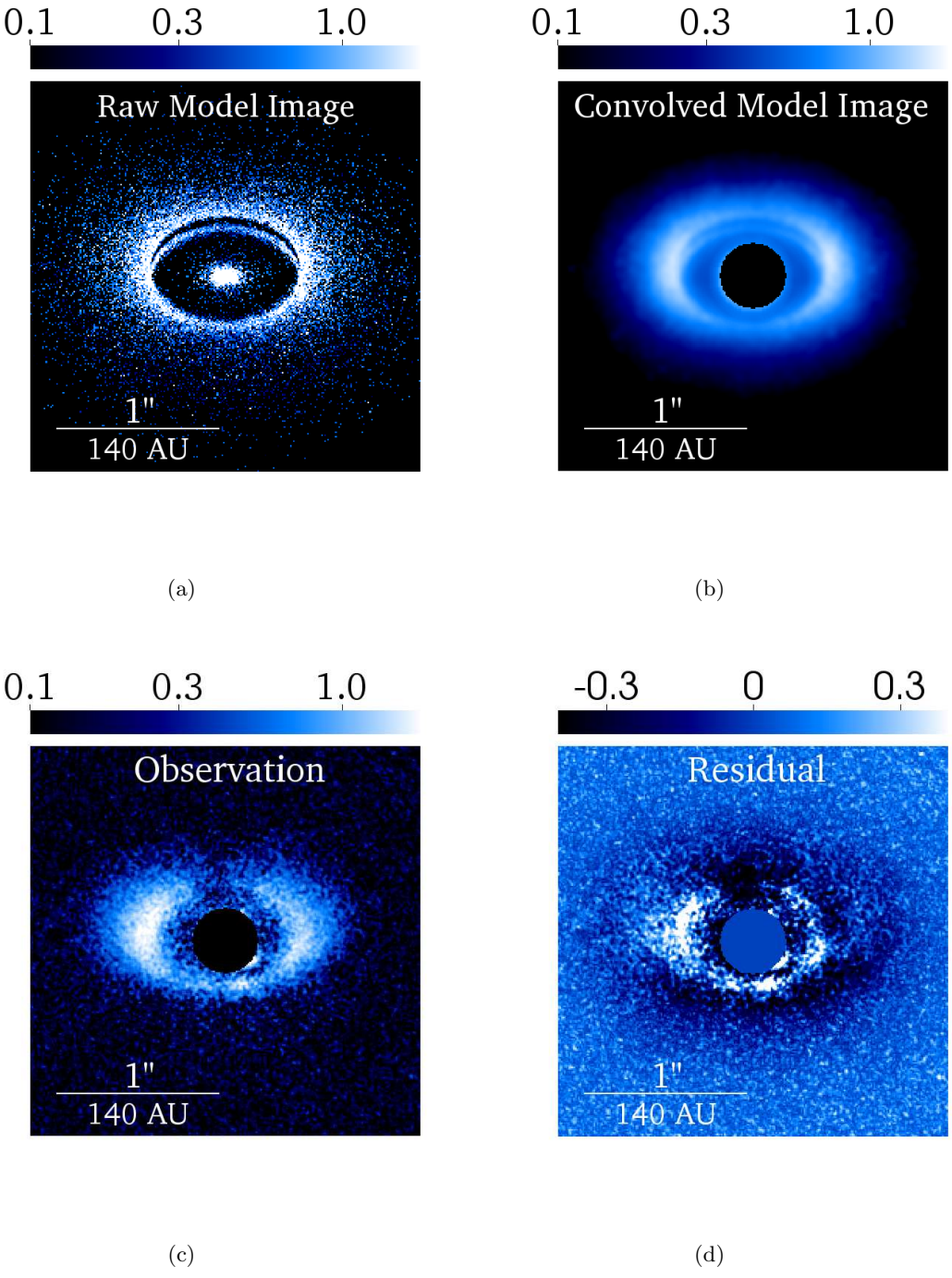

Figure 4.3 Comparison of the polarized scattered light images at H-band between our fiducial model and SEEDS observation of PDS 70. Images show the surface brightness. The convolved model image is the raw model image convolved by a HiCIAO PSF (Section 2). The observed SEEDS image is not smoothed. The residual image is the convolved model image subtracted from the SEEDS image. All images are oriented in such a way that the far side of the disk (21° from west to north) is up. The mask at the center in the convolved model image and SEEDS image indicate a $0\farcs2$ (radius) inner working angle. Labels are in unit of mJy/arcsec^2 (the residual image is on linear scale, while the other three are on log scale with the same color scheme). Our fiducial model matches the large scale characteristics in the observation well, although some local and asymmetric features are not reproduced perfectly. See Section 3 for details.

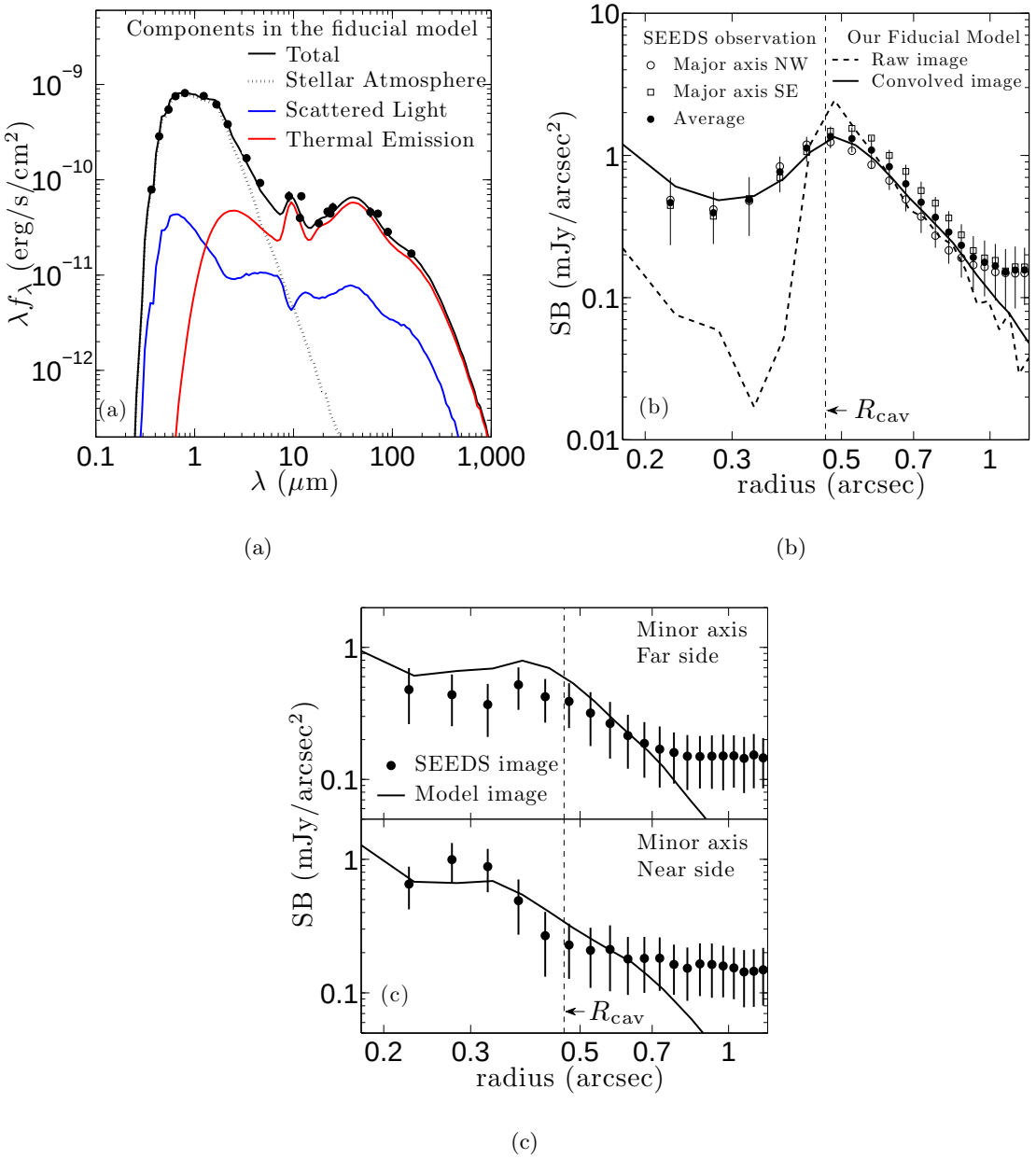

Figure 4.4 Comparison between observations and our fiducial model on the SED (a), SBRP of the scattered light image along major axes (b), and SBRP along minor axes (c). Observational data is from Hashimoto et al. (2012). In panel (a), the black dots are photometry data points (the vertical small bar indicates the error), and different components in the model SED are labeled. In panel (b) and (c), the black dots are the measured SEEDS SBRP, with error bars overplotted as vertical ticks. The individual observed SBRPs along the two directions of the semi-major axis are slightly different, and both are plotted as well. The fiducial model agrees well with the observations (particularly on the absolute scale of the surface brightness in the SEEDS image). In panel (c), due to the difficulty in measuring SBRP along the minor axes (Section 3), the agreement is worse than in panel (b), but nevertheless the basic characteristic trend is still well matched, that the SBRP on the far side of the disk peaks at larger radii and decreases slower than on the near side, due to the back illumination. Model SBRP in (b) and (c) do not flatten out to a (constant) background noise at large radii, as in the observed SBRP.

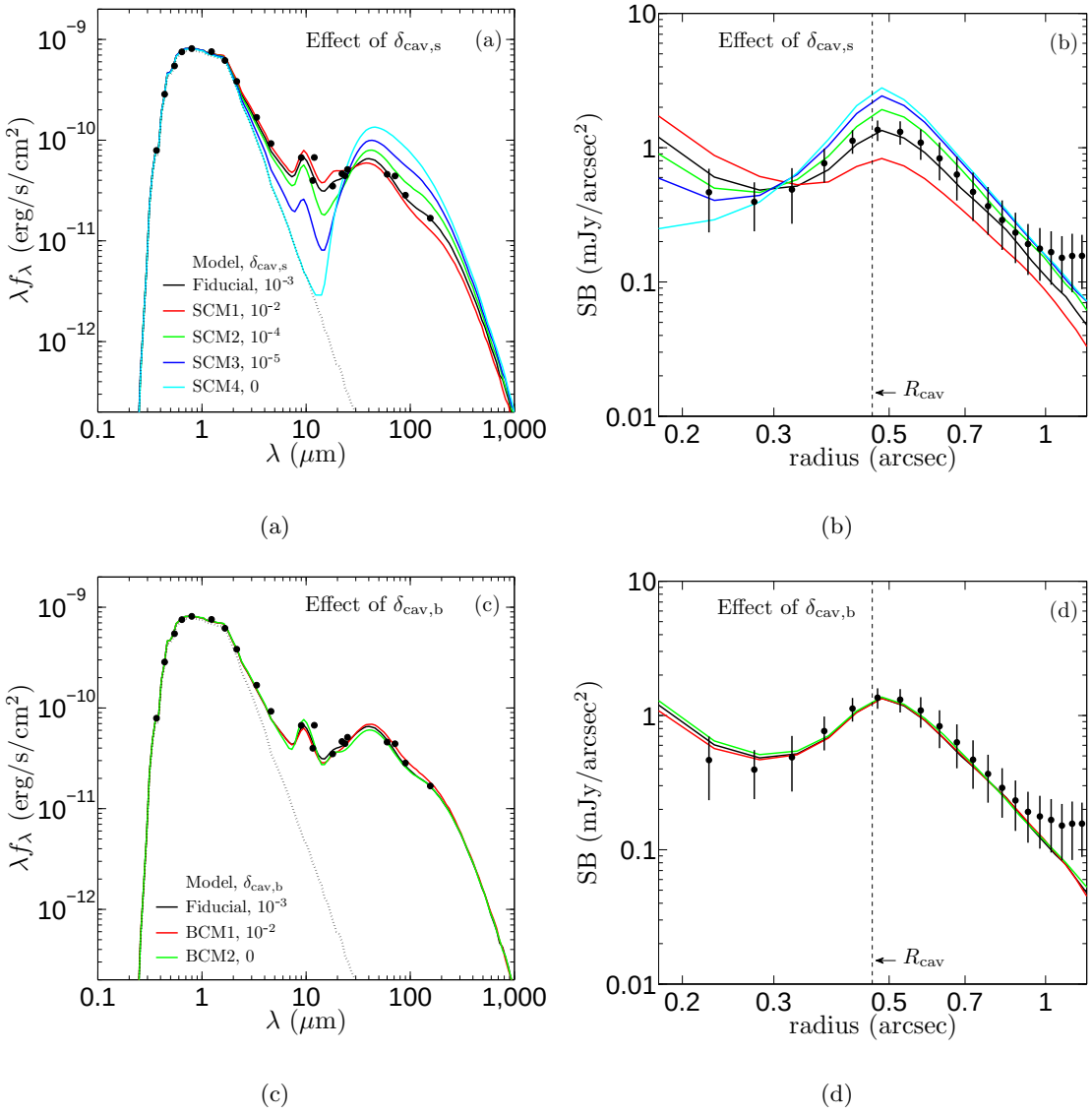

Figure 4.5 Effects of the cavity depletion factor for the small ($\delta_{\rm cav,s}$) and big ($\delta_{\rm cav,b}$) dust, on both the disk SED ((a) and (c)) and the scattered light image ((b) and (d), plotting SBRP along the major axes). The dotted line in panels (a) and (c) is the stellar spectrum and the black dots are photometric SED data point, as in Figure 4.4. The corresponding disk models are listed in the block "The Depletion Factor Inside the Cavity" in Table 5.3, and described in detail in Section 4.1. The models in the SBRP plots ((b) and (d)) have the same line types as they have in the SED plots ((a) and (c)). The results show that as long as the innermost disk is vertically optically thick, the SED only weakly depends on $\delta_{\rm cav,s}$; once $\delta_{\rm cav,s}$ drops enough for the innermost disk to be optically thin, the NIR excess becomes sensitive to the amount of small dust there. The inner disk is brighter and the outer disk is dimmer in scattered light for a bigger $\delta_{\rm cav,s}$. On the other hand, both the SED and scattered light image are almost independent of $\delta_{\rm cav,b}$.

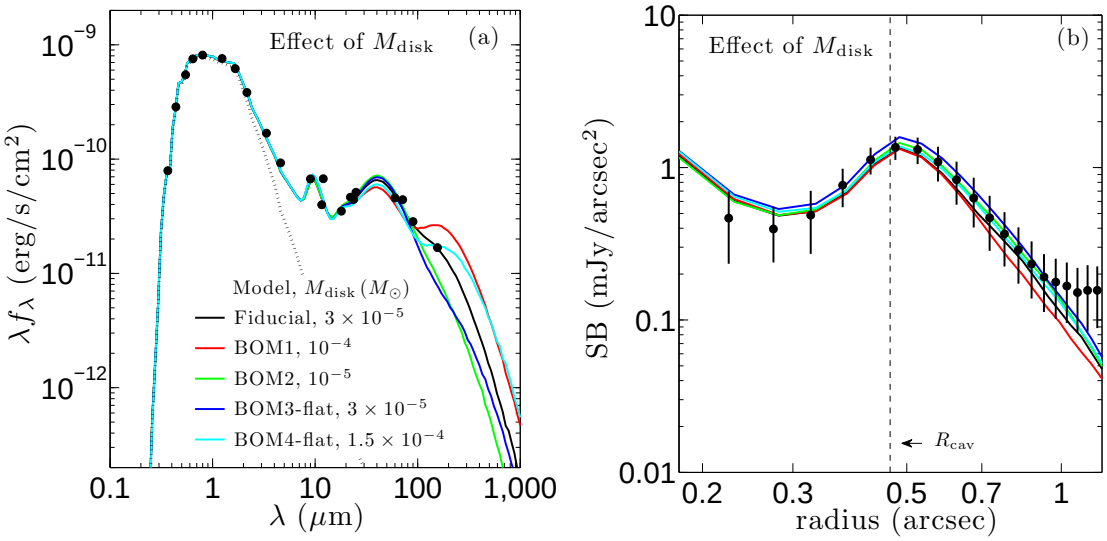

(a) (b)

Figure 4.6 The same set of plots as in Figure 4.5, but for models BOM1 to BOM4-flat, showing the effect of total disk mass $M_{\rm dust}$. The corresponding disk models are listed in the block "The Total Dust Mass of the Disk" in Table 5.3, and described in detail in Section 4.2. The dust model for the big dust in models BOM3-flat and BOM4-flat is the flat-big-dust, while the other models have the steep-big-dust model (Figure 5.1). The total mass of the disk, which in PDS 70 concentrates in the big dust in the outer disk, needs to be better constrained by observations at long wavelengths, with which different big dust models can be distinguished. The photometry at the longest wavelength available (160μm) agrees with a total disk mass $\sim 3 \times 10^{-5} M_\odot$ assuming the steep-big-dust model, or $\sim 1.5 \times 10^{-4} M_\odot$ assuming the flat-dust-model.

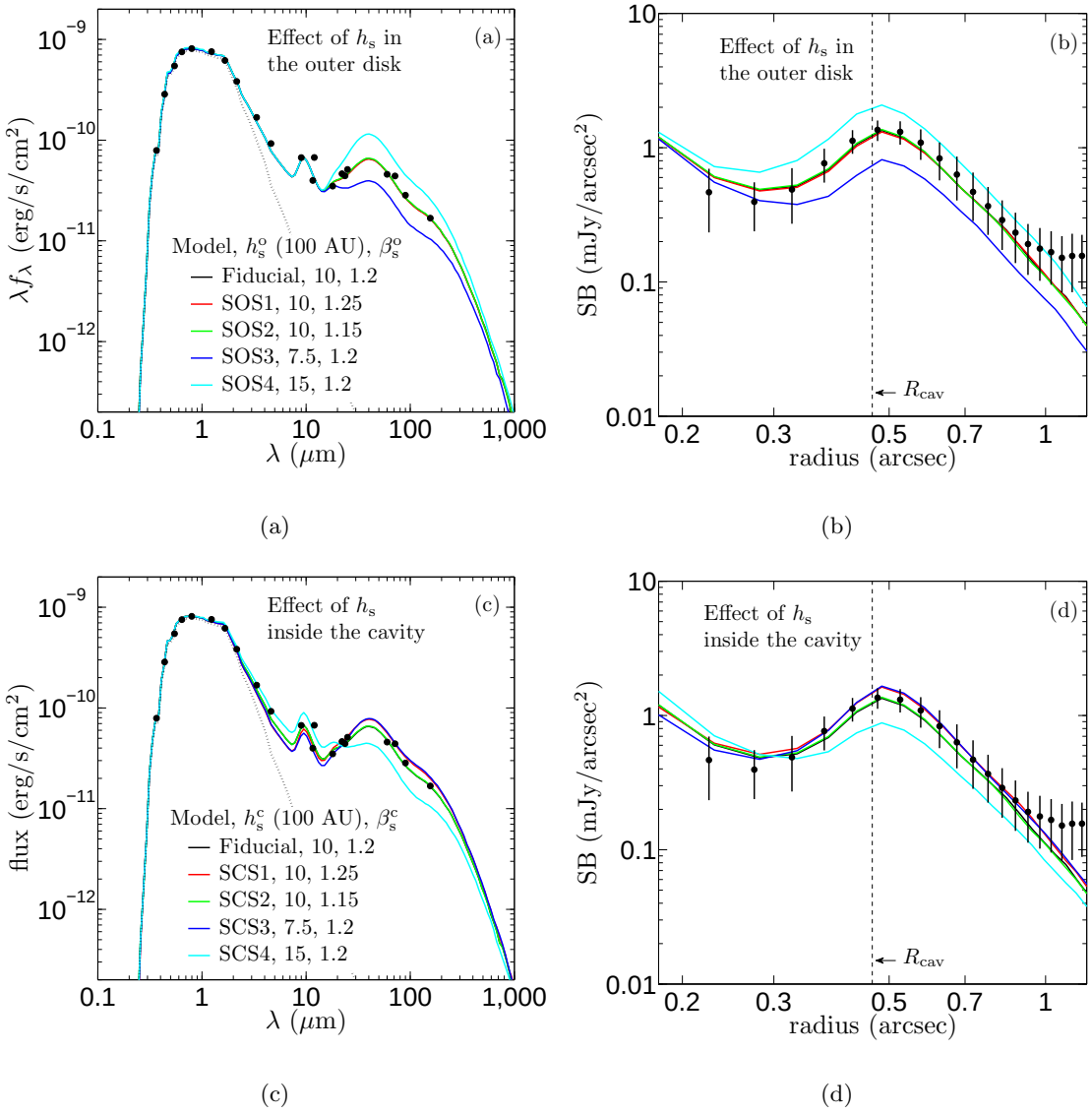

Figure 4.7 The same set of plots as in Figure 4.5, but for models SOS1-4 and SCS1-4, showing the effects of scale height of the small dust, both outside the cavity (h_s^o, (a) and (b) and inside the cavity (h_s^c, (c) and (d)). The corresponding disk models are listed in the block "The Scale Height of the Small Dust" in Table 5.3, and described in detail in Section 4.3. Both the IR excess at $\sim 40\mu$m and the brightness of the disk at the cavity edge sensitively depend on the overall scale of h_s^o (a higher cavity wall produces more MIR excess and scattered light), while if the overall scale is roughly the same, the radial dependence of h_s^o does not have a big effect. Similar results are seen in h_s^c as well.

Bibliography

Andrews, S. M., Wilner, D. J., Espaillat, C., Hughes, A. M., Dullemond, C. P., McClure, M. K., Qi, C., & Brown, J. M. 2011, ApJ, 732, 42

Andrews, S. M., Wilner, D. J., Hughes, A. M., Qi, C., Rosenfeld, K. A., Öberg, K. I., Birnstiel, T., Espaillat, C., Cieza, L. A., Williams, J. P., Lin, S.-Y., & Ho, P. T. P. 2012, ApJ, 744, 162

Artymowicz, P. & Lubow, S. H. 1994, ApJ, 421, 651

Birnstiel, T., Andrews, S. M., & Ercolano, B. 2012, A&A, 544, A79

Brown, J. M., Blake, G. A., Qi, C., Dullemond, C. P., Wilner, D. J., & Williams, J. P. 2009, ApJ, 704, 496

Calvet, N., D'Alessio, P., Watson, D. M., Franco-Hernández, R., Furlan, E., Green, J., Sutter, P. M., Forrest, W. J., Hartmann, L., Uchida, K. I., Keller, L. D., Sargent, B., Najita, J., Herter, T. L., Barry, D. J., & Hall, P. 2005, ApJ, 630, L185

Chiang, E. I. & Goldreich, P. 1997, ApJ, 490, 368

Cieza, L. A., Mathews, G. S., Williams, J. P., Ménard, F. C., Kraus, A. L., Schreiber, M. R., Romero, G. A., Orellana, M., & Ireland, M. J. 2012a, ApJ, 752, 75

Cieza, L. A., Schreiber, M. R., Romero, G. A., Williams, J. P., Rebassa-Mansergas, A., & Merín, B. 2012b, ApJ, 750, 157

Dodson-Robinson, S. E. & Salyk, C. 2011, ApJ, 738, 131

Dong, R., Rafikov, R., Zhu, Z., Hartmann, L., Whitney, B., Brandt, T., Muto, T., Hashimoto, J., Grady, C., Follette, K., Kuzuhara, M., Tanii, R., Itoh, Y., Thalmann, C., Wisniewski, J., Mayama, S., Janson, M., Abe, L., Brandner, W., Carson, J., Egner, S., Feldt, M., Goto, M., Guyon, O., Hayano, Y., Hayashi, M., Hayashi, S., Henning, T., Hodapp, K. W., Honda, M., Inutsuka, S., Ishii, M., Iye, M., Kandori, R., Knapp, G. R., Kudo, T., Kusakabe, N., Matsuo, T., McElwain, M. W., Miyama, S., Morino, J.-I., Moro-Martin, A., Nishimura, T., Pyo, T.-S., Suto, H., Suzuki, R., Takami, M., Takato, N., Terada, H., Tomono, D., Turner, E. L., Watanabe, M., Yamada, T., Takami, H., Usuda, T., & Tamura, M. 2012, ApJ, 750, 161

Dullemond, C. P. & Dominik, C. 2004a, A&A, 417, 159

Dullemond, C. P. & Dominik, C. 2004b, A&A, 421, 1075

Dullemond, C. P. & Dominik, C. 2005, A&A, 434, 971

Espaillat, C., Calvet, N., D'Alessio, P., Bergin, E., Hartmann, L., Watson, D., Furlan, E., Najita, J., Forrest, W., McClure, M., Sargent, B., Bohac, C., & Harrold, S. T. 2007a, ApJ, 664, L111

Espaillat, C., Calvet, N., D'Alessio, P., Hernández, J., Qi, C., Hartmann, L., Furlan, E., & Watson, D. M. 2007b, ApJ, 670, L135

Espaillat, C., Calvet, N., Luhman, K. L., Muzerolle, J., & D'Alessio, P. 2008, ApJ, 682, L125

Espaillat, C., D'Alessio, P., Hernández, J., Nagel, E., Luhman, K. L., Watson, D. M., Calvet, N., Muzerolle, J., & McClure, M. 2010, ApJ, 717, 441

Furlan, E., Hartmann, L., Calvet, N., D'Alessio, P., Franco-Hernández, R., Forrest, W. J., Watson, D. M., Uchida, K. I., Sargent, B., Green, J. D., Keller, L. D., & Herter, T. L. 2006, ApJS, 165, 568

Gregorio-Hetem, J. & Hetem, A. 2002, MNRAS, 336, 197

Guilloteau, S., Dutrey, A., & Simon, M. 1999, A&A, 348, 570

Hartmann, L., Calvet, N., Gullbring, E., & D'Alessio, P. 1998, ApJ, 495, 385

Hashimoto, J., Dong, R., Kudo, T., Honda, M., McClure, M. K., Zhu, Z., Muto, T., Wisniewski, J., Abe, L., Brandner, W., Brandt, T., Carson, J., Egner, S., Feldt, M., Fukagawa, M., Goto, M., Grady, C. A., Guyon, O., Hayano, Y., Hayashi, M., Hayashi, S., Henning, T., Hodapp, K., Ishii, M., Iye, M., Janson, M., Kandori, R., Knapp, G., Kusakabe, N., Kuzuhara, M., Kwon, J., Matsuo, T., Mayama, S., McElwain, M. W., Miyama, S., Morino, J.-I., Moro-Martin, A., Nishimura, T., Pyo, T.-S., Serabyn, G., Suenaga, T., Suto, H., Suzuki, R., Takahashi, Y., Takami, M., Takato, N., Terada, H., Thalmann, C., Tomono, D., Turner, E. L., Watanabe, M., Yamada, T., Takami, H., Usuda, T., & Tamura, M. 2012, ApJ, 758, L19

Hashimoto, J., Tamura, M., Muto, T., Kudo, T., Fukagawa, M., Fukue, T., Goto, M., Grady, C. A., Henning, T., Hodapp, K., Honda, M., Inutsuka, S., Kokubo, E., Knapp, G., McElwain, M. W., Momose, M., Ohashi, N., Okamoto, Y. K., Takami, M., Turner, E. L., Wisniewski, J., Janson, M., Abe, L., Brandner, W., Carson, J., Egner, S., Feldt, M., Golota, T., Guyon, O., Hayano, Y., Hayashi, M., Hayashi, S., Ishii, M., Kandori, R., Kusakabe, N., Matsuo, T., Mayama, S., Miyama, S., Morino, J.-I., Moro-Martin, A., Nishimura, T., Pyo, T.-S., Suto, H., Suzuki, R., Takato, N., Terada, H., Thalmann, C., Tomono, D., Watanabe, M., Yamada, T., Takami, H., & Usuda, T. 2011, ApJ, 729, L17

Hinkley, S., Oppenheimer, B. R., Soummer, R., Brenner, D., Graham, J. R., Perrin, M. D., Sivaramakrishnan, A., Lloyd, J. P., Roberts, Jr., L. C., & Kuhn, J. 2009, ApJ, 701, 804

Honda, M., Inoue, A. K., Okamoto, Y. K., Kataza, H., Fukagawa, M., Yamashita, T., Fujiyoshi, T., Tamura, M., Hashimoto, J., Miyata, T., Sako, S., Sakon, I., Fujiwara, H., Kamizuka, T., & Onaka, T. 2010, ApJ, 718, L199

Hughes, A. M., Andrews, S. M., Espaillat, C., Wilner, D. J., Calvet, N., D'Alessio, P., Qi, C., Williams, J. P., & Hogerheijde, M. R. 2009, ApJ, 698, 131

Hughes, A. M., Wilner, D. J., Calvet, N., D'Alessio, P., Claussen, M. J., & Hogerheijde, M. R. 2007, ApJ, 664, 536

Isella, A., Natta, A., Wilner, D., Carpenter, J. M., & Testi, L. 2010, ApJ, 725, 1735

Isella, A., Pérez, L. M., & Carpenter, J. M. 2012, ApJ, 747, 136

Itoh, Y., Tamura, M., Hayashi, S. S., Oasa, Y., Fukagawa, M., Kaifu, N., Suto, H., Murakawa, K., Doi, Y., Ebizuka, N., Naoi, T., Takami, H., Takato, N., Gaessler, W., Kanzawa, T., Hayano, Y., Kamata, Y., Saint-Jacques, D., & Iye, M. 2002, PASJ, 54, 963

Kessler-Silacci, J. E., Hillenbrand, L. A., Blake, G. A., & Meyer, M. R. 2005, ApJ, 622, 404

Kim, S.-H., Martin, P. G., & Hendry, P. D. 1994, ApJ, 422, 164

Krist, J. E., Stapelfeldt, K. R., Golimowski, D. A., Ardila, D. R., Clampin, M., Martel, A. R., Ford, H. C., Illingworth, G. D., & Hartig, G. F. 2005, AJ, 130, 2778

Kusakabe, N., Grady, C. A., Sitko, M. L., Hashimoto, J., Kudo, T., Fukagawa, M., Muto, T., Wisniewski, J. P., Min, M., Mayama, S., Werren, C., Day, A. N., Beerman, L. C., Lynch, D. K., Russell, R. W., Brafford, S. M., Kuzuhara, M., Brandt, T. D., Abe, L., Brandner, W., Carson, J., Egner, S., Feldt, M., Goto, M., Guyon, O., Hayano, Y., Hayashi, M., Hayashi, S. S., Henning, T., Hodapp, K. W., Ishii, M., Iye, M., Janson, M., Kandori, R., Knapp, G. R., Matsuo, T., McElwain, M. W., Miyama, S., Morino, J.-I., Moro-Martin, A., Nishimura, T., Pyo, T.-S., Suto, H., Suzuki, R., Takami, M., Takato, N., Terada, H., Thalmann, C., Tomono, D., Turner, E. L., Watanabe, M., Yamada, T., Takami, H., Usuda, T., & Tamura, M. 2012, ApJ, 753, 153

Laor, A. & Draine, B. T. 1993, ApJ, 402, 441

Mathews, G. S., Williams, J. P., & Ménard, F. 2012, ApJ, 753, 59

Metchev, S. A., Hillenbrand, L. A., & Meyer, M. R. 2004, ApJ, 600, 435

Muto, T., Grady, C. A., Hashimoto, J., Fukagawa, M., Hornbeck, J. B., Sitko, M., Russell, R., Werren, C., Curé, M., Currie, T., Ohashi, N., Okamoto, Y., Momose, M., Honda, M., Inutsuka, S., Takeuchi, T., Dong, R., Abe, L., Brandner, W., Brandt, T., Carson, J., Egner, S., Feldt, M., Fukue, T., Goto, M., Guyon, O., Hayano, Y., Hayashi, M., Hayashi, S., Henning, T., Hodapp, K. W., Ishii, M., Iye, M., Janson, M., Kandori, R., Knapp, G. R., Kudo, T., Kusakabe, N., Kuzuhara, M., Matsuo, T., Mayama, S., McElwain, M. W., Miyama, S., Morino, J.-I., Moro-Martin, A., Nishimura, T., Pyo, T.-S., Serabyn, E., Suto, H., Suzuki, R., Takami, M., Takato, N., Terada, H., Thalmann, C., Tomono, D., Turner, E. L., Watanabe, M., Wisniewski, J. P., Yamada, T., Takami, H., Usuda, T., & Tamura, M. 2012, ApJ, 748, L22

Paardekooper, S.-J. & Mellema, G. 2006, A&A, 453, 1129

Panić, O., Hogerheijde, M. R., Wilner, D., & Qi, C. 2008, A&A, 491, 219

Perrin, M. D., Graham, J. R., Kalas, P., Lloyd, J. P., Max, C. E., Gavel, D. T., Pennington, D. M., & Gates, E. L. 2004, Science, 303, 1345

Piétu, V., Dutrey, A., Guilloteau, S., Chapillon, E., & Pety, J. 2006, A&A, 460, L43

Piétu, V., Gueth, F., Hily-Blant, P., Schuster, K.-F., & Pety, J. 2011, A&A, 528, A81

Quanz, S. P., Schmid, H. M., Geissler, K., Meyer, M. R., Henning, T., Brandner, W., & Wolf, S. 2011, ApJ, 738, 23

Riaud, P., Mawet, D., Absil, O., Boccaletti, A., Baudoz, P., Herwats, E., & Surdej, J. 2006, A&A, 458, 317

Rice, W. K. M., Armitage, P. J., Wood, K., & Lodato, G. 2006, MNRAS, 373, 1619

Robitaille, T. P., Whitney, B. A., Indebetouw, R., Wood, K., & Denzmore, P. 2006, ApJS, 167, 256

Shakura, N. I. & Sunyaev, R. A. 1973, A&A, 24, 337

Skrutskie, M. F., Dutkevitch, D., Strom, S. E., Edwards, S., Strom, K. M., & Shure, M. A. 1990, AJ, 99, 1187

Strom, K. M., Strom, S. E., Edwards, S., Cabrit, S., & Skrutskie, M. F. 1989, AJ, 97, 1451

Suzuki, R., Kudo, T., Hashimoto, J., Carson, J., Egner, S., Goto, M., Hattori, M., Hayano, Y., Hodapp, K., Ito, M., Iye, M., Jacobson, S., Kandori, R., Kusakabe, N., Kuzuhara, M., Matsuo, T., McElwain, M., Morino, J.-I., Oya, S., Saito, Y., Shelton, R., Stahlberger, V., Suto, H., Takami, H., Thalmann, C., Watanabe, M., Yamada, H., & Tamura, M. 2010, in Society of Photo-Optical Instrumentation Engineers (SPIE) Conference Series, Vol. 7735, Society of Photo-Optical Instrumentation Engineers (SPIE) Conference Series

Tamura, M. 2009, in American Institute of Physics Conference Series, Vol. 1158, American Institute of Physics Conference Series, ed. T. Usuda, M. Tamura, & M. Ishii, 11–16

Tanii, R., Itoh, Y., Kudo, T., Hioki, T., Oasa, Y., Gupta, R., Sen, A. K., Wisniewski, J. P., Muto, T., Grady, C. A., Hashimoto, J., Fukagawa, M., Mayama, S., Hornbeck, J., Sitko, M. L., Russell, R. W., Werren, C., Curé, M., Currie, T., Ohashi, N., Okamoto, Y., Momose, M., Honda, M., Inutsuka, S.-i., Takeuchi, T., Dong, R., Abe, L., Brandner, W., Brandt, T. D., Carson, J., Egner, S. E., Feldt, M., Fukue, T., Goto, M., Guyon, O., Hayano, Y., Hayashi, M., Hayashi, S. S., Henning, T., Hodapp, K. W., Ishii, M., Iye, M., Janson, M., Kandori, R., Knapp, G. R., Kusakabe, N., Kuzuhara, M., Matsuo, T., McElwain, M. W., Miyama, S., Morino, J.-i., Moro-Martín, A., Nishimura, T., Pyo, T.-S., Serabyn, E., Suto, H., Suzuki, R., Takami, M., Takato, N., Terada, H., Thalmann, C., Tomono, D., Turner, E. L., Watanabe, M., Yamada, T., Takami, H., Usuda, T., & Tamura, M. 2012, PASJ, 64, 124

Thalmann, C., Grady, C. A., Goto, M., Wisniewski, J. P., Janson, M., Henning, T., Fukagawa, M., Honda, M., Mulders, G. D., Min, M., Moro-Martín, A., McElwain, M. W., Hodapp, K. W., Carson, J., Abe, L., Brandner, W., Egner, S., Feldt, M., Fukue, T., Golota, T., Guyon, O., Hashimoto, J., Hayano, Y., Hayashi, M., Hayashi, S., Ishii, M., Kandori, R., Knapp, G. R., Kudo, T., Kusakabe, N., Kuzuhara, M., Matsuo, T., Miyama, S., Morino, J.-I., Nishimura, T., Pyo, T.-S., Serabyn, E., Shibai, H., Suto, H., Suzuki, R., Takami, M., Takato, N., Terada, H., Tomono, D., Turner, E. L., Watanabe, M., Yamada, T., Takami, H., Usuda, T., & Tamura, M. 2010, ApJ, 718, L87

Whitney, B. A., Wood, K., Bjorkman, J. E., & Cohen, M. 2003a, ApJ, 598, 1079

Whitney, B. A., Wood, K., Bjorkman, J. E., & Wolff, M. J. 2003b, ApJ, 591, 1049

Williams, J. P. & Cieza, L. A. 2011, ARA&A, 49, 67

Wood, K., Wolff, M. J., Bjorkman, J. E., & Whitney, B. 2002, ApJ, 564, 887

Zhu, Z., Nelson, R. P., Dong, R., Espaillat, C., & Hartmann, L. 2012, ApJ, 755, 6

Zhu, Z., Nelson, R. P., Hartmann, L., Espaillat, C., & Calvet, N. 2011, ApJ, 729, 47

Chapter 5

The Structure of Transitional Disks J1604

Abstract

Transitional protoplanetary disks mark a crucial stage in disk evolution. We perform radiative transfer modeling of the disk+gap structure for the Upper Scorpius pre-transitional object [PZ99] J160421.7-213028, which has a heavily depleted gap ~ 60 AU in radius. Spatially resolved observations at both NIR and sub-mm wavelengths are combined to study the distribution of the small (sub-micron-sized) and big (mm-sized) dust. We present disk models which fit the SED, direct H-band polarized light imaging, and 880μm visibility curve simultaneously. The constraints on several key parameters which are crucial in distinguishing different gap clearing mechanisms are investigated, including the gap size, the depletion inside the gap, and the sharpness of the gap edge, all for both the small and big dust. Our modeling shows that the big and small dust in J1604 share similar gap sizes and relatively sharp gap edges. However, the small dust has to be depleted by at least a factor of 1000 at the gap edge to reproduce the H-band images, while the big dust needs to be depleted by only a factor of $\sim$10 in the same region to match the sub-mm observations, suggesting a decoupling between the two. In terms of producing such a system, dynamical interaction with companion(s) seems to be more plausible than various photoevaporation and grain growth models, though some cautions still exist for the former.

1 Introduction

Pre-transitional and transitional disks are protoplanetary disks with a central depleted region (a cavity or a gap[1]). Their existence was first suggested by the distinctive mid-infrared (MIR) dip on their spectral energy distribution (e.g. Strom et al. 1989; Skrutskie et al. 1990, using Infrared Astronomical Satellite data, and Calvet et al. 2005; Furlan et al. 2006; Espaillat et al. 2007a,b, 2008, using the Infrared Spectrograph on board the Spitzer telescope), and later confirmed by spatially resolved observations at sub-mm wavelengths (e.g. Piétu et al., 2006; Hughes et al., 2007; Brown et al., 2009; Hughes et al., 2009; Isella et al., 2010; Andrews et al., 2011; Mathews et al., 2012; Cieza et al., 2012a; Isella et al., 2012; Andrews et al., 2012). Very recently, Subaru also revealed cavities in some disks using high resolution direct imaging at NIR (Thalmann et al., 2010; Hashimoto et al., 2012; Mayama et al., 2012) and chapter 4, and mid-infrared wavelengths (Honda et al., 2012). These objects mark a crucial phase in the disk evolution from full gaseous disks to gas-depleted disks. In addition, they are likely to arise because of planet formation in protoplanetary disks, and therefore can yield a lot of information about the planet formation process (Williams & Cieza, 2011).

[1] In general, we assign the term "cavity" to a structure which extends all the way to the disk center, and the term "gap" to a structure which spans only a range in radius.

Protoplanetary disks contain both gas and dust with a range of particle sizes. The dust in disks start from the pristine interstellar medium (ISM) dust in the star forming environment, which is typically at sub-micron sizes. Observations show that protoplanetary disks disappear ~ 10 Myr after their formation (Hartmann et al., 1998), presumably because the initial ISM dust grains coagulate and grow into bigger particles, which eventually turn into planetesimals. Therefore, a "middle stage" ∼mm-sized dust population should exist in this evolutionary sequence. For the purpose of modeling observational signals, disks may be very crudely approximated by three components: (1) gas, which is vertically supported by thermal pressure and in hydrostatic equilibrium; (2) (sub-)micron-sized dust (hereafter small dust), which tends to be well coupled to the gas; and (3) ∼mm-sized dust (hereafter big dust)[2], which tends to collapse to a thin layer at the disk mid-plane due to gravitational settling (Dullemond & Dominik, 2004a,b, 2005). Various observations probe the structures of these components in different ways. For the SED, small dust dominates the excess at short wavelengths, while big dust contributes mostly at long wavelengths, due to the difference in opacity. For spatially resolved imaging, the disks are seen at NIR wavelengths via light scattered from the surface of the disk, which is dominated by the small dust, due to its larger vertical extent, higher scattering efficiency, and higher surface/mass ratio. The continuum emission at sub-mm wavelengths is mostly from the big dust, and because normally the disks are optically thin at these wavelengths, the spatial distribution of sub-mm continuum emission traces the volume density of the big dust (Andrews et al., 2011). Finally, mapping the molecular line emission provides information on the spatial distribution of the gas (Qi et al., 2004).

Several physical processes have been proposed for clearing the cavity or gap in these transitional systems, with the leading hypothesises being binary/planets, photoevaporation, and grain growth (see the discussion in Andrews et al., 2011). Currently, the situation is unclear, and different mechanisms may be responsible for different sub-groups of transitional disks (Cieza et al., 2012b; Owen & Clarke, 2012). Here we discuss the characteristic features in the disk structure which may be produced by these mechanisms, and possible ways to distinguish them observationally.

1. Tidal interaction between companions and the disk may truncate the disk. Artymowicz & Lubow (1994) investigated the gap opening process by a high mass companion in the disk, possibly a star, while the less massive companions (i.e. planets) case has been studied by Lin & Papaloizou (1986b,a) and Bryden et al. (1999). Recently, Zhu et al. (2011) and Dodson-Robinson & Salyk (2011) explored the possibility of opening a wide gap by multiple planets. Recently, companions (or candidates) which may have cleared out the cavities have indeed been found in some systems (Huélamo et al., 2011; Kraus & Ireland, 2012; Biller et al., 2012). Since gap opening by companion(s) is through gravitational interactions, we expect all disk components to show the same radial distribution (though the dust distribution inside the gap could be complicated by the dynamical coupling between the gas and dust particles at the gap edge, see Zhu et al. 2012, and point 3 below). The gap edges are predicted to be sharp. Further, since the companion may not affect the immediate area

[2]Technically, the upper limit of the size distribution in the grain growth process may be arbitrarily large, i.e. to cm-sized or larger. However since these particles are not readily detected at current observational sensitivities, they are not included in the modeling work in this chapter, and the dust size upper limit is arbitrarily cut at 1 mm.

around the central star, an innermost disk may remain, depending on how much of the accretion flow onto the central star can pass through the gap and the planet(s).

2. Photoevaporation. Stellar radiation ionizes surface layers of the disk, and can launch a wind if the thermal speed of the gas exceeds the escape velocity (Clarke et al., 2001). If the disk accretion rate is smaller than the mass loss rate due to the disk wind, as expected at later stage in the disk evolution, a gap may be opened (Owen et al., 2010). In addition, photoevaporation may be combined with the magnetorotational instability to clear the disk (Chiang & Murray-Clay, 2007). Photoevaporation works directly on gas and very small dust grains (well below micron-sized), leaving optically thin large dust that feels effects of radiation pressure from the star. Clearing of bigger grains needs a strong coupling between the solids and the gas (Alexander & Armitage, 2007). Therefore, we may see a spatial decoupling between gas and dust of different sizes inside the gap, in terms of gap size and depletion factor. This scenario does not produce a significant accretion onto the central star. The gap edge in photoevaporation models tends to be sharp (Alexander & Armitage, 2007). Some transitional disks with low disk mass and negligible accretion have been associated with photoevaporation Cieza et al. (2010).

3. Grain growth. Grain growth has been known to introduce dips in the SED of disks (Dullemond & Dominik, 2005; D'Alessio et al., 2006). Recently, Birnstiel et al. (2012) concluded that grain growth alone cannot reproduce the characteristic sub-mm cavities. On the other hand, Zhu et al. (2012) suggest that dust filtration (Rice et al., 2006; Paardekooper & Mellema, 2006) in combination with grain growth may be an alternative for gap clearing. In this model, a pressure bump, which naturally forms at the edge of a shallow gap opened by a low mass planet, acts like a filter, which traps the big dust but lets through the small dust. Spatial decoupling between the small and big dust is natural in this model. The surface density of the big dust could drop significantly inside the gap, but the small dust may only see a modest depletion across the gap edge. If grain growth occurs inside the gap, the big and small dust may have different distributions. Also, gas may exist inside the gap in this picture, with an accretion rate comparable to those of classical T-Tauri stars.

To distinguish the above scenarios, the key questions to ask are:

1. Are the cavity/gap sizes the same for various disk components?

2. How sharp are the gap edges? Are they different for different components?

3. Are the components spatially coupled, particularly inside the gap, in terms of depletion and radial profile?

4. Is there an inner disk left? If so, how much material? Are the central stars accreting?

An ideal system to test these scenarios is a pre-transitional object, [PZ99] J160421.7-213028 (hereafter J1604) in the Upper Scorpius star forming region, whose ~ 60 AU radius gap is vividly spatially revealed in both direct imaging of H-band polarized scattered light (S. Mayama et al. 2012, submitted), and interferometric observations of molecular line emission (CO J=3$\rightarrow$2) and continuum thermal emission at 880μm (Mathews et al., 2012). This system has a stellar age of ~ 3.7Myr (Preibisch & Zinnecker, 1999). The newly available NIR PI image produced by the Strategic Explorations of Exoplanets and Disks with Subaru project (SEEDS, Tamura 2009, for

AB Aur, Hashimoto et al. 2011; SAO 206462, Muto et al. 2012; MWC 480, Kusakabe et al. 2012; and UX Tau A, Tanii et al. 2012) has a very high spatial resolution ($\sim 0.07''$, or $\sim$10 AU at the distance of J1604). In addition, working with the polarized light under the polarization differential imaging mode (Hinkley et al., 2009) enables a small inner working angle, $\sim 0.2''$ or ~ 29 AU in this case, well smaller than the gap size, which allows us to study the inner gap structure.

This dataset enables us to independently probe the disk+gap structure for all three disk components. J1604 also has a well-sampled spectral energy distribution (SED) measurement covering a wide range of wavelengths (Mathews et al., 2012), providing additional constraints on the dust distribution. Using radiative transfer modeling, we fit all three observations simultaneously, and provide constraints on the disk+gap structure for this system. Particularly, resolved observations with high spatial resolution at both NIR and sub-mm wavelengths are used together in the modeling effort. The observational data used in our fitting include the photometric SED (including ground based optical photometry, 2-MASS, WISE, Spitzer IRAC, AKARI, and SMA), a Spitzer IRS spectrum, the Subaru H-band PI image and its radial profile (S. Mayama et al. 2012, submitted), and the SMA visibility curve of the 880μm continuous emission (Mathews et al., 2012). We are interested in addressing the questions raised above about distinguishing the possible gap clearing mechanisms. We focus on the basic global structures of the disk and the cavity, and defer a comprehensive discussion of the local details to future studies. We do not attempt to fit the CO line emission in this work, since our new observations provide no additional information on the gas component of the disk, and we focus only on the spatial distribution of the dust.

Following the last chapter, here we present the second study in this series of modeling the structures of transitional disks, based on SEEDS direct NIR imaging results and other observations. We introduce our radiative transfer modeling in Section 2. The fiducial model of J1604, which provides a good fit to all the available observations, is presented in Section 3. Based on the fiducial model, we explore the parameter space in Section 4, and study what kind of constraints we can cast on the disk+gap structures. We comment on various transitional system formation and gap clearing mechanisms in Section 5, followed by a short summary in Section 6.

2 Radiative transfer modeling

We carry out Monte Carlo radiative transfer modeling using the Whitney code (Whitney et al. 2003b,a, B. Whitney et al. 2012, in prep.). The physical structures of transitional disks are rather complicated. In this chapter, we aim at using relatively simple disk models, to reveal the global structure of the cavity at both NIR and sub-mm wavelengths. For this purpose, we largely adopt the disk models assumed in Andrews et al. (2011) and in chapters 3 and 4 (see also models in Andrews et al. 2009 and Hughes et al. 2010, which share similar large scale structures with the models here), which is briefly introduced below.

We use a pre-main sequence star of spectral type K2, radius 1.4 $R_\odot$, mass 1.0 $M_\odot$, and temperature 4500 K (Mathews et al., 2012). The star is considered to have no significant accretion, as shown by various accretion indicators such as hydrogen recombination lines (Mathews et al., 2012, where an upper limit of $10^{-11} M_\odot$/yr is argued). An axisymmetric dust disk starts from the dust sublimation radius $R_{\rm sub}$, corresponding to a sublimation temperature of $\sim 1600K$, and extends to the disk outer radius $R_{\rm out}$, which is assumed to be 133 AU. $R_{\rm sub}$ is ~ 0.055 AU in our models given the assumed central star, and the value of $R_{\rm out}$ is more or less arbitrary (our results do not depend on the choice of $R_{\rm out}$, as long as it is large enough). The

surface density $\Sigma(R)$ for each dust population has the functional form

$$\Sigma(R) \propto \left(\frac{R_c}{R}\right)^{\alpha} e^{-R/R_c}, \tag{5.1}$$

where R_c is the exponential cut off length scale, fixed as 100 AU in our models (Mathews et al., 2012), and α is the power law index, which may be radius dependent. Note that the exponential taper of the outer disk is supported by recent works in dust continuum and molecular gas emission observations (Hughes et al., 2008).

Following the assumptions about the dust in recent transitional disk modeling works (e.g. Andrews et al., 2011, and chapters 3 and 4), we assume two dust populations in the models: the sub-micron-sized small dust, and the ∼mm-sized big dust. We adopt the interstellar medium dust model of Kim et al. (1994) for our small dust, and dust Model 1 from Wood et al. (2002) for our big dust, which has a power law size distribution up to 1 mm (with a power law index 3) with an exponential cutoff at large size. The opacity of these dust models is shown in Figure 5.1. As we have stated in Section 1, the choice of having two dust populations is not only motivated physically by the dust evolution in disks, but also needed to account for the signals at both NIR and sub-mm wavelengths (see also Whitney et al. 2003a). In this work, we fix the big-to-small-dust mass ratio as 0.85/0.15, i.e. 85% of the total dust mass is in the big dust. Below we use subscripts "b" and "s' for various quantities relating to big and small dust, respectively. Irradiated (i.e. passive) protoplanetary disks are roughly isothermal in the vertical direction, except at the very tenuous upper layers (Dullemond et al., 2002). As a result of hydrostatic equilibrium, the density distribution of the gas in the vertical direction can be approximated by a Gaussian profile. The small grains tend to be well coupled with the gas, so that the two share similar vertical structures, while the big grains tend to settle to the disk mid-plane (Dullemond & Dominik, 2004b, 2005; D'Alessio et al., 2006). In this work, we assume Gaussian profiles for both dust populations with different scale heights (e.g. Andrews et al., 2011, chapter 3),

$$\rho(R, z) = \frac{\Sigma(R)}{\sqrt{2\pi}h} e^{-z^2/2h^2}, \tag{5.2}$$

where z is the vertical dimension, and h is the parametrized scale height, with $h_{\rm b}$ (scale height for the big dust) assumed to be much smaller than $h_{\rm s}$ (scale height for the small dust). Radially, both scale heights vary with radius as

$$h \propto R^{\beta}, \tag{5.3}$$

where β is a constant power law index. We have very little constraint over β, as choices from 1.1 to 1.2, close to the canonical value $\sim 1.25 - 1.3$ for irradiated disks (Chiang & Goldreich, 1997; Hartmann et al., 1998), result in little difference on the modeling results.

In general, our disk models have a rim+gap structure for the small dust, a cavity+gap structure for the big dust, and an outer disk for both, as illustrated in Figure 5.2. As we will see in Section 3, the rim structure is needed to account for the NIR excess, and the gap/cavity structures are needed to account for the deficit of scattered light and sub-mm emission in the resolved observations at NIR and sub-mm wavelengths. The small dust has a rim structure located at the dust sublimation radius $R_{\rm sub} \sim 0.055$ AU to 0.07 AU, a gap from inner edge $R^{\rm i}_{\rm gap,s}$ (i.e. 0.07 AU) to outer edge $R^{\rm o}_{\rm gap,s}$, and an outer disk from $R^{\rm o}_{\rm gap,s}$ to $R_{\rm out}$ (133 AU). The surface

density of the small dust $\Sigma_{\rm s}$ is given by

$$\Sigma_{\rm s}(R) = \begin{cases} \delta_{\rm rim}\Sigma_{\rm s,0}\left(\frac{R_c}{R}\right)^{\alpha_{\rm s}} e^{-R/R_c} & \text{for } R_{\rm sub} \leq R < R^{\rm i}_{\rm gap,s} \\ \delta_{\rm gap,s}\Sigma_{\rm s,0}\left(\frac{R_c}{R}\right)^{\alpha_{\rm s}} e^{-R/R_c} & \text{for } R^{\rm i}_{\rm gap,s} \leq R < R^{\rm o}_{\rm gap,s} \\ \Sigma_{\rm s,0}\left(\frac{R_c}{R}\right)^{\alpha_{\rm s}} e^{-R/R_c} & \text{for } R \geq R^{\rm o}_{\rm gap,s} \end{cases}$$

where $\Sigma_{\rm s,0}$ is the normalization factor, $\delta_{\rm rim}$ is a constant rim surface density scaling factor, and $\delta_{\rm gap,s}$ is a radius dependent gap depletion factor.

For the big dust, we assume a similar structure as in Mathews et al. (2012), which has a completely depleted cavity from 0 to $R_{\rm cav,b}$[3], a gap region from $R_{\rm cav,b}$ to $R_{\rm gap,b}$, and an outer disk from $R_{\rm gap,b}$ to $R_{\rm out}$. The surface density of the big dust $\Sigma_{\rm b}$ is given by

$$\Sigma_{\rm b}(R) = \begin{cases} 0 & \text{for } R < R_{\rm cav,b} \\ \delta_{\rm gap,b}\Sigma_{\rm b,0}\left(\frac{R_c}{R}\right)^{\alpha_{\rm b}} e^{-R/R_c} & \text{for } R_{\rm cav,b} \leq R < R_{\rm gap,b} \\ \Sigma_{\rm b,0}\left(\frac{R_c}{R}\right)^{\alpha_{\rm b}} e^{-R/R_c} & \text{for } R \geq R_{\rm gap,b} \end{cases}$$

where $\Sigma_{\rm b,0}$ is the normalization factor, and $\delta_{\rm gap,b}$ is a radius dependent gap depletion factor. We note that our choices of the surface density radial profile ($\Sigma(R) \propto \Sigma_0\left(\frac{R_c}{R}\right)^{\alpha} e^{-R/R_c}$) are common in protoplanetary disk modeling (e.g. Andrews et al., 2011, chapter 3), and are consistent with physical models of viscous accretion disks (e.g. Hartmann et al., 1998), and resolved observations at mm wavelengths (e.g. Williams & Cieza, 2011).

We produce SED, H-band polarized light images, and full intensity images of the 880 μm continuum emission using Monte Carlo radiative transfer simulations. J1604 is assumed to be at a distance of 145 pc (*Hipparcos* observation, de Zeeuw et al. 1999), so that $1''$ corresponds to 145 AU. For the H-band images, we use the PDI observational mode without a coronagraph mask in our modeling, and convolve the raw model images by an observed HiCIAO point spread function, to reproduce the SEEDS observations (see chapter 3 for details). The inner working angle of the H-band images, $\psi_{\rm in}$, is assumed to be $0.2''$ ($\sim$29 AU) in radius. For the millimeter image, we convolved the model images by a Gaussian kernel with a resolution $0.34''$, in order to be compatible with the SMA observations (Mathews et al., 2012). The disk inclination is very small, $\sim 6^\circ$ ($\cos 6^\circ = 0.99$), as determined from the CO velocity map (Mathews et al., 2012). We assume that the disk is face-on (other choices of inclination, i.e. 10° as in S. Mayama et al. 2012, submitted, make basically no difference) and axisymmetric, to calculate the surface brightness radial profile (SBRP) of the H-band images, and the visibility curve of the 880μm images. For the SBRP, we measure the 2π azimuthally averaged SB at various radial bins $0.05''$ in width. The visibility is calculated from the model 880μm brightness profile by a Hankel transform (Berger & Segransan, 2007)

$$\nu(r) = 2\pi \int_0^\infty I(a) J_0(2\pi a r) a da, \tag{5.4}$$

where a and r are the polar coordinates in the object and (u,v) plane, respectively, $I(a)$ is the brightness profile, and J_0 is the zeroth-order Bessel function of the first kind.

[3]Not true for two models in Section 4.3. See below.

3 A fiducial disk model

In this section, we introduce a fiducial model for J1604, which simultaneously fits the observed SED, direct imaging of H-band polarized light, and resolved observations at sub-mm wavelengths. Particularly, the model successfully reproduces the signals of the cavity in all three observations. The model parameters are listed in Table 5.1. The model H-band images and the comparison with the SEEDS observation (S. Mayama et al. 2012, submitted) are shown in Figure 5.3, and the model 880μm images are shown in Figure 5.4. Figure 5.5 plots the surface density profile of both dust populations (a), the model SED (b), the SBRP of the H-band images (c), and the 880μm visibility curve (d), along with the observations.

The total dust mass in the fiducial model is 0.085 $M_{\rm J}$ (85% of it is in big dust), similar to Mathews et al. (2012, $\sim 0.1 M_{\rm J}$). For the small dust we have an inner rim extended from $\sim 0.055 AU$ ($R_{\rm sub}$) to 0.07 AU, a completely depleted gap region from 0.07 AU to 60 AU, and an outer disk from 60 AU to 133 AU, while for the big dust we have a completely empty cavity inside 20 AU, a depleted gap region from 20 AU to 70 AU with a depletion factor $\delta_{\rm gap,b} = 0.1$, and an outer disk from 70 AU to 133 AU. The scale height of small dust at $R^{\rm o}_{\rm gap,s} = 60$ AU is $h/R \approx 0.11$, corresponding to a temperature of 43 K assuming an isothermal hydrostatic equilibrium disk vertical structure (chapter 3). This lies between the model disk mid-plane temperature of 33K at $R^{\rm o}_{\rm gap,s}$, and the temperature in the disk upper atmosphere, 83 K. The distribution of the big dust is largely adopted from the model by Mathews et al. (2012), of the SMA observations, while the distribution of the small dust is constrained by both the SED and the H-band image.

J1604 has been noted to be a possible variable source by Dahm & Carpenter (2009), due to the observational inconsistency between the IRAC data and the Spitzer IRS spectrum. Mathews et al. (2012) ignored the IRS spectrum, and the authors treated the system as having no IR excess up to $\sim 10\mu$m or so, corresponding to a disk model which has a completely depleted inner region. However, the newly available WISE data points at 3.4 and 4.6 μm are more consistent with the IRS spectrum, and they indicate that J1604 does have a NIR excess (at least for some of the time). This kind of rapid variation in the SED has recently been reported by Melis et al. (2012) in the case of TYC 8241 2652 1, and its origin is currently unclear. The shorter wavelength part of the IRS spectrum is a Rayleigh-Jeans tail of a blackbody at $\sim$ 1500K, and the longer wavelength part is close to a Wien tail, with a deep dip in between showing no additional contribution. Together they suggest that the disk can be approximated by two components, one inner component responsible for the NIR excess (the NIR variation largely eliminates the possibility that a companion, rather than an inner disk, produces the NIR excess), and an outer disk for the excess at tens of μm, with no additional temperature components in between. The IRS spectrum does not have any silicate feature (at both $\sim 10\mu$m and $\sim 20\mu$m), which also indicates a lack of dust at silicate-feature-emitting temperature ($\sim 100 - 300$K, Draine 2011) in the gap region. This kind of SED structure has been previously reported for the pre-transitional object UX Tau A (Espaillat et al., 2007b), and it is explained by a disk rim on sub-AU scale as the high temperature component, and an outer gap edge at tens of AU as the low temperature component, with no dust in between. We adopt this picture for J1604. The agreement between our model SED and the observations is generally good, with the only drawback occurring at MIR, where the emission from the gap wall in our model is shifted about 5μm, or $\sim$ 20%, towards shorter wavelength (which also results in that fact that the deepest point in our model SED at about 15μm is not as deep as in the IRS spectrum). This difference could be caused by two possibilities: either the wall in our model is too close to the star, or the dust properties on the

wall are slightly different from what we assume (i.e. maybe bigger in sizes). Since the wall position is quite accurately determined from the scattered light image, as will be discussed below, the second possibility is more likely. We leave this issue for future investigation.

The model images at both H-band and 880μm reveal a clear inner depleted region, and quantitatively both the H-band SBRP and the sub-mm visibility curve match the observations very well. We note that we do not aim at reproducing the local details and non-axisymmetric features in the H-band images, such as the two dips on the east and west sides of the ring, and the fact that the north and south parts are slightly asymmetric, since our disk model is axisymmetric and the system is nearly face-on. Similarly, due to these simplifying assumptions, our model does not perfectly match the sub-mm visibility, which inevitably contains the signal from local non-axisymmetric features. A discussion on the possible origins of these structures is provided in S. Mayama et al. (2012, submitted). The gap sizes for the two dust populations are slightly different in the fiducial model. We will address this issue in the next section.

We stress that the fiducial model presented here only serves as an initial reproducing all the current data reasonably well, and based on which we explore the parameter space. Due to the number of freedoms in the models, and the complicate nature of transitional disk structures, it is impossible to carry out a classical χ^2 searching for an absolute "best" fit to the data (e.g. Andrews et al., 2011; Mathews et al., 2012). Therefore, the fiducial model here does not aim at providing a best fit, but rather a reasonable disk model which is consistent with the data. Also, as the constraints on some of the disk+gap parameters are rather weak (see Section 4), the fiducial model is by no means unique, i.e. the only one which can provide a good fit to all the observations (e.g., see models in Section 4.4). At last, some features in the fiducial model, such as the distinct gap structures for the two dust populations, are not motivated physically, as the main merit of this model is that it is simple so it facilitates the parameter space exploration.

4 Variation of the disk model parameters

In this section, we explore the parameter space based on the fiducial model introduced above, and study the constraints which the current dataset can provide on the disk+gap structure. The models are listed in Table 5.3. The surface density profiles, SED, azimuthally averaged H-band SBRP, and 880μm visibility curve, are shown in Figures 5.6-5.9, whenever relevant (we skip the modeling results, if the corresponding models produce largely the same results as the fiducial model). The parameters explored are the gap size (Section 4.1), the depletion inside the gap (Section 4.2 and Section 4.3), and the sharpness of the gap edges (Section 4.4).

4.1 Gap size (block "Gap Size" in Table 5.3, Figure 5.6)

To illustrate the effect of the gap size on various observations, we show simulations with 3 gap sizes for each dust population, i.e. 50, 60, and 70 AU for the small dust, and 60, 70, and 80 AU for the big dust. The model gap edges here are infinitely sharp (i.e. a discontinuity in surface density). In general, the effect on the SED is minor, as expected, since the peak wavelength of the emission from the wall $\lambda_{\rm p}$ only weakly depends on the radius of the gap as $\lambda_{\rm p} \propto R_{\rm gap}^{1/2}$. However, the size of gap in small dust has a prominent effect on the H-band image — a 50 AU (70 AU) gap simply leads to a too small (large) gap in the images to be consistent with the observation. The root mean square scatter of the observed SBRP can roughly tolerate a range of $R_{\rm gap,b}$ from 57 AU to 64 AU. On the other hand, the size of the big dust gap also dramatically affects the 880μm

visibility curve. A smaller $R_{\rm gap,b}$ pushes the nulls on the visibility curve towards longer deprojected baseline, and vise versa. Mathews et al. (2012) determined $R_{\rm gap,b}$ to be 72±3 AU using χ^2 fitting[4].

Based on the results, we conclude that while the gap sizes of the two dust populations are similar, we tentatively see a small but probably real difference between the two, independently constrained by resolved NIR and sub-mm observations, assuming simple gap models with infinitely sharp edges. We explore models with smoother gap edge structure in Section 4.4.

4.2 Small dust gap depletion (block "Small Dust Gap Depletion" in Table 5.3, Figure 5.7)

In this section, we vary the depletion of the small dust inside its gap. The SED and the H-band SBRP are sensitive to, and can independently constrains $\delta_{\rm gap,s}$ in different regions. The SED, particularly the NIR excess and the dip around 10μm, is sensitive to the amount of material at the inner disk, on AU scale. Increasing $\Sigma_{\rm s}$ in this region raises the IR excess at NIR to $\sim 20\mu$m, produces a stronger silicate feature, and reduces the IR excess beyond 20μm. To have a dip around 10μm as deep as the fiducial model (though still shallower than in the IRS spectrum) and to suppress the silicate feature, $\Sigma_{\rm s}$ right behind the rim (at ∼0.1 AU) cannot be higher than a few $\times 10^{-3}$ g/cm^2. On the other hand, the H-band SBRP, particularly the sharpness of the gap edge, is largely determined by $\delta_{\rm gap,s}$ at the edge (chapter 3). Reducing the contrast in $\Sigma_{\rm s}$ at the gap edge smooths the ring in the H-band image. To reproduce the sharpness of the gap edge seen in the SEEDS image, the drop in $\Sigma_{\rm s}$ across the edge needs to be a factor of 1000 or higher, while the data are fully consistent with $\delta_{\rm gap,s} = 0$ as in the fiducial model. We note that the conclusion about the depletion at the gap edge is independent of the small dust model we use, since different small dust models can only affect the absolute scale of the scattered light profile at the gap edge, but the contrast of the edge is robust in a relative sense.

Last, we investigate the rim shadowing effect on the SED. Being directly illuminated by the starlight, the rim may be heated to a high temperature, puffed up under hydrostatic equilibrium (assuming small dust is well coupled to the gas), and block the starlight from reaching the other disk. This effect reduces the temperature inside the gap and in the outer disk, shrinking them vertically assuming hydrostatic equilibrium, and resulting in a reduced IR excess from these regions (Dullemond & Dominik, 2004a; Andrews et al., 2011). Effectively, some amount of material can be *hidden* behind the rim without being betrayed by the SED. Models SDGapDep5-ThinGapX illustrate this phenomenon (Figure 5.7(c)). They have the same density structure as in model SDGapDep5, but have smaller scale height $h_{\rm s}$ inside the gap. They all produce a smaller IR excess between $\sim 5 - 20\mu$m than model SDGapDep5, and their overall SED is reasonably close to the fiducial model and the observations.

To summarize, the observed SED requires a heavily depleted gap behind the small rim structure, while the narrow ring in the SEEDS image can only be explained by a factor of 1000 drop in surface density for small dust at the gap edge. A completely depleted small dust gap from 0.07 AU to 60 AU is consistent with both observations.

[4]As they noted, the quoted standard deviations in their fit results do not have the classical meaning, due to the complexity of this problem, and the goodness of the fitting can only be compared on a relative level.

4.3 Big dust gap structure (block "Big Dust Gap Structure" in Table 5.3, Figure 5.8)

We examine the effect of different gap structure in the big dust in this section[5]. The constraints on the spatial distribution of the big dust has been thoroughly investigated by Mathews et al. (2012). Here we just intend to show some of the relevant parameter space exploration results, which facilitates our discussion of the coupling between the small and big dust in Section 5. Two kinds of models are tried here. The BDCavDep series varies $\delta_{\rm gap,b}$ while keeping the gap uniformly depleted, as in the fiducial model. The BDGapSmo series employs $\Sigma_{\rm b}$ profiles in which the surface density is continuous at the gap edge while decreasing inward.

In general, all these models have similar SEDs. The IR excess around 100μm drops slightly below the observed value if the gap is completely depleted, suggesting some 100μm emitting material is probably needed inside 70 AU to produce this excess. On the other hand, the structure of the gap strongly affects the 880μm visibility curve. A too high $\delta_{\rm gap,b}$ smooths the visibility curve, shifts the first and second nulls to longer baseline, and vise versa. Mathews et al. (2012) found the best fit value for $\log \delta_{\rm gap,b}$ to be -0.83 ± 0.35. Also, the BDGapSmo models have generally inconsistent visibility comparing with the observations. All their nulls are shifted towards longer baseline, which can be interpreted as having effectively "smaller" gap sizes.

To summarize, some amount of big dust inside the gap region ($\delta_{\rm gap,b} \sim 0.1$) is required to fit both the SED and the visibility, and the surface density of the big dust cannot be completely smooth across the gap edge.

4.4 Smooth gap edge (block "Smooth Gap Edge" in Table 5.3, Figure 5.9)

In this section, we explore "smooth" gap edge structures for both dust populations. Specifically, the key question is whether the big and small dust have to have spatially decoupled gap edges, as suggested in Section 4.1 assuming sharp gap edges. Both big and small dust in the models here have a transient structure between 60 to 70 AU, which "smoothly" joins the outer disk to the gap[6]. Specifically, model SmoothEdge3 has exactly the same radial dependence of the surface density for both dust populations inside this transient region.

In general, all these models produce results similar to the fiducial model, and all are grossly consistent with observations. At H-band, introducing this transient structure in the small dust makes the gap edge slightly wider, and shifts the peak of the SBRP slightly outward, due to the fact that the edge has a finite width, but otherwise the images look quite similar (in fact the residual image of model SmoothEdge1 looks marginally better than the fiducial model). The reason for this is that although both dust populations have the same transient region between 60 to 70 AU, the *effective* gap edges for the two, in terms of determining the observational properties at H-band and sub-mm wavelengths, are different. Though $\Sigma_{\rm s}$ peaks at 70 AU, the real scattering "edge" in these models is still roughly at 60 AU, since the 60 AU wall is directly illuminated by the central star so that it produces most of the scattering. On the other hand, the disk is

[5]In these models we choose to fix the total mass of the big dust instead of fixing the surface density at a certain radius (i.e. the gap outer edge), because the total mass of the big dust is the quantity directly measured by radio continuum observations.

[6]The $\Sigma_{\rm b}$ profile in these models is fixed, and the variation is on the $\Sigma_{\rm s}$ profile, since for the big dust we need to join the outer disk to the $\delta_{\rm gap,b} = 0.1$ gap, so $\Sigma_{\rm b}$ at the two sides of the transient region is fixed, while $\Sigma_{\rm s}$ at the inner side is free.

vertically optically thin at sub-mm, therefore the peak in the sub-mm emissivity always traces the $\Sigma_{\rm b}$ peak, which is 70 AU in these models, thus all these models have sub-mm properties similar to the fiducial model.

To summarize, by using a common 10 AU wide transient structure to "smoothly" connect the outer disk to the gap for both the big and small dust, we can have modeling results reproducing observations quite well, without assuming different gap sizes for the two dust populations.

5 Discussion

First, we comment on the consistency between the low accretion rate of J1604 and the surface density of the rim constrained by the NIR excess. For a steady Shakura & Sunyaev disk, the accretion rate $\dot{M}$ is related to the gas surface density $\Sigma_{\rm gas}$ as:

$$\frac{\alpha c_{\rm s}^2 \Sigma_{\rm gas}}{\Omega} \approx \frac{\dot{M}}{3\pi}, \tag{5.5}$$

where α is the Shakura-Sunyaev viscosity parameter, Ω is the angular velocity of the disk rotation, and $c_{\rm s}$ is the sound speed in the disk, given by $c_{\rm s} \approx \sqrt{kT/\mu}$ (T is the mid-plane temperature and μ is the average weight of the particles). At $\sim$0.055 AU, the $\dot{M}$ upper limit $10^{-11} M_\odot$/yr for J1604 requires $\Sigma_{\rm gas} \lesssim 1.5$ g cm^{-2}, assuming a temperature $T \sim 1500$ K, $\alpha \sim 0.01$, and $M \sim M_\odot$. If we assume a gas-to-dust-mass ratio of 100:1, this gas surface density is well consistent with the dust surface density at the rim, ~ 0.01 g/cm^2, determined from fitting the NIR excess of J1604.

We have shown above that J1604 has a large gap structure ~ 60 AU in radius in both the small and big dust, with similar gap sizes and sharp gap edges for both. This picture well supports a scenario where multiple planets open a gap, as proposed by Zhu et al. (2011, see also Section 1). In addition, the low accretion rate might be explained by the planets intercepting accretion flow passing through the gap. However, there are two cautions in this interpretation, one specifically for J1604, the other from a statistical point of view.

1. The small dust is strongly depleted in the gap. $\delta_{\rm gap,s}$ has an upper limits of 10^{-3} in the outer part of the gap, constrained by the NIR imaging, and the data is fully consistent with $\delta_{\rm gap,s} = 0$. It is difficult to have such a low depletion factor only by dynamical interaction between the planets and the disk, although it is technically possible if the companion is very massive and the disk viscosity is very low. Also, the big dust inside the gap does not see such a heavy depletion, with data being mostly consistent with $\delta_{\rm gap,b}$ on the order of 0.1 in the same region. In the dynamical gap opening scenario, we expect $\delta_{\rm gap,s}$ and $\delta_{\rm gap,b}$ to be on the same order of magnitude. Furthermore, the sign of this difference, $\delta_{\rm gap,b} \gg \delta_{\rm gap,s}$, is inconsistent with the dust filtration mechanism, which predict that the big dust should be more heavily depleted inside the gap, because of trapping by the pressure bump at the gap edge (Rice et al., 2006; Paardekooper & Mellema, 2006). However, additional dust growth inside the gap may be able to solve these problems, as grain growth inside the gap, not suppressed by destructive collisions between big grains due to the lack of them, may turn small grains into big grains, resulting in a heavier depletion for the small grains than for the big grains.

2. Current results from various planet hunting missions suggest low rates of occurrence of giant planet(s) at large separation (tens of AU) around mean sequence (MS) solar type stars, well

below 10% from the Gemini Deep Planet Survey Lafrenière et al. (2007), the Gemini NICI survey (M. Liu & B. Bowler, private communication), and our SEEDS survey. Systems like HR 8799 (Marois et al., 2008, 2010) with multiple giant planets at the right separation for opening giant gaps may be very rare. However, transitional disks with large cavities are very common: Andrews et al. (2011) concluded that at least $\sim 20\%$ (and maybe upto $\sim 70\%$) of the millimeter-bright disks have large dust-depleted cavities with $R^{\rm o}_{\rm gap} \gtrsim 15$ AU. This apparent difference between the occurrence rate of giant planets at large separation and transitional objects with giant cavities put this scenario into question. On the other hand, we note that there is a difference in age when comparing the two factors: the vast majority of the known planets are orbiting around MS stars, while transitional systems are present at a much younger age. The apparent inconsistency might be mediated if some of the large prevalence of gapped young disks is indeed caused by the presence of large planet(s), but that these systems experience evolution at a later stage (i.e. planet-planet gravitational scattering, planetary migration, or star-star encounters which perturb the orbits of the planets), which ejects the planets from the systems or move them away from the gap/cavity regions as they advance in age. Future detailed studies are needed.

Grain growth models have also been invoked for explaining transitional disks (Birnstiel et al., 2012). As these authors pointed out, grain growth alone can account for the dips in the SED, but fails to reproduce the large sub-mm cavities in resolved observations. Also, the sharp gap edge seen in J1604 is hard to explain by grain growth alone, as such models tend to produce smooth radial profile of the dust distribution (Garaud, 2007; Birnstiel et al., 2010). In addition, it is difficult to account for the fact that the gas component of this system is depleted at the inner region as well, as suggested by the low accretion rate and revealed by the CO line observations (Mathews et al., 2012). On the other hand, the dust filtration + grain growth model (Zhu et al. 2012, see also chapter 4) may remain as an alternative to explain the structure of the dust. More grain growth modeling under the context of dust filtration will be needed to explore this scenario.

Finally, we comment on photoevaporation models, which are grossly consistent with the large gap sizes and low accretion rate in J1604 (Owen et al., 2011, 2012). Also, the sharp gap edges are consistent with photoevaporation models (Alexander & Armitage, 2007). As noted in Section 1, photoevaporation directly affects only the gas component (and the smallest grains), so that depletion of dust needs to involve gas-dust coupling. Since the efficiency of this coupling depends on the size of the grains, different distributions of the big and small dust inside the gap, as seen in J1604, may be expected. However, current models predict a faster depletion for big dust inside the gap (Alexander & Armitage, 2007), which is opposite to what is seen in J1604. Furthermore, photoevaporation models have difficulties explaining why a rim structure is left behind at ~ 0.1 AU in the disk clearing process, since the clearing of the inner disk ($\lesssim 1$ AU, for both the gas and dust) is very fast in these models. Future models for the distribution of dust in the context of photoevaporation is encouraged.

6 Summary

In this chatper, through radiative transfer modeling we study the disk+gap structure for the pre-transitional object [PZ99] J160421.7-213028, whose giant inner depleted region ~ 60 AU in radius is clearly revealed in high spatial resolution observations at both NIR and sub-mm wavelengths. By conducting simultaneous fitting to the SED, Subaru-based H-band polarized

light imaging (S. Mayama et al. 2012, submitted), and SMA-based spatially resolved 880μm observations (Mathews et al., 2012), we are able to constrain the spatial distribution of the small (sub-micron) and big (up to mm-sized) dust grains at the same time. We focus on the disk parameters related to the coupling between the two, since they are the keys in distinguishing different gap depletion mechanisms. The main findings are:

1. The gap sizes for the big and small dust populations are similar for J1604. If models are forced to have discontinuities between the outer disk and the gap, current data suggest that the small dust population has a slightly smaller gap than the big dust population ($\sim$60 AU vs $\sim$70 AU). However, the observations are also consistent with models which feature similar density structure for both populations, as long as it exhibits a narrow but smooth transition between the outer disk and the gap.

2. The gap edges for both dust populations need to be relatively sharp (i.e. within a width of $\sim$ 10 AU at 60 AU), as constrained independently from the resolved observations at two wavelengths.

3. The sharpness of the gap edge in the H-band imaging requires at least a factor of 1000 depletion for the small dust at the gap edge, and a completely empty gap is fully consistent with the data. On the other hand, the big dust in the same region is depleted only by a factor of $\sim$10 (Mathews et al., 2012, $\log \delta_{\rm gap,b} \sim -0.86 \pm 0.35$). Therefore, we suggest that there is a spatial decoupling between the two dust populations in the outer part of the gap, and it is incompatible with what the dust filtration mechanism predicts, that big dust is more heavily depleted than small dust inside the gap.

With these constraints acquired from our radiative transfer modeling, we comment on several of the leading proposals for the formation of transitional disks and disk evolution in general. The similar gap sizes for both the small and big dust populations and the sharpness of the edges support a dynamical origin of the gap. However, the fact that the small dust has a much heavier depletion inside the gap than the big dust requires additional physics, such as dust growth, to operate inside the gap. An additional problem for multiple planets opening gaps scenario comes from a statistical point of view — current data suggest a higher occurrence rate for giant cavities in disks than giant planets at large separation. Photoevaporation models are consistent with the low accretion rate and the sharp gap edges seen in J1604, however the structures of the dust inside the gap call for more detailed studies on the coupling between dust of different sizes and the gas. Grain growth model alone cannot explain the gaps seen in resolved observations, mostly because it predicts smooth instead of relatively sharp transition in the radial distribution of the dust. On the other hand, models with dust filtration plus dust growth still remain as a possibility for the dust structure, although it does not account for the low accretion rate and the gap in the gas component.

Table 5.1. Parameters in the fiducial model[a]

Parameter	Value
General disk parameters	
$M_{\rm dust}$	$0.085 M_{\rm J}$[b]
Big-to-small-dust mass ratio	0.85/0.15
$R_{\rm out}$	133 AU
R_c	100 AU
Big dust	
$R_{\rm cav,b}$	20 AU
$R_{\rm gap,b}$	70 AU
$h_{\rm b}$ at 100 AU	2 AU
$\beta_{\rm b}$ in the outer disk	1.1
$\beta_{\rm b}$ in the gap region	1.1
$\alpha_{\rm b}$ in the outer disk	0.5
$\alpha_{\rm b}$ in the gap region	0.5
$\delta_{\rm gap,b}$ in the gap region	0.1
Small dust	
$R_{\rm sub}$	0.055 AU
$R^{\rm i}_{\rm gap,s}$	0.07 AU
$R^{\rm o}_{\rm gap,s}$	60 AU
$h_{\rm s}$ at 100 AU	12 AU
$\beta_{\rm b}$ in the outer disk	1.1
$\beta_{\rm b}$ in the gap region	1.1
$\alpha_{\rm s}$ in the outer disk	2.0
$\alpha_{\rm s}$ at the rim	2.0
$\delta_{\rm gap,b}$ in the gap region	0
$\delta_{\rm rim}$ at the rim	10^{-6}

[a]See Section 2 for details.

[b]Including both dust populations.

Table 5.2 Archival SED data for J160421.7-213028

Wavelength	F_ν (mJy)	Note
$B^{a,b}$	64.6	Preibisch & Zinnecker (1999)
$V^{a,b}$	114.9	Zacharias et al. (2005)
$R^{a,b}$	194.8	Preibisch & Zinnecker (1999)
$I^{a,b}$	237.6	Preibisch & Zinnecker (1999)
2MASS $(J)^{a,b}$	216.0 ± 4.6	Cutri et al. (2003)
2MASS $(H)^{a,b}$	275.0 ± 6.1	Cutri et al. (2003)
2MASS $(Ks)^{a,b}$	292.0 ± 5.6	Cutri et al. (2003)
WISE (3.4 μm)[b]	293.4 ± 5.9	Cutri & et al. (2012)
WISE (4.6 μm)[b]	251.0 ± 4.2	Cutri & et al. (2012)
WISE (12 μm)[b]	61.5 ± 0.8	Cutri & et al. (2012)
WISE (22 μm)[b]	152.1 ± 3.4	Cutri & et al. (2012)
IRAC (4.5 μm)	62.7 ± 0.8	Carpenter et al. (2006)
IRAC (8.0 μm)	26.3 ± 0.2	Carpenter et al. (2006)
IRAC (16.0 μm)	26.8 ± 0.2	Carpenter et al. (2006)
IRAS (25 μm)	273.2 ± 60.1	Moshir (1989)
IRAS (60 μm)	2754 ± 170.7	Moshir (1989)
IRAS (100 μm)	4355 ± 1045.2	Moshir (1989)
AKARI (140 μm)	5288.7 ± 1000.0	VizieR II/298
880 μm	164 ± 6	Mathews et al. (2012a)
1.2 mm	67.5 ± 1.4	Mathews et al. (2012b)
2.6 mm	5.1 ± 0.5	Mathews et al. (2012a)
IRS	—	Spitzer Heritage Archive[c]

[a] An extinction law was adopted from Mathis (1990), assuming $A_v = 1$ for J1604 (Preibisch et al., 2002).

[b] Absolute flux conversions in optical, 2MASS, WISE photometric data were adopted from Bessell et al. (1998), Cohen et al. (2003), and Jarrett et al. (2011), respectively.

[c] This work is based in part on observations made with the Spitzer Space Telescope, obtained from the NASA/ IPAC Infrared Science Archive, both of which are operated by the Jet Propulsion Laboratory, California Institute of Technology under a contract with the National Aeronautics and Space Administration.

Table 5.3. Disk Models

Name	Description[a]
Fiducial	Section 3
	Gap Size (See Section 4.1 and Figure 5.6)[b]
SDGapSize50	$R^{\rm o}_{\rm gap,s} = 50$AU
SDGapSize70	$R^{\rm o}_{\rm gap,s} = 70$AU
BDGapSize60	$R_{\rm gap,b} = 60$AU
BDGapSize80	$R_{\rm gap,b} = 80$AU
	Small Dust Gap Depletion (See Section 4.2 and Figure 5.7)[c]
SDGapDep2	$\delta_{\rm gap,s} = 10^{-2}$ at $R^{\rm o}_{\rm gap,s}$, smoothly joins $\delta_{\rm gap,s} = 10^{-6}$ at $R^{\rm i}_{\rm gap,s}$.
SDGapDep3	$\delta_{\rm gap,s} = 10^{-3}$ at $R^{\rm o}_{\rm gap,s}$, smoothly joins $\delta_{\rm gap,s} = 10^{-6}$ at $R^{\rm i}_{\rm gap,s}$.
SDGapDep4	$\delta_{\rm gap,s} = 10^{-4}$ at $R^{\rm o}_{\rm gap,s}$, smoothly joins $\delta_{\rm gap,s} = 10^{-6}$ at $R^{\rm i}_{\rm gap,s}$.
SDGapDep5	$\delta_{\rm gap,s} = 10^{-5}$ at $R^{\rm o}_{\rm gap,s}$, smoothly joins $\delta_{\rm gap,s} = 10^{-6}$ at $R^{\rm i}_{\rm gap,s}$.
SDGapDep6	uniform depletion $\delta_{\rm gap,s} = 10^{-6}$ inside the gap.
SDGapDep7	uniform depletion $\delta_{\rm gap,s} = 10^{-7}$ inside the gap.
SDGapDep8	uniform depletion $\delta_{\rm gap,s} = 10^{-8}$ inside the gap.
SDGapDep5-ThinGap1	Same as SDGapDep5, but $h_{\rm s}$ inside the gap is reduced to 1/6.
SDGapDep5-ThinGap2	Same as SDGapDep5, but $h_{\rm s}$ inside the gap is reduced to 1/3.
SDGapDep5-ThinGap3	Same as SDGapDep5, but $h_{\rm s}$ inside the gap is reduced to 2/3.
	Big Dust Gap Structure (See Section 4.3 and Figure 5.8)[d]
BDGapDep03	A uniform gap depletion factor of $\delta_{\rm gap,b} = 0.3$
BDGapDep0	A uniform gap depletion factor of $\delta_{\rm gap,b} = 0$
BDGapSmo1	$\delta_{\rm gap,b} = 1$, $\alpha_{\rm s} = -1.5$ inside the gap
BDGapSmo1-2	$\delta_{\rm gap,b} = 1$, $\alpha_{\rm s} = -1.5$ inside the gap, big dust is extended to $R_{\rm sub}$.
BDGapSmo2	$\delta_{\rm gap,b} = 1$, $\alpha_{\rm s} = -3$ inside the gap, big dust is extended to $R_{\rm sub}$.
	Smooth Gap Edge (See Section 4.4 and Figure 5.9)[g]
SmoothEdge1	$\alpha_{\rm b} = -15$ and $\alpha_{\rm s} = -4$ from 60 to 70 AU.
SmoothEdge2	$\alpha_{\rm b} = -15$ and $\alpha_{\rm s} = -8$ from 60 to 70 AU.
SmoothEdge3	$\alpha_{\rm b} = -15$ and $\alpha_{\rm s} = -15$ from 60 to 70 AU.

[a]Description of the difference between various models and the fiducial model.

[b]The effect of the gap size on both the big and small dust.

[c]The effect of small dust population depletion inside the gap. The number at the end of the model name indicates the depletion factor at the gap edge. For models SDCavDep2 to SDCavDep6, the depletion factor at the inner gap edge ($R^{\rm i}_{\rm gap,s}$) is fixed so that the surface density there smoothly joins the rim. Models SDGapDep7 and SDGapDep8 has a uniform depletion factor inside the gap. Models SDGapDep5-ThinGapX have the same dust distribution as in SDGapDep5, but with smaller scale height inside the gap.

[d]The models in the BDGapDep series feature a uniform depletion, while the models in the BDGapSmo series have a continuous surface density distribution.

[e]Different $\alpha_{\rm s}$ (SDSlope) and $\alpha_{\rm b}$ (BDSlope). We vary $\delta_{\rm rim}$ to keep the rim structure the same in model SDSlope.

[f]Different $\Sigma^{\rm s}$ at the rim.

[g]Various models which have a transient region from 60 to 70 AU (i.e. instead of a discontinuous gap edge) to join the outer disk to the gap for both dust populations.

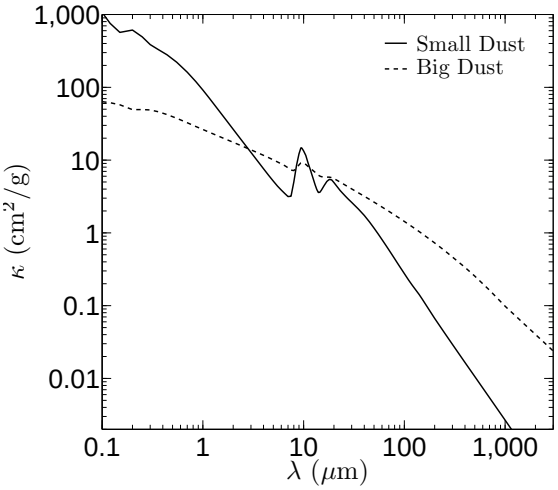

(a)

Figure 5.1 Opacity κ for different dust populations used in this study (showing the dust+gas opacity assuming a gas-to-dust-ratio of 100).

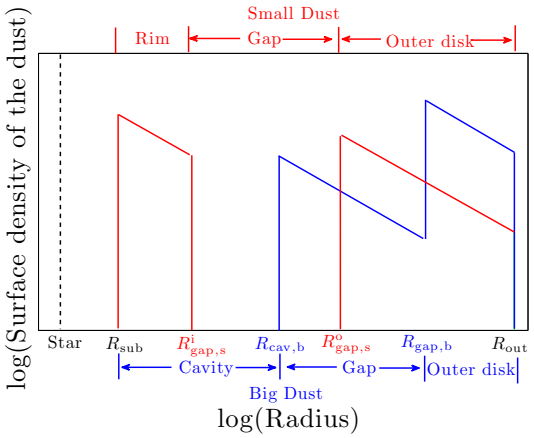

(a)

Figure 5.2 Schematic illustration of the disk+cavity structure for the small (red) and big (blue) populations. From inside out, the small dust has an inner rim structure located at the sublimation radius R_{sub} to $R^{i}_{gap,s}$, a depleted gap region from $R^{i}_{gap,s}$ to $R^{o}_{gap,s}$, and an outer disk from $R^{o}_{gap,s}$ to R_{out} (labeled on top of the figure), while the big dust has an empty cavity inside $R_{cav,b}$, a depleted gap region from $R_{cav,b}$ to $R_{gap,b}$, and an outer disk from $R_{gap,b}$ to R_{out} (labeled at bottom of the figure). See Section 2 for details.

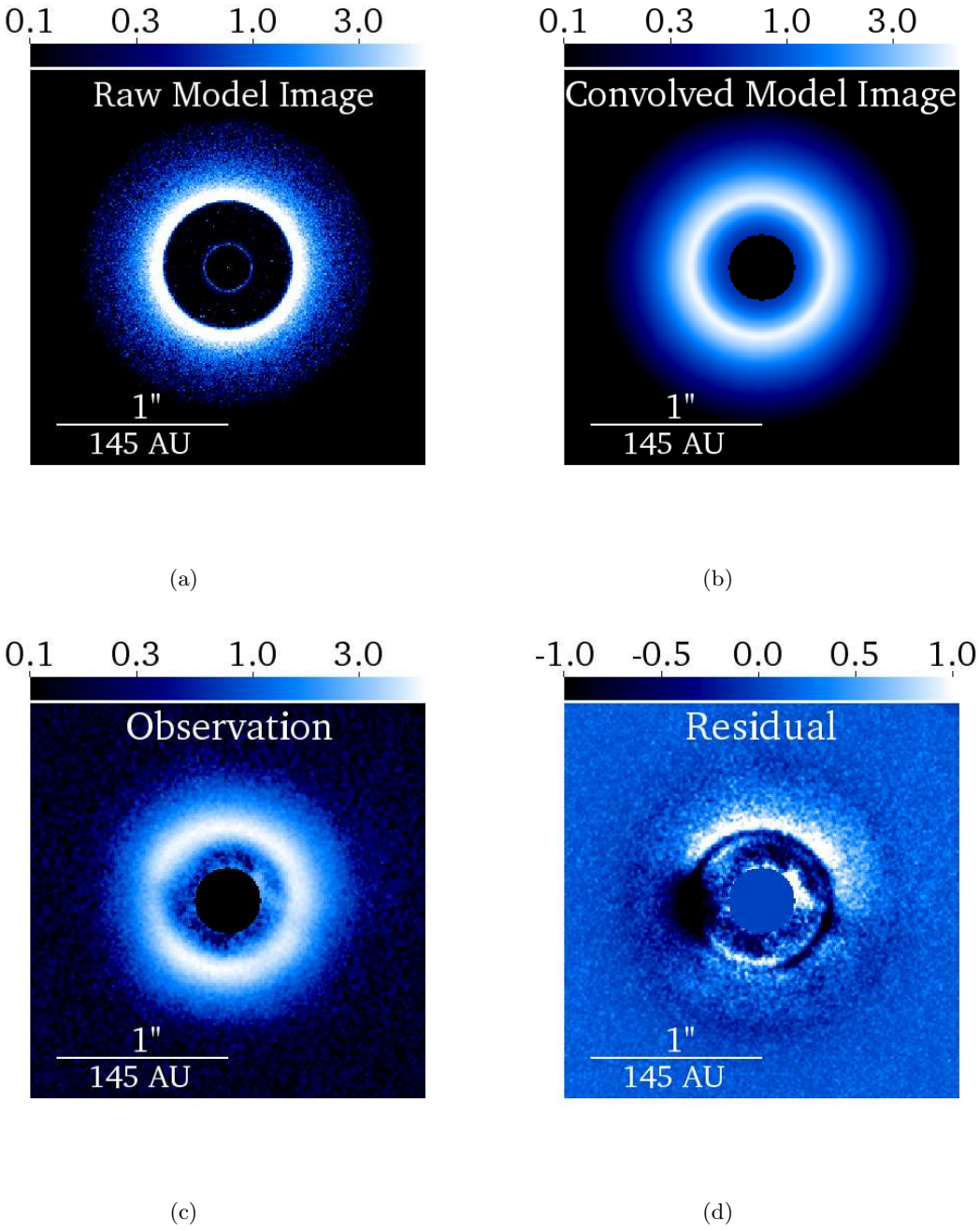

Figure 5.3 Model polarized scattered light images at H-band from our fiducial model and the SEEDS observation of J1604 (S. Mayama et al. 2012 submitted), showing the surface brightness in unit of mJy/arcsec^2. The convolved model image is the raw model image convolved by a HiCIAO PSF (Section 2). The observed SEEDS image is not smoothed. The residual image is the convolved model image subtracted from the SEEDS image. The mask at the center in the convolved model image and the SEEDS image indicate a $0.2''$ (radius) inner working angle. The residual image is on linear scale, while the other three are on log scale with the same color scheme. The model image and the observed image of J1604 match well. See Section 3 for details.

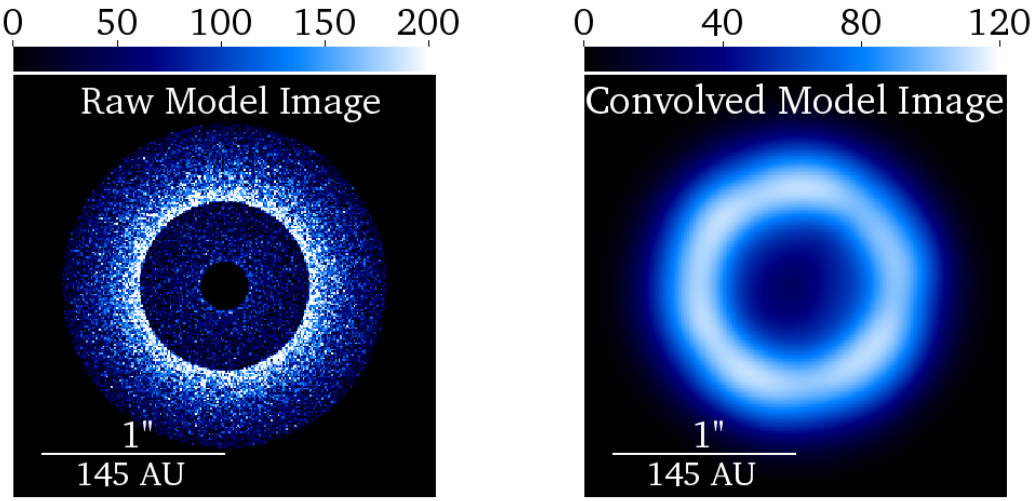

(a) (b)

Figure 5.4 Model 880μm images from the fiducial model, showing the surface brightness. We convolve the raw model image by a Gaussian Kernel with resolution 0.34″ to match the resolution in SMA observation (Mathews et al., 2012). Both panels are on linear scale with the unit of mJy/arcsec^2. See Section 3 for details.

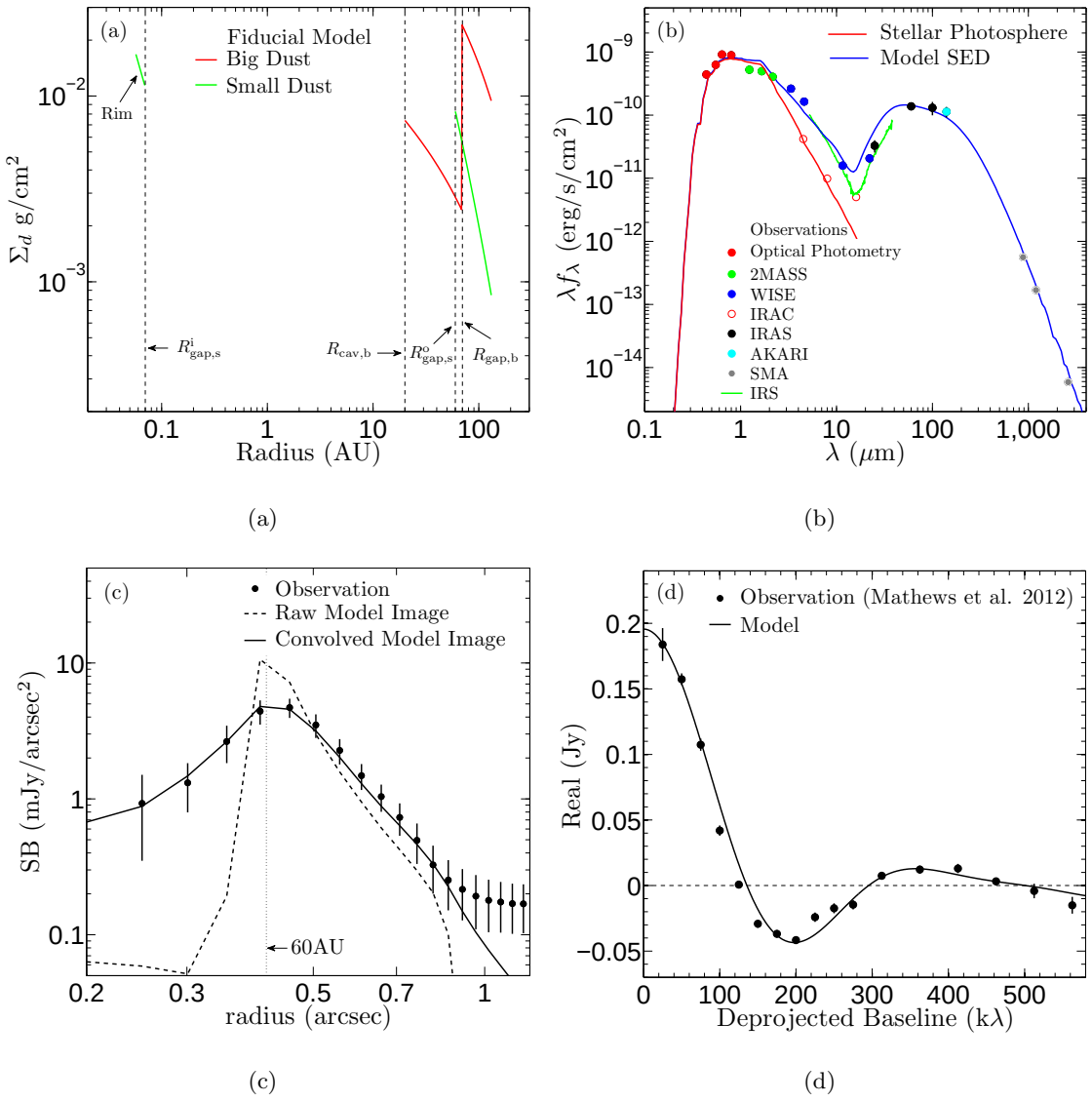

(a) (b)

(c) (d)

Figure 5.5 The characteristics of the fiducial model. The assumed surface density profile for both dust populations (a), SED (b), azimuthally averaged SBRP of the model H-band images (c), and the visibility curve of the model 880μ continuum emission (d). The SED data is collected from the literature (Table 5.2). The small vertical bars on top of the observational data points in (b) and (d) represent observational error bars, while in (c) they represent the root mean square scatter of the pixels in each annulus. The fiducial model reproduces the SED, SBRP, and visibility curve well. See Section 3 for details.

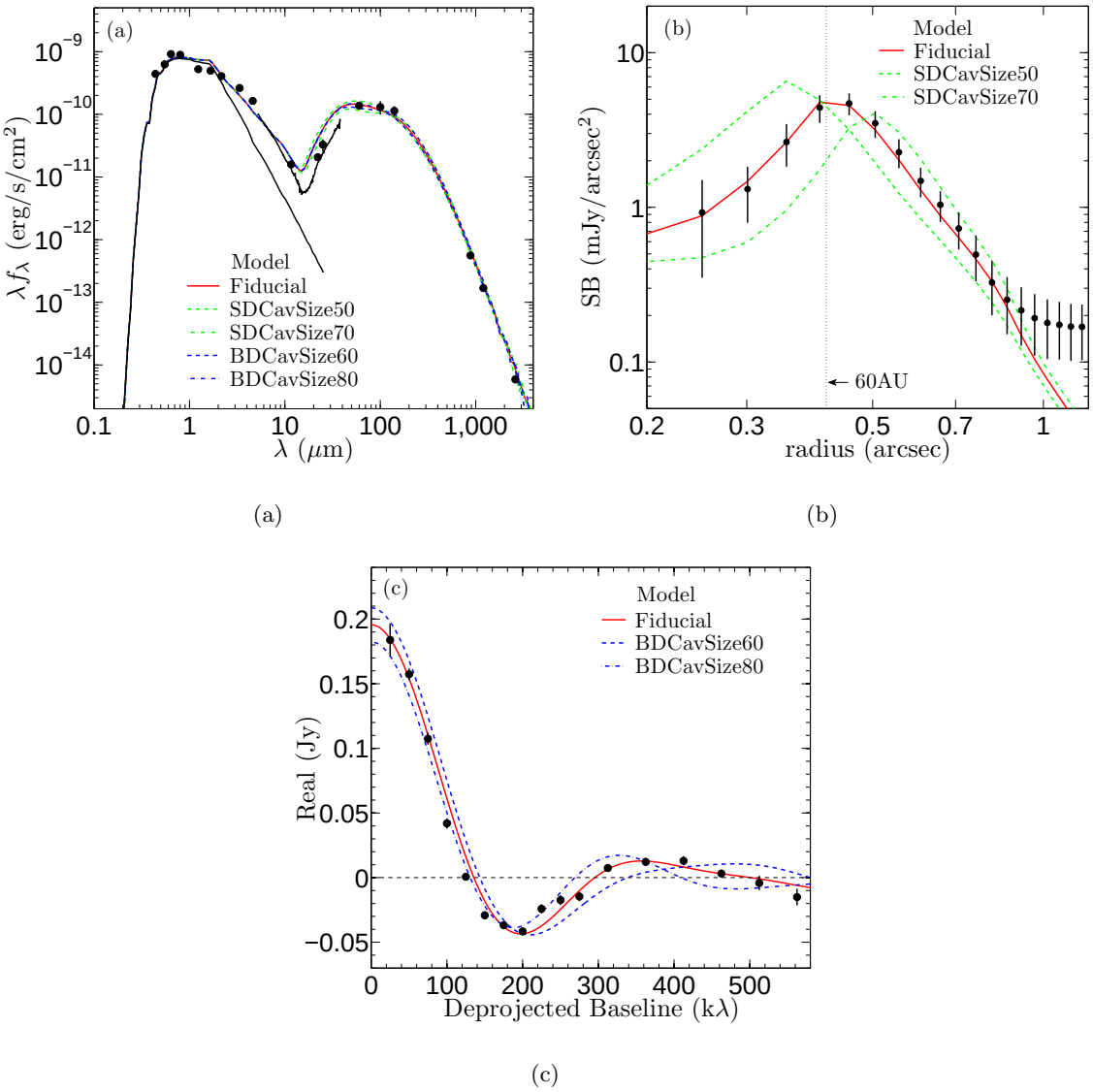

(a) (b) (c)

Figure 5.6 The effect of the gap size on the SED (a), azimuthally averaged SBRP of the H-band image (b), and the 880μm visibility curve (c). The IRAC data points are not shown on the SED plot, due to its inconsistency with WISE data and IRS spectrum (same in Figures 5.7-5.9). Within the parameter space we explore here, different gap outer radius makes no significant effect on the SED. However, the size of the gap in small dust has a prominent effect on the H-band images, while the size of the gap in big dust strongly affects the 880μm visibility curve. See Section 4.1 for details.

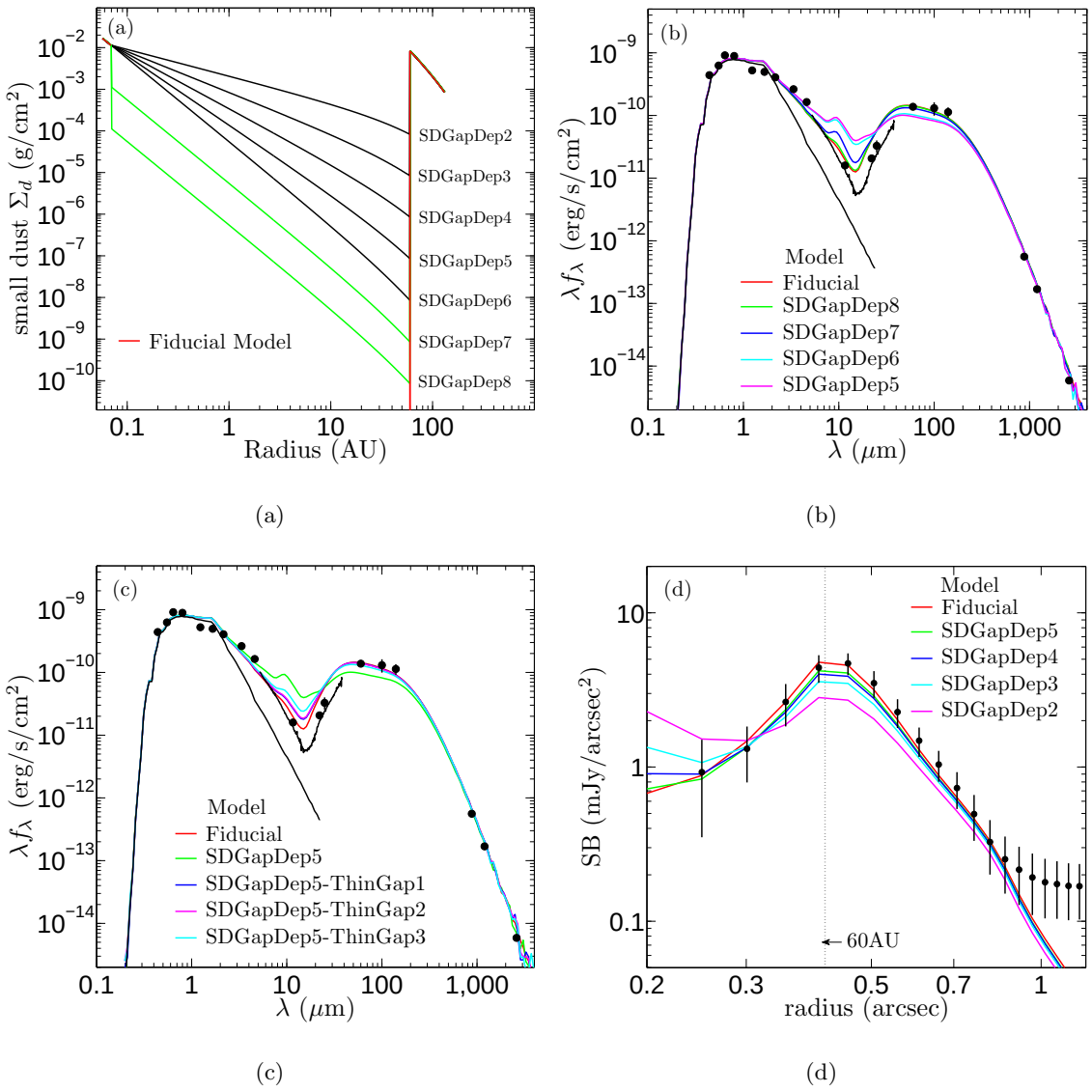

(a) (b)

(c) (d)

Figure 5.7 The effect of the small dust depletion inside the gap region (a, showing the $\Sigma_s(R)$ profile) on the SED (b,c) and azimuthally averaged SBRP of the H-band image (d). The SED requires a very substantial depletion of the small dust in the inner part of the the gap, with an upper limit of Σ_s of several $\times 10^{-3}$g/cm^2 at $\sim 0.1-1$ AU scale. The H-band image, particularly the contrast of the gap edge, provides an independent constraint on $\delta_{\rm gap,s}$ in the outer part of the gap — at least a 3 orders of magnitude depletion is needed. See Section 4.2 for details.

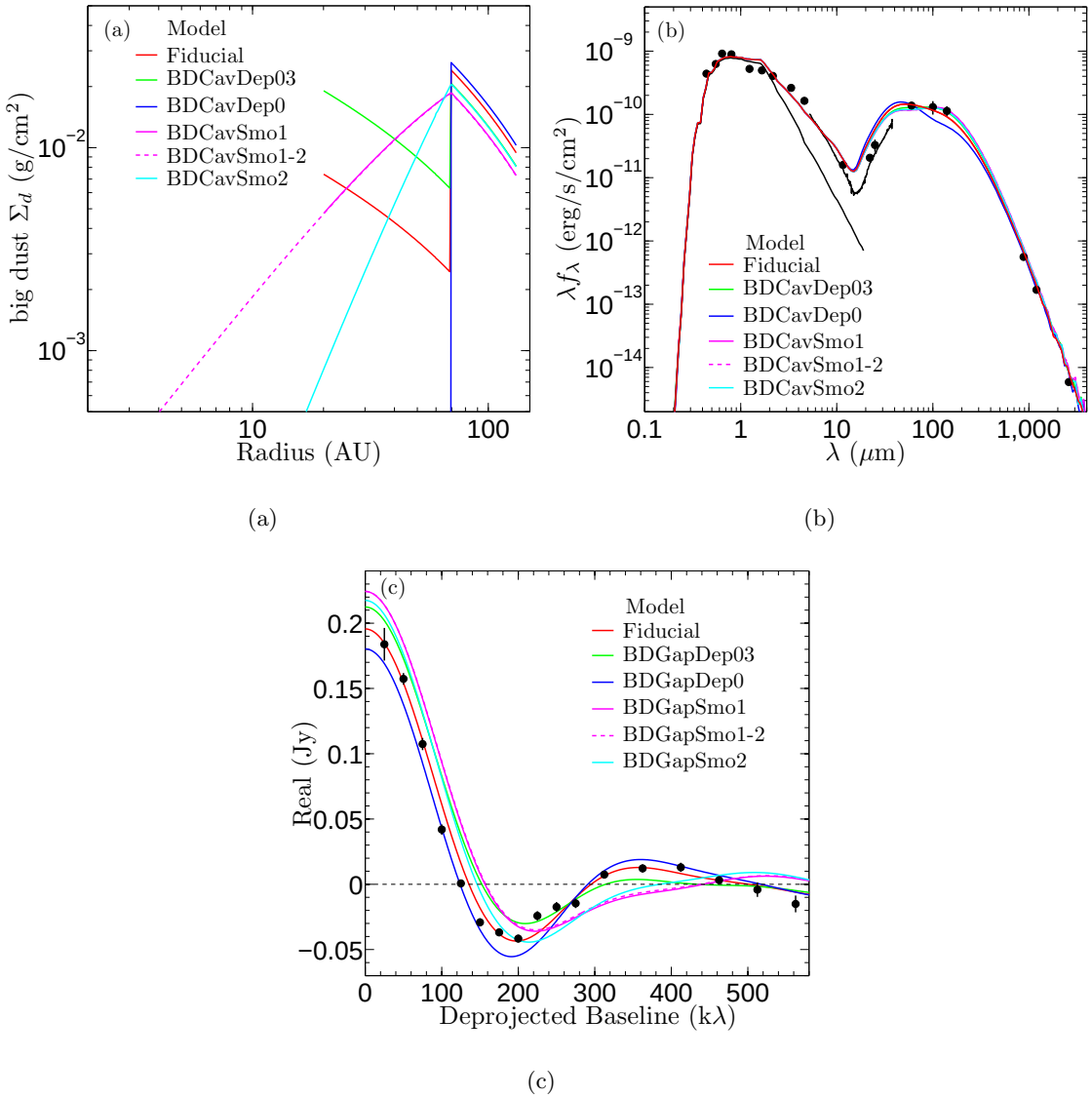

Figure 5.8 The effect of the big dust structure inside the gap (a, showing the Σ_b profile) on the SED (b) and visibility curve of the 880μm continuum emission (c). Various gap structures for big dust have only weak effect on the SED (the MIR data points around $\sim 100\mu$m requires some amount of big dust inside the gap). On the other hand, the visibility curve is much more sensitive to the distribution of big dust inside the gap. It requires roughly a factor of 10 depletion for the big dust inside the gap with a relatively sharp gap edge (see also Mathews et al. 2012). A smooth gap structure, as in various BDCavSmo models, cannot reproduce the observations. See Section 4.3 for details.

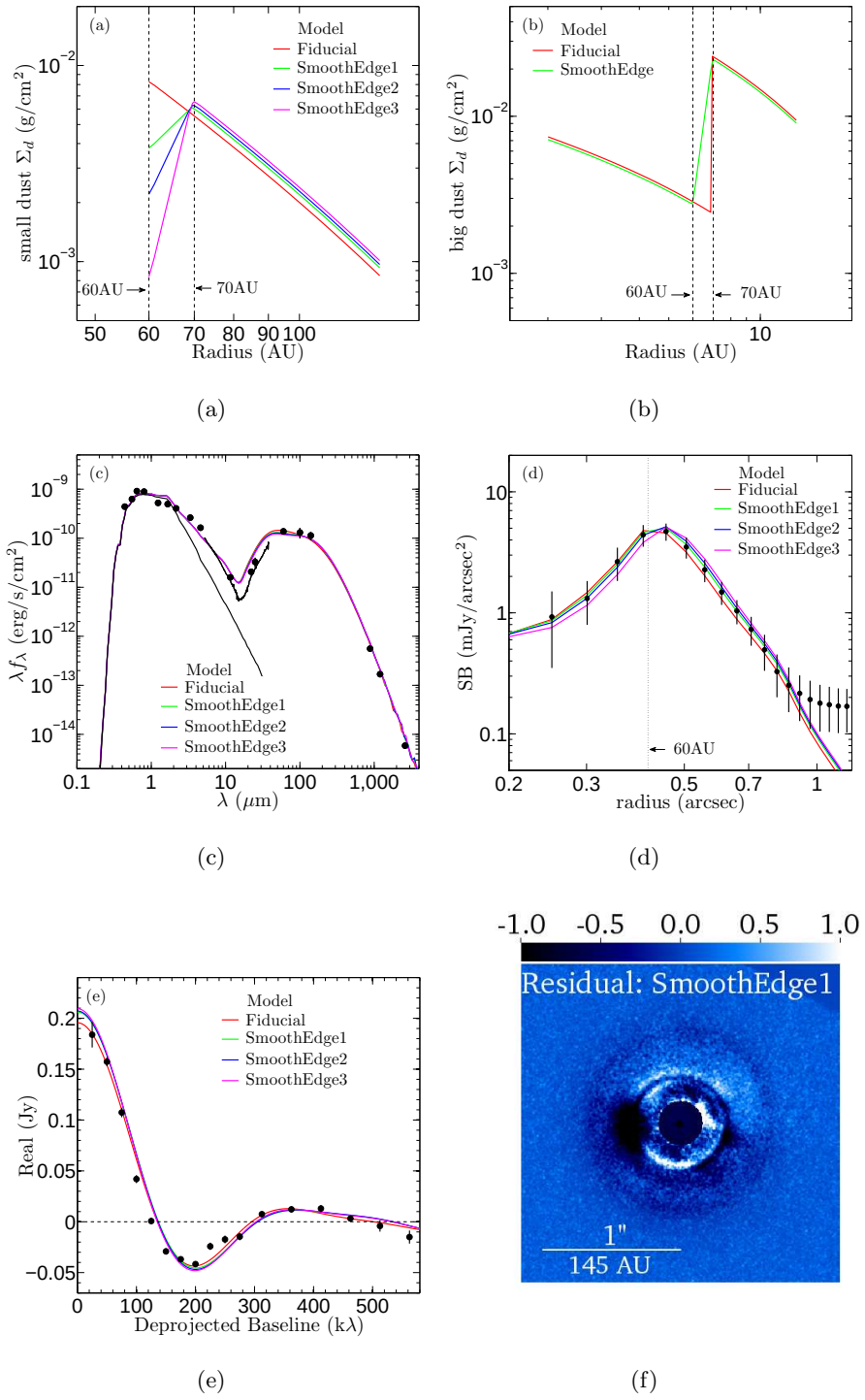

Figure 5.9 Various models with a transient structure at 60 to 70 AU, "smoothly" joining the outer disk to the gap for both dust populations. Panel (a) and (b) show the surface density profile for the small and big dust, while panel (c), (d) and (e) show the SED, azimuthally averaged SBRP of the H-band image, and the 880μm visibility curve for these models. The last panel shows the residual of the H-band image fitting (model image subtracted from the SEEDS image) for model SmoothEdge1. All these models are grossly consistent with observations. See Section 4.4 for details.

Bibliography

Alexander, R. D. & Armitage, P. J. 2007, MNRAS, 375, 500

Andrews, S. M., Wilner, D. J., Espaillat, C., Hughes, A. M., Dullemond, C. P., McClure, M. K., Qi, C., & Brown, J. M. 2011, ApJ, 732, 42

Andrews, S. M., Wilner, D. J., Hughes, A. M., Qi, C., & Dullemond, C. P. 2009, ApJ, 700, 1502

Andrews, S. M., Wilner, D. J., Hughes, A. M., Qi, C., Rosenfeld, K. A., Öberg, K. I., Birnstiel, T., Espaillat, C., Cieza, L. A., Williams, J. P., Lin, S.-Y., & Ho, P. T. P. 2012, ApJ, 744, 162

Artymowicz, P. & Lubow, S. H. 1994, ApJ, 421, 651

Berger, J. P. & Segransan, D. 2007, New A Rev., 51, 576

Bessell, M. S., Castelli, F., & Plez, B. 1998, A&A, 333, 231

Biller, B., Lacour, S., Juhász, A., Benisty, M., Chauvin, G., Olofsson, J., Pott, J.-U., Müller, A., Sicilia-Aguilar, A., Bonnefoy, M., Tuthill, P., Thebault, P., Henning, T., & Crida, A. 2012, ApJ, 753, L38

Birnstiel, T., Andrews, S. M., & Ercolano, B. 2012, A&A, 544, A79

Birnstiel, T., Ricci, L., Trotta, F., Dullemond, C. P., Natta, A., Testi, L., Dominik, C., Henning, T., Ormel, C. W., & Zsom, A. 2010, A&A, 516, L14

Brown, J. M., Blake, G. A., Qi, C., Dullemond, C. P., Wilner, D. J., & Williams, J. P. 2009, ApJ, 704, 496

Bryden, G., Chen, X., Lin, D. N. C., Nelson, R. P., & Papaloizou, J. C. B. 1999, ApJ, 514, 344

Calvet, N., D'Alessio, P., Watson, D. M., Franco-Hernández, R., Furlan, E., Green, J., Sutter, P. M., Forrest, W. J., Hartmann, L., Uchida, K. I., Keller, L. D., Sargent, B., Najita, J., Herter, T. L., Barry, D. J., & Hall, P. 2005, ApJ, 630, L185

Chiang, E. & Murray-Clay, R. 2007, Nature Physics, 3, 604

Chiang, E. I. & Goldreich, P. 1997, ApJ, 490, 368

Cieza, L. A., Mathews, G. S., Williams, J. P., Ménard, F. C., Kraus, A. L., Schreiber, M. R., Romero, G. A., Orellana, M., & Ireland, M. J. 2012a, ApJ, 752, 75

Cieza, L. A., Schreiber, M. R., Romero, G. A., Mora, M. D., Merin, B., Swift, J. J., Orellana, M., Williams, J. P., Harvey, P. M., & Evans, II, N. J. 2010, ApJ, 712, 925

Cieza, L. A., Schreiber, M. R., Romero, G. A., Williams, J. P., Rebassa-Mansergas, A., & Merín, B. 2012b, ApJ, 750, 157

Clarke, C. J., Gendrin, A., & Sotomayor, M. 2001, MNRAS, 328, 485

Cohen, M., Wheaton, W. A., & Megeath, S. T. 2003, AJ, 126, 1090

Cutri, R. M. & et al. 2012, VizieR Online Data Catalog, 2311, 0

Cutri, R. M., Skrutskie, M. F., van Dyk, S., Beichman, C. A., Carpenter, J. M., Chester, T., Cambresy, L., Evans, T., Fowler, J., Gizis, J., Howard, E., Huchra, J., Jarrett, T., Kopan, E. L., Kirkpatrick, J. D., Light, R. M., Marsh, K. A., McCallon, H., Schneider, S., Stiening, R., Sykes, M., Weinberg, M., Wheaton, W. A., Wheelock, S., & Zacarias, N. 2003, VizieR Online Data Catalog, 2246, 0

Dahm, S. E. & Carpenter, J. M. 2009, AJ, 137, 4024

D'Alessio, P., Calvet, N., Hartmann, L., Franco-Hernández, R., & Servín, H. 2006, ApJ, 638, 314

de Zeeuw, P. T., Hoogerwerf, R., de Bruijne, J. H. J., Brown, A. G. A., & Blaauw, A. 1999, AJ, 117, 354

Dodson-Robinson, S. E. & Salyk, C. 2011, ApJ, 738, 131

Draine, B. T. 2011, Physics of the Interstellar and Intergalactic Medium

Dullemond, C. P. & Dominik, C. 2004a, A&A, 417, 159

Dullemond, C. P. & Dominik, C. 2004b, A&A, 421, 1075

Dullemond, C. P. & Dominik, C. 2005, A&A, 434, 971

Dullemond, C. P., van Zadelhoff, G. J., & Natta, A. 2002, A&A, 389, 464

Espaillat, C., Calvet, N., D'Alessio, P., Bergin, E., Hartmann, L., Watson, D., Furlan, E., Najita, J., Forrest, W., McClure, M., Sargent, B., Bohac, C., & Harrold, S. T. 2007a, ApJ, 664, L111

Espaillat, C., Calvet, N., D'Alessio, P., Hernández, J., Qi, C., Hartmann, L., Furlan, E., & Watson, D. M. 2007b, ApJ, 670, L135

Espaillat, C., Calvet, N., Luhman, K. L., Muzerolle, J., & D'Alessio, P. 2008, ApJ, 682, L125

Furlan, E., Hartmann, L., Calvet, N., D'Alessio, P., Franco-Hernández, R., Forrest, W. J., Watson, D. M., Uchida, K. I., Sargent, B., Green, J. D., Keller, L. D., & Herter, T. L. 2006, ApJS, 165, 568

Garaud, P. 2007, ApJ, 671, 2091

Hartmann, L., Calvet, N., Gullbring, E., & D'Alessio, P. 1998, ApJ, 495, 385

Hashimoto, J., Dong, R., Kudo, T., Honda, M., McClure, M. K., Zhu, Z., Muto, T., Wisniewski, J., Abe, L., Brandner, W., Brandt, T., Carson, J., Egner, S., Feldt, M., Fukagawa, M., Goto, M., Grady, C. A., Guyon, O., Hayano, Y., Hayashi, M., Hayashi, S., Henning, T., Hodapp, K., Ishii, M., Iye, M., Janson, M., Kandori, R., Knapp, G., Kusakabe, N., Kuzuhara, M., Kwon, J., Matsuo, T., Mayama, S., McElwain, M. W., Miyama, S., Morino, J.-I., Moro-Martin, A., Nishimura, T., Pyo, T.-S., Serabyn, G., Suenaga, T., Suto, H., Suzuki, R., Takahashi, Y., Takami, M., Takato, N., Terada, H., Thalmann, C., Tomono, D., Turner, E. L., Watanabe, M., Yamada, T., Takami, H., Usuda, T., & Tamura, M. 2012, ApJ, 758, L19

Hashimoto, J., Tamura, M., Muto, T., Kudo, T., Fukagawa, M., Fukue, T., Goto, M., Grady, C. A., Henning, T., Hodapp, K., Honda, M., Inutsuka, S., Kokubo, E., Knapp, G., McElwain, M. W., Momose, M., Ohashi, N., Okamoto, Y. K., Takami, M., Turner, E. L., Wisniewski, J., Janson, M., Abe, L., Brandner, W., Carson, J., Egner, S., Feldt, M., Golota, T., Guyon, O., Hayano, Y., Hayashi, M., Hayashi, S., Ishii, M., Kandori, R., Kusakabe, N., Matsuo, T., Mayama, S., Miyama, S., Morino, J.-I., Moro-Martin, A., Nishimura, T., Pyo, T.-S., Suto, H., Suzuki, R., Takato, N., Terada, H., Thalmann, C., Tomono, D., Watanabe, M., Yamada, T., Takami, H., & Usuda, T. 2011, ApJ, 729, L17

Hinkley, S., Oppenheimer, B. R., Soummer, R., Brenner, D., Graham, J. R., Perrin, M. D., Sivaramakrishnan, A., Lloyd, J. P., Roberts, Jr., L. C., & Kuhn, J. 2009, ApJ, 701, 804

Honda, M., Maaskant, K., Okamoto, Y. K., Kataza, H., Fukagawa, M., Waters, L. B. F. M., Dominik, C., Tielens, A. G. G. M., Mulders, G. D., Min, M., Yamashita, T., Fujiyoshi, T., Miyata, T., Sako, S., Sakon, I., Fujiwara, H., & Onaka, T. 2012, ApJ, 752, 143

Huélamo, N., Lacour, S., Tuthill, P., Ireland, M., Kraus, A., & Chauvin, G. 2011, A&A, 528, L7

Hughes, A. M., Andrews, S. M., Espaillat, C., Wilner, D. J., Calvet, N., D'Alessio, P., Qi, C., Williams, J. P., & Hogerheijde, M. R. 2009, ApJ, 698, 131

Hughes, A. M., Andrews, S. M., Wilner, D. J., Meyer, M. R., Carpenter, J. M., Qi, C., Hales, A. S., Casassus, S., Hogerheijde, M. R., Mamajek, E. E., Wolf, S., Henning, T., & Silverstone, M. D. 2010, AJ, 140, 887

Hughes, A. M., Wilner, D. J., Calvet, N., D'Alessio, P., Claussen, M. J., & Hogerheijde, M. R. 2007, ApJ, 664, 536

Hughes, A. M., Wilner, D. J., Qi, C., & Hogerheijde, M. R. 2008, ApJ, 678, 1119

Isella, A., Natta, A., Wilner, D., Carpenter, J. M., & Testi, L. 2010, ApJ, 725, 1735

Isella, A., Pérez, L. M., & Carpenter, J. M. 2012, ApJ, 747, 136

Jarrett, T. H., Cohen, M., Masci, F., Wright, E., Stern, D., Benford, D., Blain, A., Carey, S., Cutri, R. M., Eisenhardt, P., Lonsdale, C., Mainzer, A., Marsh, K., Padgett, D., Petty, S., Ressler, M., Skrutskie, M., Stanford, S., Surace, J., Tsai, C. W., Wheelock, S., & Yan, D. L. 2011, ApJ, 735, 112

Kim, S.-H., Martin, P. G., & Hendry, P. D. 1994, ApJ, 422, 164

Kraus, A. L. & Ireland, M. J. 2012, ApJ, 745, 5

Kusakabe, N., Grady, C. A., Sitko, M. L., Hashimoto, J., Kudo, T., Fukagawa, M., Muto, T., Wisniewski, J. P., Min, M., Mayama, S., Werren, C., Day, A. N., Beerman, L. C., Lynch, D. K., Russell, R. W., Brafford, S. M., Kuzuhara, M., Brandt, T. D., Abe, L., Brandner, W., Carson, J., Egner, S., Feldt, M., Goto, M., Guyon, O., Hayano, Y., Hayashi, M., Hayashi, S. S., Henning, T., Hodapp, K. W., Ishii, M., Iye, M., Janson, M., Kandori, R., Knapp, G. R., Matsuo, T., McElwain, M. W., Miyama, S., Morino, J.-I., Moro-Martin, A., Nishimura, T., Pyo, T.-S., Suto, H., Suzuki, R., Takami, M., Takato, N., Terada, H., Thalmann, C., Tomono, D., Turner, E. L., Watanabe, M., Yamada, T., Takami, H., Usuda, T., & Tamura, M. 2012, ApJ, 753, 153

Lafrenière, D., Doyon, R., Marois, C., Nadeau, D., Oppenheimer, B. R., Roche, P. F., Rigaut, F., Graham, J. R., Jayawardhana, R., Johnstone, D., Kalas, P. G., Macintosh, B., & Racine, R. 2007, ApJ, 670, 1367

Lin, D. N. C. & Papaloizou, J. 1986a, ApJ, 307, 395

Lin, D. N. C. & Papaloizou, J. 1986b, ApJ, 309, 846

Marois, C., Macintosh, B., Barman, T., Zuckerman, B., Song, I., Patience, J., Lafrenière, D., & Doyon, R. 2008, Science, 322, 1348

Marois, C., Zuckerman, B., Konopacky, Q. M., Macintosh, B., & Barman, T. 2010, Nat, 468, 1080

Mathews, G. S., Williams, J. P., & Ménard, F. 2012, ApJ, 753, 59

Mathis, J. S. 1990, ARA&A, 28, 37

Mayama, S., Hashimoto, J., Muto, T., Tsukagoshi, T., Kusakabe, N., Kuzuhara, M., Takahashi, Y., Kudo, T., Dong, R., Fukagawa, M., Takami, M., Momose, M., Wisniewski, J. P., Follette, K., Abe, L., Akiyama, E., Brandner, W., Brandt, T., Carson, J., Egner, S., Feldt, M., Goto, M., Grady, C. A., Guyon, O., Hayano, Y., Hayashi, M., Hayashi, S., Henning, T., Hodapp, K. W., Ishii, M., Iye, M., Janson, M., Kandori, R., Kwon, J., Knapp, G. R., Matsuo, T., McElwain, M. W., Miyama, S., Morino, J.-I., Moro-Martin, A., Nishimura, T., Pyo, T.-S., Serabyn, E., Suto, H., Suzuki, R., Takato, N., Terada, H., Thalmann, C., Tomono, D., Turner, E. L., Watanabe, M., Yamada, T., Takami, H., Usuda, T., & Tamura, M. 2012, ApJ, 760, L26

Melis, C., Zuckerman, B., Rhee, J. H., Song, I., Murphy, S. J., & Bessell, M. S. 2012, Nat, 487, 74

Moshir, M. 1989, IRAS Faint Source Survey, Explanatory supplement version 1 and tape

Muto, T., Grady, C. A., Hashimoto, J., Fukagawa, M., Hornbeck, J. B., Sitko, M., Russell, R., Werren, C., Curé, M., Currie, T., Ohashi, N., Okamoto, Y., Momose, M., Honda, M., Inutsuka, S., Takeuchi, T., Dong, R., Abe, L., Brandner, W., Brandt, T., Carson, J., Egner, S., Feldt, M., Fukue, T., Goto, M., Guyon, O., Hayano, Y., Hayashi, M., Hayashi, S., Henning, T., Hodapp, K. W., Ishii, M., Iye, M., Janson, M., Kandori, R., Knapp, G. R., Kudo, T., Kusakabe, N., Kuzuhara, M., Matsuo, T., Mayama, S., McElwain, M. W., Miyama, S., Morino, J.-I., Moro-Martin, A., Nishimura, T., Pyo, T.-S., Serabyn, E., Suto, H., Suzuki, R., Takami, M., Takato, N., Terada, H., Thalmann, C., Tomono, D., Turner, E. L., Watanabe, M., Wisniewski, J. P., Yamada, T., Takami, H., Usuda, T., & Tamura, M. 2012, ApJ, 748, L22

Owen, J. E. & Clarke, C. J. 2012, MNRAS, 426, L96

Owen, J. E., Clarke, C. J., & Ercolano, B. 2012, MNRAS, 422, 1880

Owen, J. E., Ercolano, B., & Clarke, C. J. 2011, MNRAS, 412, 13

Owen, J. E., Ercolano, B., Clarke, C. J., & Alexander, R. D. 2010, MNRAS, 401, 1415

Paardekooper, S.-J. & Mellema, G. 2006, A&A, 453, 1129

Piétu, V., Dutrey, A., Guilloteau, S., Chapillon, E., & Pety, J. 2006, A&A, 460, L43

Preibisch, T., Brown, A. G. A., Bridges, T., Guenther, E., & Zinnecker, H. 2002, AJ, 124, 404

Preibisch, T. & Zinnecker, H. 1999, AJ, 117, 2381

Qi, C., Ho, P. T. P., Wilner, D. J., Takakuwa, S., Hirano, N., Ohashi, N., Bourke, T. L., Zhang, Q., Blake, G. A., Hogerheijde, M., Saito, M., Choi, M., & Yang, J. 2004, ApJ, 616, L11

Rice, W. K. M., Armitage, P. J., Wood, K., & Lodato, G. 2006, MNRAS, 373, 1619

Skrutskie, M. F., Dutkevitch, D., Strom, S. E., Edwards, S., Strom, K. M., & Shure, M. A. 1990, AJ, 99, 1187

Strom, K. M., Strom, S. E., Edwards, S., Cabrit, S., & Skrutskie, M. F. 1989, AJ, 97, 1451

Tamura, M. 2009, in American Institute of Physics Conference Series, Vol. 1158, American Institute of Physics Conference Series, ed. T. Usuda, M. Tamura, & M. Ishii, 11–16

Tanii, R., Itoh, Y., Kudo, T., Hioki, T., Oasa, Y., Gupta, R., Sen, A. K., Wisniewski, J. P., Muto, T., Grady, C. A., Hashimoto, J., Fukagawa, M., Mayama, S., Hornbeck, J., Sitko, M. L., Russell, R. W., Werren, C., Curé, M., Currie, T., Ohashi, N., Okamoto, Y., Momose, M., Honda, M., Inutsuka, S.-i., Takeuchi, T., Dong, R., Abe, L., Brandner, W., Brandt, T. D., Carson, J., Egner, S. E., Feldt, M., Fukue, T., Goto, M., Guyon, O., Hayano, Y., Hayashi, M., Hayashi, S. S., Henning, T., Hodapp, K. W., Ishii, M., Iye, M., Janson, M., Kandori, R., Knapp, G. R., Kusakabe, N., Kuzuhara, M., Matsuo, T., McElwain, M. W., Miyama, S., Morino, J.-i., Moro-Martín, A., Nishimura, T., Pyo, T.-S., Serabyn, E., Suto, H., Suzuki, R., Takami, M., Takato, N., Terada, H., Thalmann, C., Tomono, D., Turner, E. L., Watanabe, M., Yamada, T., Takami, H., Usuda, T., & Tamura, M. 2012, PASJ, 64, 124

Thalmann, C., Grady, C. A., Goto, M., Wisniewski, J. P., Janson, M., Henning, T., Fukagawa, M., Honda, M., Mulders, G. D., Min, M., Moro-Martín, A., McElwain, M. W., Hodapp, K. W., Carson, J., Abe, L., Brandner, W., Egner, S., Feldt, M., Fukue, T., Golota, T., Guyon, O., Hashimoto, J., Hayano, Y., Hayashi, M., Hayashi, S., Ishii, M., Kandori, R., Knapp, G. R., Kudo, T., Kusakabe, N., Kuzuhara, M., Matsuo, T., Miyama, S., Morino, J.-I., Nishimura, T., Pyo, T.-S., Serabyn, E., Shibai, H., Suto, H., Suzuki, R., Takami, M., Takato, N., Terada, H., Tomono, D., Turner, E. L., Watanabe, M., Yamada, T., Takami, H., Usuda, T., & Tamura, M. 2010, ApJ, 718, L87

Whitney, B. A., Wood, K., Bjorkman, J. E., & Cohen, M. 2003a, ApJ, 598, 1079

Whitney, B. A., Wood, K., Bjorkman, J. E., & Wolff, M. J. 2003b, ApJ, 591, 1049

Williams, J. P. & Cieza, L. A. 2011, ARA&A, 49, 67

Wood, K., Wolff, M. J., Bjorkman, J. E., & Whitney, B. 2002, ApJ, 564, 887

Zhu, Z., Nelson, R. P., Dong, R., Espaillat, C., & Hartmann, L. 2012, ApJ, 755, 6

Zhu, Z., Nelson, R. P., Hartmann, L., Espaillat, C., & Calvet, N. 2011, ApJ, 729, 47